The Spin Dependent Momentum Distribution of the Neutron and the Proton in Helium-3

by

Kevin Kar Lee

B.S. in Physics

California Institute of Technology

June 1988

Submitted to the Department of Physics

in partial fulfillment of the requirements for the degree of

Doctor of Philosophy

at the

MASSACHUSETTS INSTITUTE OF TECHNOLOGY

February 1996

Signature of Author _____

Department of Physics

January 22, 1996

Certified by _____

Associate Professor Richard G. Milner

Thesis Supervisor

Accepted by _____

Professor George F. Koster

Chairman of the Graduate Committee

The Spin Dependent Momentum Distribution of the Neutron and the Proton in Helium-3

by

Kevin Kar Lee

Submitted to the Department of Physics

on January 22, 1996, in partial fulfillment of the

requirements for the degree of

Doctor of Philosophy

Abstract

A polarized ^{3}He internal gas target which delivered 50% polarized atoms at a flow rate of 1×10^{17} atoms/sec was developed. This target was used in the experiment CE-25 to measure the analyzing powers and spin correlations parameters for the $^3\overrightarrow{\mathrm{He}}(\overrightarrow{\mathrm{p}},2\mathrm{p})$ and $^3\overrightarrow{\mathrm{He}}(\overrightarrow{\mathrm{p}},\mathrm{pn})$ quasielastic scatterings using the Cooler ring at IUCF at beam energies 197, 300, and 414 MeV. The target was demonstrated to have little or no depolarization in the storage cell in the elastic asymmetries measurement at 45 MeV. Analysis of the 197 MeV data is presented in this doctoral thesis. At sufficiently high momentum transfer we find $^3\overrightarrow{\mathrm{He}}(\overrightarrow{\mathrm{p}},\mathrm{pn})$ spin observables are in good agreement with free p-n scattering observables, and therefore that polarized ^{3}He can serve as a good polarized neutron target. We extract in PWIA the spin-dependent momentum distribution of the neutron and proton out to 300 MeV/c. The measured neutron (proton) distribution is in good (fair) agreement with a Faddeev caculation.

Table of Contents

1. Introduction 17
1.1 Physics with Polarized ^{3}He 17
1.2 The ^{3}He Nucleus 19
1.3 The TRIUMF Results 32

2. Quasielastic Scattering 39
2.1 Overview 39
2.2 Quasi-elastic Scattering as an Experimental Probe 39
2.3 Nucleon-Nucleon Scattering 46
2.4 Spin-Dependent Quasielastic Scattering Using Protons 52
2.5 Plane Wave Impulse Approximation 55
2.6 Monte Carlo Model 59

3. Polarized ^{3}He Internal Gas Target 63
3.1 Introduction 63
3.2 Principles 65
3.3 Polarized ^{3}He Target Apparatus 81
3.4 Depolarization Mechanisms 107
3.5 Target Operations and Performances 113

4. Description of Experiment 115
4.1 Overview 115
4.2 Polarized Proton Beam in the IUCF Cooler Ring 116
4.3 The Detectors 127
4.4 Electronics and Data Acquisition 131

5. Analysis 136
5.1 Introduction 136
5.2 Reduction of the Event 5 Data 137
5.3 Detector Calibrations 145

5.4 Selection of the Event 5 Data 156
5.5 Background 161
5.6 Analysis of the Event 9 Data 165
5.7 Analysis of the Event 6 Data 169
5.8 Extraction of the Asymmetries 171
5.9 Experimental Uncertainties 178

6. Summary of the Results and Discussion 181
6.1 The 197 MeV and 415 MeV Beam Asymmetry with Unpolarized Hydrogen Target 181
6.1 The Elastic Results 182
6.3 The 197 MeV Quasielastic Results 185
6.3.1 The ^{3}He(p,pn) Results 185
6.3.2 The ^{3}He(p,2p) Results 189
6.4 Extraction of the Neutron and the Proton Spin-Dependent Momentum distributions 193
6.5 Summary 196

Appendix A The 197 MeV Quasielastic Data 207

Appendix B Polarized Nucleon-Nucleon Elastic Scattering 211

Appendix C Proton Spin-Dependent Quasielastic Scattering off ^{3}He 218

Appendix D Detector Electronics and Scalers 226

Appendix E Time of Flight Calibration 231

Acknowledgement

Foremost, my thanks go to God whose grace and truth were given to us in the historic person Jesus Christ.

There are many people I am thankful of for the work related to the experiment. First, I would like to thank my advisor who allowed me to work on such a rare project as building a polarized ^{3}He internal gas target. Also, I am thankful of him for his guidance and support on the project. Moreover, he has shown me how to analyze the complex task of obtaining and optimizing polarized ^{3}He.

During the prototyping of the polarized ^{3}He flow system, our group received much support from the technical staff at Bates-LNS and MIT-LNS. Particularly, I would like to mention Scott Ottaway for his help and George Dodson, Jim Grenham, and Ernie Ihloff for letting us use the laboratory vacuum equipments. Moreover, the target chamber was designed by Jim Kelsey and Bates-MIT staff.

I would also like to thank Tom Gentile from Caltech for sharing generously with us his knowledge on the LNA laser, the optical polarimetry, and the optical pumping of ^{3}He. I am thankful of him particularly for taking his time usually for discussion and answering questions.

I would like to mention also of Gerhard Finkenbeiner's inputs on the design of the target glass cell.

Also, the technical staff at IUCF provided much support on the target work. Particularly, I am very thankful of Jack Doskow for often taking his time to help. I would like to mention also Jeff Self and Bob Palmer for letting us used often the leak detector.

As for the researchers whom I worked closely with, I would like to mention Jo van den Brand, Ole Hansen, Cathleen Jones, Wolfgang Korsch, Laird Kramer, Mike Miller, Stephen Pate, Adam Smith, and Pat Welch for their important contributions at different stages of the experiment. The idea of the "pressure divider" in the optical pumping source was essentially of Jo as much as I could recall. Also, he had shown me while he was at MIT the importance of starting with a simpler system than what we want in experimental works. Next, the work with the laser beam transport and the target control and monitor system was due essentially to Ole. Next, the Mylar windowed storage target cell was made by Mike. Moreover, most components of the analyzer used at MIT were written by Pat Welch and Mike. Lastly, I would like to thank Adam Smith for often going out of his way to help.

I would like to acknowledge R.-W. Schulze and P.U. Sauer for providing us their ^{3}He spectral functions via Ole Hansen. I would also like to acknowledge Mike Titko for generating the asymmetries from the spectral functions that helped us understand the spin-dependence of the different components of the wavefunction in detail.

I would also like to thank of my advisor who with much patience went through the text and gave me many useful comments over the course of writing the thesis. Moreover, I am thankful of him for his kindness of allowing me more time than usual to complete the thesis. Also, I would like to thank Laird Kramer for his useful comments. Lastly, Dave McCurrly and Ron Filosa provided helps with the printing of a few AutoCad drawings.

Also, I am very much thankful of many people whom I have come to know in the last seven and a half year. It is difficult to mention everyone but I would like to thank Hojoon Park for his generosity and friendship, and Xiaobing Chen and Shiao-bin Soong also for their generosities. Moreover, I am thankful of Eric Birgbauer, Jerry Chen, Marilyn Chen, David Gonzales, Joel Haynes, and Jeff Kuo for their friendships. David Chang, Alex Chung, Jimmy Fang, Caleb King, Chester Liu, Grace May, Douglass Maloof, Alex Wei, and Kevin Wilson were more than friends to me sometime ago. Furthermore, I am thankful of, for their friendships, Franklin Frias, Mike Clark, Bob Palmer, Larry Skirvin, Bill Stark, and John Taylor at Bates and IUCF. Lastly, I would very much like to thank Taeksu for his helps at numerous times, Mark Rapo for his timely help before my defence, and Leslie Loo for his gracious help with the final printing of thesis.

I am also appreciative of my officemates Alaine Young, Jeff Grandy, Kyungseon Joo, Thomas Kettler, Bill Schmitt, and Mike Niczyporuk for their friendships. They have enriched my life in a number of areas.

Also, I am thankful of my parents Mr. Stanley and Mrs. Yan J. Lee and my brothers Wilfred and Wayne for their concerns and encouragements as I worked to complete the last requirement of my graduate study. I will be always grateful of them for giving me many opportunities for study. Lastly, I am thankful to the Lord for continuing to set me free and molding me into a new person.

List of Figures

Figure 1.1. A collection of measurements on the ^{3}He charge form factor . . 19

Figure 1.2. A collection of measurements on the ^{3}He magnetic form factor . 20

Figure 1.3. Bates and Saclay data for the longitudinal $R_L(q,\omega)$ and the transverse $R_T(q,\omega)$ response functions at $|\mathbf{q}| = 500$ MeV/c 21

Figure 1.4. Proton momentum distribution of ^{3}He for (a) 2-body and (b) 3-body breakup 22

Figure 1.5. The spin-dependent momentum distribution of (a) the neutron (solid line) and the proton (dashed line) 25

Figure 1.6. The relative contributions of the 2-body channel (dashed) and the 3-body channel (dotted) 27

Figure 1.7. The spin-dependent distribution of the neutron (solid line) and the proton (dashed line) for 3-body channel 29

Figure 1.8. The absolute value of the 3-body channel E integrated scalar functions $P^n_{2_{3b}}$, $P^n_{2_{3b}}$, and $P^n_{2_{3b}}$ 30

Figure 1.9. The absolute value of the p_N integrated scalar functions $Q^n_{2_{3b}}$, $Q^n_{2_{3b}}$, and $Q^n_{2_{3b}}$ 31

Figure 1.10. Spin observables for the ^{3}He(p,2p) reaction and the left scintillator array (conjugate angle) 33

Figure 1.11. Spin observables for the ^{3}He(p,2p) reaction and the right scintillator array (nonconjugate angle) 34

Figure 1.12. Spin observables for the ^{3}He(p,pn) reaction and the left scintillator array (conjugate angle) 35

Figure.1.13. Beam-related analyzing powers for the $^3\overrightarrow{\text{He}}(\overrightarrow{\text{p}},2\text{p})^{\text{pn}}_{\text{d}}$ and $^3\overrightarrow{\text{He}}(\overrightarrow{\text{p}},\text{pn})\text{pp}$ reactions 36

Figure.1.14. Spin correlation parameters for the$^3\overrightarrow{\text{He}}(\overrightarrow{\text{p}},2\text{p})^{\text{pn}}_{\text{d}}$ and $^3\overrightarrow{\text{He}}(\overrightarrow{\text{p}},\text{pn})\text{pp}$ reactions 37

Figure.1.15. Target-related analyzing powers for the $^3\overrightarrow{\text{He}}(\overrightarrow{\text{p}},2\text{p})^{\text{pn}}_{\text{d}}$ and $^3\overrightarrow{\text{He}}(\overrightarrow{\text{p}},\text{pn})\text{pp}$ reactions 38

Figure 2.1. A generic inclusive electron scattering spectrum 41

Figure 2.2. Missing energy E_m distributions at different ranges of p_m obtained from $^{12}C(e,e'p)$ scattering reaction 44

Figure 2.3. Comparison of the proton momentum distribution of the ^3He system between proton beam data...with electron beam 45

Figure 2.4. SAID Summer93' solutions of the proton-proton scattering at 200 MeV 50

Figure 2.5. SAID Summer93' solutions of the proton-neutron scattering at 200 MeV 51

Figure 2.6. Quasielastic scattering reaction ($p + {}^3He \rightarrow p + N + X_{A-1}$) of the proton from the ^3He nucleus 53

Figure 2.7. Plane Wave Impulse Approximation scattering where a nucleon is ejected from the nucleus due to interaction with the probe particle 55

Figure 2.8. Algorithm for the experimental Monte Carlo 60

Figure 2.9. The comparison between the Schulze and Sauer...and the Blankleider and Woloshyn spin-independent momentum distribution 61

Figure 2.10. The comparison between the Schulze and Sauer...and the Blankleider and Woloshyn spin-dependent momentum distribution 62

Figure 3.1. Hyperfine states in the 2^3S_1 and the 2^3P levels 67

Figure 3.2. $C_1, \ldots, C_9$ allowed transitions between the 2^3S_1 levels and the 2^3P levels 68

Figure 3.3. Optical pumping process for the C_8 and C_9 transitions with photons re-emitted along the direction of incidence 69

Figure 3.4. Electron clouds are exchanged between a metastable atom and a ground state atom 70

Figure 3.5. Ratios of the nuclear polarization P_n to the measured optical polarization P at 668 nm 74

Figure 3.6. A schematic diagram of the internal target 77

Figure 3.7. A schematic drawing of gas density in the storage target 78

Figure 3.8. Calibration of ρ_p vs. ρ_i 79

Figure 3.9. A schematic diagram of the CE-25 polarized ^3He internal gas target 82

Figure 3.10. The design drawing of the aluminum chamber and the top flange for mounting the optical glass cell 83

Figure 3.11. The optical pumping glass system to be mounted in the well of the aluminum flange 85

Figure 3.12. Schematic drawing of the gas feed system 87

Figure 3.13. A schematic layout of the target cell 89

Figure 3.14. A schematic layout of the differential vacuum system 91

Figure 3.15. The laser system 92

Figure 3.16. Laser output power *vs.* lamp current 94

Figure 3.17. The laser beam transport to the target pumping cell 97

Figure 3.18 Schematic drawing of the nuclear polarization optical polarimeter 98

Figure 3.19. Calibration of the DC amplifier 100

Figure 3.20. Calibration of the lockin amplifier with a sinusoidal signal . 101

Figure 3.21. Measured light polarization *vs.* orientation angle α of the circular polarizer sheet 105

Figure 3.22. Target polarization as a function of time 114

Figure 4.1. Quasielastic nucleon knockout by an incident proton 115

Figure 4.2. (a) A schematic layout of the experiment 117

Figure 4.3. A schematic layout of the IUCF Cooler Ring 119

Figure 4.4. Calibration of PCT output voltage to wire current values . . 120

Figure 4.5. A schematic figure of the time structure of the experiment . . 121

Figure 4.6. The IUCF acclerator floor plan 124

Figure 4.7. Schematic diagram of an atomic-beam polarized-ion source . 125

Figure 4.8. Energy level diagram of the hydrogen ground state atom in a magnetic field 125

Figure 4.9. A side view of the main detector arm 127

Figure 4.10 Schematic block diagram of the electronics and data acquisition system 131

Figure 4.11. Schematic diagram of the trigger system 133

Figure 5.1. Flowchart for the analysis of the 197 MeV data 138

Figure 5.2. (a) Particle trajectory traversing the two sets of MWPC and the E detector and (b) rotation from detector coordinates 139

Figure 5.3. The 197 MeV ^{3}He target proton dE/dx total energy loss . . . 146

Figure 5.4. (a) ϕ_R - ϕ_L as a function of θ_L 148

Figure 5.5. Elastic asymmetry of $^1H(\overrightarrow{p},2p)$ data for 414 MeV and 197 MeV 149

Figure 5.6. Events that triggered all six scintillator bars were recorded as cosmic muons 151

Figure 5.7. Proton time-of-flight ^{1}H(p,2p) data fit to a calculation for the 197 MeV beam kinetic energy 153

Figure 5.8. Missing energy E_m plot of 197 MeV ^{1}H(p,2p) data 154

Figure 5.9. Missing momentum $\mathbf{p}_{m_x}$, $\mathbf{p}_{m_y}$, and $\mathbf{p}_{m_z}$ plots of 197 MeV ^{1}H(p,2p) data 155

Figure 5.10. Missing momentum p_m plots of 197 MeV ^{3}He(p,2p) and ^{3}He(p,pn) data. 155

Figure 5.11. The 197 MeV ^{3}He target data E detector pulse height *vs.* tof plot 157

Figure 5.12. The 197 MeV hydrogen target data E detector pulse height *vs.* tof plot 158

Figure 5.13. The 197 MeV hydrogen target data tdc_{dEL} *vs.* tdc_{dER} . . . 159

Figure 5.14. The 197 MeV ^{3}He target data tdc_{dEL} *vs.* tdc_{dER} 160

Figure 5.15. Opening angle distribution of ^{1}H(p,2p) elastic scattering . . 161

Figure 5.16. The vertex distributions of 197 MeV data along the cell . . 162

Figure 5.17. The 197 MeV hydrogen target data. Events were sorted . . 163

Figure 5.18. The 197 MeV ^{3}He target data. Events were sorted 164

Figure 5.19. In (a) and (b), respectively the time difference scaler spectra offastOR and fastTrig triggers as functions of the cycle time . . . 166

Figure 5.20. Fit to the PCT data to determine the total charge of each beam and target spin configuration 168

Figure 5.21. Histogram of the ratio of the luminosity monitor1 to PCT normalizations...at 197 MeV 169

Figure 5.22. A 197 MeV beam kinetic energy, Monte Carlo simulation of the weightings by $\cos^2(\phi_{scat})$ and $\sin^2(\phi_{scat})$ 173

Figure 5.23. Unpolarized "cross section" yield for ^{3}He(p,2p) reaction . . 177

Figure 5.24. Unpolarized "cross section" yield for ^{3}He(p,pn) reaction . . 178

Figure 6.1. Elastic asymmetry of $1H(\overrightarrow{p},2p)$ data for 414 MeV and 197 MeV 181

Figure 6.2. Target asymmetry A_{000n} of p-^{3}He elastic scattering at 45 MeV 183

Figure 6.3. Beam asymmetry $\mathcal{A}_{00n0}$ (a), target asymmetry $\mathcal{A}_{000n}$ (b), ...of p-^{3}He elastic scattering at 197 MeV 184

Figure 6.4. At 197 MeV incident energy target and beam asymmetries ...for ^{3}He(p,pn) scattering as a function of missing momentum p_m 186

Figure 6.5. At 197 MeV incident energy the target (open symbols) and beam (filled symbols) asymmetries,...for ^{3}He(p,pn) scattering at $p_m <$ 100 MeV/c as a function of the 3-momentum transfer to the struck neutron q 187

Figure 6.6. At 197 MeV incident energy the spin-correlation parameter for ^{3}He(p,pn) scattering at p_m <100 MeV/c as a function of the 3-momentum transfer to the struck neutron q 188

Figure 6.7. At 197 MeV incident energy the target and beam asymmetries ...for ^{3}He(p,2p) scattering as a function of missing momentum p_m 190

Figure 6.8. At 197 MeV incident energy the target and beam asymmetries ...for ^{3}He(p,2p) scattering at $p_m <$ 100 MeV/c as a function of 3-momentum transfer q 191

Figure 6.9. The neutron polarization in ^{3}He obtained from the ratio of the 197 MeV $\mathcal{A}^{pn}_{00nn}$ data and the asymmetry $\mathcal{A}^{pn}_{00nn}(100\%)$ 194

Figure 6.10. The proton polarization in ^{3}He obtained from the ratio of the 197 MeV $\mathcal{A}^{2p}_{00nn}$ data and the asymmetry $\mathcal{A}^{2p}_{00nn}(100\%)$ 195

Figure D.1. Electronics schematic diagram of the dE and E detectors . . 226

Figure D.2. Electronics schematic diagram of the side microstrip detectors, forward microstrip detectors, forward scintillator, ... 227

Figure D.3. Electronics schematic diagram of the "fast" and the "slow" trigger system 228

Figure D.4. Electronics schematic diagram of the backing scintillators . . 229

Figure E.1. The difference of intersection position...left side detector . . 232

Figure E.2. The difference of intersection position...right side detector . . 233

Figure E.3. Momentum fit of the 197 MeV hydrogen data for the proton tof mechanism in the left detector for bars 0, 1, and 2 235

Figure E.4. Momentum fit of the 197 MeV hydrogen data for the proton tof mechanism in the left detector for bars 3, 4, and 5 236

Figure E.5. Momentum fit of the 197 MeV hydrogen data for the neutron tof mechanism in the left detector for bars 0, 1, and 2 237

Figure E.6. Momentum fit of the 197 MeV hydrogen data for the neutron tof mechanism in the left detector for bars 3, 4, and 5 238

Figure E.7. θ_{open} is plotted as a function of θ_{L}; the calculated θ_{open} as a function of θ_{L} 240

Figure E.8. Missing momentum distributions of the 197 MeV hydrogen data for the pp reaction 241

Figure E.9. Missing momentum distributions of the 197 MeV hydrogen data for the LnRp reaction 242

Figure E.10. Missing momentum distributions of the 197 MeV hydrogen data for the LpRn reaction 243

Figure E.11. Missing energy distributions of the 197 MeV hydrogen data 244

List of Tables

Table 1.1. The partial wave channels of the three-nucleon wavefunction within the Derrick-Blatt scheme 23

Table 3.1. The admixture amplitude values and relative energy values in the 2^3S_1 and 2^3P levels 67

Table 3.3. Relative energies of the nine allowed dipolar transitions 68

Table 3.4. Relative probabilities for C_8 and C_9 transitions 68

Table 3.5 Average thermal velocities and Doppler widths for optical pumping 73

Table 3.6. The dimensional factor K for different ratios of the rectangular conductor side dimensions. 89

Table 3.7. Fit parameters of the polarization response function 103

Table 3.8. Polarizations P_l and P_c of the light 104

Table 3.9. Spin-lattice relaxation times due to collisions with impurity . . 107

Table 4.1. The event 5 triggers 134

Table 4.2. The event 6 triggers 135

Table 5.1. The average and the rms values of the E detector scintillator bar tfc-position offsets of the analyzed 197 MeV data 151

Table 5.2. Beam polarization measured with the CE-01 experiment at 197 and 414 MeV 170

Table 5.3. The systematic uncertainties 179

Table 5.4. The result systematic uncertainties 180

Table A.1. $\mathcal{A}_{000n}$, $\mathcal{A}_{00n0}$, and $\mathcal{A}_{00nn}$ for left-proton-right-neutrons 207

Table A.2. $\mathcal{A}_{000n}$, $\mathcal{A}_{00n0}$, and $\mathcal{A}_{00nn}$ for left-neutron-right-protons 207

Table A.3. $\mathcal{A}_{000n}$, $\mathcal{A}_{00n0}$, and $\mathcal{A}_{00nn}$ for left-neutron-right-protons with a cut $\mathbf{p_m}$ <100 MeV/c 208

Table A.4. $\mathcal{A}_{000n}$, $\mathcal{A}_{00n0}$, and $\mathcal{A}_{00nn}$ for left-proton-right-neutrons with a cut $\mathbf{p_m}$ <100 MeV/c 208

Table A.5. $\mathcal{A}_{000n}$, $\mathcal{A}_{00n0}$, and $\mathcal{A}_{00nn}$ for left-proton-right-neutrons with a cut $|\mathbf{q}|$ >500 MeV/c 209

Table A.6. $\mathcal{A}_{000n}$, $\mathcal{A}_{00n0}$, and $\mathcal{A}_{00nn}$ for proton-protons 209

Table A.7. $\mathcal{A}_{000n}$, $\mathcal{A}_{00n0}$, and $\mathcal{A}_{00nn}$ for proton-protons...$\mathbf{p}_m$ <100 MeV/c 210

Table B.1. ...the interaction probabilities for combinations of the specified spin directions. 213

Table D.1. The CE-25 scalers. 230

Table E.1. Missing momentum and energy resolutions for the reactions pp, LnRp, and LpRn 239

Chapter 1

Introduction

1.1 Physics with Polarized ^{3}He

The ^{3}He nucleus has several properties which make the study of its spin particularly interesting. The three body system is unique, in that although it is relatively tightly bound, essentially exact solutions in nonrelativistic approximation of the ground state have been obtained using a variety of two-nucleon potentials. In addition, unlike a heavy nucleus where the total spin is usually determined by only a few valence nucleons, the spin of ^{3}He involves all the nucleons in the nucleus. Further, Faddeev calculations predict that the ground state spin of the ^{3}He nucleus is dominated by the neutron. This property has motivated great interest in the use of polarized ^{3}He as an effective neutron target. Finally, because the ^{3}He atom has a closed electron structure, the polarized atom does not depolarize with high probability when colliding with container walls. Thus, a number of different ^{3}He targets have been constructed for scattering experiments. In addition, the spin-dependent spectral function, calculated from a Faddeev solution to the ^{3}He ground state, has become available.

At present there is great interest in the use of the polarized ^{3}He nucleus as an effective polarized neutron target in deep inelastic scattering to measure the neutron spin structure function $g_1^n(x)$. This has been motivated in large part by data on the proton spin structure function $g_1^p(x)$ obtained by the European Muon Collaboration (1989) [1.1]. The integral of $g_1^p(x)$ over x has been observed to be smaller than the prediction of the Ellis-Jaffe sum rule [1.2]. This discrepancy has been interpreted to imply that the fraction of the proton spin carried by the quarks is only $\approx \frac{1}{3}$. Because there exists an essentially model-independent relation between g_1^p and g_1^n measurements on the neutron are of high priority. Unlike the proton, the neutron exists freely with a mean life time of 888.9±3.5 sec (14.8 min) [1.3]. Neutron sources using high flux neutron beams from nuclear reactors or secondary neutrons knocked out by intense proton beams from neutron rich nuclear targets yield relatively low intensities. Thus, two stable light nuclei with a weakly bound neutron, *i.e.* the deuteron and ^{3}He, have come to be employed as effective neutron targets to measure the neutron spin structure function g_1^n [1.2, 1.4, 1.5] and also the neutron form factors, $G_E^n(Q^2)$ and $G_M^n(Q^2)$ [1.6- 1.12]. The deuteron is a weakly bound system of a proton and a neutron with the nucleon spins predominantly parallel

to each other and from which neutron information is extracted by subtracting the proton contribution. As a result, measurements are limited by the systematic error associated with the proton subtraction. On the other hand, the ^{3}He nucleus is a relatively tightly bound system whose spin is dominated by the spin of the neutron, and therefore, spin dependent information on the neutron can be determined with a smaller correction due to the protons, provided the small correction is precisely known. It is now widely accepted that the polarized ^{3}He nucleus is a competitive target with the deuteron target to measure the spin and charge properties of the neutron. Motivated by these considerations, measurements of spin-dependent scattering from polarized ^{3}He are either underway or planned at Bates [1.13], SLAC [1.14], Mainz, DESY, CEBAF [1.15], NIKHEF, and Saskatchewan.

Accurate interpretation of the ^{3}He measurements to extract information on the neutron will depend on a precise knowledge of the ^{3}He nuclear wavefunction and of the nuclear interaction with probe particles. To relate the nuclear wavefunction to the electron scattering reaction mechanism, a complete spin dependent spectral function has been obtained from Faddeev solutions [1.16,1.17]. For quasielastic and deep inelastic scattering, the respective electron-nucleon interaction tensor is convoluted with the spin-dependent spectral function to obtain the scattering cross sections.

As a test of our understanding of the ground state spin structure of ^{3}He, a series of spin dependent quasielastic scattering measurements were conducted at TRIUMF using polarized proton beams at energies 220 MeV and 290 MeV. The results showed a large discrepancy with the Plane Wave Impulse Approximation (PWIA). The TRIUMF results are described at the end of this chapter. These results cast doubt on the validity of using a polarized ^{3}He target to extract neutron spin properties. In the experiment that is described here, a more expansive kinematic range was examined using large acceptance nonmagnetic detector arms at beam energies 197, 300, and 414 MeV. Further, the experiment was carried out using the novel technique of a polarized ^{3}He internal gas target in a storage ring. The 197 MeV data for the ^{3}He(p,pn) and ^{3}He(p,2p) reactions provide the central results of this thesis. The primary goal was to experimentally constrain the spin dependent spectral function of the ^{3}He ground state.

The ^{3}He(p,2p) and ^{3}He(p,pd) data at 197 MeV beam kinetic energy have been presented as a doctorate thesis at the University of Wisconsin—Madison [1.18]. The remaining data at 300 and 414 MeV beam kinetic energies for the ^{3}He(p,2p) and ^{3}He(p,pn) reactions along with the elastic data at the three energies have been

presented as a doctorate thesis at the IUCF [1.19]. Moreover, the early experimental results of elastic and quasielastic data at lower energies and results of quasielastic data at 197 MeV have been already published [1.20,2.21].

1.2 The ^{3}He Nucleus

1.2.1 Propertities

The ^{3}He nucleus is a calculable fewbody nuclear system in norelativistic approximation using the Faddeev 3-body equations or variational calculus, and nucleon-nucleon realistic force models. It is a spin $\frac{1}{2}$ system with positive parity and has 2808.414 MeV/c^2 mass. Its binding energy is 7.710 MeV and its magnetic moment is -2.13 μ_N in nuclear magnetons. In fact, the binding energy and magnetic moment of the ^{3}He nucleus are so precisely known that they have been used to probe sensitivity to sub-nucleon degrees of freedom.

The ^{3}He charge and magnetic form factors have been determined at low momentum transfer using elastic (e,e′) scattering [1.22].

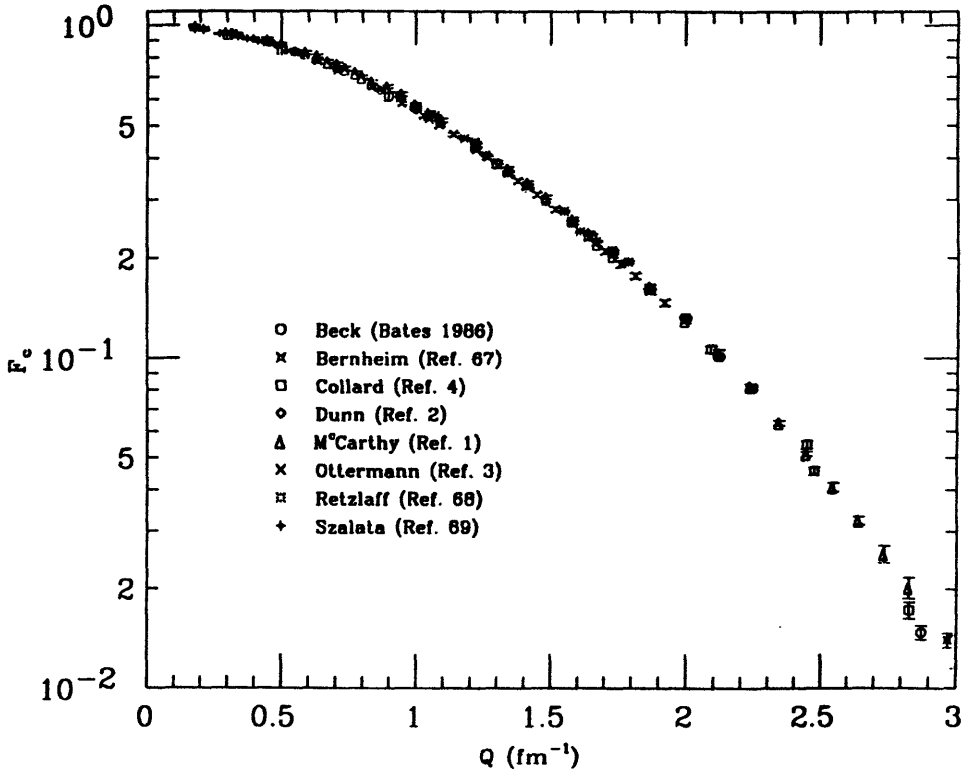

Figure 1.1. A collection of measurements on the ^{3}He charge form factor [1.22].

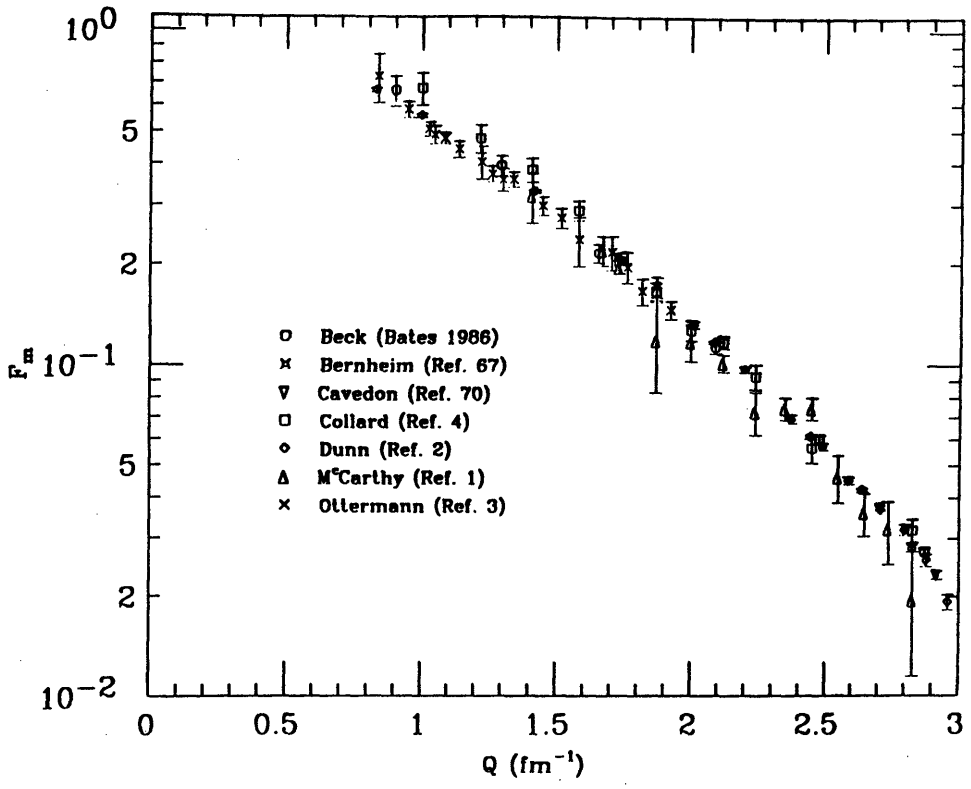

Figure 1.2. A collection of measurements on the ^{3}He magnetic form factor [1.22].

Also, the structure functions $R_L(q,\omega)$ and $R_T(q,\omega)$ in the quasielastic and the dip regions have been measured [1.23].

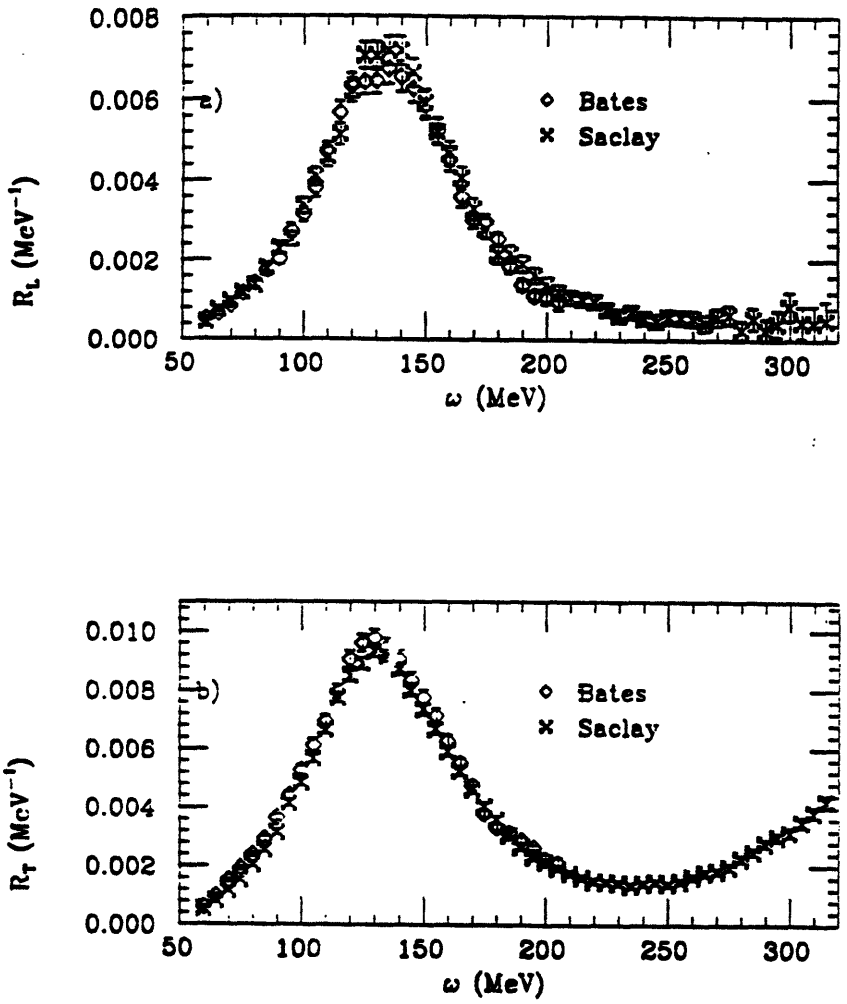

Figure 1.3. Bates and Saclay data for the longitudinal $R_L(q,\omega)$ and the transverse $R_T(q,\omega)$ response functions at $|\mathbf{q}| = 500$ MeV/c.

Also, there exists a determination of the proton momentum distribution by measurement of exclusive (e,e'p) quasielastic scattering [1.24].

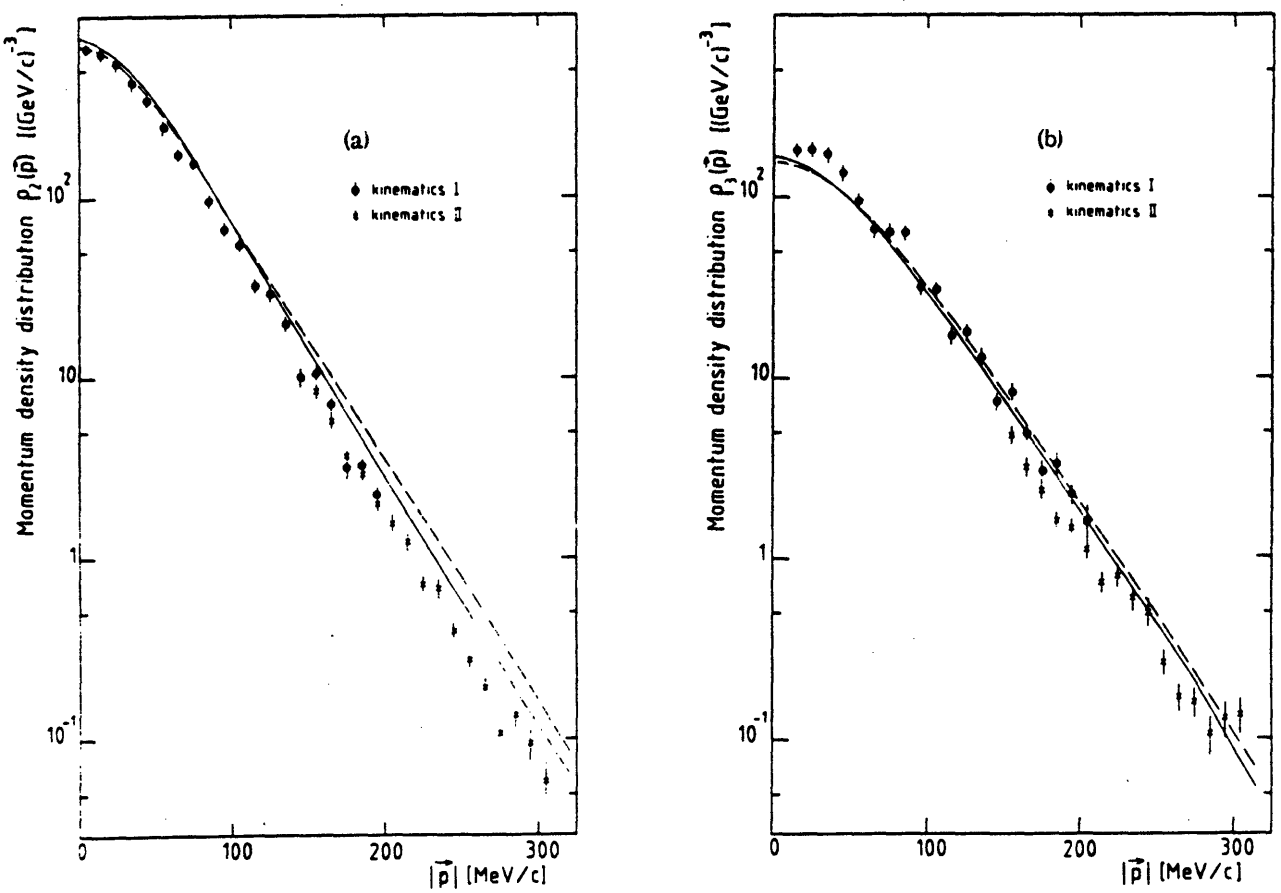

Figure 1.4. Proton momentum distribution of ^{3}He for (a) 2-body and (b) 3-body breakup. The 3-body breakup contribution has been obtained by integration up to a missing energy of 20 MeV. Dots and crosses correspond to measurements in kinematics I and II, respectively. The solid curves represent the calculation of Dieperink *et al.* , the dashed lines that of Ciofi degli Atti *et al.* . The error bars include both the statistical error and an 8% error due to estimated uncertainty in the absolute normalization [1.24].

1.2.1 Wavefunction Components

The ^{3}He nuclear wave function of the Faddeev 3-body equations or the variational calculus have been obtained using different nucleon-nucleon forces. The nuclear wavefunction consists of a dominant S-state ~90%, an S'-state ~1-2%, a P-state ~0.1%, and a D-state ~8% [1.27]. The S-state is symmetric spatially and has the protons always anti-aligned; the small S'-state has mixed spatial symmetry and contributes to the protons spin-momentum correlation; and the D-state has the protons always aligned together with the neutron in the opposite direction of the ^{3}He polarization and is important at large $p_m \approx 400$ MeV/c.

Channel Number	L	S	l_α	L_α	P	K	Probability (%)
1	0	0.5	0	0	A	1	87.44
2	0	0.5	0	1	M	2	0.74
3	0	0.5	1	1	M	1	0.74
4	0	0.5	2	2	A	1	1.20
5	0	0.5	2	2	M	2	0.06
6	1	0.5	1	1	M	1	0.01
7	1	0.5	2	2	A	1	0.01
8	1	0.5	2	2	M	2	0.01
9	1	1.5	1	1	M	1	0.01
10	1	1.5	2	2	M	2	0.01
11	2	1.5	0	2	M	2	1.08
12	2	1.5	1	1	M	1	2.63
13	2	1.5	1	3	M	1	1.05
14	2	1.5	2	0	M	2	3.06
15	2	1.5	2	2	M	2	0.18
16	2	1.5	3	1	M	1	0.37

Table 1.1. The partial wave channels of the three-nucleon wavefunction within the Derrick-Blatt scheme [1.27].

1.2.2 Spectral Function

As previously mentioned, the ^{3}He nuclear wavefunction is incorporated into the electron scattering formalism as a convolution of the spin dependent spectral function with the scattering tensor. The spectral function has been formulated by Schulze and Sauer [1.28] as the tensor product of the projection of the nuclear wavefunction onto the plane wave states of the ejected nucleon and the recoiling system and includes the possibility of 2-body and 3-body breakup in the scattering reaction $^3\overrightarrow{He}(\overrightarrow{p},pN)A\text{-}1$. In the case of 2-body breakup, the ejected nucleon is a proton and the recoiling system is a bound deuteron, and in the case of 3-body breakup, the ejected nucleon can be either a proton or a neutron and correspondingly the recoiling system is two unbound nucleons. All allowed states of the recoiling system are included in the spectral function. Note, the wavefunction used does not include effects of the Coulomb interaction.

In operator form, the spectral function may be written as,

$$\widehat{S}(p_N, E, t_N) = \frac{1}{2}\{\, f_0(p_N, E, t_N) + \sigma_N \cdot \sigma_A \,[\, f_1(p_N, E, t_N) - \frac{1}{3} f_2(p_N, E, t_N)\,] + \sigma_N \cdot \hat{p}_N \sigma_A \cdot \hat{p}_N \, f_2(p_N, E, t_N)\,\} \tag{1.1}$$

where p_N and t_N are the momentum and isospin of the nucleon and E is the separation energy of the nucleon from the nucleus A with resulting excitation energy of the system A-1. The spin averaged contribution f_0 and the two spin-dependent contributions f_1 and f_2 are scalar functions which depend only on the magnitude of $\mathbf{p}_N$. In the expression for quasielastic electron scattering cross section, the spectral function tensor is convoluted with the e-N half-off-mass-shell scattering, or in quasielastic proton scattering cross section with the nucleon-nucleon half-off-mass-shell scattering. In plane wave impulse approximation, the quantities p_N and E are identified respectively with the missing momentum p_m and the missing energy E_m. The spectral function is also an essential ingredient in the convolution model for spin-dependent deep inelastic electron scattering.

Assume the contribution to the cross section associated with the third term is small. The function f_2 is small compared to f_0 and f_1 so one can rewrite the spectral function neglecting the third term,

$$\widehat{S}(p_N, E, t_N) \approx \frac{1}{2}\{\, f_0(p_N, E, t_N) + \sigma_N \cdot \sigma_A \,[\, f_1(p_N, E, t_N) - \frac{1}{3} f_2(p_N, E, t_N)\,]\,\} \,. \tag{1.2}$$

When integrated over the separation energy E, a momentum density operator

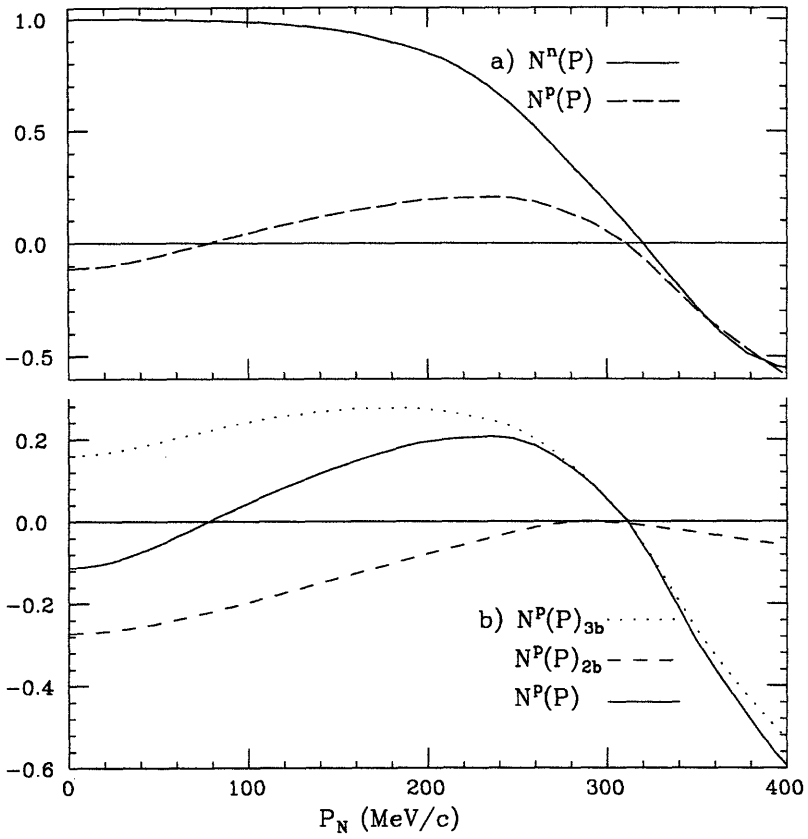

Figure 1.5. The spin-dependent momentum distribution of (a) the neutron (solid line) and the proton (dashed line) plotted *vs.* nucleon momentum p_N. In (b) the 2-body contribution (dashed), the 3-body contribution (dotted) and the total (solid) proton distributions are plotted *vs.* p_N. The spectral function is of Schulze and Sauer [1.28] and uses the Paris NN-potential. The spectral function is integrated over E to 500 MeV.

is obtained,

$$\begin{aligned} \hat{\rho}(p_N, t_N) &= \int \mathrm{dE}\ \widehat{\mathrm{S}}(\mathrm{p_N}, \mathrm{E}, \mathrm{t_N}) \\ &= \frac{1}{2}\{\ \mathrm{P_0}(\mathrm{p_N}, \mathrm{t_N}) + \sigma_\mathrm{N} \cdot \sigma_\mathrm{A}[\ \mathrm{P_1}(\mathrm{p_N}, \mathrm{t_N}) - \frac{1}{3}\mathrm{P_2}(\mathrm{p_N}, \mathrm{t_N})\ ]\} \\ \text{where } \mathrm{P_i} &= \int \mathrm{dE}\ \mathrm{f_i}(\mathrm{p_N}, \mathrm{E}, \mathrm{t_N})\ . \end{aligned} \tag{1.3}$$

Again, the approximate spectral function has been used here, and the momentum density operator is diagonal in the space of the spin s_N. Thus, one can obtain spin-dependent momentum distributions defined for nucleon spin in the "up" direction as

$$\rho_{s_A,s_N+}(p_N,t_N) \;=\; \langle s_A, s_N = +|\; \hat{\rho}(p_N,t_N)\; |s_A, s_N = +\rangle \;, \tag{1.4a}$$

and for nucleon spin in the "down" direction as

$$\rho_{s_A,s_N-}(p_N,t_N) \;=\; \langle s_A, s_N = -|\; \hat{\rho}(p_N,t_N)\; |s_A, s_N = -\rangle \;.$$

Then, an asymmetry ratio in terms of these two distributions

$$N(p_N,t_N) \;=\; \frac{\rho_{s_A,s_N+} \;-\; \rho_{s_A,s_N-}}{\rho_{s_A,s_N+} \;+\; \rho_{s_A,s_N-}} \tag{1.4b}$$

defines the "polarization" of the proton or the neutron in the nucleus. In plane wave impulse approximation, this polarization can be measured, *see section* 2.4. For the neutron, the polarization is 100% for $p_N < 100$ MeV/c, indicating that at low p_N there are only the S and the small S' for both of which the neuteron spin is "up". See figure 1.5(a). The polarization crosses the zero and becomes negative above 300 MeV/c where the D-state begins to dominate. For the proton, the polarization is identically zero for the S-state. However, in the S'-state there is an asymmetry of -12% at low p_N values.

In quasielastic scattering, the ^{3}He nucleus can fragment into the 2-body channel, a deuteron and a proton, or into the 3-body channel, a neutron and two protons. In the case of proton knockout, the reaction can go via both channels while in the case of neutron knockout, the reaction can proceed only via the 3-body channel. At low p_N values, the S-state proton has a polarization of $\sim -25\%$ for the 2-body channel and $\sim +25\%$ for the 3-body channel, adding up to zero polarization. The reason for nonzero polarization in separate channels in the S-state is that the 2-body channel preferentially selects the struck proton spin "down"; and the 3-body channel preferentially selects with equal probability the struck proton spin "up". Still another way of looking at it, the protons have a 50% probability to be "up" and 50% to be "down". If the struck proton is spin "up", the reaction has a higher probability to go into the 3-body channel; if the struck proton is spin "down", the reaction has an equally high probability to go into the 2-body channel.

The S-state probabilities can be estimated using the Clebsch-Gordon coefficients. The symmetric spin wave function of three nonidentical particles can be written as, representing particle 1, 2, and 3 in that order,

$$|\chi_3\rangle \;=\; \frac{1}{\sqrt{3}} \left[\; |{}^{+\frac{1}{2}}\, {}^{+\frac{1}{2}}\, {}^{-\frac{1}{2}}\rangle \;+\; |{}^{+\frac{1}{2}}\, {}^{-\frac{1}{2}}\, {}^{+\frac{1}{2}}\rangle \;+\; |{}^{-\frac{1}{2}}\, {}^{+\frac{1}{2}}\, {}^{+\frac{1}{2}}\rangle \;\right] \tag{1.5}$$

However, in the ^{3}He S-state one of the three spin states is not allowed due to the Pauli exclusion principle. If the nucleons are represented as neutron, proton, and proton in that order, then the symmetric spin wave function becomes

$$|\chi^{^3He}\rangle = \frac{1}{\sqrt{2}}\left[|+\tfrac{1}{2}\ +\tfrac{1}{2}\ -\tfrac{1}{2}\rangle + |+\tfrac{1}{2}\ -\tfrac{1}{2}\ +\tfrac{1}{2}\rangle \right]. \quad (1.6)$$

This can be rewritten in terms of the 2-particle cluster and 1 particle as

$$|\chi^{^3He}\rangle = \frac{1}{\sqrt{2}}\left[\left(|1^+1\rangle|\tfrac{1}{2}\ -\tfrac{1}{2}\rangle + \frac{1}{\sqrt{2}}|1\ 0\rangle|\tfrac{1}{2}\ +\tfrac{1}{2}\rangle \right) + \frac{1}{\sqrt{2}}|0\ 0\rangle|\tfrac{1}{2}\ +\tfrac{1}{2}\rangle \right], \quad (1.7)$$

where the terms inside the parentheses represent the 2-body channel and the term outside the 3-body channel. The polarization of the proton in the 2-body channel is -25% and in the 3-body channel $+25\%$. This simple argument would also predict that the probability to find the proton in the 2-body channel is 75% and in the 3-body channel is 25% in approximate agreement with the spectral function at low p_N values in figure 1.6. The difference is expected to be due to the S'-state. When the 2-body and the 3-body momentum distributions are integrated out to about 190 MeV/c, the 2-body contribution is 74% and the 3-body contribution is 26%.

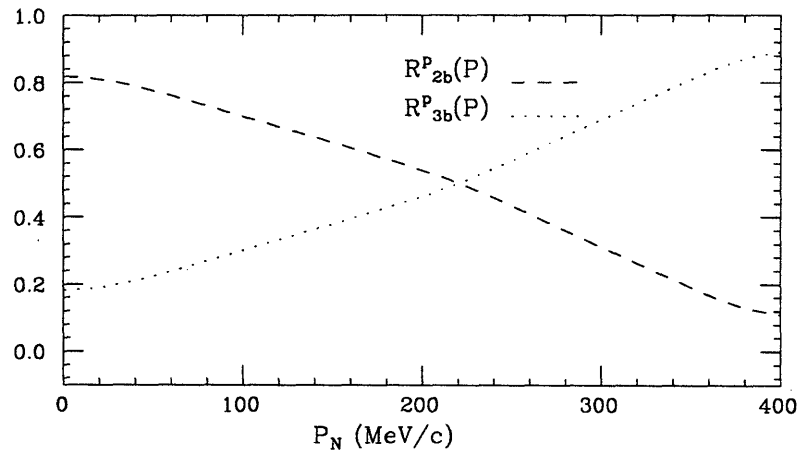

Figure 1.6. The relative contributions of the 2-body channel (dashed) and the 3-body channel (dotted) are plotted *vs.* nucleon momentum p_N. The spectral function is integrated over nucleon separation energy E to 500 MeV.

The nonzero polarization of the S'-state is due to a small difference in neutron-proton force between when the proton spin is parallel and when anti-parallel to the

neuteron spin. The former has a stronger attractive potential than the latter, and a proton with parallel spin tends to form a deuteron like cluster, remaining closer to the center. Therefore, it has a larger momentum value than the other proton which remains further out. The correlation of proton polarization with momentum can be seen in figure 1.5(b) where the curve is the sum polazation of the S, S', and D-state. The polarization changes from -12% at low p_N to $+20\%$ at around 250 MeV/c, crossing the zero at around 90 MeV/c. The D-state is significant only at p_N above 450 MeV. Despite this correlation, the proton spins of the S'-state are always anti-parallel to each other.

Similarly, when the approximate spectral function in equation (1.2) is integrated over the nucleon momentum $\mathbf{p}_N$, a separation energy density operator is obtained,

$$\begin{aligned} \hat{q}(p_N, t_N) &= \int p_N^2 dp_N \, \hat{S}(p_N, E, t_N) \\ &= \frac{1}{2}\{ \, Q_0(p_N, t_N) \, + \, \sigma_N \cdot \sigma_A \big[\, Q_1(p_N, t_N) \, - \, \frac{1}{3} Q_2(p_N, t_N) \, \big] \} \\ \text{where } Q_i &= \int p_N^2 dp_N \, f_i(p_N, E, t_N) \, . \end{aligned} \tag{1.8}$$

The density operator obtained is diagonal in the space of the spin s_N. Therefore, one can obtain spin-dependent separation energy distributions defined for nucleon spin in the "up" direction as

$$q_{s_A, s_N +}(E, t_N) \; = \; \langle s_A, s_N = + | \; \hat{q}(E, t_N) \; | s_A, s_N = + \rangle \; , \tag{1.9a}$$

and for nucleon spin in the "down" direction as

$$q_{s_A, s_N -}(E, t_N) \; = \; \langle s_A, s_N = - | \; \hat{q}(E, t_N) \; | s_A, s_N = - \rangle \; .$$

Then, an asymmetry ratio in terms of these two distributions

$$N(E, t_N) \; = \; \frac{q_{s_A, s_N +} \; - \; q_{s_A, s_N -}}{q_{s_A, s_N +} \; + \; q_{s_A, s_N -}} \tag{1.9b}$$

defines the "polarization" of the proton or the neutron in the nucleus as a function of the separation energy E as in figure 1.7.

It has been assumed that the contribution due to the scalar function $f_2(p_N, E, t_N)$ is negligible. Comparisons are made of the integrated scalar functions plotted *vs.* p_N in figure 1.8 and *vs.* E in figure 1.9. These show that the assumption

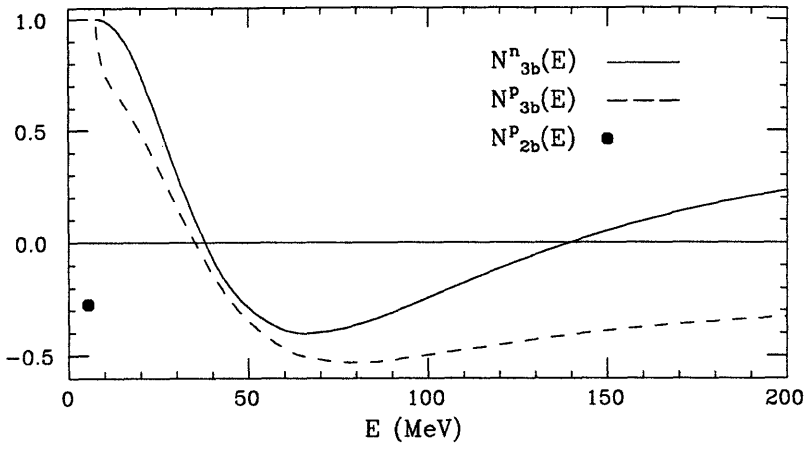

Figure 1.7. The spin-dependent distribution of the neutron (solid line) and the proton (dashed line) for 3-body channel plotted *vs.* nucleon separation energy E. A solid circle is the proton 2-body channel nucleon polarization. The spectral function is integrated over nucleon momentum p_N to 6 GeV/c.

is valid for the proton when the nucleon momentum p_N is less than 150 MeV/c and the nucleon separation energy E less than 30 MeV and for the neutron when p_N less than 300 MeV/c and E less than 30 MeV. However, the factor $\sigma_N \cdot \hat{\mathbf{p}}_N \sigma_A \cdot \hat{\mathbf{p}}_N$ in the spectral function in equation (1.1) is expected to keep the third term small at high nucleon momentum p_N for the CE-25 experimental azimuthal angle acceptance. Also, in figure 1.9 the spectral function is three orders of magnitude smaller at the 3-body channel separation energy E = 30 MeV than at threshold separation energy E 7.74 MeV and therfore only has a negligible contribution to the spin dependent momentum distributions.

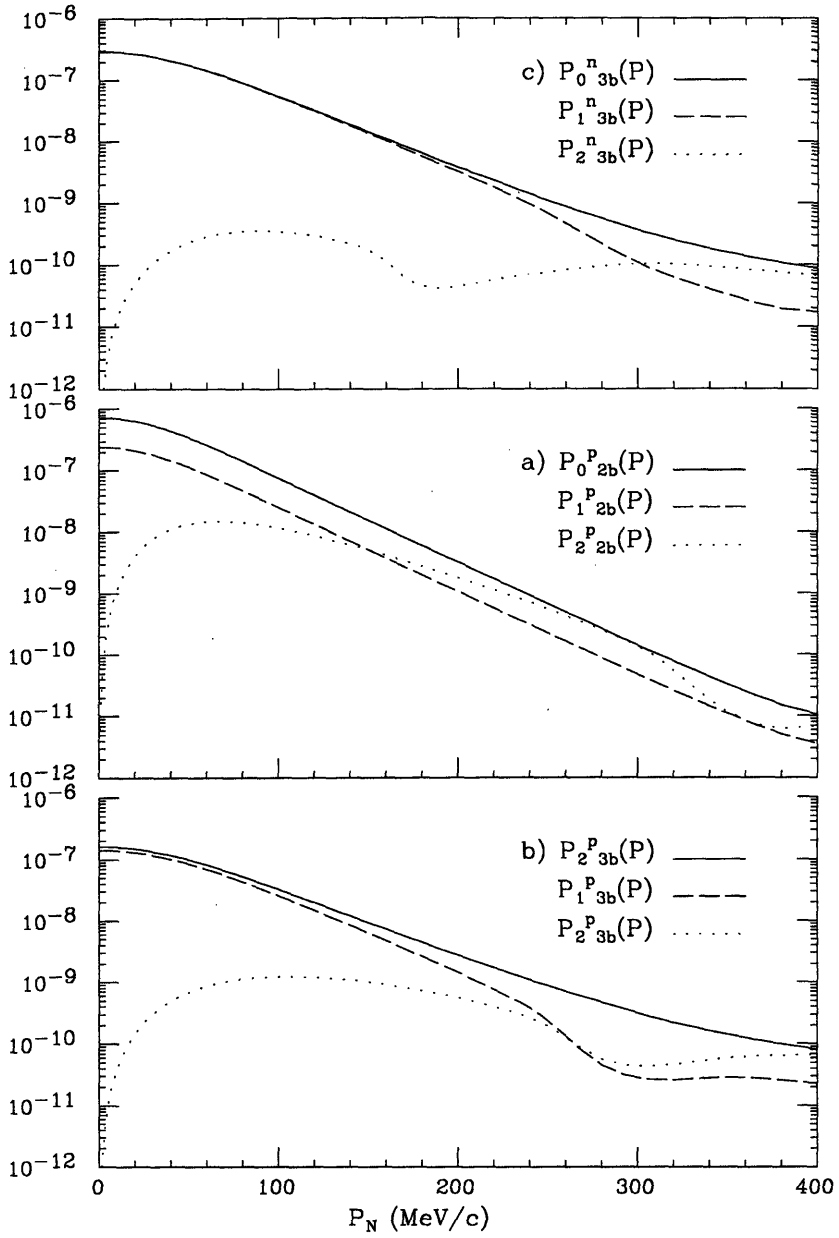

Figure 1.8. The absolute value of the 3-body channel E integrated scalar functions $P^n_{2_{3b}}$, $P^n_{2_{3b}}$, and $P^n_{2_{3b}}$ for the neutron in (a); the 2-body channel E integrated scalar functions $P^p_{0_{2b}}$, $P^p_{1_{2b}}$, and $P^p_{2_{2b}}$ for the proton in (b); and the 3-body channel E integrated scalar functions $P^p_{2_{3b}}$, $P^p_{2_{3b}}$, and $P^p_{2_{3b}}$ for the proton in (c); plotted *vs.* nucleon momentum p_N. The scalar functions are integrated over nucleon separation energy E to 500 MeV and weighted with $(p_N)^2$.

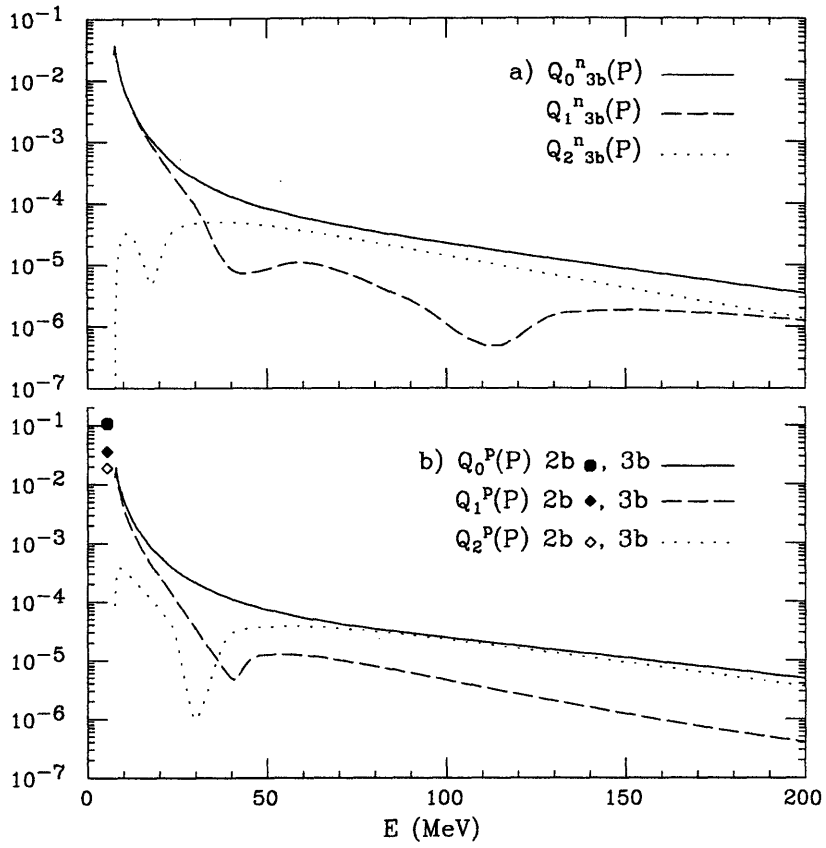

Figure 1.9. The absolute value of the p_N integrated scalar functions $Q^n_{2_{3b}}$, $Q^n_{2_{3b}}$, and $Q^n_{2_{3b}}$ for the neutron in (a) and the p_N integrated scalar functions Q^p_0, Q^p_1, and Q^p_2 of the 2-body and the 3-body channels for the proton in (b) plotted *vs.* nucleon separation energy E. The scalar functions are integrated over nucleon momentum p_N to 6 GeV/c.

1.3 The TRIUMF Results

Two measurements of spin-dependent quasielastic scattering of polarized protons from polarized ^{3}He were carried out at TRIUMF to probe the ground state spin structure of ^{3}He. The first experiment took data at 290 MeV [1.29] and the second, with a better statistical precision at 220 MeV beam energy [1.31]. Large discrepancies between neutron beam and target analyzing powers and PWIA calculations were observed at both energies.

The 290 MeV asymmetry data are shown for different recoiling proton angles and as a function of energy transfer in figures 1.10 and 1.11. The data for the neutron knockout is combined for all recoiling neutron angles due to lack of statistics in figure 1.12.

The 220 MeV asymmetry data have significantly higher statistical precision and are shown as a function of energy transfer for different angles of the struck neutron in figures 1.13-1.15.

The proton asymmetries were small as expected from PWIA. The TRIUMF results cast serious doubt on the validity of using polarized ^{3}He as an effective polarized neutron. Why was the target asymmetry of ^{3}He(p,pn) close to zero? Were final state interactions playing a major role? Why were the target asymmetry of ^{3}He(p,2p) data reasonable? These questions were the primary motivation for the work in this thesis. Could medium energy polarized proton scattering be used to extract any information on the ground state spin structure of ^{3}He?

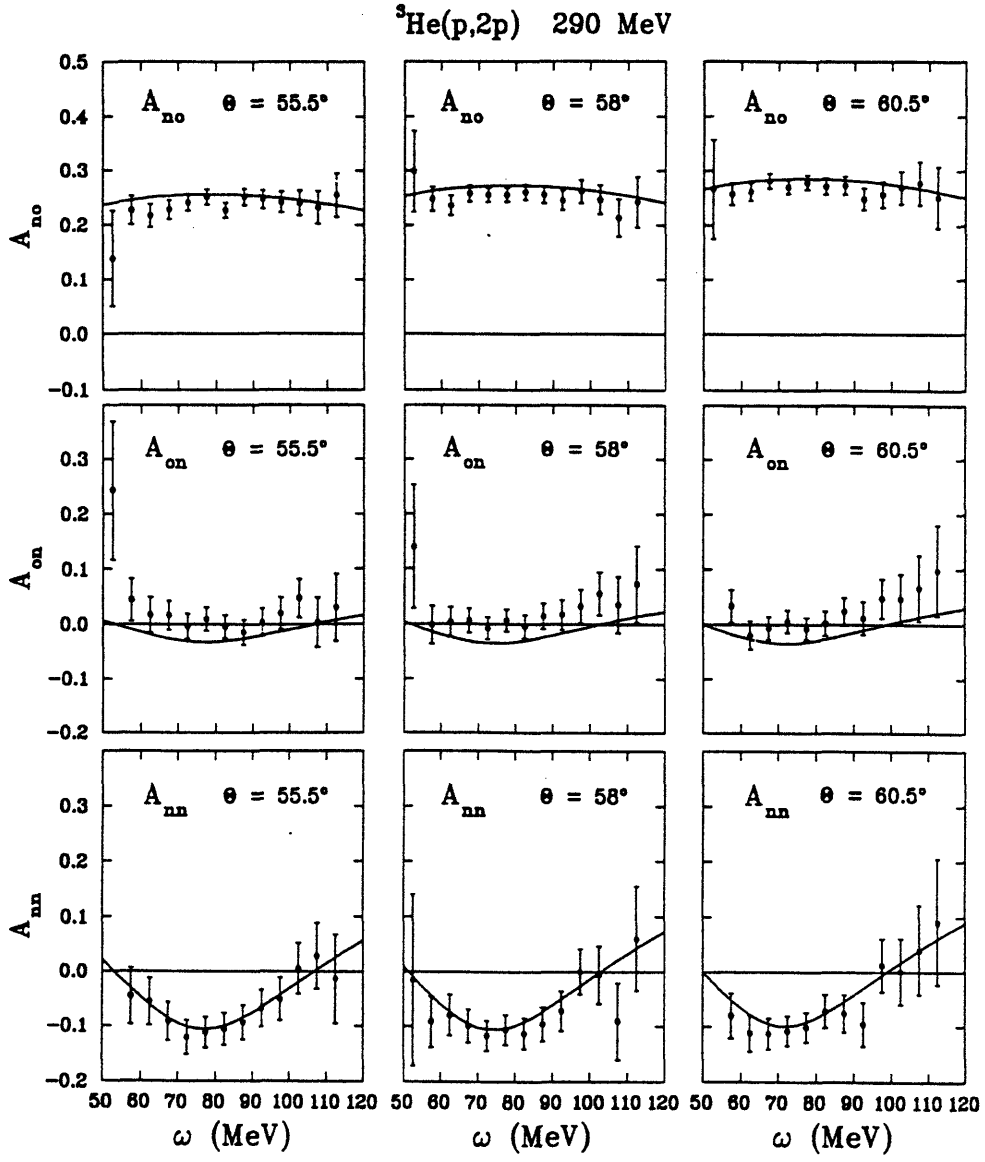

Figure 1.10. Spin observables for the ^{3}He(p,2p) reaction and the left scintillator array (conjugate angle).

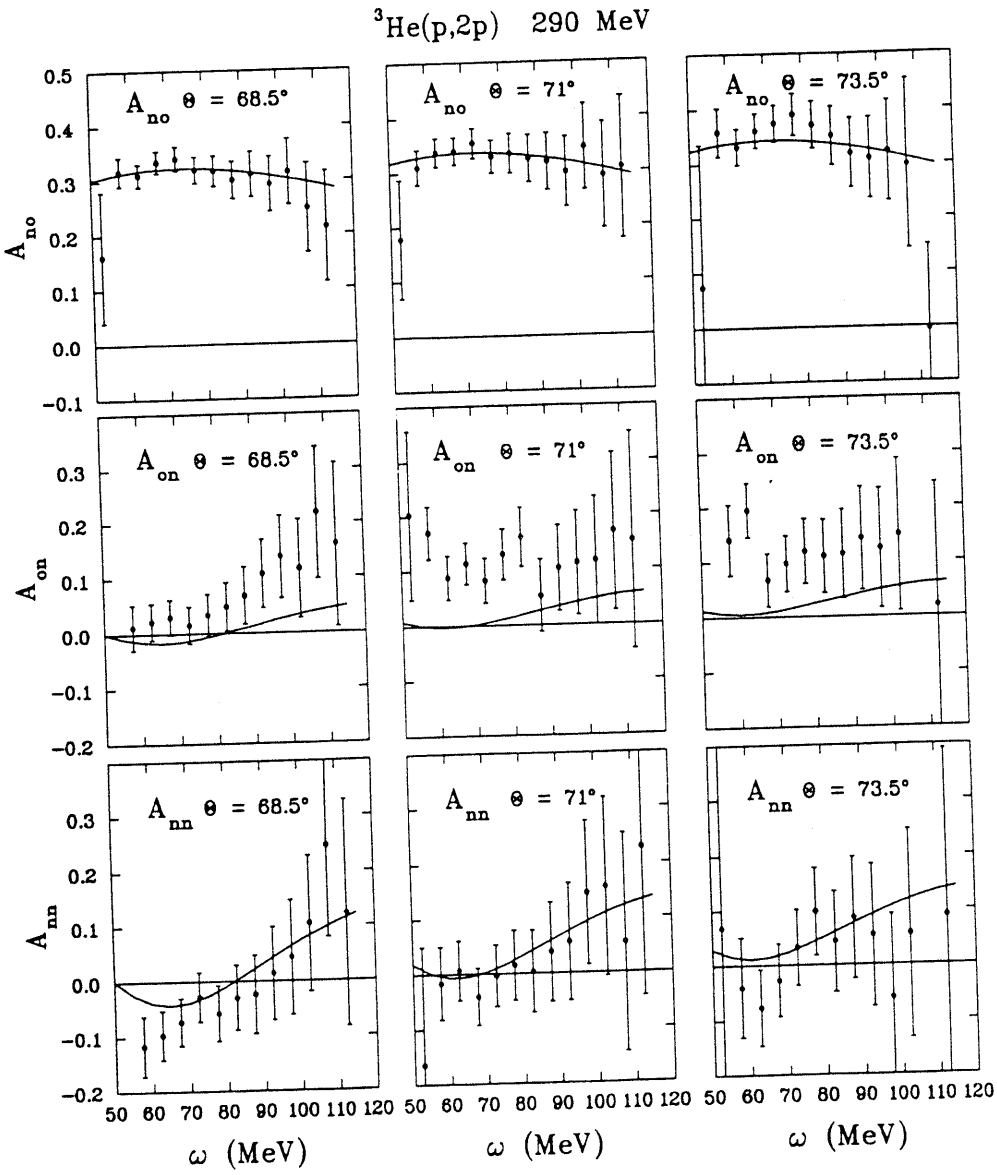

Figure 1.11. Spin observables for the ^{3}He(p,2p) reaction and the right scintillator array (nonconjugate angle).

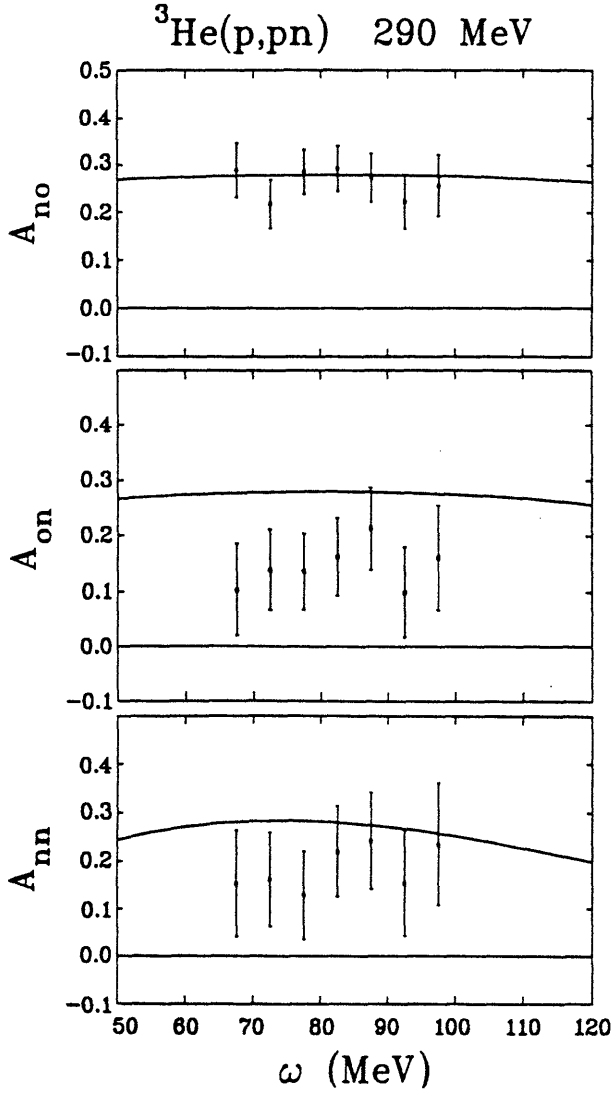

Figure 1.12. Spin observables for the ^{3}He(p,pn) reaction and the left scintillator array (conjugate angle).

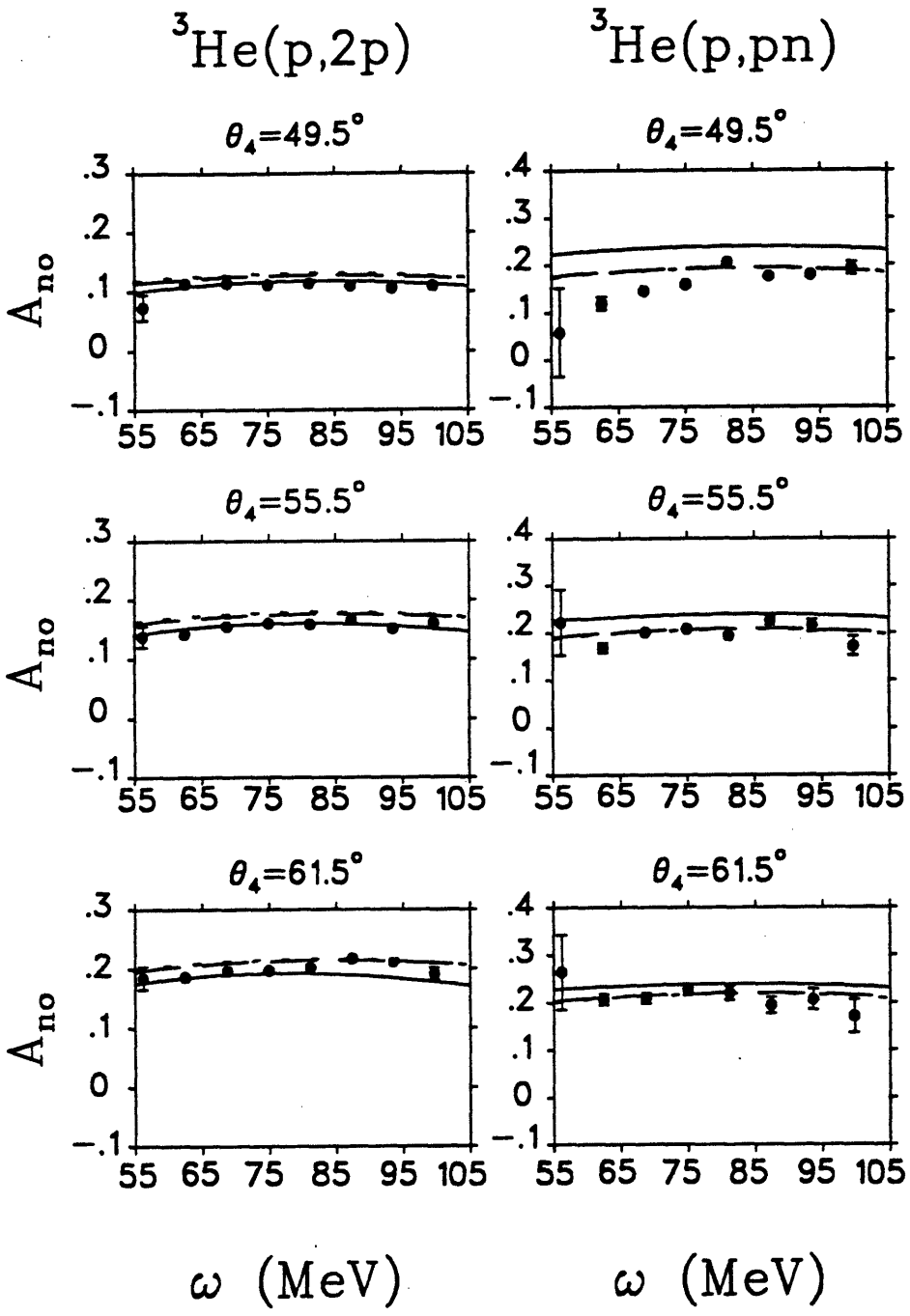

Figure.1.13. Beam-related analyzing powers for the $^3\overrightarrow{\text{He}}(\overrightarrow{\text{p}},2\text{p})^{\text{pn}}_{\text{d}}$ and $^3\overrightarrow{\text{He}}(\overrightarrow{\text{p}},\text{pn})$pp reactions. The solid line is the PWIA calculation of Woloshyn [1.27]. The short dashed line is the calculation with final state interactions between nucleons of the two-body recoil state included. The long dashed line is the same calculation with these final state interactions removed.

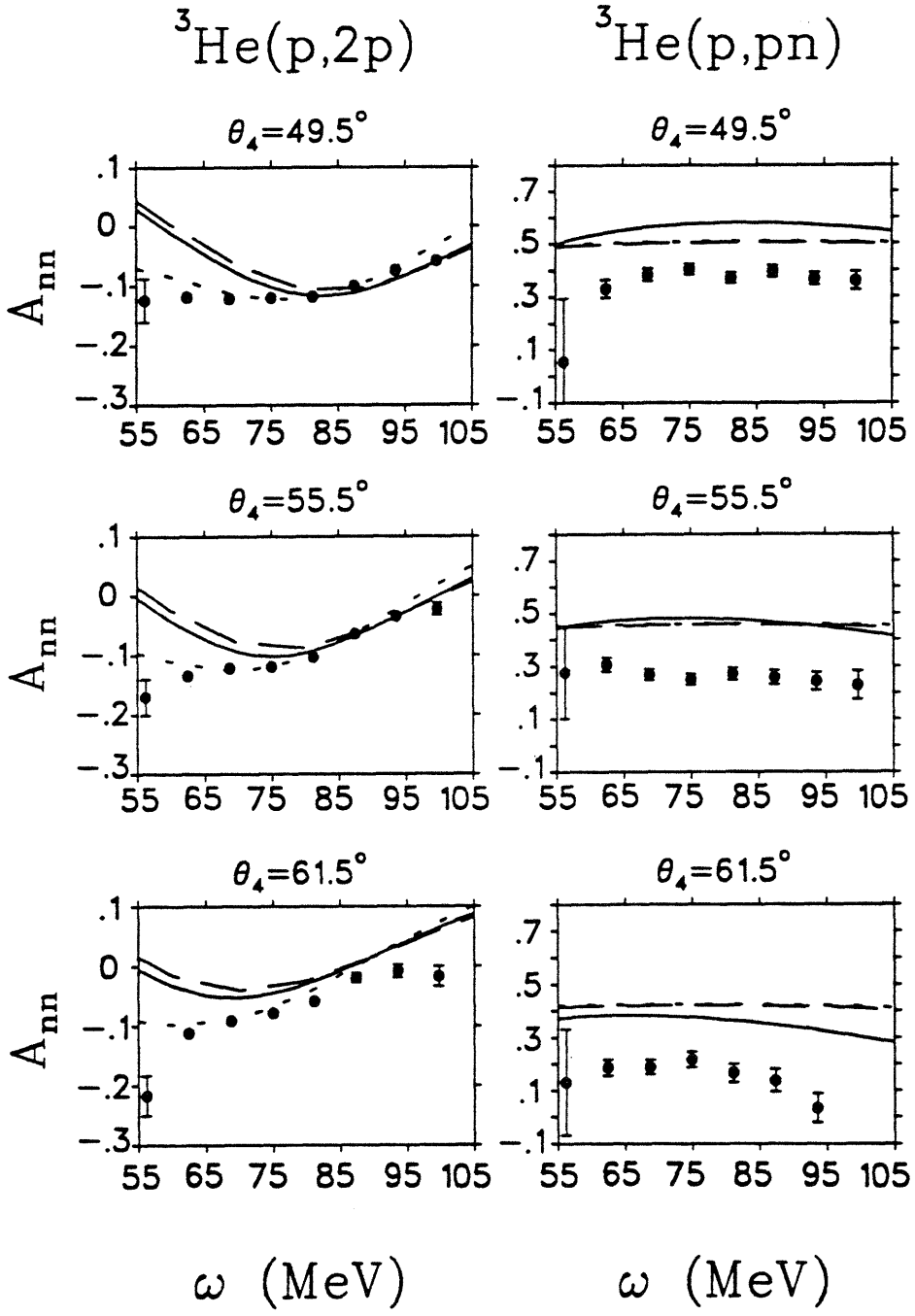

Figure.1.14. Spin correlation parameters for the $^3\overrightarrow{He}(\overrightarrow{p},2p)^{pn}_d$ and $^3\overrightarrow{He}(\overrightarrow{p},pn)pp$ reactions. The solid line is the PWIA calculation of Woloshyn [1.27]. The short dashed line is the calculation with final state interactions between nucleons of the two-body recoil state included. The long dashed line is the same calculation with these final state interactions removed.

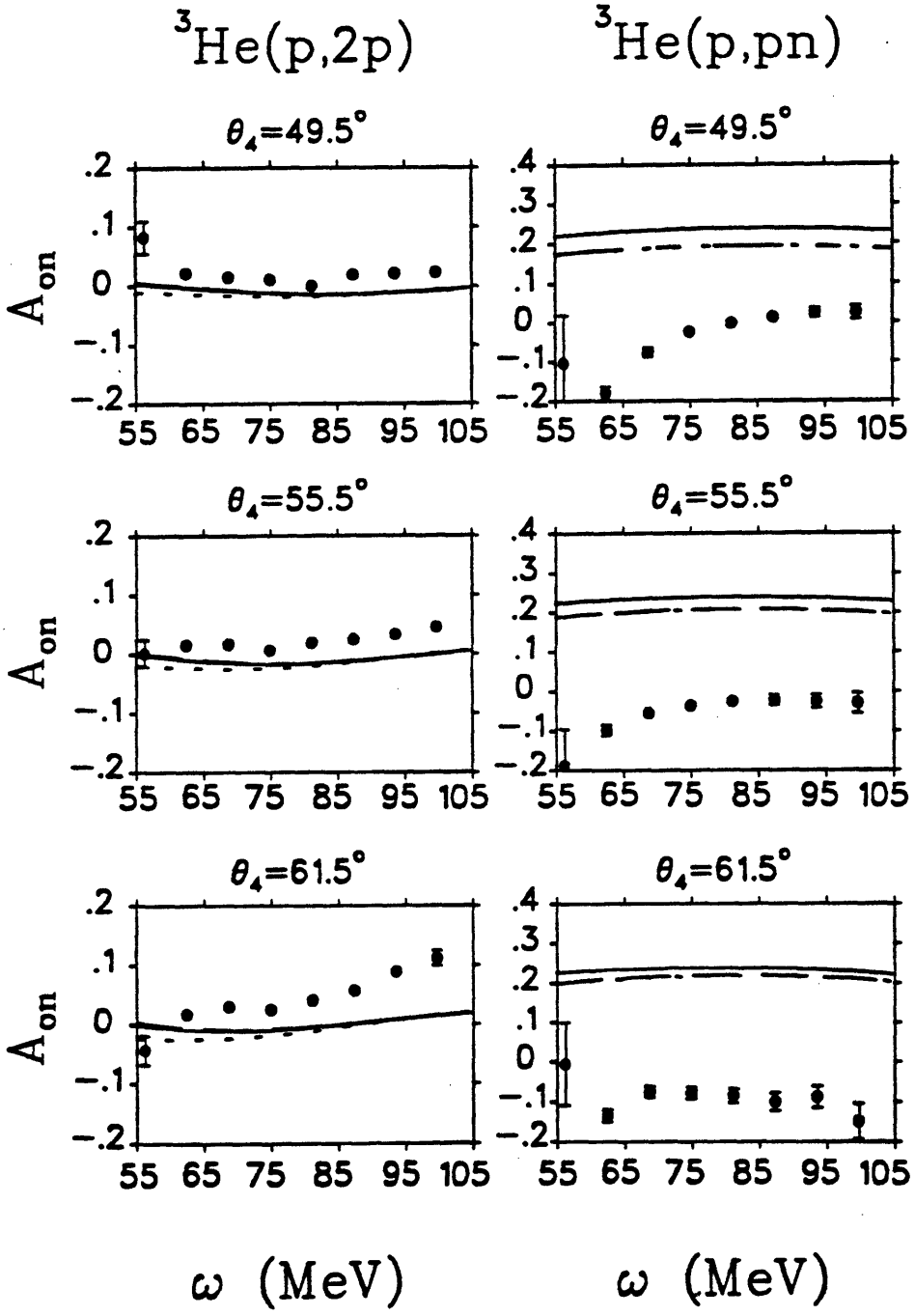

Figure.1.15. Target-related analyzing powers for the $^3\overrightarrow{He}(\overrightarrow{p},2p)^{pn}_d$ and $^3\overrightarrow{He}(\overrightarrow{p},pn)pp$ reactions. The solid line is the PWIA calculation of Woloshyn [1.27]. The short dashed line is the calculation with final state interactions between nucleons of the two-body recoil state included. The long dashed line is the same calculation with these final state interactions removed.

Chapter 2

Quasielastic Scattering

2.1 Overview

In this chapter, the use of quasielastic scattering as a tool to study the nucleon momentum distribution in nuclei is discussed. In particular, the Plane Wave Impulse Approximation (PWIA), which is used to interpret the experimental results is described. Starting from a general quasielastic scattering formalism, the PWIA is developed. Finally, a Monte Carlo model of the experiment using the PWIA is presented.

2.2 Quasielastic Scattering as an Experimental Probe

Scattering allows one to measure the dynamics of nuclear systems. Electron and photon scattering reactions in nuclear physics in the last thirty to forty years have provided a large body of information on nuclear structure. Reactions using hadron beams, such as proton, neutron, and pion have also provided much information on nuclear systems. In medium energy, beam kintetic energy ~200-1000 MeV, there is some probability for a scattering reaction to go into each of the following final states: elastic scattering, nuclear resonances, quasielastic scattering, and nucleon resonances. While the probe particle scatters coherently from the nucleons of a nuclear system in the elastic reaction and nuclear resonances, the probe particle in the quasielastic reaction and nucleon resonances, transfers dominantly an impulse to a single nucleon and scatters as if from a free nucleon with a momentum distribution.

In order to study nuclear systems, particularly single nucleon properties, it is important to have:

- the interaction of the probe particle with nucleons simple, well understood and calculable;
- the observed effects be dominated by the dynamics of the nucleons;
- the product of its passage time τ and interaction strength V with the nucleus is small compared to $\hbar$.

Under the third condition, the quasielastic scattering reaction can be approximated by a single impulse interaction of the probe particle with an almost free nucleon having an initial momentum. The nucleon is almost free because the nucleon is not on-shell with a nonzero binding energy. In this framework, the single nucleon momentum distributions could then be measured to understand the dynamics in nuclei.

By constrast when the third condition is not satisfied, multiple interactions are not negligible, and the observed effects may not be easily interpreted. In the initial state the beam particle can have interactions with multiple nucleons instead of an impulse interaction, resulting in a large background to the experimental signal of single nucleon properties in the nucleus. Such effects are called "initial state interactions". When there are interactions between the scattered particle and the nucleons after the impulse interaction, the outgoing momenta can be altered, similarly resulting in poor sensitivity of single nucleon properties. Such effects have been termed "final state interactions". Some examples are: the electron beam is distorted from the plane wave state due to Coulomb interaction with nuclear charge; similarly, the hadron beams generally interacts more than once with target nucleons due to the strong interaction; and the beam particle interacts with the meson exchange currents in the nucleus.

For the photon and the electron, the impulse scattering condition is easily satisfied in the medium energy range. Moreover, electromagnetic scattering is well understood and calculable to high precision using Quantum Electrodynamics. Given that the electron and the photon probes easily satisfy the impulse scattering condition, they do not disturb the rest of the nuclear system in the quasielastic scattering process, and therefore, they can be used to probe the dynamics of single nucleons with high precision. Furthermore, it allows one to extract off-shell nucleon form factors in light nuclei, if the nuclear properties and the the multiple scattering effects are known [2.1] and minimized. Even if electromagnetic processes are calculable to high precision, the description of nonquasielastic effects are model dependent and prescriptive. One such model is the distorted wave impulse approximation that is often used to correct for the distortion in the plane wave of the incident electron due to the Coulomb interaction with the nuclear charge.

However, proton beams are technically easier to produce and have interaction cross sections with nuclear targets three to four orders of magnitude larger than those of lepton or photon beams due to the strong interaction. Since hadron probes interact strongly with nuclear matter, the product of the passage time τ and the interaction strength V is not going to be much less than $\hbar$. Multiple interactions in the nucleus can dominate, and there is not likely to be a simple impulse interaction with one nucleon as in the case of the electromagnetic probes. Due to multiple scatterings of the probe, the observed effects may not be easily interpreted in terms of the dynamics of target nucleons. In the future, few body calculations can serve to give a detail account of the nonquasielastic processes [2.2] for both electromagnetic

probes and hadron probes.

Despite the higher probability for multiple interactions, proton beams have been sucessfully used as quasielastic scattering probes in the beam kinetic energy range ~200-1000 MeV to study nuclear systems from heavy nuclei to light nuclei. The quasielastic scattering process of knocking out a single proton from nuclear targets was first used in proton scattering experiments in 1952 at the 350 MeV synchrocyclotron in Berkeley where strongly correlated proton pairs were observed emerging from a Li target. In addition, the cross section was found to be Z (= 3) times the proton-proton cross section. Using the 185 MeV synchrocyclotron in Uppsala, the shell structure in nuclei was confirmed by the quasielastic (p,2p) scattering reaction in 1957. For a review of proton quasielastic scattering on nuclei heavier than ^{4}He, see the article by P. Kitching *et al.* [2.3].

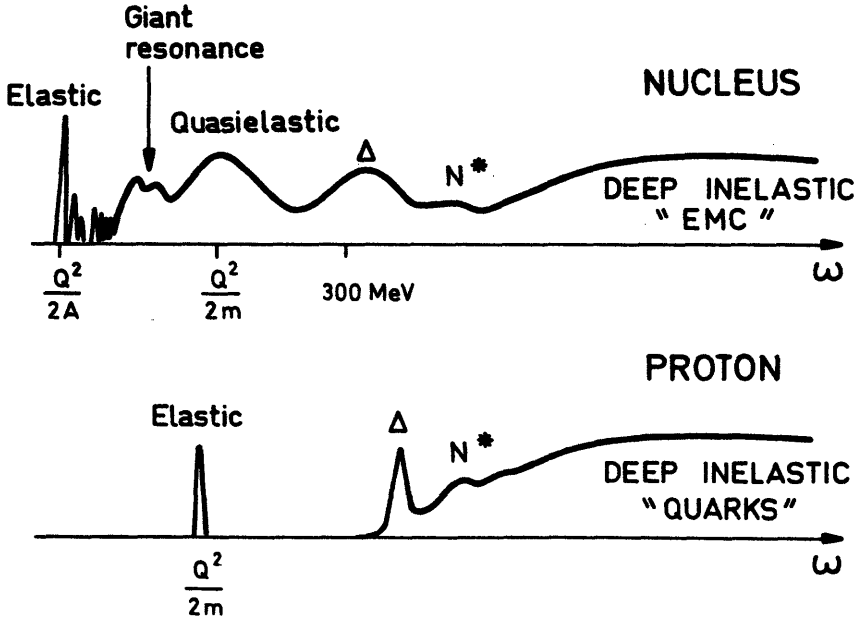

Figure 2.1. A generic inclusive electron scattering spectrum. The figure is taken from Frois and Papnicolas [2.4].

In the intermediate range of beam kinetic energies from ~200-1000 MeV of the proton, the electron, or the photon beams, there can be a number interaction channels with varying strengths depending on the kinematics: elastic scattering, resonances, single nucleon excited states, quasielastic scattering, pion production, and the delta resonance. Indeed, in Figure 2.1, a typical intermediate energy electron scattering cross section of the "inclusive reaction"—where only the scattered particle is detected—is plotted as a function of energy transfer ω for a fixed 4-

momentum transfer squared Q^2, showing the structures of the different channels. The structures are defined by only the kinematic variables Q^2 and ω. Specifically, the elastic and quasielastic peaks are at energy transfers of

$$\omega_{e.} = Q^2/2m_A \tag{2.1a}$$

and

$$\omega_{q.e.} = Q^2/2m_N + E_b \ , \tag{2.1b}$$

where both cases are similar in form and in the second case E_b is the nucleon removal energy from the nucleus, indicating that the ejected nucleon is a bound nucleon.

One can extend the picture to describe the quasielastic scattering peak as a hole excitation which results from the ejection of a single nucleon from one of the energy shells of the nucleus. This picture of using the shell model is limited to nuclear systems with mass greater than A = 4. When the nuclear system is just 3-nucleons or 4-nucleons, the shell model is no longer valid. However, few body calculations have recently become available for the 3-nucleon system where nucleon momentum distributions or spectral functions have been formulated for use in electron quasielastic scattering [1.27, 1.28].

As discussed above, each component in the electron scattering cross section in Figure 2.1 is a function of Q^2 and ω only, with its strength diminishing with increasing Q^2. Each peak has a total mass energy M_x that results from energy and 3-momentum transfer to the nuclear system,

$$\begin{aligned} M_x^2 &= (\omega + M_A)^2 - \mathbf{q}^2 \\ &= -Q^2 + M_A^2 + 2\omega M_A \ . \end{aligned} \tag{2.2}$$

Upon substitution of the quasielastic condition into the mass equation above, the total mass energy M_x becomes a function of either Q^2 or $\omega_{q.e.}$:

$$\begin{aligned} M_{x\ q.e.}^2 &= Q^2(\frac{M_A}{M_N} - 1) + 2E_b M_A + M_A^2 \\ &= 2\omega(M_A - M_N) + 2E_b M_N + M_A^2 \ , \end{aligned} \tag{2.3}$$

from which one can estimate the minimum value of Q^2 and ω. If the quasielastic scattering process can be described by a simple removal of a nucleon from the nucleus, the minimum of $M_{x\ q.e.}$ is just

$$M_{x\ q.e.(min)} = E_b + M_A \ . \tag{2.4}$$

Therefore, the minimum value of Q^2 and $\omega_{q.e.}$ is:

$$\begin{aligned} Q^2_{(min)} &= \frac{E_b^2}{(M_A/M_N - 1)} \\ \omega_{q.e.(min)} &= E_b \ . \end{aligned} \tag{2.5}$$

At the minimum values of the kinematic variables, the nonquasielastic processes can dominate, and one can minimize the nonquasielastic processes in inclusive reactions by choosing kinematic regimes far above the minimum values. On the other hand, as mentioned earlier, the signal strength of each structure in Figure 2.1 is decreasing with increasing Q^2. Therefore, one has to optimize the signal to noise ratio over the kinematic regimes.

Experimentally, the ejected nucleon in quasielastic scattering is often detected in coincidence with the scattered particle, allowing a reconstruction of single nucleon momentum distributions in nuclei [2.5,2.3] and exclusively detecting a particular reaction, such as in the "exclusive reactions" ^{3}He(p,p'N)A$-$1 or ^{3}He(e,e'N)A$-$1— where one or more coincident particles in addition to the scattered particle are detected. In the energy and momentum conservation equations,

$$\begin{aligned} E_0 + M_A &= E_1 + E_2 + E_{A-1} \\ \mathbf{p}_0 + \mathbf{p}_A &= \mathbf{p}_1 + \mathbf{p}_2 + \mathbf{p}_{A-1} \ , \end{aligned} \tag{2.6}$$

the energy and momentum of the recoiling A$-$1 system are constrained once the energy and momentum of the scattered and the ejected particles are determined. Therefore, the energy and momentum E_{A-1} and $\mathbf{p}_{A-1}$ are measured and can be used to define the "missing energy" E_m and the "missing momentum" $\mathbf{p}_m$ as

$$\begin{aligned} E_m &= \sqrt{E^2_{A-1} - \mathbf{p}^2_{A-1}} + m_{beam} - m_A \\ \mathbf{p}_m &= \mathbf{p}_{A-1} \ . \end{aligned} \tag{2.7}$$

In quasielastic scattering when the initial and final state interactions are negligible, the removal energy E and the nucleon momentum $\mathbf{p}_N$ are identified with the missing energy E_m and the missing momentum $\mathbf{p}_m$. Figure 2.2 shows plots of the measured missing energy distributions at different missing momentum ranges obtained from the ^{12}C(e, e'p) scattering reaction.

The use of proton beams to measure the proton momentum distribution in ^{3}He was shown by Epstein *et al.* to be in good agreement with results obtained using electron beams up to the nucleon momentum ~200 MeV/c, beyond which the proton probe has been interpreted as not reliable [2.6].

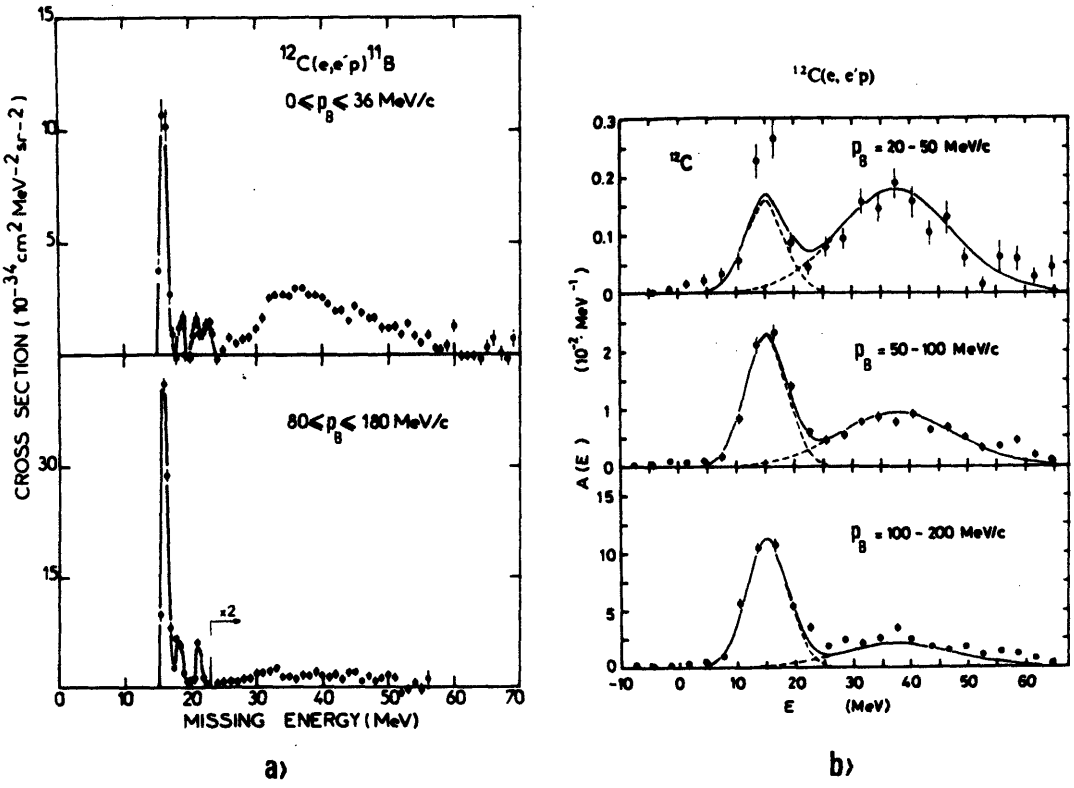

Figure 2.2. Missing energy E_m distributions at different ranges of $\mathbf{p}_m$ obtained from $^{12}C(e,e'p)$ scattering reaction [2.5].

When the ejected nucleon is detected to measure the single nucleon momentum in nuclei, one needs to minimize the final state interaction of the ejected nucleon by selecting kinematic conditions for which the ejected particle moves through the medium in a very short time so that the product of its average interaction strength V and the transit time τ is small compared to $\hbar$. Equivalently, its momentum must be large compared to the average nucleon momentum which is $\sim$ 100 MeV/c in light nuclei since the average nucleon momentum is determined by the average interaction strength V between nucleons. This condition of large ejected nucleon momentum will be used as a test on the spin-dependent quasielastic neutron results of this thesis.

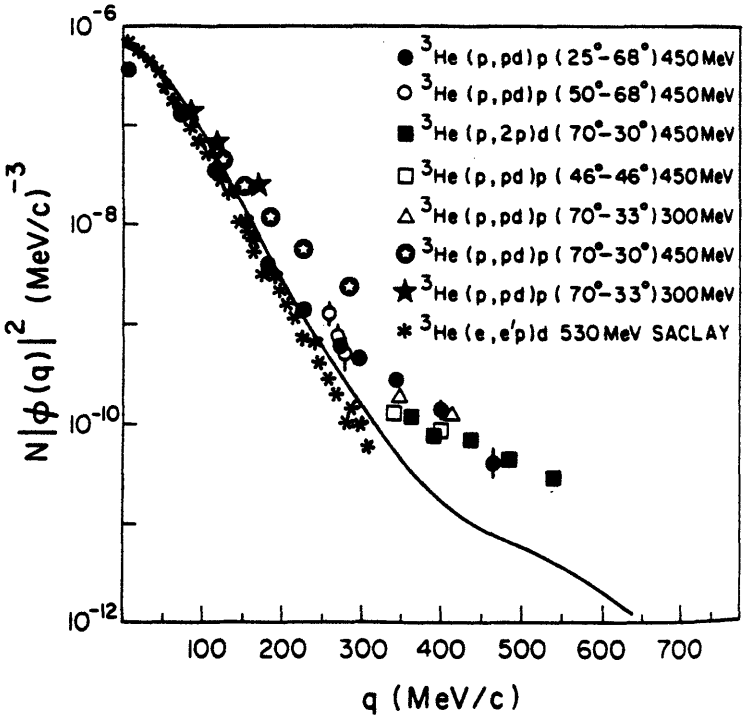

Figure 2.3. Comparison of the proton momentum distribution of the ^{3}He system between proton beam data at various kinematic conditions with electron beam data and a calculation by C. degli Atti [2.6].

2.3 Nucleon-Nucleon Elastic Scattering

Nucleon-nucleon elastic scattering is discussed in this section. A nucleon with an incoming momentum $\mathbf{k}$ is scattered into momentum $\mathbf{k}'$ in the c.m. frame of the two nucleons. The nucleon-nucleon elastic scattering matrix operator in the c.m. frame can be written, assuming parity conservation, time-reversal invariance, the Pauli exclusion principle, and isospin invariance, in terms of only the invariant scattering amplitudes a, b, c, d, and e [2.7],

$$\begin{aligned} M^{NN}(\mathbf{k}',\mathbf{k}) = \frac{1}{2}\Big\{ & (a+b) + (a-b)(\sigma_1\cdot\hat{\mathbf{n}})(\sigma_2\cdot\hat{\mathbf{n}}) \\ & + (c+d)(\sigma_1\cdot\hat{\mathbf{m}})(\sigma_2\cdot\hat{\mathbf{m}}) \\ & + (c-d)(\sigma_1\cdot\hat{\mathbf{l}})(\sigma_2\cdot\hat{\mathbf{l}}) + e\big[(\sigma_1\cdot\hat{\mathbf{n}}) + (\sigma_2\cdot\hat{\mathbf{n}})\big]\Big\} \end{aligned} \tag{2.8}$$

where the Pauli matrices σ_1 and σ_2 act on the wavefunction of particles 1 and 2 and the unit vectors are defined by the incident and the scattered momentum vectors as

$$\hat{\mathbf{l}} = \frac{\mathbf{k}'_{c.m.} + \mathbf{k}_{c.m.}}{|\mathbf{k}'_{c.m.} + \mathbf{k}_{c.m.}|}\,, \quad \hat{\mathbf{m}} = \frac{\mathbf{k}'_{c.m.} - \mathbf{k}_{c.m.}}{|\mathbf{k}'_{c.m.} - \mathbf{k}_{c.m.}|}\,, \quad \hat{\mathbf{n}} = \frac{\mathbf{k}_{c.m.} \times \mathbf{k}'_{c.m.}}{|\mathbf{k}_{c.m.} \times \mathbf{k}'_{c.m.}|}\,. \tag{2.9}$$

Only in the c.m. frame, the matrix element is symmetric between the two particles which is important if one is to do calculation of the scattering cross section. In this section, the discussion is going to be limited to looking at the spin-dependent formalism, and there is no need to write out explicitly the form of the operator. Therefore, in what follows the nucleon-nucleon scattering operator M^{NN} is no longer defined in the c.m. frame as in equation (2.8) but is given for any frame. While one set of unit vectors is sufficient to describe the spin directions of the initial and the final states of the particles, four sets are needed in an unspecified frame:

$$\begin{aligned} &\hat{\mathbf{n}} = \frac{\mathbf{p}_0 \times \mathbf{p}_1}{|\mathbf{p}_0 \times \mathbf{p}_1|}\,, \quad \hat{\mathbf{k}} = \frac{\mathbf{p}_0}{p_0}\,, && \hat{\mathbf{s}} = \hat{\mathbf{n}} \times \hat{\mathbf{k}}\,; \\ &\hat{\mathbf{n}}\,, && \hat{\mathbf{k}}_N = \frac{\mathbf{p}_N}{p_N}\,, && \hat{\mathbf{s}}_N = \hat{\mathbf{n}} \times \hat{\mathbf{k}}_N\,; \\ &\hat{\mathbf{n}}\,, && \hat{\mathbf{k}}_1 = \frac{\mathbf{p}_1}{p_1}\,, && \hat{\mathbf{s}}_1 = \hat{\mathbf{n}} \times \hat{\mathbf{k}}_1\,; \\ &\hat{\mathbf{n}}\,, && \hat{\mathbf{k}}_2 = \frac{\mathbf{p}_2}{p_2}\,, && \hat{\mathbf{s}}_2 = \hat{\mathbf{n}} \times \hat{\mathbf{k}}_2\,; \end{aligned} \tag{2.10}$$

where $\mathbf{p}_0$ and $\mathbf{p}_1$ are the incident and scattered momenta of particle 1 while $\mathbf{p}_N$ and $\mathbf{p}_2$ are the initial and ejected momenta of particle 2. The unit vector $\hat{\mathbf{n}}$ remains

the same as in the c.m. frame while the the other unit vectors are different. If the target nucleon motion is slow compared to the incident nucleon, and it is on the average stationary, then the set of unit vectors for the incident nucleon can be used for the target nucleon since a stationary or near stationary particle can have its spin state defined in any direction. In what follows, only the incident nucleon unit vectors set will be used for the target nucleon.

The matrix amplitude is squared to obtain the elastic scattering probability,

$$\Gamma^{NN} = \left| \langle \mathbf{p}_1 \mathbf{s}_1 t_1,\ \mathbf{p}_2 \mathbf{s}_2 t_2 |\ M^{NN}\ | \mathbf{p}_0 \mathbf{s}_0 t_0,\ \mathbf{p}_N \mathbf{s}_N t_N \rangle \right|^2 \tag{2.11}$$

where the initial and final momentum, spin, and isospin states are respectively $|\mathbf{p}_0 \mathbf{s}_0 t_0\rangle$ and $|\mathbf{p}_1 \mathbf{s}_1 t_1\rangle$ for particle 1 and respectively $|\mathbf{p}_N \mathbf{s}_N t_N\rangle$ and $|\mathbf{p}_2 \mathbf{s}_2 t_2\rangle$ for particle 2. The spin-dependent scattering cross section can be expressed as,

$$\begin{aligned} d\sigma^{NN} = & \frac{1}{\text{flux}^{NN}} \frac{1}{2E_0 2E_N} (2\pi)^4\ \delta^{(4)}(p_1 + p_2 - p_0 - p_N) \\ & \times \Gamma^{NN} \frac{d^3\mathbf{p}_1}{(2\pi)^3 2E_1} \frac{d^3\mathbf{p}_2}{(2\pi)^3 2E_2} . \end{aligned} \tag{2.12}$$

where

$$\frac{1}{\text{flux}^{NN}} = \frac{p_0 \cdot p_N}{\sqrt{(p_0 \cdot p_N)^2 - m_0^2 m_N^2}} .$$

Moreover, the matrix element M^{NN} in equation (2.11) can be written for a combination of isospin singlet and triplet configurations of T=0 and T=1 to describe the proton-neutron scattering reaction or only isospin triplet configuration of T=1 to describe the proton-proton scattering reaction. While the total isospin of the reaction is conserved, the total spin can change, allowing therefore, sixteen different combinations of the initial and final nucleon spin states and resulting in 256 different spin combinations of the scattering probability Γ. In the particles' spin space, the cross section and the asymmetries are formulated in general as [2.7]

$$\begin{aligned} \frac{d\sigma_\circ^{NN}}{d\Omega} & \propto \frac{1}{4} \text{Tr}\ M^\dagger M \\ \frac{d\sigma_\circ^{NN}}{d\Omega} X_{pqij} & \propto \frac{1}{4} \text{Tr}\ (\sigma_1 \cdot \hat{\mathbf{p}})(\sigma_2 \cdot \hat{\mathbf{q}})\ M^\dagger\ (\sigma_1 \cdot \hat{\imath})(\sigma_2 \cdot \hat{\jmath})\ M\ . \end{aligned} \tag{2.13}$$

where $(\sigma_1 \cdot \hat{\mathbf{p}})$ and $(\sigma_2 \cdot \hat{\mathbf{q}})$ operate on respectively the scattered and ejected particle states, and $(\sigma_1 \cdot \hat{\imath})$ and $(\sigma_2 \cdot \hat{\jmath})$ operate on respectively the incident and target particle states. The indices p, q, i, and j indicate respectively the spin directions of the scattered, ejected, beam, and target particles to be along one of the corresponding

unit vector directions in equation (2.10). If the particle has zero spin or its spin states are not known, then the index letter is replaced with zero. Including the unpolarized cross section, there is a total of 256 such asymmetry observables. If the spin states of the scattered and ejected particles are not known, then the number of experimental observables is reduced to sixteen. They are the unpolarized cross section and the fifteen asymmetries which are summarized as

$$\begin{aligned}
\frac{d\sigma_\circ^{NN}}{d\Omega} &\propto \frac{1}{4}\mathrm{Tr}\ M^\dagger M \\
\frac{d\sigma_\circ^{NN}}{d\Omega} A_{00i0} &\propto \frac{1}{4}\mathrm{Tr}\ M^\dagger\ ((\sigma_1 \cdot \hat{\jmath}))\ M \\
\frac{d\sigma_\circ^{NN}}{d\Omega} A_{000j} &\propto \frac{1}{4}\mathrm{Tr}\ M^\dagger\ ((\sigma_2 \cdot \hat{\jmath}))\ M \\
\frac{d\sigma_\circ^{NN}}{d\Omega} A_{00ij} &\propto \frac{1}{4}\mathrm{Tr}\ M^\dagger\ ((\sigma_1 \cdot \hat{\imath}))((\sigma_2 \cdot \hat{\jmath}))\ M\ ,
\end{aligned} \tag{2.14}$$

where $(\sigma_1 \cdot \hat{\imath})$ and $(\sigma_2 \cdot \hat{\jmath})$ operate on the incident and target particle states. Of the sixteen physical observables, half of these are zero due to parity conservation. They are A_{00k0}^{NN}, A_{00m0}^{NN}, A_{000k}^{NN}, A_{000m}^{NN}, A_{00nk}^{NN}, A_{00kn}^{NN}, A_{00ns}^{NN}, and A_{00sn}^{NN}.

The elastic scattering cross section in the c.m. frame can be then written in terms of the polarizations and the remaining nonzero observables as

$$\begin{aligned}
\frac{d\sigma^{NN}}{d\Omega} = \frac{d\sigma_\circ^{NN}}{d\Omega} \Big\{ & 1 + (\hat{\mathbf{n}} \cdot \mathbf{P}_b) A_{00n0}^{NN} \\
& + (\hat{\mathbf{n}} \cdot \mathbf{P}_t) A_{000n}^{NN} + (\hat{\mathbf{n}} \cdot \mathbf{P}_b)(\hat{\mathbf{n}} \cdot \mathbf{P}_t) A_{00nn}^{NN} \\
& + (\hat{\mathbf{k}} \cdot \mathbf{P}_b)(\hat{\mathbf{k}} \cdot \mathbf{P}_t) A_{00kk}^{NN} \\
& + (\hat{\mathbf{s}} \cdot \mathbf{P}_b)(\hat{\mathbf{s}} \cdot \mathbf{P}_t) A_{00ss}^{NN} \\
& + (\hat{\mathbf{k}} \cdot \mathbf{P}_b)(\hat{\mathbf{s}} \cdot \mathbf{P}_t) A_{00ks}^{NN} + (\hat{\mathbf{s}} \cdot \mathbf{P}_b)(\hat{\mathbf{k}} \cdot \mathbf{P}_t) A_{00sk}^{NN} \Big\}\ .
\end{aligned} \tag{2.15}$$

The derivation of equation (2.15) from equation (2.12) is given in Appendix B.

The normal asymmetries A_{00n0}^{NN} and A_{000n}^{NN} and similarly, the interference asymmetries A_{00sk}^{NN} and A_{00ks}^{NN} are equal to each other due to symmetry of the nucleons which is the case in proton-proton scattering and is also the case in proton-neutron scattering assuming that charge symmetry breaking is negligible. Furthermore, the proton-proton scattering observables are symmetric with respect to the c.m. scattering angle.

There exists now an extensive set of world data on nucleon-nucleon scattering up to a few GeV of beam kinetic energy [2.8, 2.9]. Phase shift analyses have been performed on the data to generate solutions which allow reconstruction of nucleon-nucleon cross sections and asymmetries within the experimental kinematic ranges.

These solutions are available in the form of an interactive program called Scattering Analysis Interactive Dialup (SAID), compiled by Arndt *et al.* [2.10]. The program can generate experimental scattering observables defined using the laboratory coordinate vectors as functions of the c.m. angle, the laboratory angle, beam kinetic energy in the lab frame, and so on. The program's solutions are updated regularly to include recent data or analyses. The version used for the Monte Carlo calculation was updated in the Summer of 93' (SM93) and has

$$\begin{aligned} \chi^2/\mathrm{N_{data}} &= 23224/12768 && \mathrm{p-p\ scattering\ data} \\ &= 18237/10619 && \mathrm{n-p\ scattering\ data\ .} \end{aligned}$$

There are also other phase shift solutions such as Bugg-Bryan, Bonn, Paris, *etc.* available in the program. These solutions can be used to generate the asymmetry observables that can vary up to 10%, one from the other, particularly for proton-neutron scattering since there are less of precision data on proton-neutron scattering than on proton-proton scattering. However, recently high precision data for proton-neutron scattering have become available, improving the accuracy of the phase shift results [2.9]. Below are plots of the cross sections and asymmetries defined in the laboratory coordinates and generated by the SM93' solution of the SAID program at 200 MeV beam energy. Besides the nucleon-nucleon elastic scattering observables, the program can also provide generate scattering observables for pion-nucleon and kaon-nucleon interactions. Below are the nucleon-nucleon elastic scattering observables defined by the set of unit vectors for the incident nucleon as in equation (2.15) but are plotted as functions of the c.m. angle.

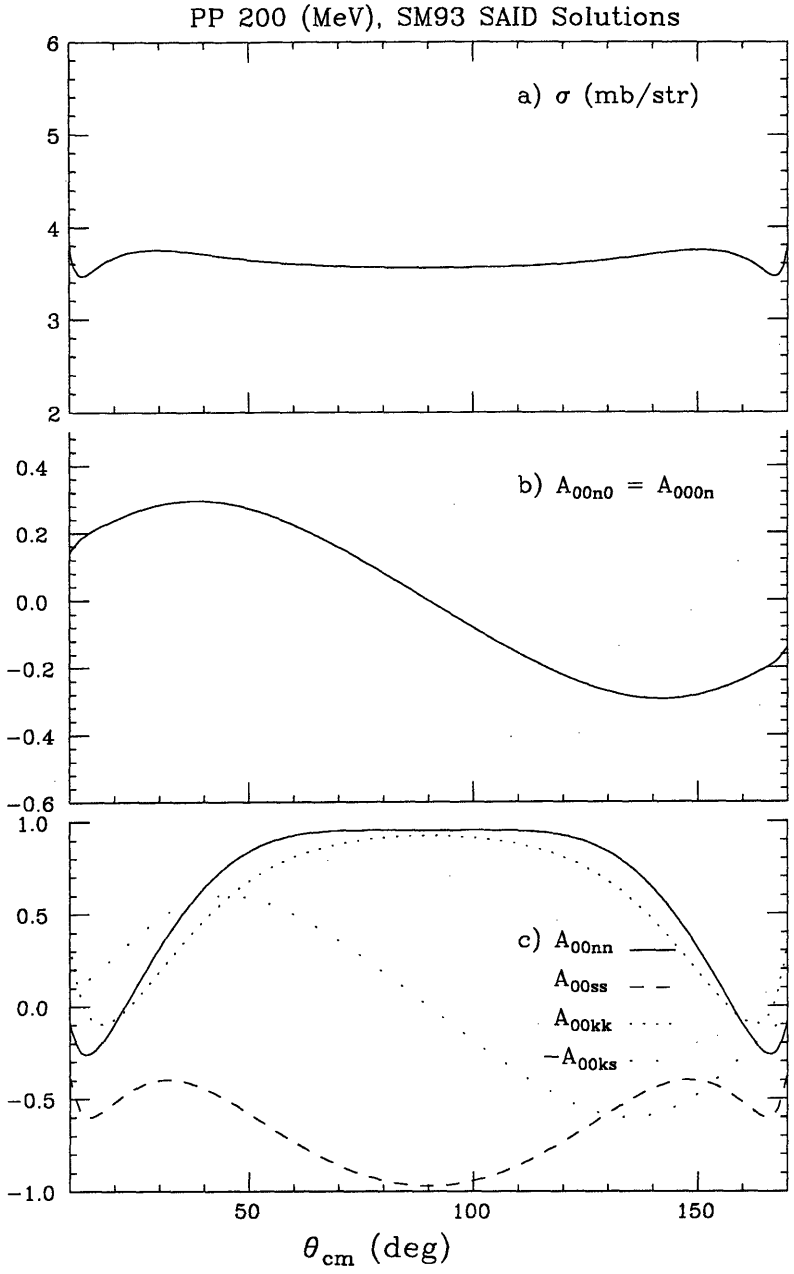

Figure 2.4. SAID Summer93' solutions of the proton-proton scattering at 200 MeV. The cross section $d\sigma_0^{pp}/d\Omega_{c.m.}$ (mb/str) in (a), the normal asymmetry A_{00n0}^{pp} or A_{000n}^{pp} in (b), and in (c) the spin-correlation parameters A_{00nn}^{pp} in solid line for normal direction, A_{00kk}^{pp} in dotted line for longitudinal direction, A_{00ss} in dashed line for side direction, and $(-A_{00ks}^{pp})$ in sparse dotted line for longitudinal and side directions.

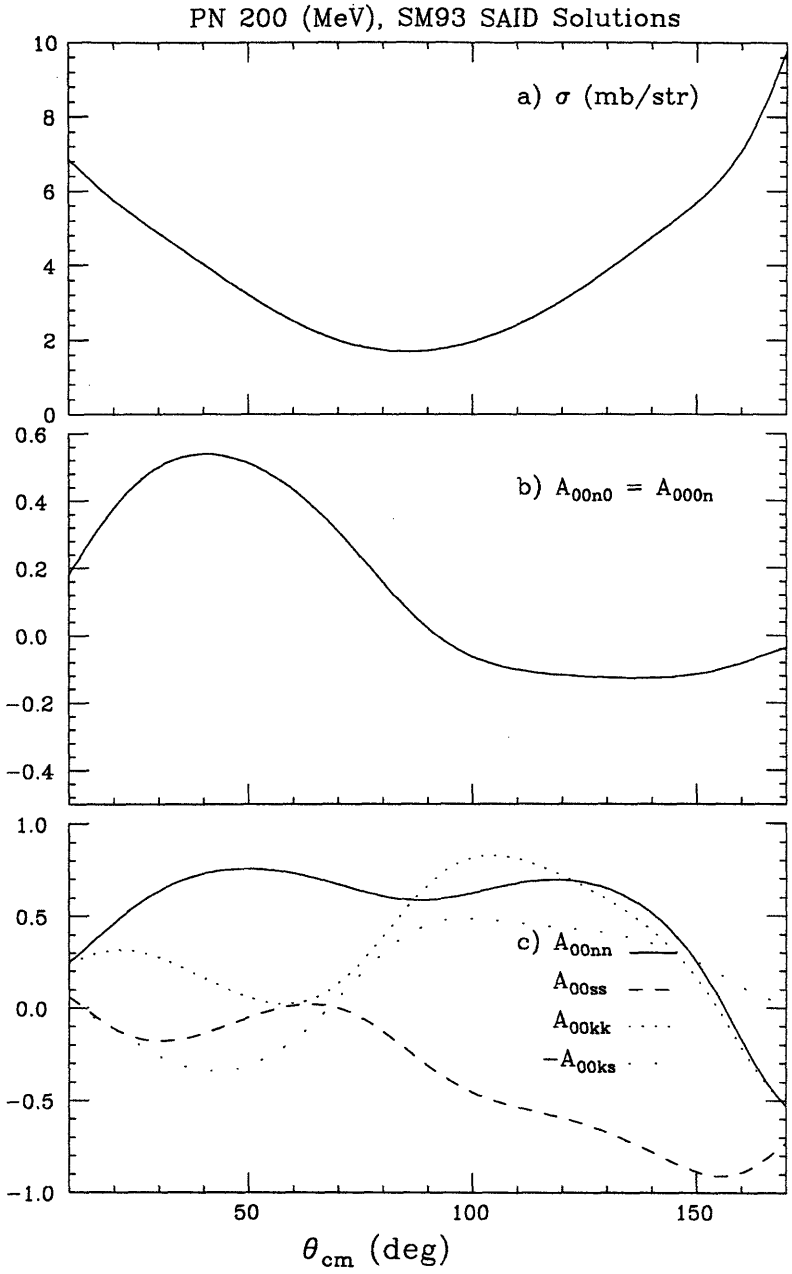

Figure 2.5. SAID Summer93' solutions of the proton-neutron scattering at 200 MeV. The cross section $d\sigma_\circ^{pn}/d\Omega_{c.m.}$ (mb/str) in (a), the normal asymmetry A_{00n0}^{pn} or A_{000n}^{pn} in (b), and in (c) the spin-correlation parameters A_{00nn}^{pn} in solid line for normal direction, A_{00kk}^{pn} in dotted line for longitudinal direction, A_{00ss} in dashed line for side direction, and $(-A_{00ks}^{pn})$ in sparse dotted line for longitudinal and side directions.

2.4 Spin-Dependent Quasielastic Scattering Using Protons

Spin-dependent quasielastic scattering allows one to look at small signals in nuclear physics. Recently, the quasielastic $^3\overrightarrow{He}(\overrightarrow{e},e')$ inclusive reaction was used to measure the neutron (very small) electric and magnetic form factors, $G_E^n(Q^2)$ and $G_M^n(Q^2)$ [1.6-1.10] which are obtained from experimental asymmetries. The asymmetries result from: (i) the polarized neutron (ii) the nonzero polarization of the protons in ^{3}He, (iii) meson exchanged currents, and (iv) the elastic tail.

The signal from the neutron alone is an order of magnitude or two smaller than these signals. Although the measurement was carried out on the quasielastic peak, there were still interference processes and in this case, they were used to measure small signals. Detection of the coincident neutron has been used to enhance the small signals in the $^3\overrightarrow{He}(\overrightarrow{e},e'n)$ reaction [1.11] where the following backgrounds were eliminated: (i)the nonzero proton polarization, (ii) the meson exchanged currents, and (iii) the elastic tail. Similarly, the quasielastic $d(\overrightarrow{e},e'\overrightarrow{n})$ reaction [1.12] has been used to measure the electric and magnetic form factors of the neutron. Detection of the knocked out neutron can "filter out" comparable asymmetry contributions to the scattering from the protons in ^{3}He. However, there is the added complication of final state interactions with detection of the ejected neutron.

As mentioned in Chapter 1, comparison of theory to experiment for the spin-dependent single nucleon dynamics in ^{3}He will be important to the interpretation of results from experiments of polarized ^{3}He as an effective polarized neutron target. The CE-25 experiment at IUCF was carried out to measure spin-dependent nucleon properties using exclusive reactions $^3\overrightarrow{He}(\overrightarrow{p},2p)$ and $^3\overrightarrow{He}(\overrightarrow{p},pn)$ extending the kinematic regimes of the previous measurements at TRIUMF [1.29,1.31]. Here, the formalism of spin-dependent quasielastic scattering is developed to allow interpretation of the data and to motivate a Monte Carlo simulation for comparison to the data.

As discussed previously, the quasielastic scattering exclusive reaction allows one to measure the nucleon momentum distribution as in $^3\overrightarrow{He}(\overrightarrow{p},pN)A-1$. By polarizing the beam protons and the target ^{3}He's, one is further able to measure the the spin-dependent nucleon momentum distributions of ^{3}He. The derivations in this section and in Appendix C show how the spin-dependent nucleon momentum distributions can be determined.

The quasielastic scattering reaction on ^{3}He using a proton beam can be seen as a 4-body interaction process in which the dominant interaction takes place between the beam proton and a single off mass shell target nucleon. In this reaction, the

4-body system evolves from the initial state of

$$|\mathbf{p}_0\mathbf{s}_0, \mathbf{p}_A\mathbf{s}_A\rangle \ , \tag{2.16}$$

where $|\mathbf{p}_0\rangle$ and $|\mathbf{p}_A\rangle$ are the beam and target particle plane wave state vectors—in addition, the state vector $|\mathbf{p}_A\rangle$ includes the ^{3}He wavefunction obtained from 3-body calculations— to the final state as below

$$\mathcal{A}\,|\mathbf{p}_1\mathbf{s}_1,\ \mathbf{p}_2\mathbf{s}_2,\ \mathbf{p}_{A-1}\mathbf{s}_{A-1}\mathrm{f}_{A-1}\rangle \ , \tag{2.17}$$

where $\mathbf{p}_1$ and $\mathbf{p}_2$ are respectively the scattered and ejected particle plane wave states and $\mathbf{p}_{A-1}$ is the recoiling system plane wave state of the deuteron or an unbound system of the proton and neutron or of the two protons. The operator $\mathcal{A}$ is used to asymmetrize the outgoing plane wave states. The recoiling system A$-$1 can be a deuteron as in the 2-body breakup of the ^{3}He nucleus or a free neutron and proton or two free protons as in the 3-body breakup. Again, the dominant interaction is with a single nucleon; the energy and momentum of the beam proton is transferred largely to the nucleon.

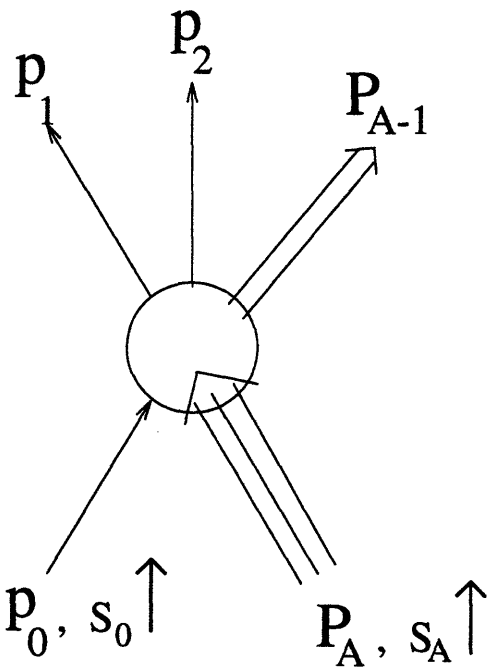

Figure 2.6. Quasielastic scattering reaction (p + ^{3}He $\rightarrow$ p + N + X_{A-1}) of the proton from the ^{3}He nucleus showing the knockout of a nucleon along with the remaining A$-$1 nuclear system which can be an unbound system or the bound deuteron. The interaction transfer energy and momentum largely to a single nucleon in order for the process to be quasielastic.

As the beam particle approaches the target nucleus, an interaction with the target nucleons takes place. The mutual pair interactions among the four nucleons exist until the particles are far enough separated. Any single realistic-potential model such as the Reid, Paris, or Bonn models can be used to describe the interaction between pairs of nucleons. Carrying out a 4-body calculation would completely describe the evolution of the scattering process assuming the following:

- no pion production;
- point and nonrelativistic particles;
- the mutual interaction can be described by nucleon-nucleon potentials;
- and furthermore, for the interaction to be quasielastic, the product of the beam passage time τ and its average interaction V with the nucleons in ^{3}He is small compared to $\hbar$, satisfying the condition of quasielastic scattering; equivalently, the beam proton motion is much faster than the nucleon motion ($\sim$ 100 MeV/c) in the ^{3}He nucleus.

A general spin-dependent quasielastic scattering cross section for the ^{3}He(p,2p) and ^{3}He(p,pn) can be written as

$$\begin{aligned} d\sigma(\mathbf{s}_0, \mathbf{s}_A) = & \frac{1}{\text{flux}} \frac{1}{2E_0 2E_A} (2\pi)^4 \, \delta^{(4)}(p_1 + p_2 + p_{A-1} - p_0 - p_A) \\ & \times \Gamma(\mathbf{s}_0, \mathbf{s}_A) \frac{d^3\mathbf{p}_1}{(2\pi)^3 2E_1} \frac{d^3\mathbf{p}_2}{(2\pi)^3 2E_2} \frac{d^3\mathbf{p}_{A-1}}{(2\pi)^3 2E_{A-1}} , \end{aligned}$$

where

$$\frac{1}{\text{flux}} = \frac{p_0 \cdot p_A}{\sqrt{(p_0 \cdot p_A)^2 - m_0^2 m_A^2}} ,$$

and

$$\Gamma(\mathbf{s}_0, \mathbf{s}_A) = \sum_{\substack{\mathbf{s}_1, \mathbf{s}_2 \\ \mathbf{s}_{A-1}, f_{A-1}}} \left| \mathcal{A}(\mathbf{p}_1\mathbf{s}_1, \ \mathbf{p}_2\mathbf{s}_2, \ \mathbf{p}_{A-1}\mathbf{s}_{A-1}f_{A-1} | \ t_{q.e.} \ |\mathbf{p}_0\mathbf{s}_0, \ \mathbf{p}_A\mathbf{s}_A\rangle \right|^2 , \tag{2.18}$$

in which as usual there are the flux factor, the phase space factor, and the "spin-specified" interaction probability with the 4-body system quasielastic scattering $t_{q.e.}$ operator. The spin states $\mathbf{s}_1$ and $\mathbf{s}_2$ and the spin state $\mathbf{s}_{A-1}$ and the internal state f_{A-1} have been summed over in $\Gamma(\mathbf{s}_0, \mathbf{s}_A)$ since the polarizations of the outgoing particles and the internal states of the A$-$1 system in the final state were not detected in the experiment.

2.5 Plane Wave Impulse Approximation

The quasielastic scattering reaction can be further discussed in terms of the Plane Wave Impulse Approximation (PWIA). In this approximation, the following conditions are assumed:

- the initial and final states of the particles can be described by plane waves;
- an impulse interaction takes place only with a single nucleon and there is no initial and final state interactions; the ejected nucleon is removed from the nucleus without disturbing the remaining A−1 system which remains in its initial state f_{A-1};
- interaction with meson exchange currents is neglected.

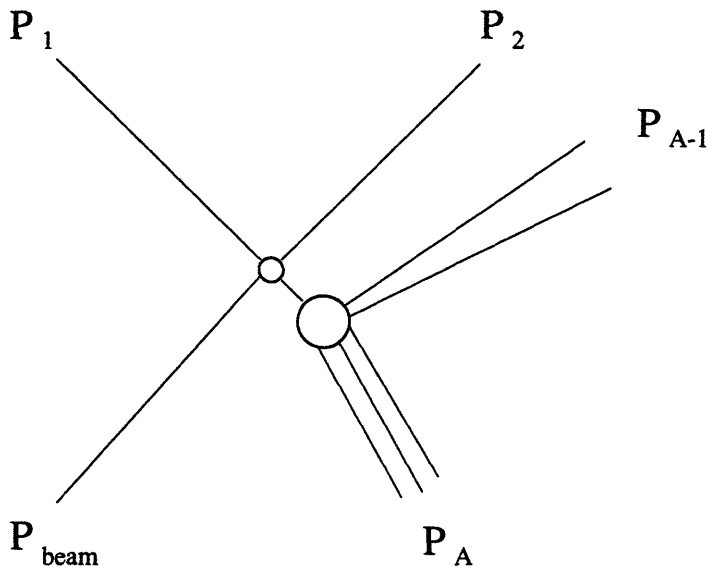

Figure 2.7. Plane Wave Impulse Approximation scattering where a nucleon is ejected from the nucleus due to interaction with the probe particle. The A−1 nuclear system recoils without any interaction.

Therefore, the general quasielastic $t_{q.e.}$ operator that includes nonquasielastic corrections can be replaced by the half off-shell nucleon-nucleon t^{NN} operator as

$$\mathcal{M} = \sqrt{A}\,\langle \mathbf{p}_1\mathbf{s}_1,\ \mathbf{p}_2\mathbf{s}_2,\ \mathbf{p}_{A-1}\mathbf{s}_{A-1}f_{A-1}t_{3A-1}|\ t^{NN}\ |\mathbf{p}_0\mathbf{s}_0,\ \mathbf{p}_A\mathbf{s}_A t_{3A}\rangle\ , \qquad (2.19)$$

where the factor $\sqrt{A}$ results from approximation of the asymmetrized final state in PWIA.

Inserting the completeness relation

$$\sum_{s_N, t'_{3N}} \int d^3p'_N \quad |p'_N s_N t'_{3N}\rangle \langle p'_N s_N t'_{3N}| \;=\; 1 \tag{2.20}$$

into equation (2.19) the matrix element becomes

$$\mathcal{M} = \sum_{s_N, t'_{3N}} \int d^3p'_N \sqrt{A} \langle p_1 s_1,\; p_2 s_2,\; p_{A-1} s_{A-1} f_{A-1} t_{3A-1}|\; t^{NN} \;|p'_N s_N t'_{3N}\rangle$$
$$\langle p'_N s_N t'_{3N}| p_0 s_0,\; p_A s_A t_{3A}\rangle \;. \tag{2.21}$$

Letting

$$\langle p_1 p_2|\; t^{NN} \;|p_0, p'_N t'^{3}_{N}\rangle \;=\; M^{NN}$$

and

$$\langle p'_N t'^{3}_{N}, p_{A-1} f_{A-1} t_{3A-1}| p_A t_{3A}\rangle \;=\; \hat{g}(p'_N t'_{3N}, p_{A-1} f_{A-1})$$
$$\delta(p'_N + p_{A-1} - p_A)\; \delta_{t'_{3N}+t_{3A-1}, t_{3A}} \;, \tag{2.22}$$

the matrix element can be rewritten as

$$\mathcal{M} = \sum_{s_N, t'_{3N}} \int d^3p'_N \sqrt{A} \langle s_1 s_2|\; M^{NN} \;|s_0 s_N\rangle \langle s_N, s_{A-1}|\; \hat{g} \;|s_A\rangle$$
$$\times \delta(p'_N + p_{A-1} - p_A)\; \delta_{t'_{3N}+t_{3A-1}, t_{3A}} \;. \tag{2.23}$$

Note that there is no corresponding simple delta relation for the spins between the initial and the final states as the spins are coupled to the orbital angular momentum also. The dependence on the spins is then implicitly kept in the operator $\hat{g}$. After summing over the isospin t'_{3N} and integrating over the nucleon momentum p'_N, the matrix element becomes,

$$\mathcal{M} = \sum_{s_N} \sqrt{A} \langle s_1 s_2|\; M^{NN}(p_1 p_2 p_0 p_N, t_{3N}) \;|s_0 s_N\rangle$$
$$\langle s_N s_{A-1}|\; \hat{g}(p_N t_{3N} f_{A-1}) \;|s_A\rangle \tag{2.22}$$

where t_{3N} and p_N are the nucleon isospin third component and the nucleon momentum respectively, which are defined as

$$\begin{aligned} t_{3N} &= t_{3A} - t_{3A-1} \\ p_N &= p_A - p_{A-1} \;. \end{aligned} \tag{2.24}$$

Next, the matrix element is squared to obtain the interaction probability in equation (2.18). After the summation over the final spin states, the spin-dependence is reduced to that of the beam and target spins. Notice that the 4-momentum delta function has a dependence on the internal states f_{A-1} in the mass M_{A-1}. Therefore, a delta function below is artificially introduced to transfer the dependence on the internal states f_{A-1} to the dependence on the separation energy E.

$$\begin{aligned}\delta(E_0 + E_A - E_1 - E_2 - E_{A-1}) = \\ \int_{\min(m_N+M_A-M_{A-1})}^{+\infty} dE\ \delta\big(E_0 + E_A - E_1 - E_2 - E_{A-1}(E - m_N + M_A)\big) \\ \times\delta(E - m_N + M_A - M_{A-1})\end{aligned} \tag{2.25}$$

where $E_{A-1} = \sqrt{{p_m}^2 + (E - m_N + M_A)^2}$ depends only on f_{A-1} through the nucleon separation energy E, and where the delta function $\delta(E - m_N + M_A - M_{A-1})$ contains all the f_{A-1} dependence. The result is that the energy delta function can be pulled out of the summation over the f_{A-1} states,

$$\begin{aligned}\Gamma(s_0, s_A) = \sum_{\substack{s_1,s_2 \\ s'_N,s_N}} \langle s_0 s'_N|\ M^{NN\dagger}\ |s_1 s_2\rangle\ \langle s_1 s_2|\ M^{NN}\ |s_0 s_N\rangle \\ \times\ \langle s_A s_N|\ \widehat{S}(p_N, E, t_N)\ \ |s'_N s_A\rangle\ ,\end{aligned} \tag{2.26}$$

where

$$\begin{aligned}\langle s_A, s_N|\ \widehat{S}(p_N, E, t_N)\ |s'_N, s_A\rangle = \Big\{ \sum_{s_{A-1},f_{A-1}} \delta(E + m_N + m_{A-1} - m_A) \\ \times\langle s_A|\ \hat{g}^\dagger\ |s'_N, s_{A-1}\rangle\ \langle s_N, s_{A-1}|\ \hat{g}\ |s_A\rangle\ \Big\}\ .\end{aligned} \tag{2.27}$$

Substituting the interaction probability $\Gamma(s_0, s_A)$ in the cross section equation (2.18) and integrating over part of the phase space the quasielastic cross section expression can be written as

$$\begin{aligned}\frac{d\sigma(s_0, s_A)}{d\Omega_1 d\Omega_2 dp_{A-1}} = \frac{1}{\text{flux}}\ \frac{1}{2E_0 2E_A} \\ \times\Big[\int \frac{p_1^1 dp_1}{(2\pi)^3 2E_1}\ \frac{p_2^2 dp_2}{(2\pi)^3 2E_2}\ \frac{p_{A-1}^2 d\Omega_{A-1}}{(2\pi)^3 2E_{A-1}} (2\pi)^3 \delta(p_0 - p_1 - p_2 - p_{A-1})\Big] \\ \times\int dE\ (2\pi)\ \delta\big(E_0 + M_A - E_1 - E_2 - E_{A-1}(E)\big)\ \Gamma(s_0, s_A)\ .\end{aligned} \tag{2.28}$$

Experimentally only the polarization of the beam and target particles can be detected instead of the spin state itself. Therefore, the cross section expression in equation (2.28) needs to be recast in terms of beam and target polarizations as

$$\begin{aligned}\frac{d\sigma}{d\Omega_1 d\Omega_2 dp_{A-1}} = \frac{d\sigma_\circ}{d\Omega_1 d\Omega_2 dp_{A-1}} \Big\{ & 1 + (\hat{\mathbf{n}}\cdot\mathbf{P}_b)A_{00n0} \\ & + (\hat{\mathbf{n}}\cdot\mathbf{P}_t)A_{000n} + (\hat{\mathbf{n}}\cdot\mathbf{P}_b)(\hat{\mathbf{n}}\cdot\mathbf{P}_t)A_{00nn} \\ & + (\hat{\mathbf{k}}\cdot\mathbf{P}_b)(\hat{\mathbf{k}}\cdot\mathbf{P}_t)A_{00kk} + (\hat{\mathbf{s}}\cdot\mathbf{P}_b)(\hat{\mathbf{s}}\cdot\mathbf{P}_t)A_{00ss} \\ & + (\hat{\mathbf{k}}\cdot\mathbf{P}_b)(\hat{\mathbf{s}}\cdot\mathbf{P}_t)A_{00ks} + (\hat{\mathbf{s}}\cdot\mathbf{P}_b)(\hat{\mathbf{k}}\cdot\mathbf{P}_t)A_{00sk} \Big\}\end{aligned} \tag{2.29}$$

where $d\sigma_\circ/d\Omega_1 d\Omega_2 dp_{A-1}$ is the unpolarized cross section, $\mathbf{P}_b$ and $\mathbf{P}_t$ are the beam and target polarizations and A_{00ij}'s are the asymmetries. The unpolarized cross section and the asymmetries are proportional to different combinations of target and beam spin states of the cross section expression in equation (2.28). The derivation steps from equation (2.28) to (2.29) are detailed in appendix C. Below the unpolarized cross section and the asymmetries are expressed in terms of the nucleon-nucleon unpolarized cross section and asymmetries and the nuclear structure functions,

$$\frac{d\sigma_\circ}{d\Omega_1 d\Omega_2 dp_{A-1}} = \int dE p_{A-1}^2 d\Omega_{A-1} \frac{d\sigma_\circ^{NN}}{d\Omega_1 d\Omega_2} S(p_N, E, t_N) , \tag{2.30a}$$

$$A_{00n0}\frac{d\sigma_\circ}{d\Omega_1 d\Omega_2 dp_{A-1}} = \int dE p_{A-1}^2 d\Omega_{A-1} A_{00n0}^{NN} \frac{d\sigma_\circ^{NN}}{d\Omega_1 d\Omega_2} S(p_N, E, t_N) , \tag{2.30b}$$

and

$$\begin{aligned}A_{00ij}\frac{d\sigma_\circ}{d\Omega_1 d\Omega_2 dp_{A-1}} = \int dE p_{A-1}^2 d\Omega_{A-1} & A_{00ij}^{NN} \frac{d\sigma_\circ^{NN}}{d\Omega_1 d\Omega_2} \\ & r(p_N, E, t_N)\, S(p_N, E, t_N) ,\end{aligned} \tag{2.30c}$$

where the index {ij} is either {0n} the target asymmetry or {nn} a spin-correlation parameter. Note for the neutron, r^n is 1.0 at low p_N values, and since the beam related neutron-proton scattering asymmetry is identical to the target related neutron-proton asymmetry, the target related asymmetry A_{000n}^n becomes identical to the beam related asymmetry A_{00n0}^n in the PWIA model. The cross section expression in equations (2.29a-c) can be further integrated over the angular acceptance of the experiment to obtain the quantities measured in the experiment: $\mathcal{A}_{00n0}$, $\mathcal{A}_{000n}$, and $\mathcal{A}_{00nn}$.

2.6 Monte Carlo Model

No complete theoretical calculation of spin-dependent quasielastic scattering from ^{3}He exists. An experimental Monte Carlo simulation is necessary to quantify the effects of the experimental geometry on measured physical quantities to allow a precise comparison between theory and experiment. The angular range of particles detected by the large acceptance detectors varies over the length of the extended target, which moreover, has a varying target density with a triangular distribution. See Figure 3.13 in the chapter on target apparatus. The basics assumptions and inputs of the model are:

- Schulze and Sauer spin-dependent spectral functions; Blankleider and Woloshyn spin-dependent momentum distributions;
- on mass shell nucleon-nucleon interaction cross section and asymmetries from SAID;
- no initial state or final state interactions;
- no meson exchange current, isobar configuration, or relativistic correction considered.

The calculation was carried out in two steps. First, events that satisfied the kinematic conditions and detector and target cell geometry requirements were generated. Each event consisted of numerical values of the nucleon-nucleon on mass shell cross section and asymmetries and components of the spectral functions. Second, events were binned into histograms of the recoiling system momentum p_{A-1} or the 3-momentum transfer q for a specific beam and target spin state with weighting of the spectral function, cross sections, asymmetries, and the factors p^2_{A-1}, $\cos\phi$, $\cos^2\phi$, and $\sin^2\phi$. Here, the kinematic variables were smeared to simulate the experimental resolution, and events with detection of three or four nucleons were rejected. From four histograms of specific beam and target vertical spin states, a relative yield and three experimental asymmetries $\mathcal{A}_{00n0}$, $\mathcal{A}_{000n}$, and $\mathcal{A}_{00nn}$ were formed. A box diagram for the Monte Carlo simulation is given in Figure 2.8. In addition, the experimental asymmetries were calculated with the target nucleon polarization 100% for use in the thesis to extract the nucleon polarization from the data in chapter 5 and chapter 6.

It was pointed that in the laboratory frame the azimuthal angle ϕ of the scattered particle, although well defined in the (p,pn) reaction, is ambiguous in the (p,2p) reaction particularly when the three body phase space is considered [2.11]. When only the two body phase space is considered, the angle ϕ is the same for

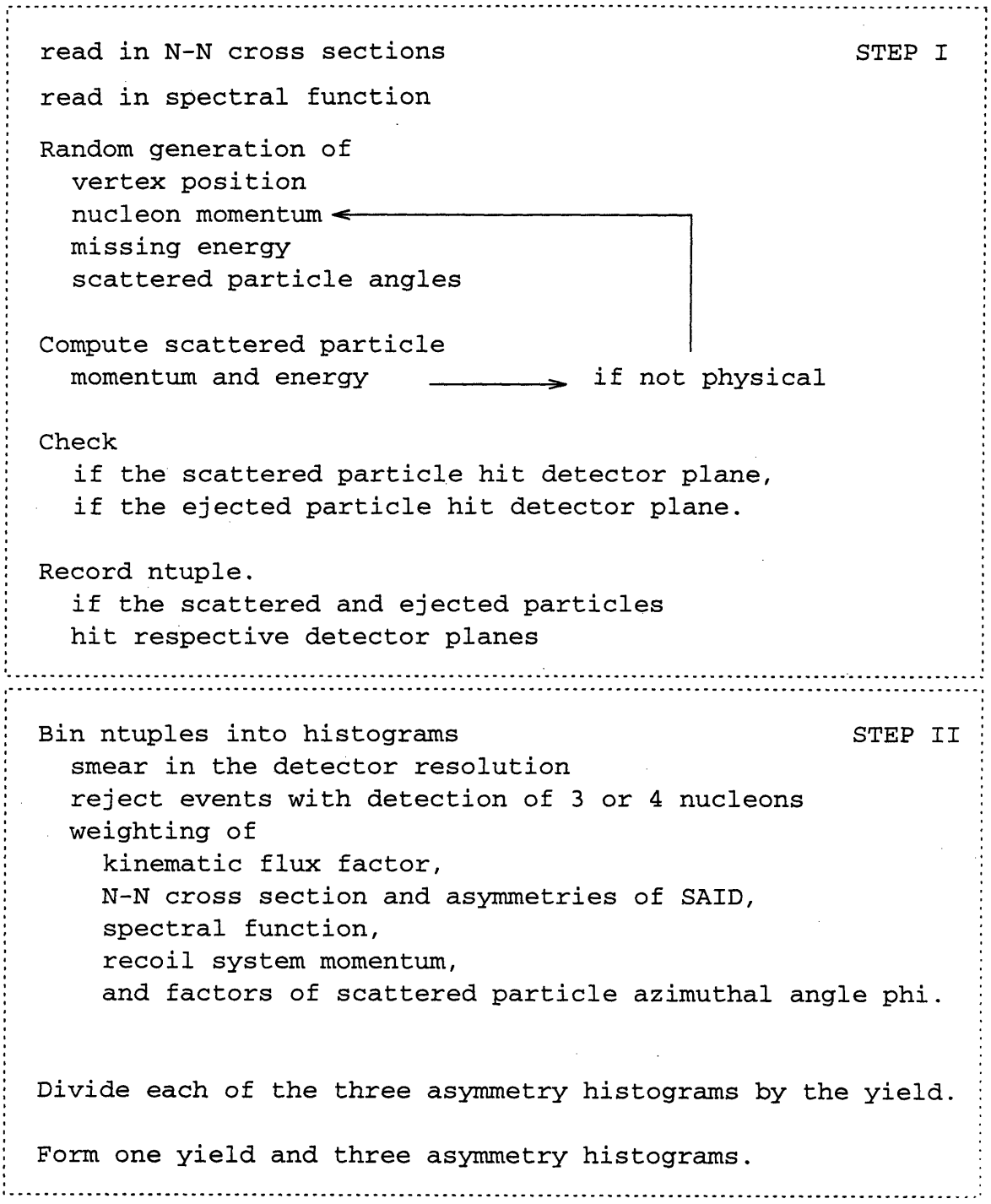

Figure 2.8. Algorithm for the experimental Monte Carlo.

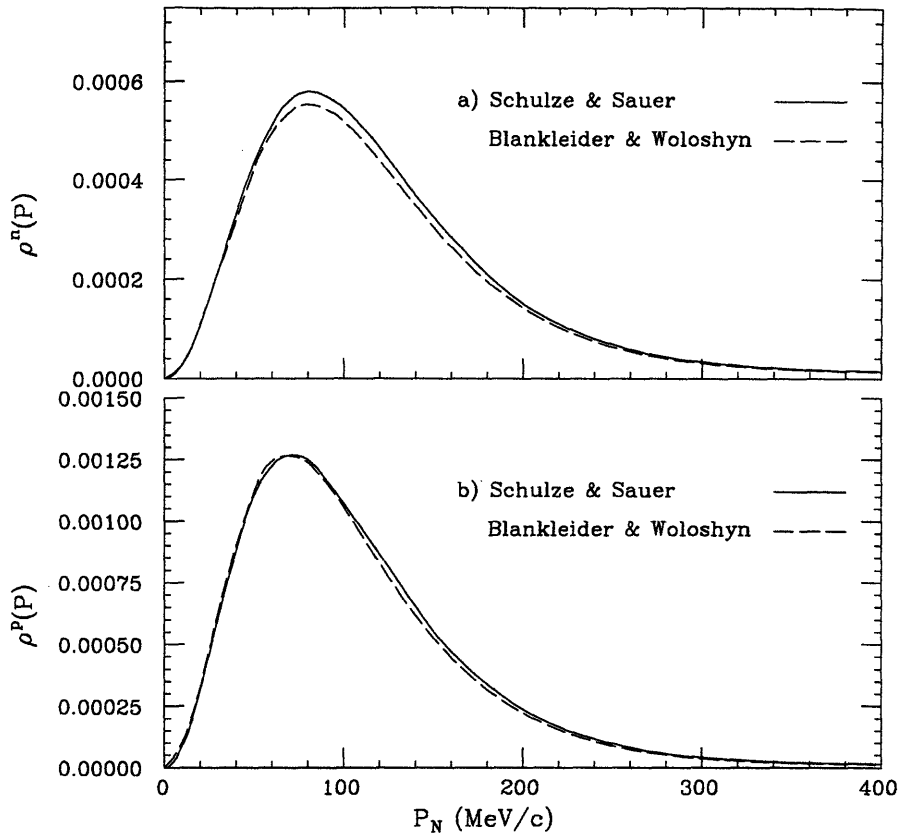

Figure 2.9. The comparison between the Schulze and Sauer spectral function integrated over the separation energy E and the Blankleider and Woloshyn spin-independent momentum distribution for the neutron polarization in (a) and the proton polarization in (b).

either the left-scattered proton and the right-scattered proton. In the calculations presented in the thesis, the asymmetries were determined for the left-scattered proton and the right-scattered proton separately, and the average of the two was used as the result.

The ambiguity can be resolved by transforming from the lab frame to the c.m. frame of the beam and the struck proton momentum and spin for the initial kinematics or the two outgoing proton momenta and spins for the final kinematics calculation. In the c.m. frame, one particle is always moving diametrically opposite in direction of the other, requiring only a single ϕ value. The trasformation of the proton momenta is a well understood problem on one hand, however on the other, it is not understood how the spin can be transformed as there will be a time component of the spin. Prior to any numerical calculation, a detail formalism is

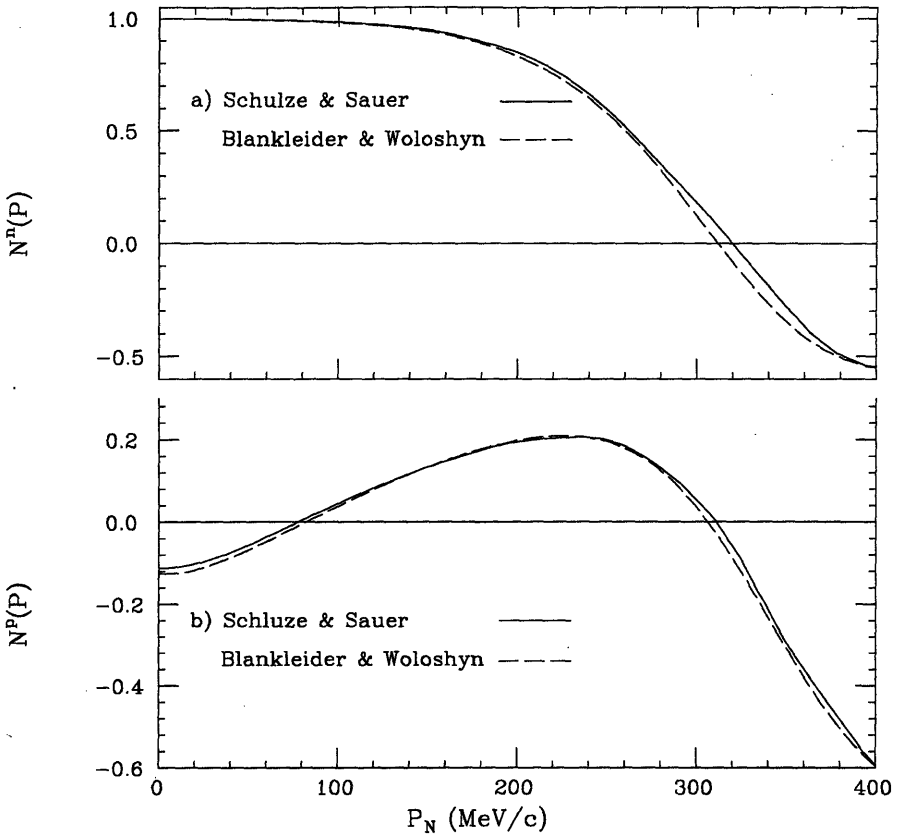

Figure 2.10. The comparison between the Schulze and Sauer spectral function integrated over the separation energy E and the Blankleider and Woloshyn spin-dependent momentum distribution for the neutron in (a) and the proton in (b).

necessary.

The spin-dependent momentum distributions of Blankleider and Woloshyn have also been used. Although no direct comparison has been made between using the two different nuclear momentum distribution inputs, the results are expected to be different only at high recoil momentum due to the nonzero missing energy. In fact, the difference was seen to be most pronounced in the asymmetries plotted *vs.* the 3-momentum transfer q. Below a comparison between the Schulze and Sauer spectral function integrated in separation energy E from 0 to 500 MeV and the Blankleider and Woloshyn spin-dependent momentum distributions is made in figures 2.9 and 2.10. They show good agreement between the two solutions at low recoil momentum for the neutron polarization. The proton calculations differed by at most 10%.

Chapter 3

Polarized ^{3}He Internal Gas Target

3.1 Introduction

Internal targets refer to gas targets constructed for use as an integral part of a storage ring where charged particles are stored. To date jet targets and storage cell targets have been constructed, although because of the highly efficient use of the gas, the storage cell target can give rise to a significantly increased target thickness [1.13, 1.5, 3.1]. In a jet target, a stream of gas is directed at the intersection point with the beam, and the interaction vertex is precisely determined. The jet target can be made more diffusive as in the CE-25 calibration measurement, to reduce sensitivity of the beam position to the loss of luminosity. Gas can also be contained in an open ended, ultra thin walled storage cell to achieve a thicker target. This configuration is particularly useful for polarized targets. By careful choice of the transverse dimensions of storage cells, interaction of beam halo with cell walls can be minimized to achieve essentially ideal beam and nuclear target interaction. Further, energy losses of beam and reaction products are negligible in the ultra thin gas, and sub-MeV reaction products can be detected outside the thin walls of the target cell.

Polarized internal gas targets have been of considerable current interest in nuclear and particle physics, *e.g.* for use at the HERA collider ring to measure the neutron quark structure function $g_1^n(x)$. There are also plans to use a polarized ^{3}He internal gas target in the Bates South Hall Ring. The work described here represented the first measurement of a scattering asymmetry with a polarized internal gas target and a polarized stored, charged particle beam. In the polarized ^{3}He internal gas target described here, pure ^{3}He gas is polarized by the metastability exchange optical pumping technique and flowed into the storage cell. The metastability exchange optical pumping technique to polarize ^{3}He gas was first demonstrated by Walters, Colgrove, and Schearer in 1962 [3.2]. Using a ^{4}He discharge lamp, they achieved a 4% ^{3}He nuclear polarization in 1 Torr of ^{3}He gas in a sealed Pyrex glass cell and later increased the polarization [3.3] as measured by the laser light transmission technique. Their work had its origins in an earlier effort that successfully aligned ^{4}He metastables using a bright ^{4}He discharge lamp and soon led to the construction of a closed cell polarized ^{3}He gas target for nuclear reactions with a target polarization of 8.5% at Rice University [3.4]. The low polarization in the target was caused by the increased relaxation rate from mechanisms such as

the metal wall and beam ionization depolarization. Optical pumping rates much higher than those available using discharge ^{4}He lamps are necessary to obtain high polarization and also to overcome the increased relaxation rate for application in nuclear physics targets. With the commercial availability of tunable Nd:YAP CW lasers in the 1.05-1.1 μm wavelength region in the early 80's [3.5], there was renewed interests in polarizing ^{3}He atoms for applications in a number of fields. A cyrogenically cooled double, closed cell system was developed by Leduc *et al.* [3.6] and later adapted to a target by Milner *et al.* [3.1] for scattering experiment. In this target, an Nd:YAP laser tuned to the Doppler width of the metastable optical pumping transition provided several hundred mWatts of the intense circularly polarized light, and target polarizations close to 30% were maintained during the experiment [1.6].

In recent years, with the commercial introduction of the Nd:LMA tunable CW lasers, 4-6 Watts of the output laser power [3.7] at the Doppler width of the metastable optical pumping 1.0834 μm transition have become routinely available. The increased laser power nearly doubled the polarization of the double cell target in the recently completed $^3\overrightarrow{\text{He}}(\overrightarrow{e},e')$ measurement at Bates Linac [1.9,1.10]. Corresponding to 4-6 Watts of laser powers at the transition, high pumping rates of 10^{18} (10^{19}) atoms/sec and respectively 82% (50%) polarizations in sealed Pyrex cells have been achieved [3.8]. Finally, the increased laser power also made possible high polarization with high flow rate in this polarized ^{3}He internal gas target used in the IUCF Cooler Ring. The increased laser power provided sufficient pumping rate to replenish the polarized ^{3}He atoms in the target. The target was prototyped and designed at MIT-Bates in 1989-91 and was installed in the Cooler Ring at IUCF in 1992. The target flowed polarized ^{3}He gas at a stable rate of 1×10^{17} atoms/sec with polarizations approximately $\pm$50% [3.9, 3.10]. This target was the first laser pumped source of polarized atoms used to feed an internal target in a storage ring.

3.2 Principles

3.2.1 The Metastability Exchange Optical Pumping Technique

Optical pumping is the transfer of angular momentum from polarized photons to atoms to create a nonthermal population in their magnetic substates, *i.e.* to polarize the atoms. Optical pumping is to date by far a more efficient technique than alignment by strong magnetic field. The versatility of the technique is that it can also be used to polarize the excited states of atoms.

In the ground state of the ^{3}He atom, the spins of the two electrons are anti-aligned to form the 1^1S_0 parahelium ground state and only the spin I=$\frac{1}{2}$ of the nucleus contributes to the magnetic moment. In thermal equilibrium, the magnetic ground states are equally populated by the ^{3}He atoms. To create a nonthermal population in the magnetic ground states by direct optical pumping requires excitation to the 2^1P_1 parahelium state using 0.5844 μm ultraviolet radiation [3.11]. However, the ^{3}He atoms in the metastable 2^3S_1 orthohelium state can be polarized by optical pumping with excitation to a 2^3P orthohelium state using 1.0834 μm infrared radiation. The angular momentum imparted by circularly polarized photons to the metastable atoms then resulted in polarized ground state atoms by exchange of electron clouds in collisions between the polarized metastable atoms and the ground state atoms. The ground state atoms can also be polarized by a buffer gas of polarized Rb atoms through a very weak dipolar spin exchange interaction [3.12] between the polarized electron cloud of the Rb atoms and the spin of the ^{3}He nucleus. In the former technique, to be discussed further in detail below, the metastable atoms form only a tiny fraction 2×10^{-6} of the ^{3}He gas and act as a separate species from the ground state atoms.

When external electrons collide with enough energies, the ^{3}He atoms are excited to higher energy levels, including ones not acessible by single photon excitations. By coupling to RF fields from a few hundreds of kHz to tens of MHz, the ^{3}He atoms are also excited to higher energy levels as in excitations by electron collisions. A weak RF field maintained in the ^{3}He gas creates a fluorescent discharge that populates a small fraction 2×10^{-6} of atoms in the the 2^3S_1 metastable state. It is important to note that the fluorescent discharge can only be maintained at pressures of a few Torr in the ^{3}He gas.

Due to the hyperfine interaction with the nuclear spin I=$\frac{1}{2}$, the 2^3S_1 metastable state separates into the hyperfine sublevels F=$\frac{3}{2}$, $\frac{1}{2}$ with 6.7 GHz separation. The corresponding magnetic sublevels are m_F=$-\frac{3}{2}$,$-\frac{1}{2}$,$+\frac{1}{2}$,$+\frac{3}{2}$ and m_F=$-\frac{1}{2}$,$+\frac{1}{2}$. The

metastable atoms are then optically pumped by excitation to 2^3P levels with circularly polarized photons of 1.0834 μm. Due to hyperfine interactions, the quantity J from the fine interaction is no longer a good quantum number and there are five 2^3P levels called P_0, P_x, P_1, P_y, and P_2 from highest to lowest energies with admixtures of different J values as

$$|2^3\mathrm{P},\mathrm{F}\rangle \;=\; \mathrm{x}_1\;|2^3\mathrm{P},\mathrm{J}_1\rangle \;+\; \mathrm{x}_2\;|2^3\mathrm{P},\mathrm{J}_2\rangle\;,$$

where x_1 and x_2 are admixture amplitudes. See table 3.1. The P_0 and P_1 states have a hyperfine value F=$\frac{1}{2}$ and are admixtures of J = 0 and 1 states respectively. Similarly, the P_x and P_y states have a hyperfine value F=$\frac{3}{2}$ and are admixtures of J=1 and 2 states. The P_2 state with the lowest energy value has a hyperfine value F=$\frac{5}{2}$ and is just a single J=2 state. The corresponding magnetic substates of the hyperfine 2^3S_1 levels and the ^3P levels are labelled as $A_1,\ldots,A_6$ and $B_1,\ldots,B_{18}$ respectively as in figure 3.1 for ease of discussion.

Between the 2^3S_1 levels and the 2^3P levels, there are nine allowed dipole (E_1) transitions labelled $C_1,\ldots,C_9$ as in figure 3.2 with increasing energy values as given table 3.2. In the dipole transition, only the orbital angular momentum is changed by the selection rule, ΔL=$\pm$1 and Δm=0,$\pm$1; *neither the electron spin nor the nuclear spin is reversed in the transitions.* Transitions that involve the electron spin or the nuclear spin are orders of magnitude smaller in strength.

The dipole transition rate between the individual states $\mathrm{A_i}$ and $\mathrm{B_j}$ is given by

$$\frac{1}{\tau_{\mathrm{ij}}} \;=\; \frac{\mathrm{e}^2}{\hbar^2}\mathrm{E}^2\;\frac{\Gamma'}{(\frac{\Gamma'}{2})^2+(\omega-\omega_{\mathrm{k}})^2}\;|\;\langle \mathrm{A_i}|\;\hat{\mathbf{e}}_\lambda\cdot\mathbf{R}\;|\mathrm{B_j}\rangle\;|^2, \tag{3.1}$$

where $\mathrm{E}\hat{\mathbf{e}}_\lambda$ and $\frac{\omega}{2\pi}$ are the electric field and the frequency of the absorbed radiation. Γ', ω_k and $\mathrm{e}\mathbf{R}$ are the damping factor, the frequency, and the dipole operator of the transition. For a comparison between the transition rates, the relative value of transition between two states is given by

$$\mathrm{T_{ij}} \;=\; \beta\;|\;\langle \mathrm{A_i}|\;\hat{\mathbf{e}}_\lambda\cdot\mathbf{R}\;|\mathrm{B_j}\rangle\;|^2, \tag{3.2}$$

where β is a normalization factor to give $\mathrm{T_{11}}=1$. The $\mathrm{T_{ij}}$ coefficients range between 0 and 1 and are given in the paper by Nacher and Leduc [3.13], tabulated according to the different C_k transitions and the polarization of the radiation. These transition coefficients are just the square of the projection amplitude of the angular momentum and spin wavefunction of the A_i states onto the B_j states for the same magnetic

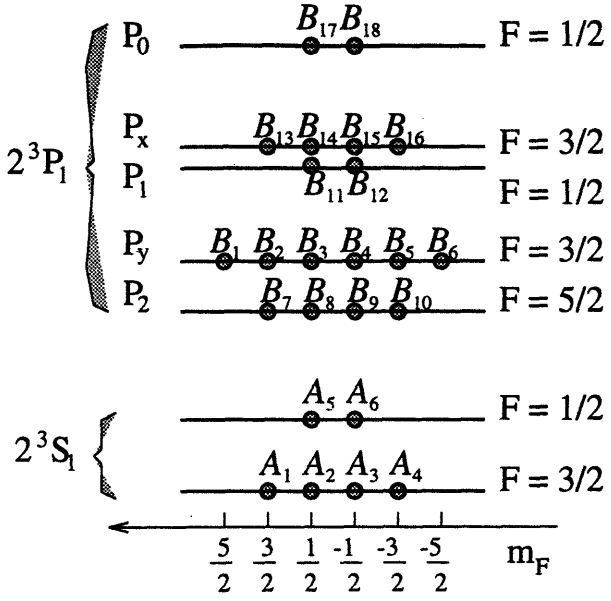

Figure 3.1. Hyperfine states in the 2^3S_1 and the 2^3P levels.

Level	x_1	x_2	(GHz)
P_0	0.994	-0.109	0.0
P_x	0.553	-0.833	-27.39
P_1	0.109	0.994	-28.13
P_y	0.833	0.553	-32.64
P_2	1.0	0.0	-34.41
$2^3S_1, F = \frac{1}{2}$			0.0
$2^3S_1, F = \frac{3}{2}$			-6.7397

Table 3.1. The admixture amplitude values and relative energy values in the 2^3S_1 and 2^3P levels.

values of the electrons and nuclear spins, *i.e.* spin directions are conserved in the dipole transition. See table 3.4 for the T_{ij} values of the C_8 and C_9 transitions.

Under absorption of a circularly polarized photon of $\sigma^{(\pm)}$ polarization at one of the C_k transitions, the metastable atom is excited to a 2^3P level with a transfer of one unit of $\pm\hbar$ of angular momentum from the photon that changes the magnetic m_F value by $\pm\hbar$ where m_F quantization axis is defined by the incident direction. See figure 3.3 for the optical pumping scheme. The atom then decays back to the metastable state emitting a photon with $\sigma^{(-)}$, π, or $\sigma^{(+)}$ polarization, say in the incident direction and changing the m_F value by +1, 0, or −1 with equal probability. Note here that the photon can be emitted with some probability in all directions. When the photon is emitted in the direction opposite to the incident

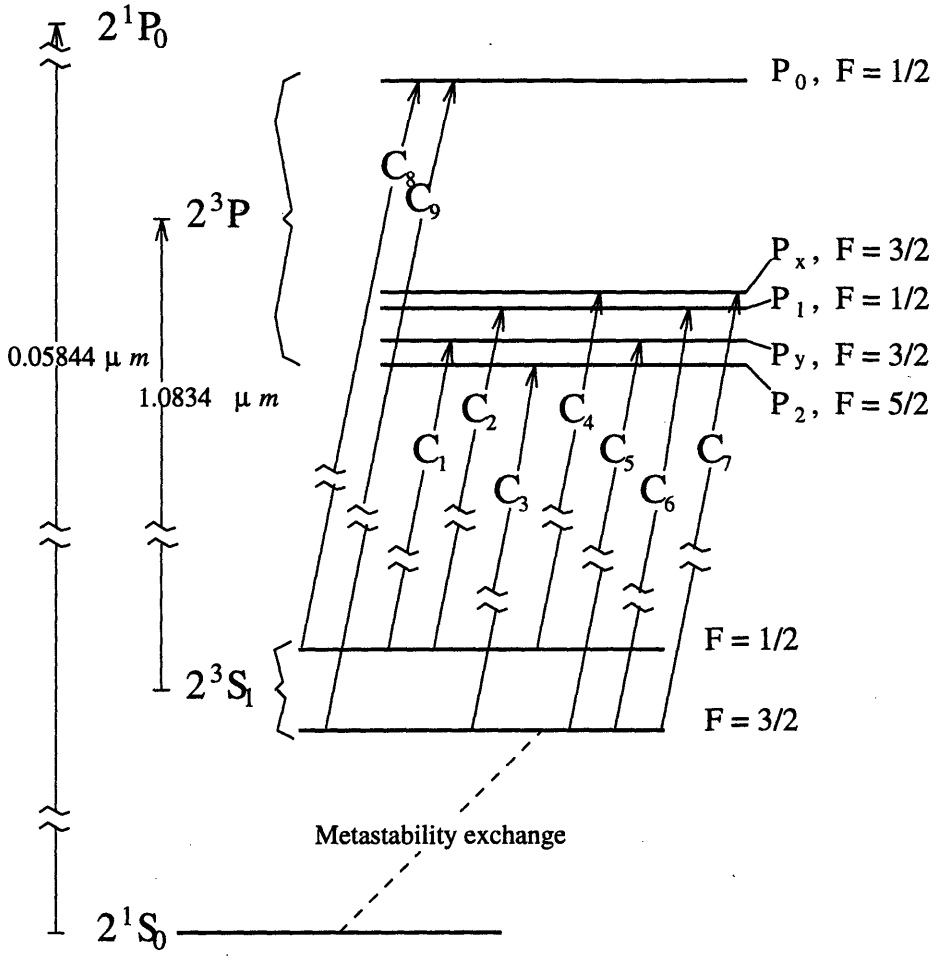

Figure 3.2. $C_1, \ldots, C_9$ allowed transitions between the 2^3S_1 levels and the 2^3P levels.

	C_1	C_2	C_3	C_4	C_5	C_6	C_7	C_8	C_9
(GHz)	0	4.51	4.97	5.25	6.74	11.25	11.99	32.64	39.38

Table 3.3. Relative energies of the nine allowed dipolar transitions.

j / i	5	6
17	0.1465 (π)	0.2931 (σ^+)
18	0.2931 (σ^-)	0.1465 (π)

j / i	1	2	3	4
17	0.2801 (σ^-)	0.1867 (π)	0.0934 (σ^+)	
18		0.0934 (σ^-)	0.1867 (π)	0.2801 (σ^+)

Table 3.4. Relative probabilities for C_8 and C_9 transitions.

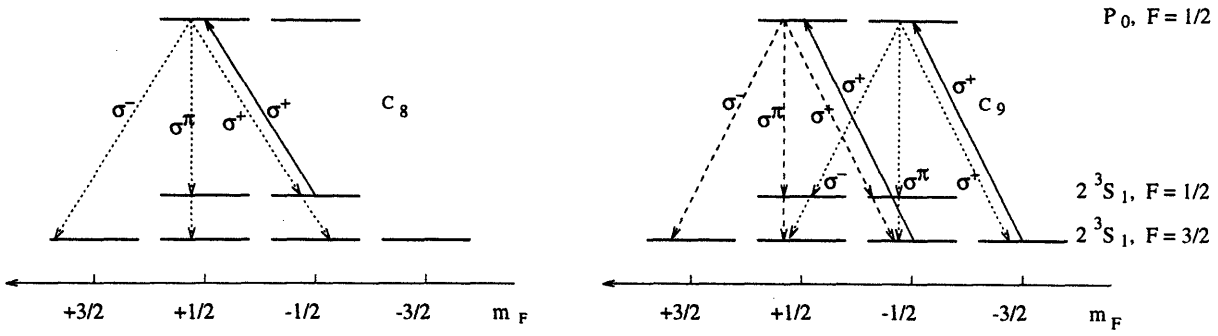

Figure 3.3. Optical pumping process for the C_8 and C_9 transitions with photons re-emitted along the direction of incidence.

direction, the m_F value changes by -1, 0, or $+1$. The metastable atom now has $\frac{1}{3}$ probability to be in its previous m_F value, $\frac{1}{3}$ to be in the next higher value, and $\frac{1}{3}$ to be in the even higher value. When the atom decays from the 2^3P state to the 2^3S_1 state, the atom can be in magnetic hyperfine states with high m_F values, indicating that the nuclear spin has also changed even though the dipole transition allows no flipping of the electron spin or the nuclear spin. The reason that the nuclear spin direction could be changed is that the atom in the 2^3P state sits for long enough time and has sufficient coupling between the electrons and nuclear spin spin and the orbital angular momentum to mix into different electrons and nuclear spin states, allowing dipole decay transitions into states with different electrons and nuclear spin states from the initial 2^3S_1 hyperfine state. Under absorption of a second circularly polarized photon, the metastable atom in its new m_F state is excited and then decays again to redistribute equally in the same or higher m_F state as long as the dipole transition is allowed. This is the principle of the optical pumping process.

As shown in the diagrams in figure 3.3, the atoms can decay to both the $F = \frac{1}{2}$ and $F = \frac{3}{2}$ levels, allowing the atoms to be pumped into the $m_F = +\frac{3}{2}$ ($m_F = -\frac{3}{2}$) state and the $m_F = +\frac{1}{2}$ ($m_F = -\frac{1}{2}$) state. At first glance, the atoms in the $m_F = +\frac{1}{2}$ ($m_F = -\frac{1}{2}$) state can not further be pumped, thus limiting the nuclear polarization to 50% when the atoms are equally populated at $m_F = +\frac{3}{2}$ ($m_F = -\frac{3}{2}$) and $m_F = +\frac{1}{2}$ ($m_F = -\frac{1}{2}$). However, due to the dominant exchange collision rate described below, the different metastable states can be described as coupled to each other through the ground state, resulting in further optical pumping to obtain nuclear polarizations beyond the 50% barrier. The $m_F = +\frac{1}{2}$ ($m_F = -\frac{1}{2}$) state is coupled to the states $m_F = +\frac{3}{2}$ ($m_F = -\frac{3}{2}$) and $m_F = -\frac{1}{2}$ ($m_F = +\frac{1}{2}$), the latter of which can absorb another circularly polarized photon $\sigma^{(+)}$ ($\sigma^{(-)}$), thus allowing

further optical pumping. By illumination of $\sigma^{(+)}$ ($\sigma^{(-)}$) light, the metastable atoms then become populated in the highest (lowest) m_F state. At the same time, the coupling of the $m_F = +\frac{3}{2}$ ($m_F = -\frac{3}{2}$) state with the $m_F = +\frac{1}{2}$ ($m_F = -\frac{1}{2}$) state limits the maximum nuclear polarizations to below 100%.

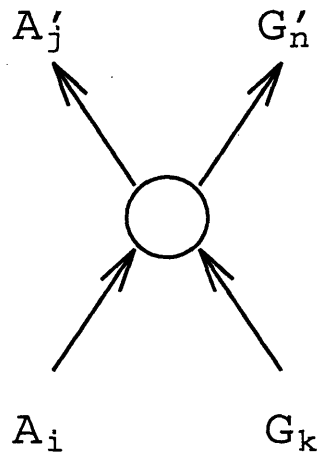

Figure 3.4. Electron clouds are exchanged between a metastable atom and a ground state atom to form a metastable atom and a ground state in different magnetic substates.

Angular momentum imparted by circularly polarized photons to the metastable atoms results in polarization of the ground state atoms through the metastability exchange collision. In the RF discharged ^{3}He gas medium, atoms are in constant collision, and there are many different collisions: with each other, with the surrounding walls, and from different initial states and into different final states. In the collision of the metastable atoms with ground state atoms, there is a small cross section of $\sigma_o \approx 7.6 \times 10^{-16}$ cm^2 [3.14] to exchange electron clouds with the ground state atoms. The exchange collision is sufficiently short in time that the polarizations of the electron clouds and the nuclear spins are preserved. After the exchange interaction, the metastable electron cloud is coupled to the ground state nuclear spin and the ground state electron cloud to the metastable state nuclear spin, resulting in a ground state atom with nuclear polarization of the initial metastable atom. See figure 3.4. The exchange interaction matrix element can be expressed as

$$\langle G'_n A'_j | \widehat{M} | G_k A_i \rangle = \sigma_o \langle G'_n | G_{k\{\text{electronic}\}} A_{i\{\text{nuclear}\}} \rangle \quad \langle A'_j | G_{k\{\text{nuclear}\}} A_{i\{\text{electronic}\}} \rangle . \tag{3.3}$$

where $\widehat{M}$ is the electron cloud exchange operator, σ_o the total cross section given above, and the subscripts on the right side of the equation to indicate spin components that are being combined together. When final spin states of the matrix element are summed over, it becomes

$$\begin{aligned}\sum_{\substack{n=1,2\\ j=1\ldots6}} \langle G'_n A'_j|\, \widehat{M}\, |G_k A_i\rangle &= \sigma_o \sum_{n=1,2} \langle G'_n|\, G_{k\{\text{electronic}\}} A_{i\{\text{nuclear}\}}\, \rangle \\ &\quad \times \sum_{j=1\ldots6} \langle A'_j|\, G_{k\{\text{nuclear}\}} A_{i\{\text{electronic}\}}\, \rangle\ , \\ &= \sigma_o\ (1)\ (1).\end{aligned} \tag{3.4}$$

Moreover, the average rates of the exchange collision per ground state atom and per metastable atom are respectively given by

$$\begin{aligned}\frac{1}{T_e} &= \sigma_o \bar{v} n_m \ = \ \frac{1}{0.3\ \text{sec}} \\ \frac{1}{\tau_e} &= \sigma_o \bar{v} N \ = \ \frac{1}{0.2\ \mu\text{sec}}\end{aligned} \tag{3.5}$$

where $\sigma_o = 7.6 \times 10^{-17}$ cm^2, $\bar{v} = 2.06 \times 10^5$ cm/sec, $n_m = 2.1 \times 10^{10}$ atoms cm^{-3} [3.15], and $N = 3.2 \times 10^{16}$ atoms cm^{-3}. The metastablity exchange collision rate is much higher than the rates of depolarization of ground state atoms and of optical pumping of the metastable atoms so that the polarization of the ground state atoms is directly proportional at all times to the nuclear polarization of the metastable atoms.

3.2.2 Model of Density of States

A detailed equation of motion for the ground state polarization and the metastable densities can be found in the paper by Nacher and Leduc [3.13]. Essential details of the model are discussed here for completeness. To facilitate discussion, the densities of the ground state atoms G_k, the metastable state atoms A_i, and the 2^3P state atoms B_i are defined as g_k, a_i, and b_j where

$$N = \sum_{k=1,2} g_k \quad \text{and} \quad n_m = \sum_{i=1}^{6} a_i\ . \tag{3.6}$$

First, the metastability exchange polarization transfer mechanism is considered. The interaction rate between the atoms in th A_i and G_k states are given by

$$|\langle G'_n|\, G_{k\ \{\text{electronic}\}} A_{i\ \{\text{nuclear}\}}\, \rangle|^2 |\langle A'_j|\, G_{k\ \{\text{nuclear}\}} A_{i\ \{\text{electronic}\}}\, \rangle|^2\ \sigma_o \bar{v}\ a_i\ g_k\ , \tag{3.7}$$

which can be used to write the equation of motion for the densities a_i and g_k as

$$\begin{aligned}
\frac{da_i}{dt} &= \frac{1}{\tau_e}\left(a_i + \frac{1}{N}\sum_{\substack{k=1,2\\ l=1\ldots6}} |\langle A_i'|\, G_{k\ \{\text{nuclear}\}} A_{l\ \{\text{electronic}\}}|^2 a_l g_k \right) \\
\frac{dg_k}{dt} &= \frac{1}{T_e}\left(-g_k + \frac{1}{n_m}\sum_{\substack{h=1,2\\ i=1\ldots6}} |\langle G_k'|\, G_{h\ \{\text{electronic}\}} A_{i\ \{\text{nuclear}\}}|^2 a_i g_h \right) \qquad (3.8)\\
&= \frac{1}{T_e}\left(-g_k + \frac{N}{n_m}\sum_{i=1}^{6} |\langle G_k'|\, A_{i\ \{\text{nuclear}\}}|^2 a_i \right).
\end{aligned}$$

Furthermore, the energy difference between the $F = \frac{3}{2}$ and $F = \frac{1}{2}$ levels with the A_i state is small and its effect on the equation of motion is ignored.

Secondly, the optical pumping mechanism is considered. Under illumination of the optical pumping radiation, there are absorption and spontaneous emission, and stimulated emission of photons changing the density of the 2^3P and the metastable magnetic states. Using the transition rate for the absorption and the spontaneous emission per atom from equation (3.1), the equation governing the density of the A_i and B_j states can be written as

$$\begin{aligned}
\frac{db_j}{dt} &= \sum_{i=1}^{6} -\frac{1}{\tau_{ij}'} b_j + \frac{1}{\tau_{ij}}(a_i - b_j) \\
\frac{da_i}{dt} &= \sum_{j=1}^{18} \frac{1}{\tau_{ij}}(b_j - a_i) + \frac{1}{\tau_{ij}'} b_j ,
\end{aligned} \qquad (3.9)$$

where τ_{ij}^{-1} is the transition rate for absorption and spontaneous emission and $\tau_{ij}'^{-1}$ the rate of stimulated emission between states A_i and B_j. The stimulated emission causes the ^{3}He atom in state B_j to emit a photon in the same state as the photon beam and decay to a state A_i with nuclear polarization opposite to photon beam helicity direction. It has the effect of lowering the maximum possible polarization. However, the process is not important compared to the spontaneous emission for the intensities of the laser light at the optical pumping cell where the beam is blown up to the dimensions of the cell.

Thirdly, the different relaxation mechanisms are considered. The excited B_j states and metastable A_i states are constantly being mixed into different states by the incessant collisions of the atoms with each other in similar states or in states other than had already been mentioned, with impurities in the gas, and with container walls. The ground state, although it has a closed electron structure and

thus is not changed by direct collisions, can also get mixed into the state with opposite spin direction by interaction with transverse gradients in the magnetic holding field, with local fields of container walls when they are adsorbed on each bounce, and with local fields of ^{3}He molecular ions created by beam ionization. The relaxation rates for individual density due to corresponding mechanisms can be parameterized by time constants τ_b, τ_a, and τg and the respective equations of motion are given by

$$\begin{aligned}
\frac{db_j}{dt} &= \frac{1}{\tau_b}\left(\sum_{l=1}^{18}\frac{b_l}{18} - b_j\right) \\
\frac{da_i}{dt} &= \frac{1}{\tau_a}\left(\sum_{l=1}^{6}\frac{b_l}{6} - a_j\right) \\
\frac{dg_k}{dt} &= \frac{1}{\tau_g}\left(\sum_{n=1,2}\frac{g_n}{2} - g_n\right).
\end{aligned} \tag{3.10}$$

Combining equations (3.8-3.10) together gives a set of equations of motion to completely describe the density of states b_j, a_i, and g_k. The equations above although have different notations and forms from that in the paper by Nacher and Leduc [3.13], the mechanics are identical.

One important effect that has not been discussed up to now is the Doppler broadening of the laser radiation frequency seen by the ^{3}He atom by its thermal motion. Each transition has at a given temperature a frequency width

$$\frac{\omega_k}{2\pi}\frac{\overline{v}}{c}$$

where $\overline{v}$ is the average thermal speed. It is an important effect that needs to be accounted for in the model of equations of motions especially if each frequency component in the Doppler width does not get the same amount of laser light radiation due to a laser line width more narrow than the Doppler width. A simple way of treating the unequal matching between the Doppler width and the laser line width is discussed also in the paper by Nacher and Leduc [3.13]. The table below gives the frequency width in three different temperatures of experimental interest.

T [K]	300	77	4.2
$\overline{v}[10^5$ cm/sec]	1.29	0.653	0.152
D [GHz]	1.19	0.603	0.141

Table 3.5 Average thermal velocities and Doppler widths for optical pumping absorption at three different temperatures [3.13].

3.2.3 Optical Detection of ^{3}He Polarization

For low ^{3}He nuclear polarization, an optical pumping light transmission technique was used in the early ^{3}He polarization experiments to monitor the metastable polarization of the ^{3}He gas. The difference in light transmission at the optical pumping wavelength between the unpolarized state and a partially polarized state is related to the polarization of the metastable atoms and thereby to the nuclear polarization. This technique has been limited by the difficulty in measuring with precision a small difference in light transmission. An optical technique was developed by Pavolic *et al.* [3.16] to measure the nuclear polarization by detection of the circular polarization of the $3^1D \rightarrow 3^1P$ $(1s3d \rightarrow 1s2p)$ transition which has a wavelength of 667.815 nm [3.17].

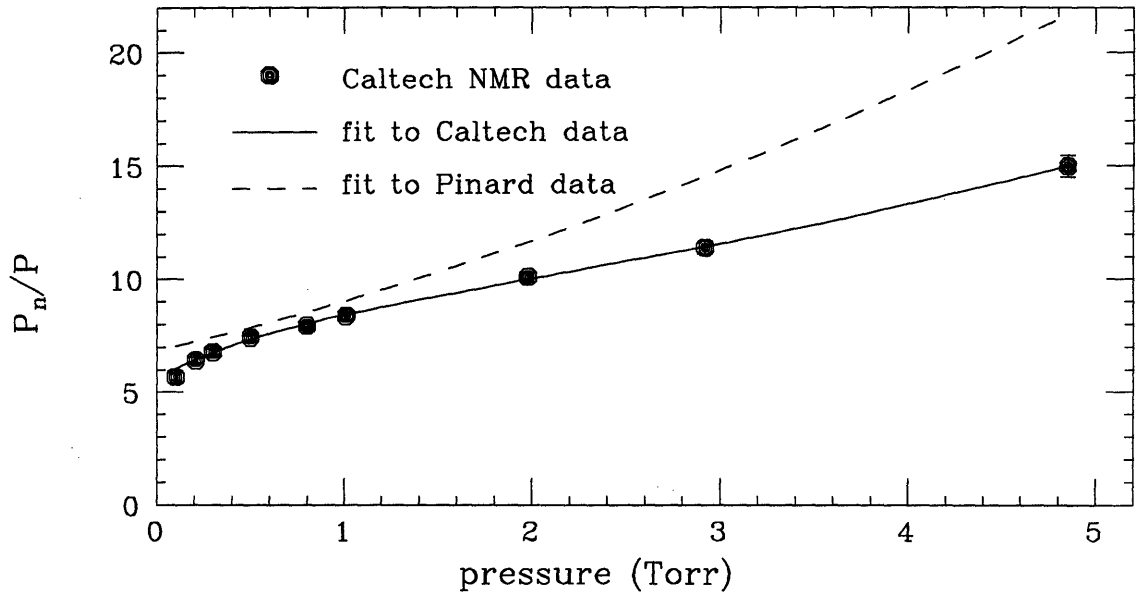

Figure 3.5. Ratios of the nuclear polarization P_n to the measured optical polarization P at 668 nm measured using NMR by Lorenzon *et al.* [3.18] and using laser light transmission by Pinard *et al.* [3.19].

In the RF-discharge, a small fraction of the atoms is excited from the ground state to the 3^1D state, in which, the nuclear polarization is transferred to the atomic polarization of the 3^1D state via the hyperfine interaction. The photons of the spontaneous emission $3^1D \rightarrow 3^1P$ then carry a fraction of the nuclear polarization on average. In the limit of zero gas pressure, the ratio of optical

polarization to nuclear polarization is given by

$$\begin{aligned}\frac{P_\sigma}{P_n} &= \frac{a^2(J+1)/2}{\Gamma^2 + a^2\left(J+\frac{1}{2}\right)^2} \\ &= \frac{0.24}{1 + \left(\Gamma/\frac{5}{2}a\right)^2}\end{aligned} \tag{3.11}$$

where $J = 2$ for the 3^1D level, Γ (=6.58 $\times$ 10^7 /sec is the transition rate to the 2^1P level, a (=3.496$\times 10^8$ Hz [3.18]) is the hyperfine coupling constant defined by the hyperfine Hamiltonian, $a\mathbf{I}\cdot\mathbf{J}$.

At finite gas pressures, disorientation and disalignment of the 3^1D state can modify the ratio of the polarizations. The effects can be parametrized with some modifications to the above formula as

$$\frac{P_\sigma}{P_n} = \frac{a^2(\Gamma+\gamma_2)J(J+1)/2}{(\Gamma+\gamma_2)(\Gamma+\gamma_1)^2 + a^2J(J+1)(\Gamma+\gamma_1)(\Gamma+\frac{2}{3}\gamma_2)/\Gamma + a^2(\Gamma-\gamma_1+2\gamma_2)/4}, \tag{3.12}$$

where γ_1 and γ_2 are the disorientation and disalignment rates, respectively with $\gamma_i = N\sigma_i v_r$. N is density of the gas, σ_i is an associated cross section, and v_r is the average relative velocity between atoms. This ratio has been calibrated as a function of gas pressure using the optical pumping light transmission technique [3.19] and nuclear magnetic resonance technique [3.18]. The calibrated polarization ratio curve in figure 3.5 then serves for conversion of the measured optical polarization of the 668 nm line to the nuclear polarization of the ^{3}He discharge gas.

3.2.4 Polarized ^{3}He Source

To carry out the CE-25 experiment, a new polarized ^{3}He internal gas target was developed at MIT-Bates. A schematic diagram of the target is shown in figure 3.6. The ^{3}He atoms flow through a glass pumping cell of volume V at a rate of F atoms/sec. As shown, the ^{3}He gas has an input density of ρ_i and traverses an input conductance C_1. The gas in the pumping cell has an average density of ρ_p and exits through a conductance C_2 to the storage cell. The average residence time of an atom in the pumping cell, t_r, is given by

$$t_r = \frac{\rho_p V}{F} . \tag{3.13}$$

For equilibrium flow with $\rho_0 \approx 0$, one has

$$F = C_1(\rho_i - \rho_p) = \rho_p C_2 , \tag{3.14}$$

and so

$$t_r = \frac{V}{C_2} . \tag{3.15}$$

Thus, the average residence time of an atom in the pumping cell depends only on the quantities V and C_2. Further, from equation (3.14) we have

$$\frac{\rho_p}{\rho_i} = \frac{C_1}{C_1 + C_2} , \tag{3.16}$$

and so a measurement of ρ_p as a function of ρ_i measures the ratio of conductances C_1 and C_2. Note that in the intermediate flow region C_1 and C_2 are functions of ρ_p and ρ_i.

In the pumping cell the atoms are polarized by absorption of angular momentum from the laser pumping light at the 1.083 μm transition. Consider a sample of ^{3}He atoms in a valved cell, i.e. a pumping cell where there is no flow and the sample of ^{3}He atoms is static. In the approximation that the polarization rate does not depend upon polarization, the ^{3}He atoms will be polarized to an equilibrium polarization P_0^v with a pump-up time-constant of t_p^v given by

$$P(t) = P_0^v(1 - e^{-\frac{t}{t_p^v}}) . \tag{3.17}$$

Similarly, the atoms in an identical pumping cell but flowing at a rate F atoms/sec. will be polarized to an equilibrium polarization P_0^f witha pump-up time constant t_p^f where

$$\frac{1}{t_p^f} = \frac{1}{t_r} + \frac{1}{t_p^v} . \tag{3.18}$$

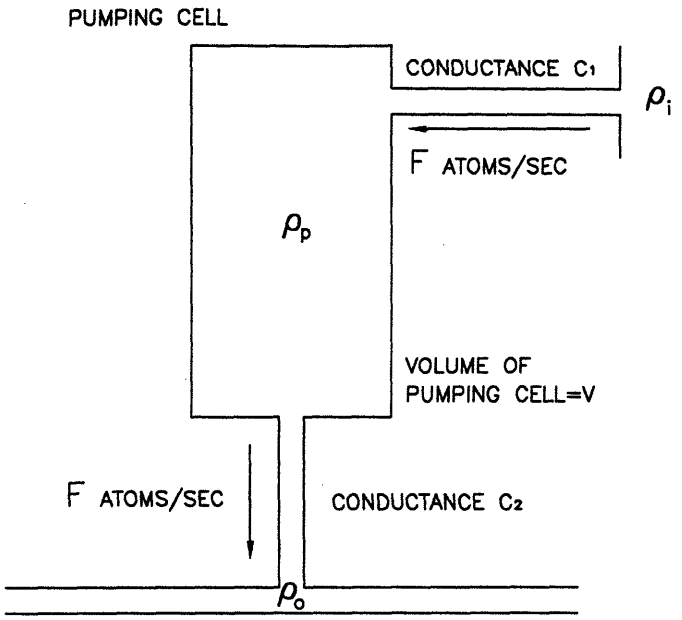

Figure 3.6. A schematic diagram of the internal target. Typically $\rho_i \approx 5$ Torr, $\rho_p \approx 0.5$ Torr, and $\rho_0 \approx 10^{-3}$ Torr.

The equilibrium polarization obtained with a flowing system, P_0^f, and the equilibrium polarization obtained on a valved copy of the pumping cell, P_0^v, are related by

$$P_0^f = P_0^v \frac{t_r}{t_r + t_p^v} , \tag{3.19}$$

where the difference between valved and flowing systems is the presence of a polarization relaxation with time constant t_r due to unpolarized atoms entering the pumping cell through C_1. t_r is equal to the residence time of the atoms in the pumping cell. From (3.19) we see that for high polarization in the flowing system we require that $t_r \gg t_p^v, t_p^f$, i.e. the pump-up time must be much shorter than the residence time in the pumping cell. A pumping cell of volume 500 cm^3 containing ^{3}He gas at a pressure of 0.66 mbar and flowing at a rate of 10^{17} atoms/sec will have a residence time of $t_r = 75$ sec. As such a cell can be polarized to $\sim 65\%$ with a pump-up time $t_p^f \sim 10$ sec, we see that the condition $t_r \gg t_p^v, t_p^f$ is well satisfied and we expect an equilibrium polarization in the flowing system, P_0^f, greater than 50%.

To study the operation of the flowing system it is convenient to define two quantities. First, we define the polarization rate of a sample of ^{3}He, R, to be

$$R = \frac{NP_0}{t_p} , \tag{3.20}$$

where the sample contains N ^{3}He atoms which are polarized to an equilibrium polarization P_0 with a pump-up time constant t_p. Secondly, the ^{3}He atoms are polarized by means of a discharge whose intensity is characterised by τ_d, which is the time constant associated with the polarization decay in the absence of optical pumping and in the presence of the discharge. As we shall see below, the performance of the polarized ^{3}He internal target is strongly dependent on R and τ_d.

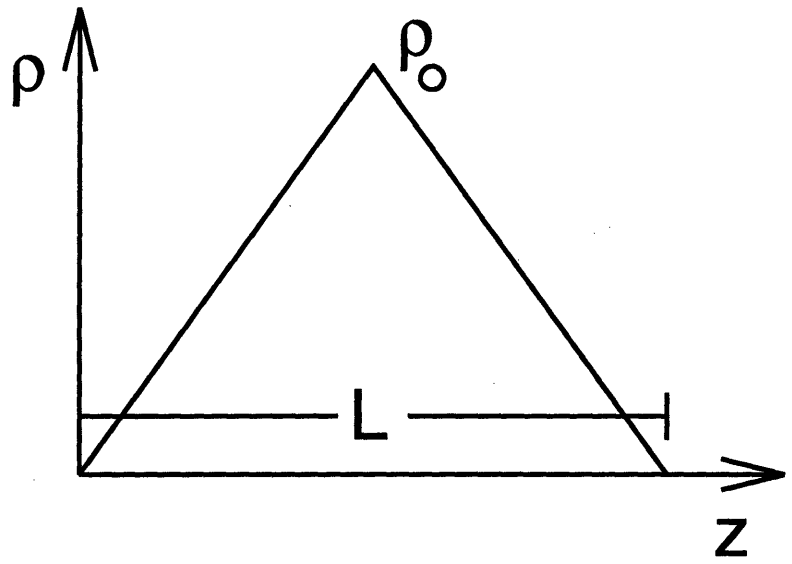

Figure 3.7. A schematic drawing of gas density in the storage target cell of length L.

As the gas exits into the storage cell, it diffuses out the two ends at very low pressures ≈mTorr's and forms approximately a triagular distribution with the maximum density ρ_o at the exit capillary as shown in figure 3.7. The density ρ_o is given by

$$\rho_o = \frac{F}{4C_{cell}}, \tag{3.21}$$

where C_{cell} the molecular conductance for the entire length of the storage cell. One then obtains the target density,

$$s = \rho_o \frac{L}{2} = \frac{FL}{8C_{cell}}, \tag{3.22}$$

where L is the length of the target cell.

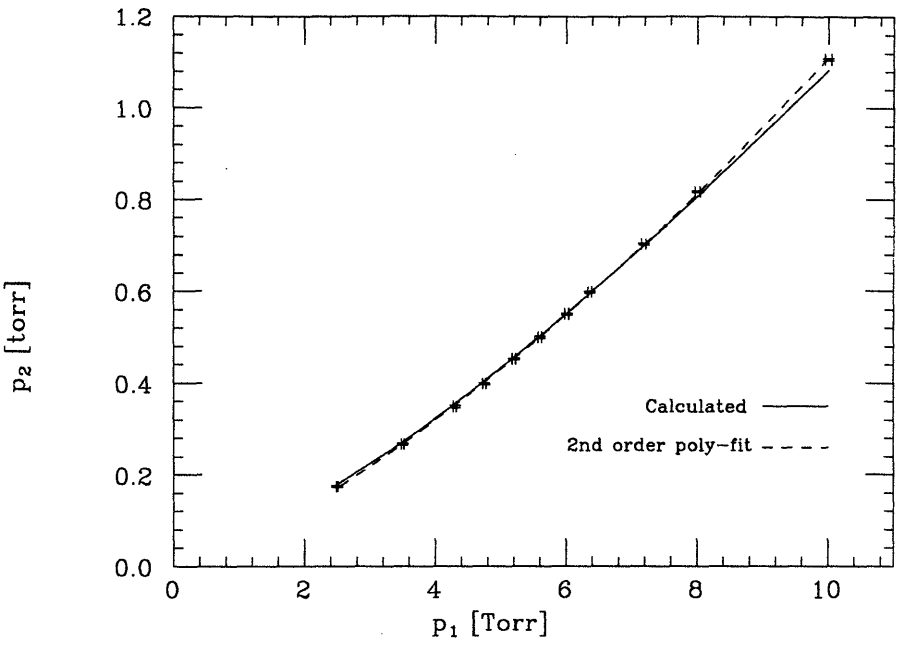

Figure 3.8. Calibration of ρ_p *vs.* ρ_i. The solid curve is a calculation using the Knudsen conductance equation in the intermediate flow region with parameters fitted to ^{3}He and ^{4}He gas flow data from known volumes. The dashed curve is a second order polynomial fit to the data.

Knowledge of the pressure in the pumping cell, ρ_p is necessary for use of the optical calibration for a nuclear polarization measurement, for calculation of the flow-rate from equation (3.14) above, and for optimization of polarization as a function of the gas pressure. Measurement of ρ_p is accomplished by temporarily attaching a baratron gauge by means of a mini-conflat flange attached to a glass nipple to the pumping cell. Then the pressure of the ^{3}He atoms in the pumping cell, ρ_p, is measured as a function of the input pressure ρ_i. The pressure calibration data for the flow through system are shown in figure 3.8. The solid curve is a calculation of the equation (3.16) using the Knudsen equation for intermediate flow and is in good agreement with the data. The Knudsen equation is given in Roth [3.20] as

$$C_{capillary} = \left(c_1 D^4 \overline{P} + c_2 D^3\right)\frac{1}{L}$$

where

$$c_1 = \frac{\pi}{128\eta},$$

$$c_2 = 3.81 \times 10^3 \sqrt{\frac{T}{M}} \frac{1 + 1.10 \times 10^{-4}\sqrt{M/T}D\overline{P}/\eta}{1 + 1.36 \times 10^{-4}\sqrt{M/T}D\overline{P}/\eta}, \qquad (3.23)$$

and where $C_{capillary}$ is the capillary conductance in [cm^3/sec], T the temperature in [K], M the atomic mass in [amu], $\overline{P}$ the average gas pressure accross the capillary in [Torr], D the capillary diameter in [cm], L the capillary length in [cm], and η a temperature dependent parameter associated with the size of atoms in [Torr sec]. The parameter η in the coefficient c_1 was adjusted to fit ^{4}He gas flow data at pressure >1 Torr for a known, large volume. Moreover, the numerical values in the coefficient c_2 were slightly modified from values given in Roth to fit ^{3}He gas flow data for individual pumping cell at pressure <1 Torr. In both cases, the volume was filled with the corresponding gas of He isotope, and the pressure was monitored as the gas flowed out. The data obtained from using the large volume had a much higher precision than from using pumping cells with much smaller volumes. A set of numerical values used in c_2 was obtained for individual cells. However, it was not understood why there was no unique set of numerical values for all the pumping cells.

After the calibration, attachment for the baratron gauge is removed from the pumping cell. The flow rate F was determined by measurement of ρ_p and calculation of C_2. This resulted in a $\pm 10\%$ systematic error in the knowledge of F. Only knowledge of the relative target thickness was necessary in this experiment, and absolute cross section measurements in the future using the internal gas target would require a high precision determination of the flow rate F for gases of different masses and of the target cell geometry conductance.

3.3 Polarized ^{3}He Target Apparatus

The target operated by flowing ^{3}He atoms through a glass cylindrical optical pumping cell, made by Finkenbeiner G. Inc. [3.21], of volume 400 cm^3 at a rate of 1.2×10^{17} atoms/sec [3.9]. The ^{3}He gas was fed at an input pressure of 5 Torr and traversed an input precision capillary with a conductance of 0.9 cm^3/sec into the glass pumping cell where the gas is polarized by laser radiation. The polarized gas in the pumping cell had an average pressure of 0.5 Torr and exited through a second precision capillary with a conductance of 8 cm^3/sec to an open ended aluminum target cell. figure 3.9 shows the schematic layout of the target apparatus. This configuration resulted in a target thickness of 1.4×10^{15} atoms/cm^2. The target was polarized along the holding magnetic field in the vertical direction provided by a 40.0 in (101.6 cm) diameter Helmholtz-like coil pair. The original Helmholtz pair was opened up slightly from the separation of 20 in (50.8 cm) to 20.6 in (52.3 cm)—extracted from CAD drawings— so that the optical pumping glass cell on the target chamber is centered in the uniform magnetic field region. The target assembly was mounted on a single aluminum flange, which was attached to the top of an aluminum ultra-high vacuum chamber. The chamber rested on top of the lower coil in order that the pumping cell, located in a well in the target flange, was centered within the uniform field region of the coils to minimize the effects of depolarizing field gradients. The optical pumping laser radiation was directed onto the pumping cell by the optics mounted above the coils. Also, a polarimeter which viewed the 668 nm line of the ^{3}He discharge in the pumping cell was mounted on the table. The vacuum chamber, the Helmholtz coil pair, and the optics table were all mounted on an aluminum stand with vertical and lateral adjustments, which in turn was placed on top of a 36 in (91.4 cm) high steel frame to bring the target cell to the beam height, 77.0 in (195.6 cm).

3.3.1 Target Vacuum Chamber

The target vacuum chamber was designed to be an all nonmagnetic metal bakeable ultra high vacuum system, to have a large angle range in θ and ϕ for an extended target cell, and to be placed inside the Helmholtz coil pair. It was manufactured from a single forged block of 6061-T6 aluminum. Nonmagnetic metal was used to minimize the depolarizing effects of nonuniform magnetic fields in the vicinity of the target pumping cell. The chamber was designed at MIT-Bates and was contracted out to Meyer Tool & Mfg., Inc. for manufacturing [3.22]. The seals used were aluminum conflat from Ulvac Ltd. [3.23] and Viton rubber seals designed

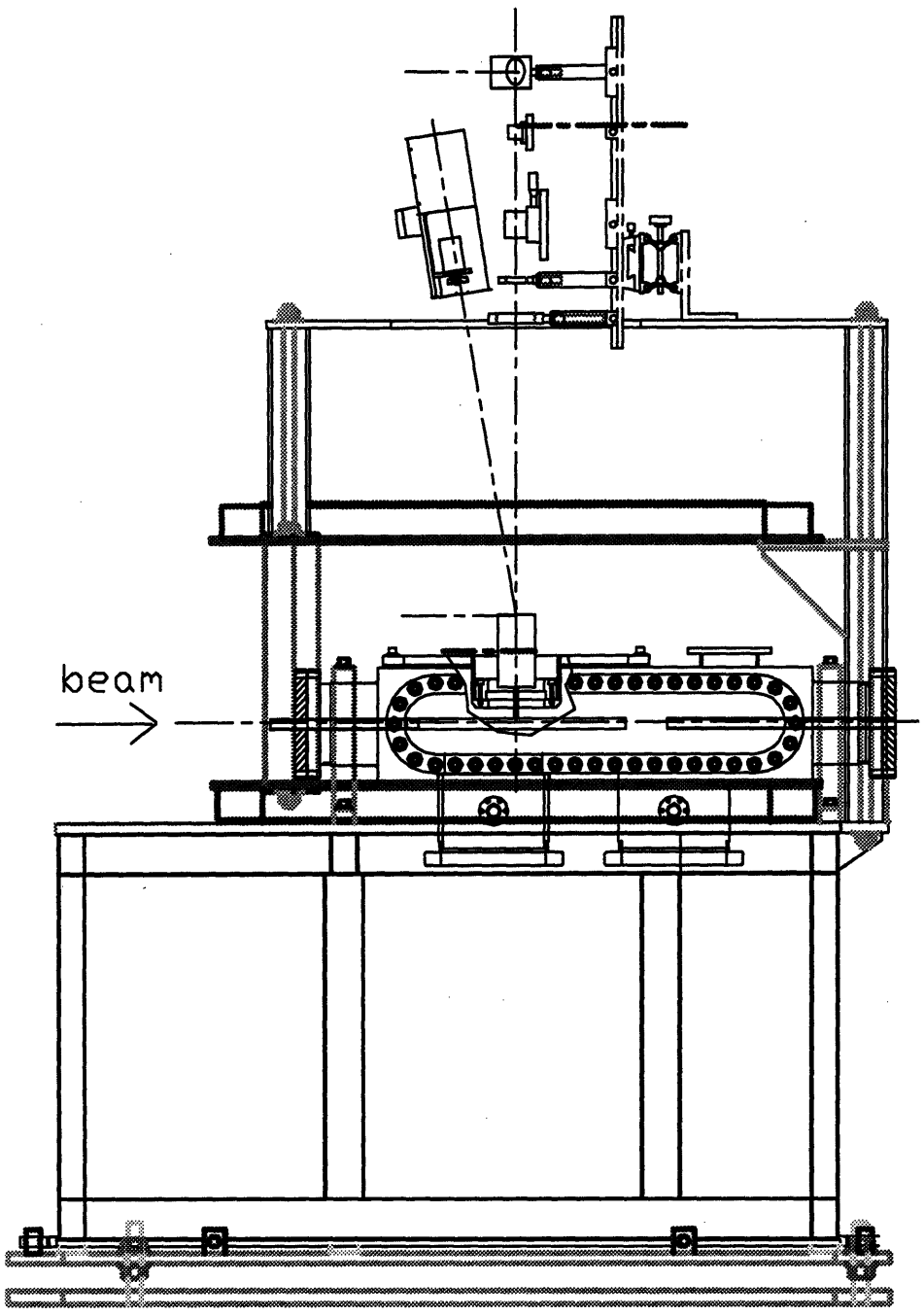

Figure 3.9. A schematic diagram of the CE-25 polarized ^{3}He internal gas target.

at MIT-Bates. The complete vacuum chamber assembly was coated with titanium nitride to harden the sealing surfaces.

The chamber was constructed from a single block of aluminum, and circular pipes were welded to the chamber. Figure 3.10 shows the top and side views of the chamber with an optical pumping glass cell in the top oval flange. The aluminum

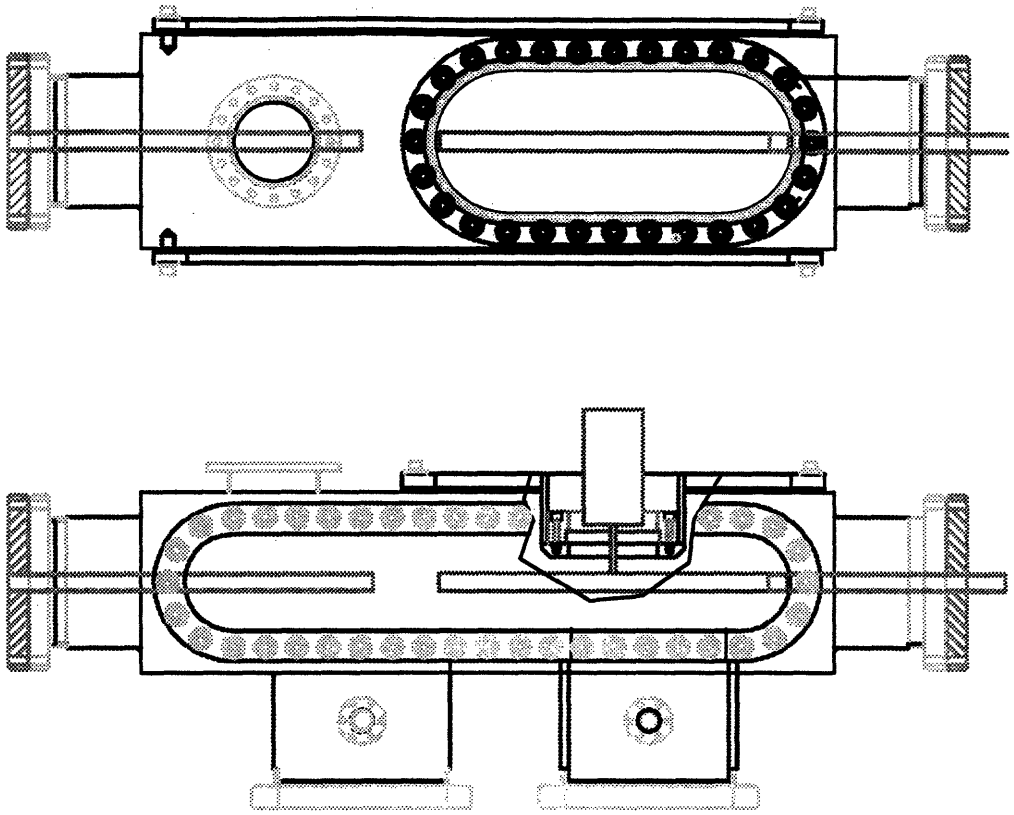

Figure 3.10. The design drawing of the aluminum chamber and the top flange for mounting the optical glass cell.

chamber, without the end pipes and the windows, had the dimensions of 43 in length × 9.75 in width 8.25 in height (109.2 cm × 24.8 cm × 21.0 cm). Prior to machining, the block of aluminum was examined by X-ray for internal cavities which could cause imperfections on sealing surfaces. The block was machined through the sides forming a long oval slot 4.25 in height × 37.4 in length (10.8 cm × 95.0 cm). A short oval opening 10.8 in breadth × 22.2 in length (27.4 cm × 56.4 cm) for the target assembly flange was machined out on the top side toward the upstream end of the chamber. The location was chosen so that the center of a 40 cm long storage target cell has a 15° forward angle line of sight with the front end of the oval slot openings on both the left and the right side, *i.e.* scattered particles can exit at the 15° forward angle. The ends were bored out circular holes to which Ulvac UHV aluminum knife-edge flanges with aluminum pipes of 6.0 in (15.24 cm) diameter were attached by welding. These flanges were used for coupling the chamber to an accelerator storage ring. The bottom side was bored out also with two circular holes

to which were attached aluminum knife-edge flanges via a short 8.0 in (20.32 cm). These flanges served either as ports for mounting turbo molecular pumps (TMP) or for making electrical connections to detectors installed inside the chamber. In addition, three smaller ports with aluminum knife-edge flanges had been attached to the chamber for installation of ionization vacuum gauges. All knife-edge conflats were from Ulvac Ltd.

The UHV chamber was designed so that custom made Helicoflex seals with a delta edge were to be used in sealing all the oval shaped ports, model no. H-301742 for the top oval port and model no. H-301743 for the side oval ports. For protection of the sealing surfaces the chamber was hardened with titanium nitride coating similar to that on the Ulvac UHV aluminum knife-edge flanges. However, double Viton O-rings race track seals designed at the Bates linac were found to be satisfactory. A high 10^{-9} Torr vacuum was achieved with the double Viton O-rings race track seals while a 2200 liter/sec TMP was pumping on the emptied chamber after a moderate bake out for three to four days at 80° C. The Viton O-rings seals were significantly lower in cost than the Helicoflex seals and during the course of the experiment it was necessary to open and reclose the side windows frequently requiring the seals to be reusable several times.

3.3.2 Optical Pumping Pyrex Glass System

The glass system for polarizing the ^{3}He gas was constructed from a cylindrical cell of volume V with an entrance capillary of conductance C_1 and an exit capillary tube of conductance C_2 and UHV compatible components for interfacing to ^{3}He or ^{2}H gas sources and to the vacuum chamber. The capillary tubes were of precision drawn Pyrex with inner diameter (ID) uncertainty of $\pm$0.002 in ($\pm$0.0051 cm) from Wilmad [3.24]. The entrance capillary connected a top corner of the glass cell to a glass-to-metal mini-conflat flange UHV compatible transition which used the magnetic Kovar material. The presence of the small amount of Kovar material approximately 10 in (25 cm) away from the glass pumping cell did not have noticable depolarizing effect on the ^{3}He polarization. Tests with different materials that were slightly magnetic, such as a stainless steel bolt, showed that the ^{3}He polarization was decreased slightly only when the bolt was within 1 in (1-2 cm) of the glass pumping cell. A 0.25 in (0.64 cm) ID glass tube with a Kontes teflon valve [3.25] also connected the top of the glass cell to the glass-to-metal transition as a by-pass tube to allow for faster vacuum pump-out. At the bottom, the exit capillary connected the glass cell to the center of a flat glass disk of 4.72 in diameter $\times$

0.5 in thick (12.00 cm × 1.27 cm) and polished to optical smoothness via an 11 mm (.433 in) ID glass tube as in figure 3.11 for interfacing the glass cell to the vacuum chamber. As the connection of the exit capillary to the external glass tube was the weakest in the glass system, reinforcements were made between the side of the glass cell to the top of the disk at three equally spaced locations.

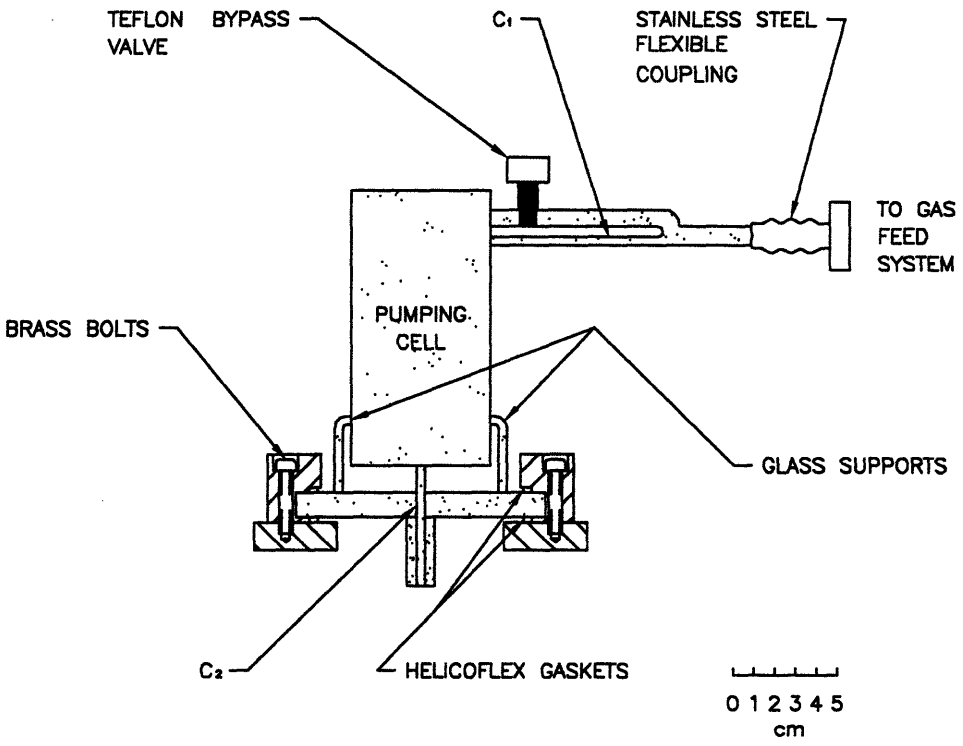

Figure 3.11. The optical pumping glass system to be mounted in the well of the aluminum flange.

The glass disk was then clamped onto the well of the top oval flange by a circular aluminum flange, compressing the double Helicoflex aluminum seals. The double seals configuration used a delta ring seal at the bottom and a C ring seal at the top of the glass disk and was designed with the help of an engineer at Helicoflex [3.26]. The delta seal was designed to require just a few lb per linear in, thus suitable for use with the glass disk. The C seal having the same diameter as the delta seal was used only for uniform compression directly on top of the delta seals. The circular aluminum flange was carefully tightened down by the brass

screws to obtain an vacuum of 10^{-5} or 10^{-6} Torr at the initial pumping. The brass screws were tightened down further iteratively while closely monitoring vacuum leaks around the delta seal.

A small gap of 5 mm between the bottom of the glass cell and the top of the glass disk was left for a split gold coated filter Schott glass [3.27] that reflected the optical pumping laser radiation while absorbing the 668 nm radiation for polarization monitoring. Tests using sealed cells had shown that retro-reflecting the optical pumping laser radiation for a second passage through the ^{3}He gas increased from 5% to 15% the nuclear polarization depending on the laser beam spot size at the cell and the length of the cell. A filter glass was used to minimize reflected light into the 668 nm polarimeter. As the filter glass could not be heated to the Pyrex glass annealing temperature of 580° C, the filter glass was split in two pieces to be installed, after the annealing, around the exit capillary tube. In addition, the cylindrical glass cell was completely wrapped in black electrical tape, allowing only the discharge radiation to exit through the top glass window of the cell.

At the top, a short 0.25 in (0.64 cm) ID glass stem connected the cell to a mini-conflat flange for connection with a baratron that was used for calibrating ^{3}He or ^{2}H gas pressure in the glass cell as a function of input pressure to the glass system. The entrance end of the glass system was connected to gas supplies via UHV compatible 0.75 in (1.92 cm) manifold with a baratron that was used for monitoring the input pressure. After calibration, the glass system was dismounted from the chamber and the glass stem was removed by the glass blower.

3.3.3 Gas Feed System

The gas feed system was assembled with UHV components to flow gas from stainless steel ^{3}He or ^{2}H gas bottles. As shown in figure 3.12, gas bottles were connected on each end of the T manifold via a UDV Balzers thermal valve. There were normally two to three ^{3}He gas bottles and only one ^{2}H gas bottle. At the ^{2}H gas bottle side of the T manifold, there were a 0-100 Torr baratron and an electro-pneumatic valve that opened to an Alcatel 100 liter/sec turbo molecular pump.

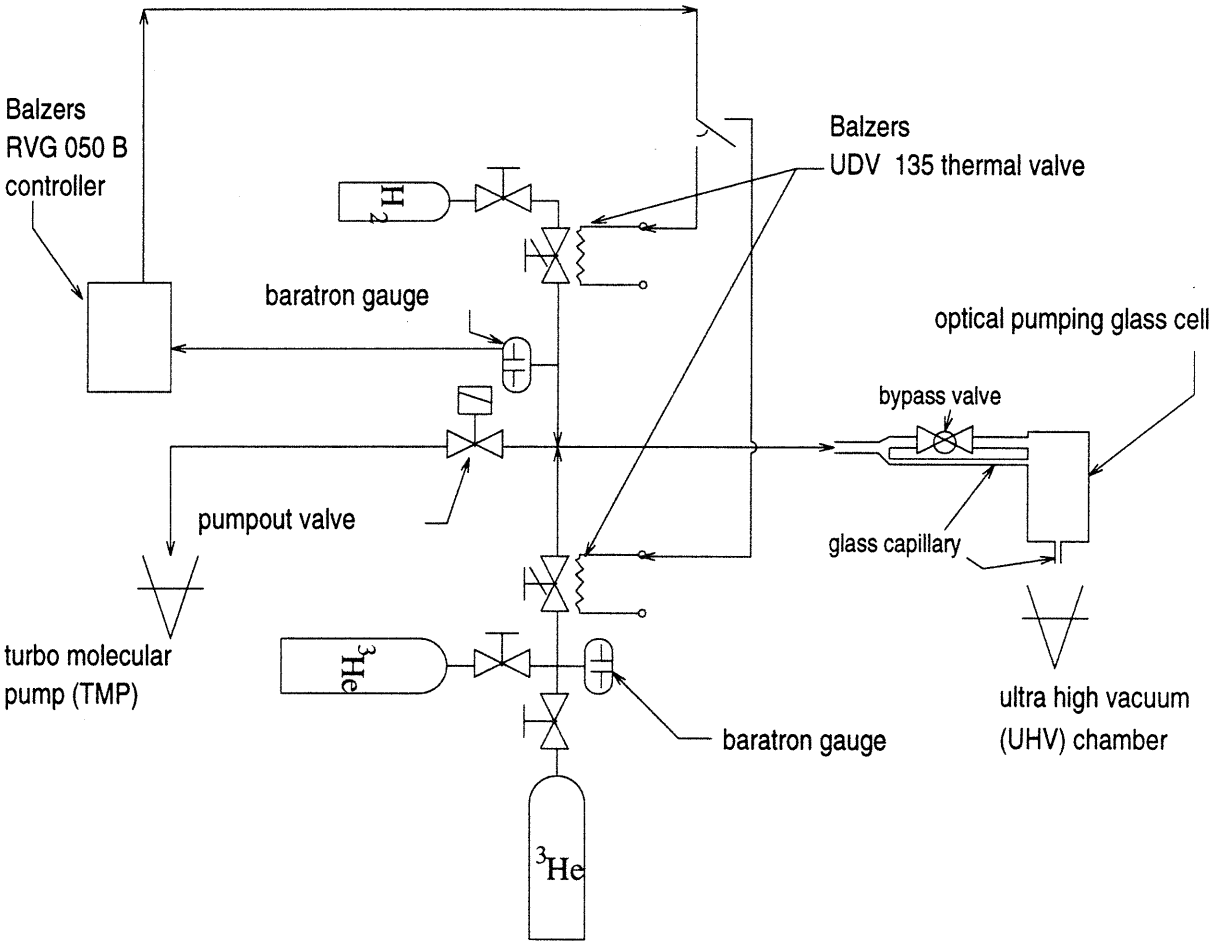

Figure 3.12. Schematic drawing of the gas feed system.

The vacuum valve was opened only for pumping out the manifold and the glass system. When ^{3}He gas was flowing through the glass system, the ^{2}H gas UDV thermal valve was closed either manually or thermally. The UDV valve operated by pressing a polished Sapphire flat disc onto a metal valve seat with a rod which

was in turn pressed down mechanically with a manually controlled lever. Thermal expansion of the rod by electrical heating was used for closing the valve or by a pressure feedback controller for maintaining a stable pressure in the manifold, and hence a stable flow. The manifold and the glass system were pumped out by opening the vacuum valve before switching to ^{2}H gas.

It was found in the development of a prototype target that constructing the manifold with UHV compatible components greatly improved the ^{3}He polarization from 30% to over 50%. All parts in the manifold including the UDV thermal valves were UHV compatible to decrease or eliminate sources of depolarizing impurities flowing into the ^{3}He gas as the level of impurity must be limited to just 10^{-4} mm Hg partial pressure [3.3] or ~100 ppm (*see section* 3.7.1). At a few Torr of ^{3}He gas pressure in the manifold any small leak would degrade the system's cleanliness over a few hours. Only the Kontes teflon valve on the glass by-pass stem was rated for high vacuum and therefore, the base vacuum estimate in the glass cell was approximately 10^{-6} Torr when the base vacuum near the TMP was 10^{-8} Torr, well below the 10^{-4} mm Hg partial pressure limit.

3.3.4 Storage Target Cell

The exit capillary of the ^{3}He pumping cell was connected to a glass flange which was in turn attached to the top of the target chamber. The lower end of the capillary extended into the chamber and was coupled to the target cell with a short teflon sleeve. The target cell, which was 400 mm long, 16.6 mm high and 13.1 mm wide, was constructed from 0.2 mm thin aluminum as shown in figure 3.13. The sides of the cell, which served as exit windows for reaction products including low energy recoil particles, were 1.7 μm thin aluminized mylar sheets attached to the target cell with Torr Seal low vapor pressure resin from Varian [3.29]. The cell dimensions, which were chosen to meet the designed storage ring acceptances at the target location, provided 35π mm mrad acceptance in the vertical direction and 30π mm mrad in the horizontal plane.

The thickness of the gas target can be estimated using the molecular flow conductance equation for a straight conductor of uniform cross section [3.20]

$$C_{cell} = \frac{3.44 \times 10^4 K}{\sqrt{\pi}} \sqrt{\frac{T}{M}} \left(\frac{A^2}{BL}\right), \tag{3.24}$$

where C_{cell} is the target conductance in [cm^3/sec], T the temperature in [K], M the mass number of atoms in [amu], A cross sectional area in [cm^2], B the parimeter in [cm], L the length in [cm], and K a dimensionless factor for rectangular shaped

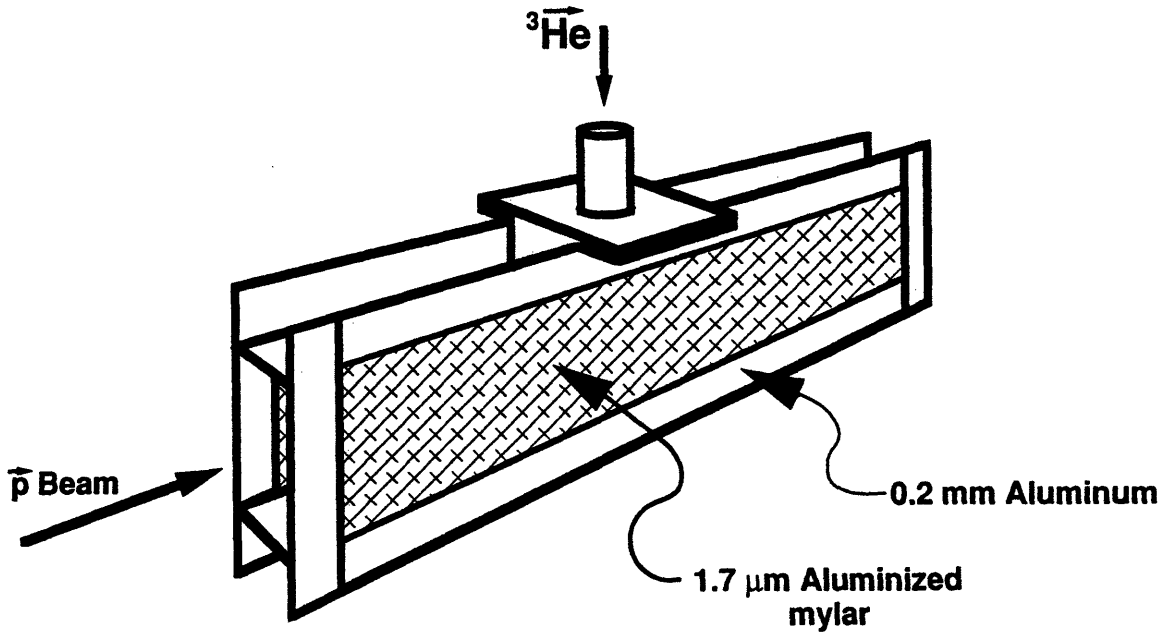

Figure 3.13. A schematic layout of the target cell.

conductor. Substituting the numbers for the target cell dimensions into equations (3.22) and (3.24) and using the table below, the target thickness S_{cell} was estimated to be 1.4×10^{15} atoms/cm^2 for a flow rate F of 1.2×10^{17} atoms/sec.

b/a	K
1	1.108
0.667	1.126
0.5	1.151
0.333	1.198
0.2	1.297
0.125	1.400
0.1	1.444

Table 3.6. The dimensional factor K for different ratios of the rectangular conductor side dimensions. K is 1 for circular conductor.

The scattering chamber was centered along the beam axis using a transit and crosshairs placed in the end flanges. The target cell, transport tube and pumping cell were attached rigidly to the top flange, which was bolted to the chamber. Pins were placed in two of the bolt holes so that the top flange could be removed and

replaced at a reproducible position. Initial alignment of the target cell was done using apertures placed in the two ends of the cell. Measurements of the position of target cell relative to the top flange allowed the cell to be removed and replaced with an alignment accuracy of less than ± 1 mm in both horizontal and vertical directions.

3.3.5 Differential Vacuum System

Significantly lower vacuums are required in storage rings than when conventional nuclear physics techniques are employed. In the IUCF cooler ring the base vacuum is typically 10^{-9} Torr. A comparable vacuum in the absence of target gas was attained in the target chamber. This allowed for routine operation of the storage ring for other experiments. When the target was in operation a gas flow of 1.2×10^{17} ^{3}He atoms/sec was pumped away in the target region and differential pumping stages were used to attain the storage ring vacuum in as short a distance as possible.

The ^{3}He gas leaving the cell was pumped differentially along the beam axis. Removal of this background gas was important because it contributed to the stored beam loss rate, and thus adversely affected the average luminosity. Therefore, the design goal of the differential pumping system was to minimize the thickness of the background gas. In the present experiment this was accomplished with three turbomolecular and two cryogenic pumps in an arrangement shown in figure 3.14.

Turbo pumps were located on the scattering chamber (Balzers TPH 2200, nominal ^{4}He pumping speed: 3200 liter/sec) and on each neighboring pumping stage (Balzers TPH 1500, nominal ^{4}He pumping speed: 1500 liter/sec). On the two outer stages, which connected the experimental area to the rest of the ring, cryo pumps (Leybold RPK 3000S12, nominal ^{4}He pumping speed: 1300 liter/sec) were employed. Cryo pumps have a limited capacity to store helium which made frequent regeneration necessary (typically once or twice a day in this experiment). For this reason, the cryo pumps were equipped with an internal heater which could be activated remotely to regenerate the pumps within a few minutes.

The differential pumping stages were separated by gas flow limiters which, like the target cell, were located outside the ring acceptance, both vertically and horizontally. Their position and length were optimized, within the constraints imposed by particle detection requirements, such that the thickness of the ^{3}He gas outside the target cell was a minimum, and amounted to only 2% of the target thickness. The two limiters upstream of the target cell were 11.3 mm wide by 15.3 mm high.

Downstream, the first limiter was 16.6×17.6 mm^2 and the second 26.8×23.3 mm^2 in width and height, respectively. The typical pressures at a ^{3}He flow rate of 1.2×10^{17} atoms/sec, measured by ionization gauges in the differential pumping stages, were (from upstream) 6, 140, 1500, 210 and 20 $\times 10^{-9}$ Torr.

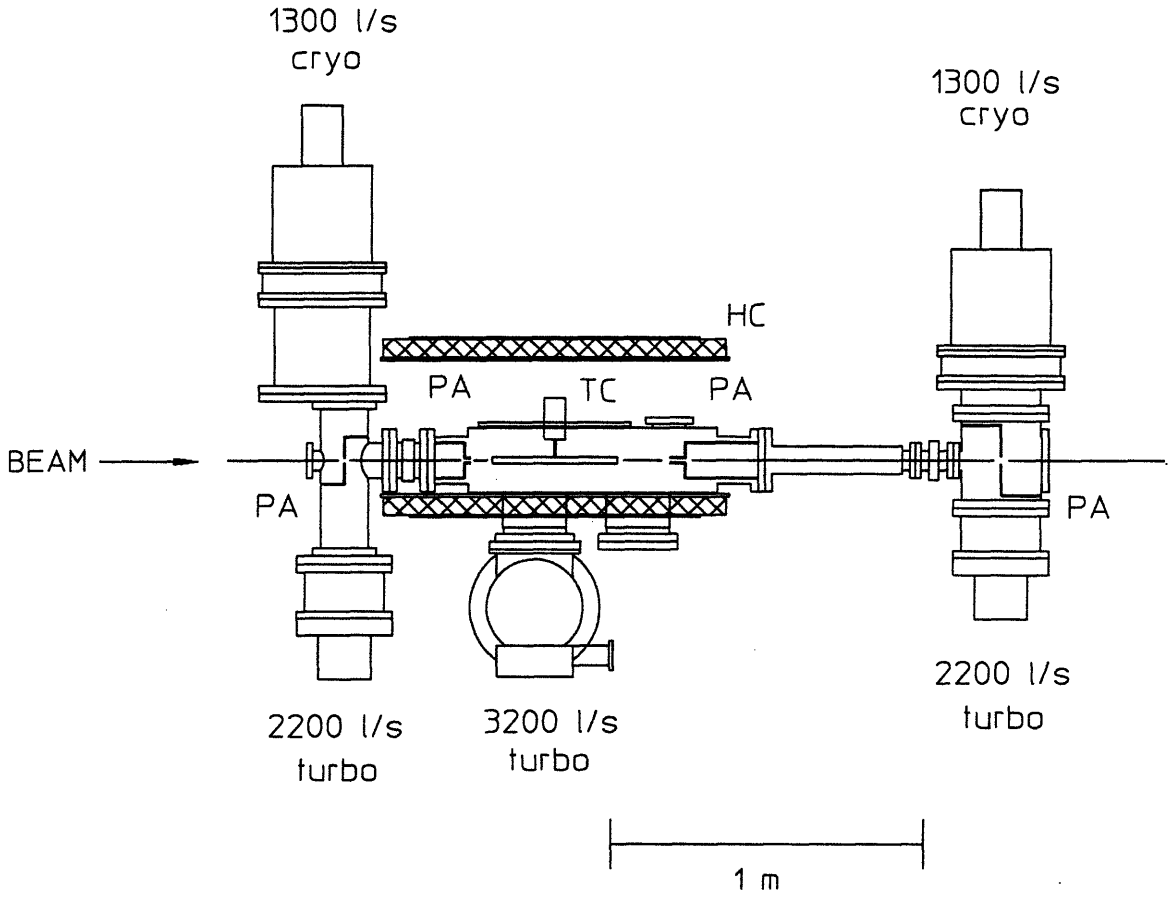

Figure 3.14. A schematic layout of the differential vacuum system. The flow limiters between pumping stages are labeled FL. The target cell is labeled TC and the Helmholtz coils HC.

3.3.6 The Laser Light Source

An LNA laser was a source of the 1.083 μm photons for metastability exchange optical pumping of the ^{3}He gas. A single LNA or Nd:LMA ($La_{1-x}Nd_xMgAl_{11}O_{19}$) crystal was the lasing medium in a cavity for Nd:YAG krypton-arc-lamp pumped laser system model 9550 from Lasermetrics [3.31]. The crystal rod, made by the Union Carbide Corp., was 4 mm diameter $\times$ 79 mm long and had 15% in atomic weight of Neodymium (Nd) doping [3.32]. Its ends were ground concave with radius of 60 cm to correct for thermal lensing due to temperature gradients between the central axis and outsides of the rod. The laser cavity had a nominal length of 30 cm with an HR flat mirror at one end and at the other end an output coupler, a flat mirror with reflectivity $\approx$99.25% at 1.083 μm. A single uncoated etalon of 0.5 mm thickness was used to tune to the C_8 or the C_9 transition. Tuning was facilitated by passing a small beam of light that leaked out from the HR mirror through a tuning cell containing ^{3}He with discharge on. Typical output powers were 3 to 4 Watts at 14 Amp lamp current when the laser was tuned to one of the transitions.

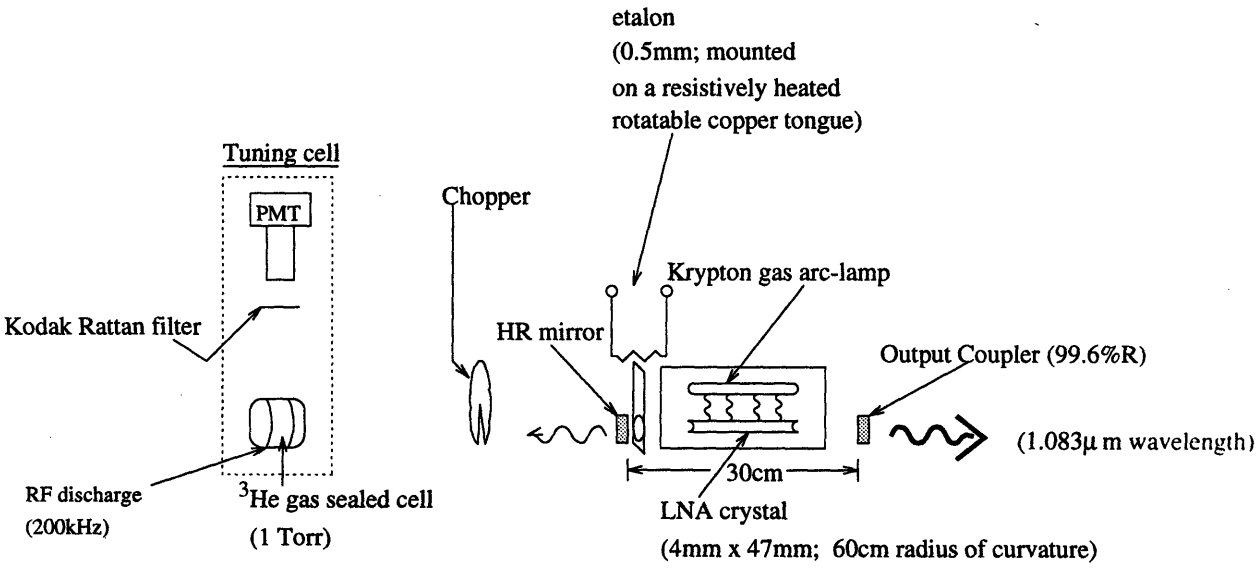

Figure 3.15. The laser system.

The LNA crystal has a hexagonal unit cell with unit lengths a=b=5.57 A° and c=21.97 A°and grows naturally in the plane along the directions a and b. Hence, for use in transversely pumped cavities, crystal rods longer than a few centimeters are grown and cut with the long axis along the direction a (or b) although lasing efficiency is higher for light propagation along the direction c. In the free running mode, the LNA laser spectrum has peaks at 1.054 μm and 1.083 μm , and depend-

ing on doping level of Nd, one peak dominates over the other; at 15% level, the 1.054 μm peak is negligible. Thermal conductivity of the LNA crystals is poor, and with increasing laser power the rods suffer from increasing temperature gradients between the insides and outsides of the rod which causes thermal lensing as mentioned above. At high output powers this effect can cause the crystal to heat, thus limiting the laser operation to low power.

The laser crystal performance was characterized by its output power as a function of lamp current as in figure 3.16. A typical output power curve had a threshold, a slow rise, a rapid rise, and saturation. The lasing threshold was caused by the de-focussing of the concave ends designed for use when the thermal lensing effect set in; a crystal with flat ends had lower lasing theshold than a crystal with concave ends. The laser power increased slowly at first and then linearly as a function of lamp current until the thermal lensing effect became greater than the de-focussing by the concave ends at which point the laser power increased slowly again as a function of lamp current. As the lamp current was increased slightly further, the power decreased indicating a transition to the next higher transverse mode, accompanied by a change in the beam spot profile as seen on an infrared photo-luminescent Kodak card. In fact, at lamp currents below the saturation region for a particular rod and cavity configuration, the laser operated dominantly in the TEM_{00} mode with one large diamond shaped spot in the center and two very small spots on opposite corners. In the saturation region, the two small spots increased in size to that of the the center spot until the beam profile changed to a central large spot surrounded by four small spots uniformly spaced around the central spot. The output power dropped noticeably at this point with increasing lamp current.

The laser crystal performance also depended on the cavity length as shown in figure 3.16and on curvature of the end surfaces of the crystal rod and the mirrors [3.34]. Only flat mirrors were used in the laser system. For the configuration with concave ends rod and flat mirrors, the lasing threshold was lowest for the shortest cavity length. While the concave end curvature (60 cm) corrects for the thermal lensing effect to some degree, when the cavity length was shortened by moving in the mirrors neither the thermal lensing nor lensing from the concave curvature becomes important. The mirror holders of the laser system were slightly modified to reduce the shortest possible cavity length to 30 cm from 33 cm.

The tuning of the laser was carried out in three steps. With the mirrors positioned for shortest possible cavity length, the mirrors were first aligned to be exactly perpendicular to the central axis using the beam of a small He-Ne laser.

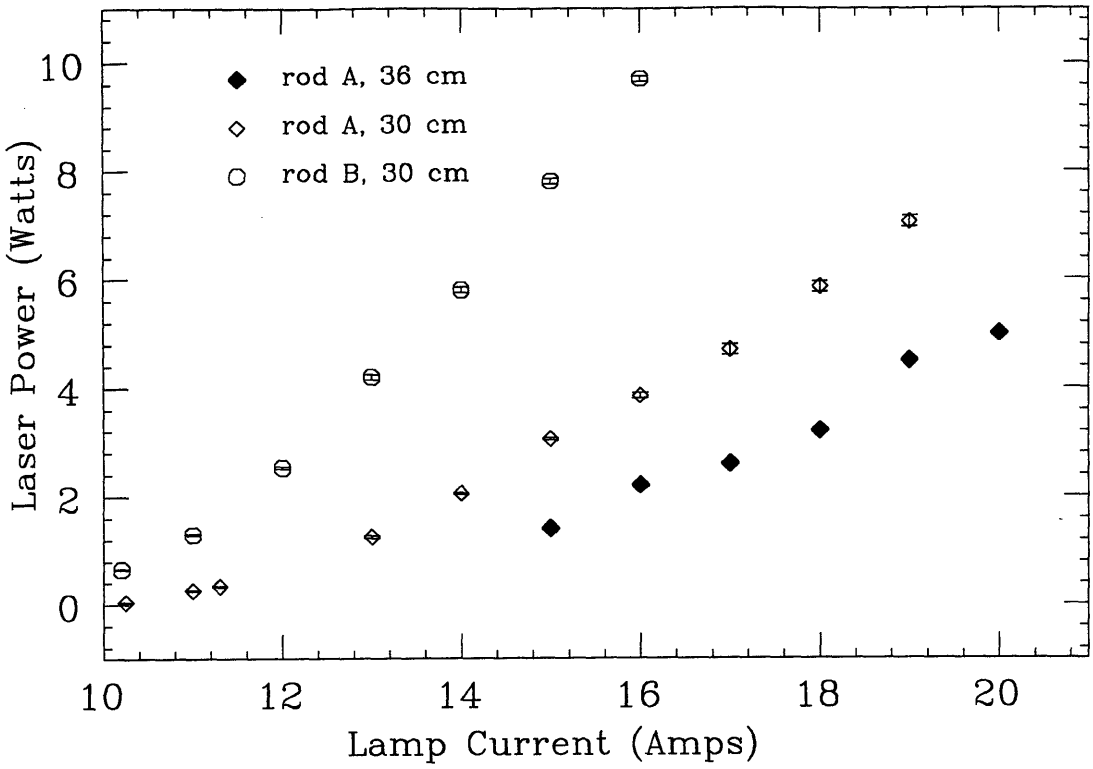

Figure 3.16. Laser output power *vs.* lamp current without any etalon in cavity for LNA laser rods A and B. Different cavity configuration, *i.e.* different cavity length and similar output coupler, produced different output power as seen in the data for rod A. The solid diamond data points were measured at Caltech [3.33] while the other two data sets were measured at MIT.

The He-Ne laser beam was first aligned to the LNA crystal longitudinal axis by orienting the He-Ne laser until the strongest reflection from the crystal end surface appeared right back on the output coupler of the He-Ne laser. With the He-Ne laser beam aligned, a mirror for the LNA laser was inserted at the far end of the crystal and was adjusted in angular position until the reflection from the inserted mirror appeared on the crystal. Since the 79 mm long crystal was contained inside a laser head with small openings on each end to the crystal, it was enough to adjust the inserted mirror until the reflection was directed into the opening of the laser head. Then, a second mirror was inserted at the close end of the crystal and was adjusted until the reflection appeared back on the output coupler of the He-Ne laser. This mirror alignment procedure was critical to tune the laser when an Nd:YAP crystal

was used. When the Nd:YAP crystal was replaced with an LNA crystal, this mirror alignment procedure became less critical, and was used only to obtain optimal performance. This step was often omitted during the experiment when time was valuable.

In the second step, mirrors were adjusted to maximize power at threshold. Each mirror mount had two degrees of freedom in angle orientations. It was found to be most efficient to reduce the tuning procedure to a two dimensional problem by adjusting the mirrors in pairs to iteratively step in one degree of freedom followed by optimization in the second degree of freedom. Following this procedure, laser power at threshold was optimized by adjusting the two mirrors first for only one degree of freedom, and then for the second degree of freedom. Afterwards the first degree of freedom was stepped in one direction followed by an optimization in the second degree of freedom to determine if the first degree of freedom should be stepped in the same direction or the reverse direction depending on whether the laser power had slightly increased or decreased. Once the optimal mirror orientations was found, only a slight adjustments of mirrors was necessary as the laser power was brought to an operational level by by increasing the lamp current slowly in steps between 0.5 Amp to 1 Amp. The laser was usually operated at lamp currents well below its plateau region, and an output power of 4 Watts was more than enough to polarize the ^{3}He gas, ie. ^{3}He polarization of the target saturated at powers above 2 Watts.

In the third step, a 0.5 mm thick solid etalon mounted on a copper support was inserted in the laser cavity to tune to a narrow bandwidth at one of the optical pumping C_k transitions. The etalon was oriented as close as possible to the zero degree incidence by optimizing the laser power. A low Ω resistor heater above the etalon on the support was used to heat the etalon via heat conduction along the support. As the etalon temperature was slowly rising, the copper support, which was mounted on a motor-mike rotation stage was stepped in its tilt angle orientation until tuning cell fluoresence signal was seen. There was usually a large peak called C_5 and two smaller peaks called C_8 and C_9 at larger tilt angles. At this point, the motor mike could be stepped in the reverse direction to find the corresponding fluoresence peaks at etalon tilt angles on opposite side of the zero degree, with the C_5 being at smallest tilt angles in either directions. The temperature was then decreased slowly moving the C_5 peaks toward the zero tilt angle where the C_5 peaks merged into one peak and finally disappeared. The temperature was lowered until the C_8 peaks were close to the zero tilt angle at which point there was little power loss from tilting the etalon. There was no temperature sensor or feedback control

on the etalon heater used in the experiment for rapid stabilization, and therefore temperature changes were made by changing current to the resistor heater in small steps at a time. However, once a stable electrical current setting was found, the laser was further fine tuned to the peak of the C_8 or the C_9 transition with the motor-mike, and the tune was found to be extremely stable for a few hours.

Furthermore, cleanliness of the optics inside the cavity was critical to obtaining optimal power output. Laser power was seen to decrease over days, and careful cleaning of the mirrors and the etalon usually restored the laser output power at the ^{3}He transitions.

3.3.7 The Laser Light Transport

The laser beam at the output coupler was then transported to the glass optical pumping cell using a series of lenses and mirrors. The laser light transport system is shown in figure 3.17. Lenses were anti-reflectivity coated at the 1.06 μm wavelength. There were three beam compressor lenses and one beam expander lenses right above the optical pumping cell. The four mirrors were high-reflective 45° angle mirrors at 1.06 μm wavelength. Still, the beam transport efficiency from the point before the mirror M1 to the point after the Pockel's cell [3.35] was only 80%. The laser power in the beam path was monitored continuously by a thin polished glass disc which reflected about 4% of the laser power at a laser power meter.

The spot size of the laser beam was maintained at $\approx$1 cm diameter along most of the transport path until it was reduced to $\approx$1.5-2 mm for entrance into the Pockel's cell. Immediately after the Pockel's cell, the beam spot size was expanded reaching 5 cm$\times$ 7 cm in elliptical shape at the top of the optical pumping glass cell. The spot size could be made more circular by rotating the etalon to 0° incident angle and adjusting the heat applied to the etalon to maintain the laser tune on C_8 or C_9. Finally, the spot size was adjusted by changing the beam expander to optimize polarization.

It was critical to have the beam to be true along the optics rail in the last section of the transport path in order to obtain optimum laser polarizations for both laser light helicities. Ordinarily with thin $\frac{\lambda}{4}$ wave plates, errors with the laser beam direction could be acceptable up to a few degrees. With the Pockel's cell, a few cm long crystal, used as a $\frac{\lambda}{4}$ wave retarder, a slight angle error from the crystal longitudinal axis caused asymmetric polarizations between the two helicities.

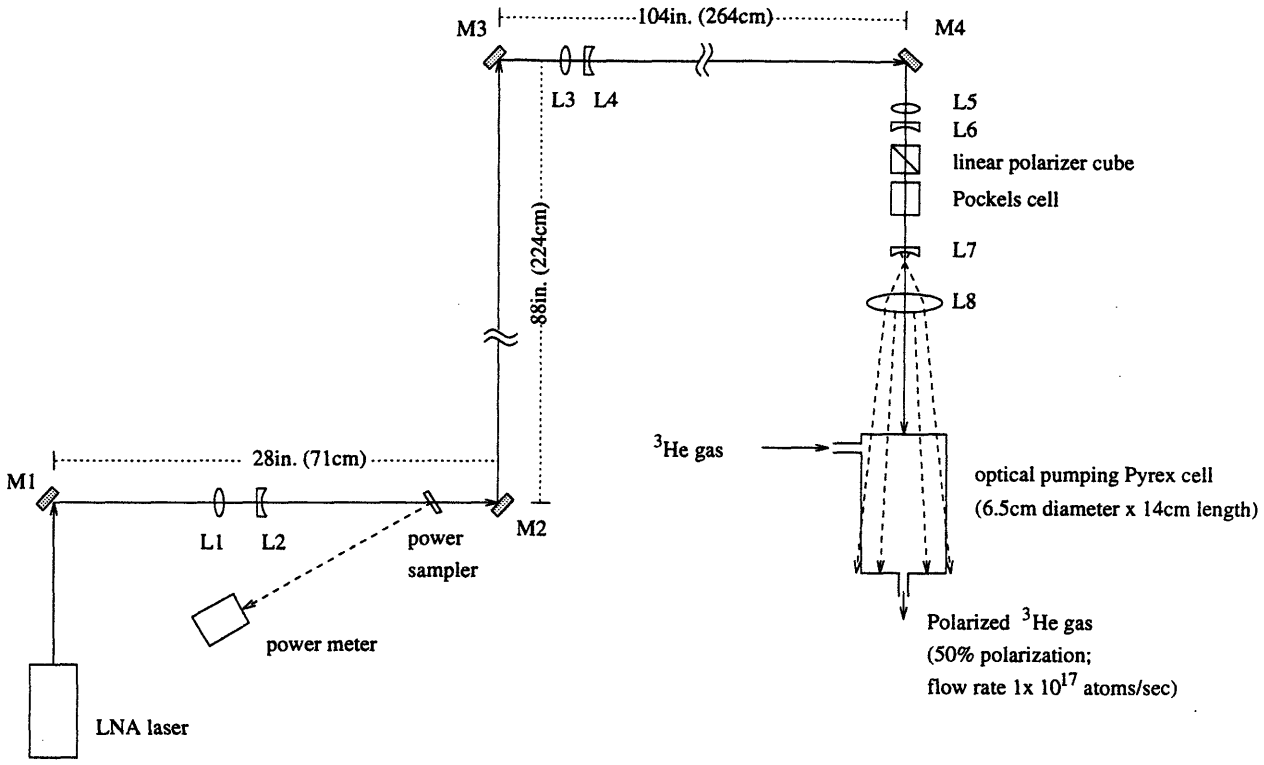

Figure 3.17. The laser beam transport to the target pumping cell.

3.3.7 The ^3He Optical Polarimeter

A polarimeter was mounted on the optics table above the Helmholtz coils as shown in figure 3.9. As discussed in the section on the optical technique to measure the ^{3}He nuclear polarization, the 668 nm $3^1D \rightarrow 2^1P$ discharge line carries a fraction of the nuclear polarization, and the circular polarization of the discharge line was analyzed continuously by the polarimeter.

3.3.7.1 Components and Measurement

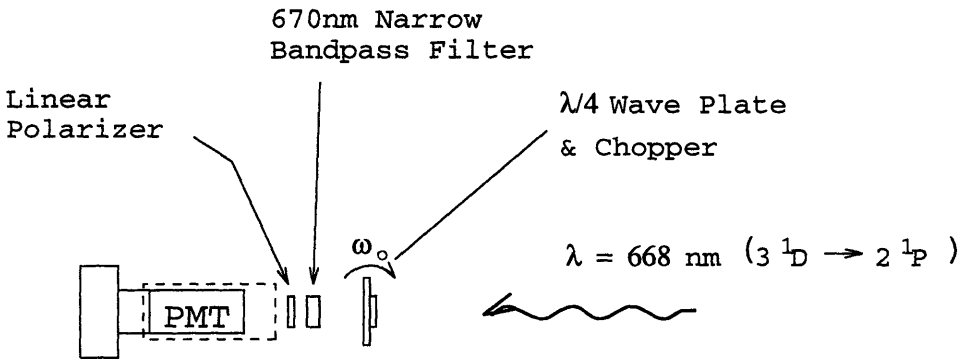

Figure 3.18 Schematic drawing of the nuclear polarization optical polarimeter.

The polarimeter consisted of four principal compenents: an Amperex XP2023B photomultiplier tube (PMT), an ORIEL narrow bandpass filter [3.36], a Polaroid linear polarizer sheet [3.37], and a CVI 1.0" QWPM-667-10-4 $\frac{\lambda}{4}$ wave-plate [3.38] mounted on a rotating tube. The tube rotated at high speed, 20 Hz, on two light duty, thin ball-bearings and was belt driven by a DC motor. See figure 3.18. The rotating tube also had a bi-slotted circular chopper that momentarily allowed passage of light from an infrared light emitting diode (LED) to a sensor, thereby generating electrical pulses at twice the rotation frequency for triggering a lock-in amplifier described below. The 668 nm radiation of nonzero circular polarization, passing through the rotating wave-plate and the linear polarizer, produced a light signal with intensities modulated at twice the rotation frequency, which was converted by the PMT into an electrical signal having a small AC voltage at twice the wave-plate rotation frequency and a constant small negative DC voltage; the ratio of the AC amplitude to the DC value is proportional the polarization of the photons [3.18],

$$P = \frac{V_{AC}}{V_{DC}} \frac{1}{\cos\theta} . \tag{3.25}$$

The high voltage applied on the PMT between its photo-cathode and anode was typically negative 1.0-1.2 kV. The PMT signal was then input into an EG&G 5290 lock-in amplifier to amplify the small AC component oscillating at twice the wave-plate rotation frequency and into a DC amplifier constructed by the LNS electronic facility to amplify the DC component. The lock-in amplifier was triggered by a TTL signal which was converted from the pulsed signal generated by the infrared LED switch. The lock-in amplifier served to detect the small AC component of the modulating signal and suppress all signals not at the modulating frequency.

The ouput PMT signal had a DC level of negative 100 mV and an AC signal of 5 mV. There were four types of noise in the output signal. The white noise (<1 mV) inherent in the PMT, the RF Noise ($\approx$1-2 mV) due to the RF discharge of the ^{3}He gas, and the ambient electromagnetic noise ($\approx$1 mV) at 60 Hz were all easily suppressed by the lock-in amplification technique. The fourth type of noise, at or close to the modulation frequency, contributed to the lock-in output as an offset. Although it could be subtracted, this noise offset was found to be dependent on the magnetic field direction. The noise was a few μV and its shape and phase with respect to the trigger signal changed slightly when the field direction was changed, resulting in a difference of 2% nuclear polarization between field directions. The effect was seen to be relatively constant from a few to 30 Gauss (3 mT) of field in the center of the Helmholtz coils pair. A secondary layer of magnetic mu-metal sheets, electrically insulated from the primary layer, was wrapped around the PMT, together with additional sheets placed at the front of the PMT. This reduced the magnetic field strength inside the polarimeter such that the effect only decreased from 2% to 1.8%.

3.3.7.2 Calibration of the Polarimeter

Components critical to the polarization measurement were the DC amplifier, the lockin amplifier, and the optics of the polarimeter. The DC amplifier was checked for its linearity for a range of voltages and for the 10$\times$ gain setting. The DC amplifier was checked several times over the course two years, and the gain and linearity remained unchanged. The data shown in figure 3.19were taken before the experiment. The slope of a linear fit to the data was used to correct for any difference from the nominal gain of the DC amplifier, and the correction was implemented in the target data acquisition software as an input parameter.

Similarly, the lockin amplifier was checked for linearity for a range input sinusoidal signal voltages at $\sim$ 40 Hz and for three different voltage scale settings. The

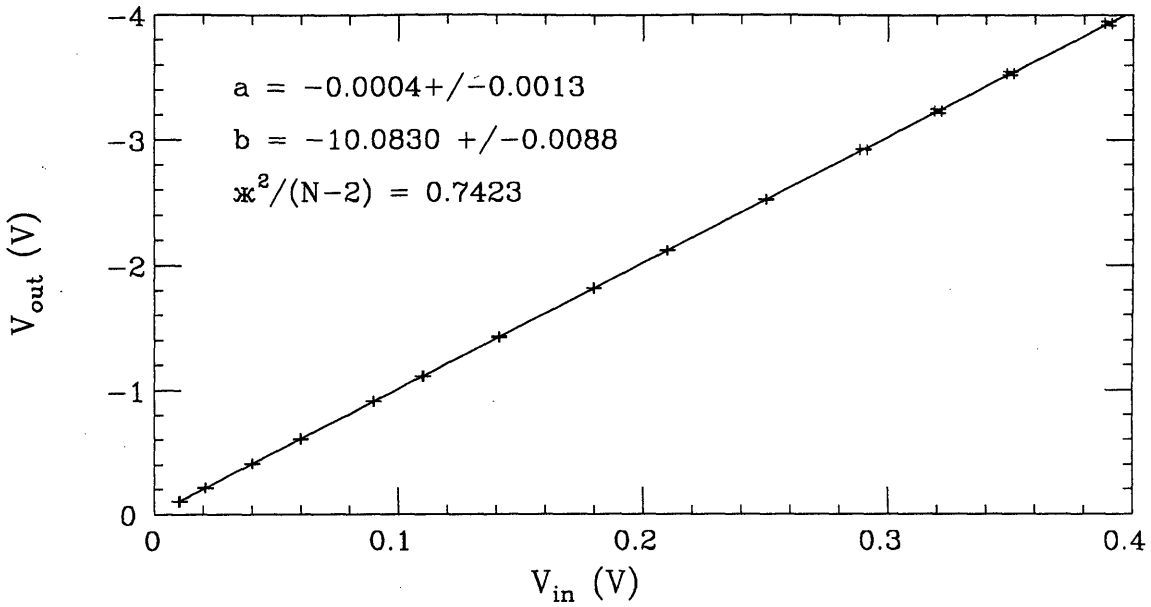

Figure 3.19. Calibration of the DC amplifier.

input sinusoidal signal was generated by a Phillips PM 5191 function generator and was fed into the amplifier through a variable voltage divider. The input signal at the lockin amplifier was measured using a Tektronix oscilloscope. The lockin amplifier output value was found to have the specified gain for the 100 mV scale setting and a deviation of 1% larger than the specified gain for the lockin scales 10 mV and 3 mV as shown in figure 3.20. The voltage values in the figure are shown as peak-to-peak values of the sinusoidal signal.

Lastly, the optics in the polarimeter was checked. This included the rotating CVI $\frac{\lambda}{4}$ multiple order wave plate at 667 nm wavelength, the ORIEL 690 nm narrow band pass filter, and the Polaroid linear polarizer sheet in the polarimeter optics.

First, the polarization attenuation of the linear polarizer sheet was determined to be $\epsilon^2 = 0.0102 \pm 0.0022$. In place of the rotating $\frac{\lambda}{4}$ wave plate, a similar size linear polarizer sheet was used. The rotating linear polarizer produced a sinusoidal light signal that gave approximately 100% "polarization" upon illumination of the ^{3}He discharge light. The narrow band-pass filter allowed only the 668 nm wavelength of the discharge light to be detected at the PMT (*see section* 3.3.7). Furthermore, the "polarization" can be related to the linear polarizer sheet attenuation coefficient ϵ of linearly polarized light as, assuming the coefficient to be same for both sheets in

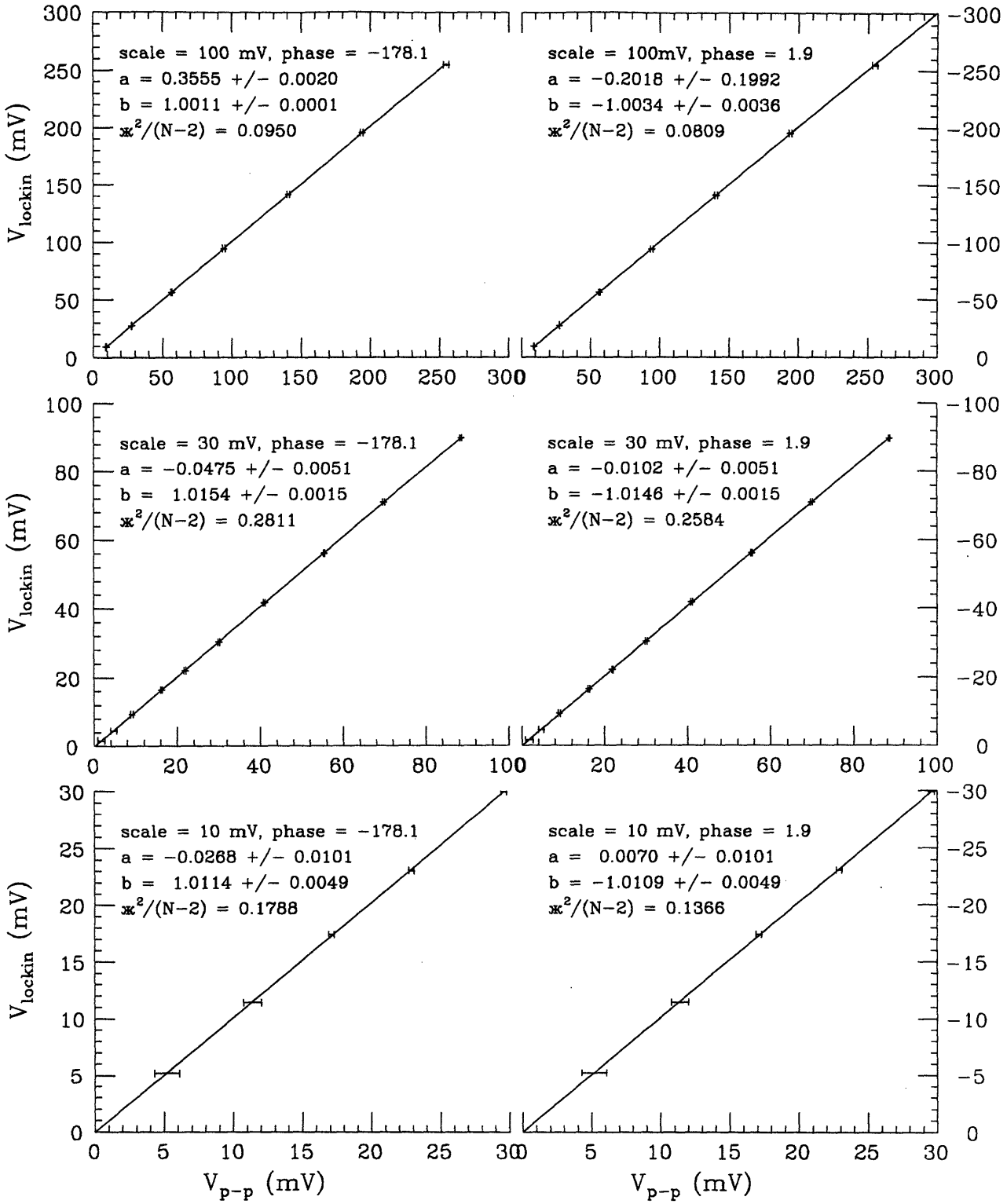

Figure 3.20. Calibration of the lockin amplifier with a sinusoidal sigal.

the setup,

$$\left(\frac{1 - \epsilon^2}{1 + \epsilon^2}\right)^2 = P_{l.p.}\ , \tag{3.27}$$

where $P_{l.p.}$ was the measured "polarization". Figure 3.21 shows the $V_{p-p}/2$ of the polarimeter signal measured with the lockin amplifier (used a digital voltmeter to measure its analog output) as a function of the its DC level measured via the DC amplifier with the same digital voltmeter. The DC amplifier was set to the 10× gain. The $V_{p-p}/2$ value and the DC level had been corrected for the deviation from specified gain of corresponding amplifier. The slopes of the linear fit to the two data sets in the figure were the measured "polarizations" for two 180° opposite phase angle settings of the lockin amplifier. The phase angle setting was adjusted to minimize to zero output at the two 180° opposite phase angle settings that were 90° apart from the former two phase angle settings. The average result of the two measurements was determined to be 96.0 ± 0.9% which was used to obtain the coefficient ϵ^2.

Under the illumination of a known 100% circularly polarized light, the measured polarization must also be 100%. After accounting for calibrations of the DC amplifier, the lockin amplifier, and the linear polarizer finite value attenuation coefficient for one linear polarization direction, a deviation from 100% polarization would be attributed to the $\frac{\lambda}{4}$ wave plate and the band pass filter in the polarimeter analyzer optics. It was assumed that the filter meet the design specification as narrow band pass filter. To check the $\frac{\lambda}{4}$ wave plate, a Polaroid circular polarizer sheet was placed between the discharge light source and the polarimeter. When a 100% circularly polarized light source was not available such as with using a circular polarizer plastic sheet, the response of the polarimeter could not simply be determined from one measurement. It was necessary to make numerous measurements with the polarizer sheet at different angles rotated along the optics axis, from which the polarization of the light and the retarding phase of the polarimeter $\frac{\lambda}{4}$ wave plate were determined. The response of the polarimeter system using a lock-in amplifier was given as, similar to that in the reference Lorenzon *et al.* [3.18],

$$P_m = \frac{\left(\frac{1-\epsilon^2}{1+\epsilon^2}\right) P_c \sin\phi_r}{1 + P_l\left(\frac{2\epsilon^2}{1+\epsilon^2} + \frac{1-\epsilon^2}{1+\epsilon^2}\cos^2\frac{\phi_r}{2}\right)\cos 2\alpha}\ , \tag{3.26}$$

where P_c and P_l are respectively the circular and the linear polarization of the light source, ϕ_r the retardation angle of the $\frac{\lambda}{4}$ wave plate in the analyzer optics, ϵ^2 the

attenuation of light in one linear polarization direction, and α the rotation angle of the optics axis of the circular polarizer sheet with respect to the polarimeter.

The polarization response equation gave values from below to above the 100% value as a function of the rotation angle α for an elliptically polarized light. The response equation turned out to be sensitive to the polarization of the light and not very sensitive to the the analyzer optics in the polarimeter. It is therefore, suggested in the reference [3.18] to use two stock identical sets of a $\frac{\lambda}{4}$ wave plate and a linear polarizer one for the construction of a good circular polarizer and the other for the polarimeter analyzer. However, calibration data using plastic sheet circular polarizers were taken right after the experiment and a year later, and the importance of having two good identical optics sets was not realized then. Furthermore, a number of attempts to construct a 100% circular polarizer using one of the $\frac{\lambda}{4}$ wave plate and a CVI broadband linear polarizer BBLPG10-57 were not successful. The constructed polarizer appeared to perform similarly to a platic circular polarizer sheet.

Here, the last set of data taken with a plastic sheet circular polarizer is discussed. In order to facilitate the discussion, the response equation is rewritten in the form used for fitting the data,

$$P_m = \frac{c_1}{1 + c_2 \cos(2\alpha + c_3)}, \tag{3.27}$$

where c_i's are the fit parameters given in table 3.7 below.

Quantity	phase(-47.6)	phase(132.4)
c_1	-0.9502 $\pm$ 0.0005	0.9514 $\pm$ 0.0004
c_2	-0.0990 $\pm$ 0.0007	-0.0990 $\pm$ 0.0006
c_3	-35.02 $\pm$ 0.36	-34.70 $\pm$ 0.30

Table 3.7. Fit parameters of the polarization response function in equation (3.27) to data for lockin phase settings at $-47.6°$ and $132.4°$.

Identifying the parameters c_1 and c_2 with the quantities in the expression in equation (3.26), two nonlinear equations were found, from which the polarization of the light source and the retarding phase angle of the $\frac{\lambda}{4}$ wave plate were determined. Figure 3.21 shows a fit of equation (3.26) to the polarization data as a function of the rotation angle. There is an increase in polarization around 200° for both phase settings, which did not show up in earlier data. From the parameters obtained, two

solutions were found to the nonlinear equations and are summarized in the table below. Finally, under illumination of a 100% circularly polarized light, the measured polarization was estimated using equation (3.26) to be 96.49±0.67% (97.33±0.55%) corresponding to the $\frac{\lambda}{4}$ wave plate retarding angle ϕ_r 80.0±1.7 deg (96.6±1.7 deg).

Soln	Parameters	phase(-47.6°)	phase(132.4°)
1st	P_l	0.166 ± 0.003	0.166 ± 0.003
	P_c	0.986 ± 0.0005	0.986 ± 0.0005
	ϕ_r	80.0 ± 1.7 deg	80.0 ± 1.9 deg
2nd	P_l	0.218 ± 0.006	0.216 ± 0.008
	P_c	0.976 ± 0.0013	0.976 ± 0.0018
	ϕ_r	96.6 ± 1.7 deg	96.1 ± 1.8 deg

Table 3.8. Polarizations P_l and P_r of the light after the circular polarizer sheet and the retarding phase ϕ_r of the $\frac{\lambda}{4}$ wave plate in the polarimeter.

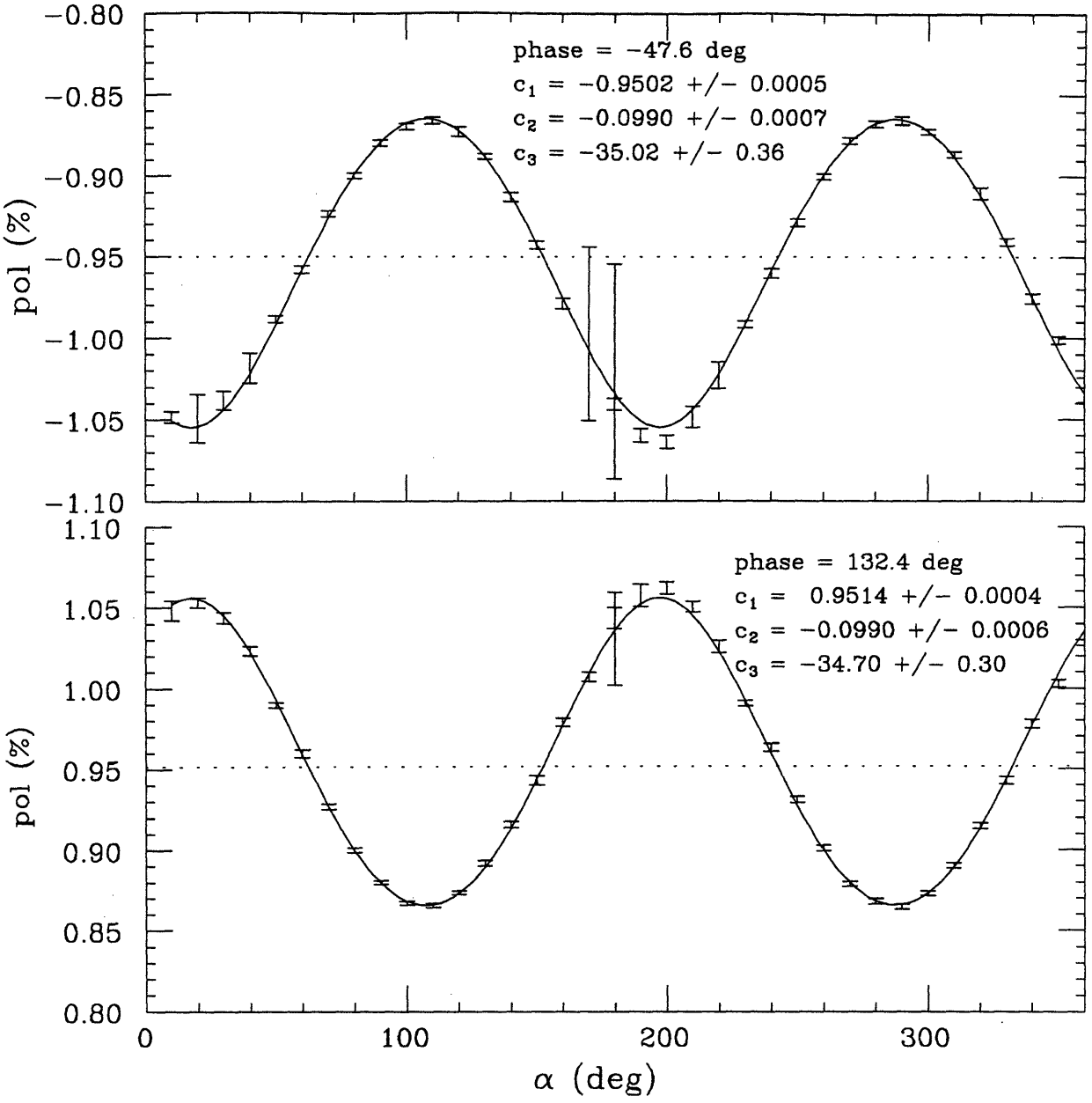

Figure 3.21. Measured light polarization *vs.* orientation angle α of the circular polarizer sheet.

3.3.8 Target Electronics and Data Acquisition System

The target was controlled and its status and target polarization were monitored via a CAMAC crate interfaced with a micro-VAX computer. An ORTEC EG&G lock-in amplifier, a DC amplifier, and two ADC's were used to monitor the discharge light polarization of the ^{3}He gas in the target glass cell. These were the primary components of the data acquisition system and have been in use from its predecessor polarized ^{3}He external cryogenic gas target constructed at Caltech. The data acquisition system for the MIT internal gas target was similarly developed during the prototype period. For the CE-25 experiment, new features were added to the target data acquisition system. Two important additions were the capability to flip periodically the target polarization and to set and monitor remotely the input gas pressure to the target glass cell from the micro-VAX computer. A low voltage level was sent from the CAMAC crate to set the Pockel's cell bipolar high voltage controller of Fastpulse Technology, model 8403 [3.39]. The polarity and magnitude of the applied high voltage to the Pockel's cell determined the helicity and the circular polarization of the optical pumping light. In the experiment, the target polarization was flipped by only reversing the helicity of the light periodically. The input gas pressure was regulated by a Balzers UDV 135 leak valve and its controller with feedback of the input gas pressure from a Baratron. The pressure set point of the controller was remotely fixed also with a low voltage level via the CAMAC crate. The gas pressure was maintained around set point values but had a 2.5% fluctuation throughout the course of the experiment. Thus, it was important to be able to monitor the gas pressure continuously for realtime calculation of the target nuclear polarization. Other additions were the nulling of the ^{3}He polarization, the shuttering of the laser, the flipping and monitoring of the target holding B field, and the monitoring of the laser power, target chamber vacuum gauge readings, ambient temperature, and settings on various electronics devices. Although there were important and new features added to the data acquisition system, there were also a number of devices operated remotely at the hardware level such as the laser and its power supply. The remote capabilities of the target electronics and data acquisition system were important to the quality of the target operation during the experiment.

3.4 Depolarization Mechanisms

We consider four potential sources for depolarization of the ^{3}He target atoms in nuclear physics experiment. They are: molecular impurities, field gradients, container surface, and ions created by the passage of the charged particle beam.

3.4.1 Molecular Impurities

A small trace of molecular impurity can decrease the lifetime of the metastable atom polarization in the ^{3}He discharge gas, limiting the polarization and pump up rate. The criteria for allowed level of impurity is that the spin-lattice relaxation time of the metastable atoms ($\sim 10^{-4}$ sec) must not be appreciably shortened by collision with impurities [3.3] (*see table* 3.9). In practice, ^{3}He gas vessels were cleaned until the discharge was spectroscopically pure, *i.e.* there were only six distinct lines visible through a spectroscope. The relaxation rate by impurities is given by

$$\frac{1}{\tau_r} >> \sigma_i \bar{v} n \ , \tag{3.28}$$

where σ_i is $\approx 10^{-14}$ cm^2 [3.3] for collision by impurities, $\bar{v} = 2.06 \times 10^5$ cm/sec [3.15] the relative thermal speed, and n_i the impurity gas density. It is likely that the contamination fo the gas in the pumping cell is the limiting factor in the polarization.

τ_{m-i} (msec)	n (atoms/cm^3)	ppm
0.0100	5×10^{10}	1.51
0.0010	5×10^{11}	15.1
0.0001	5×10^{12}	151

Table 3.9. Spin-lattice relaxation times due to collisions with impurity at different contamination levels.

3.4.2 Magnetic Field Gradients

The ^{3}He nuclear spin precesses around the holding magnetic field with the Larmor frequency ω_o. If there were an oscillating magnetic field in the transverse direction with frequency ω_o, the precession motion of the atom's spin is changed to the precession motion plus a precession around the transverse field direction resulting in the reversal of the atom's spin if the oscillating field can be turned on for a short enough time. In the presence of magnetic holding field, the atom's spin

reverses indefinitely, resulting in depolarization of the polarized ^{3}He gas. If the holding field and the oscillating field were perfectly uniform, the polarization of the gas would reverse indefinitely. However, any small gradients in the holding or the oscillating field would cause a phase difference in the precession at different regions in the gas volume. Combined with the fast diffusion of the atoms in the gas, the polarization would be zeroed in a very short time ($\sim\mu$sec).

When there is a gradient in the magnetic holding field, the ^{3}He atom in its rest frame sees an oscillating field as it moves in a Brownian motion. The oscillating field has directions along the direction of the gradient and a distribution in frequency. At or near the Larmor frequency, the random oscillation causes, as discussed above, the reversal of the atom's spin. In a gas sample, each atom sees an oscillating field that is not correlated to each other in phase and strength of the field. This is sufficient to cause the atom spins to go out of phase with each other resulting in zero polarization. The time constant of spin-lattice depolarization of the ^{3}He gas in a vessel has been formulated as [1.7,3.40]

$$\frac{1}{\tau} = \frac{2}{3}\frac{|\Delta \mathbf{B}_t|^2}{|\mathbf{B}_l|^2}\langle v^2\rangle \frac{\tau_c}{\omega_o^2\tau_c^2+1}, \tag{3.28}$$

where $\omega_o = 3.24|\mathbf{B}_l|$ kHz and $\tau_c = (2.2\pm0.2)\times10^{-7}\cdot p^{-1}$ sec with p in [Torr] [3.41]. Note that the holding field strength can be increased while keeping the transverse field gradient constant to increase the time constant. Also, if the gas pressure is increased, thus decreasing the mean free path, or if the gas temperature is lowered, thus reducing the collision rate of Brownian motion, the time constant becomes longer.

3.4.3 Surface Depolarization

As introduced in chapter 1, because the ^{3}He atom has a closed electron shell, the polarized atom does not depolarize with high probability from collisions with vessel surfaces. Although the nuclear spin does not have direct contact on each collision, it can become coupled to the local magnetic field of surface atoms as it is adsorbed to the surface for a short time on each bounce. At high temperature, gas atoms are absorbed onto surfaces by permeation while at low temperature, gas atoms are adsorbed by chemical potentials. The relaxation time for Pyrex at room temperature has been determined to be 10^4 sec [3.42], long compared to relaxation from field gradients. Morever, the choice of the vessel surfaces and coatings applied has proven to be an effective way to lower the adsorption chemical potential at low temperature [1.7].

The surface materials that have been used widely now for making polarized ^{3}He gas targets are: Pyrex glass, Aluminum, copper, and Mylar. Any nonmagnetic material is expected to be a good candidate for specific applications as long as it does not introduce too much contaminants into the gas. Aluminum and copper are used for their high thermal conductivity in cryogenic targets [3.1,3.43].

3.4.4 Storage Target Cell Depolarization

The degree of depolarization can be estimated from the mean residence time and the number of bounces off surfaces in the capillary tube and storage cell. First, the decay time in a clean glass cell is dominated by depolaration due to the field gradient mechanism, typically 400 sec measured with a $\sim$ 80 cc sealed glass cell. In contrast to the 400 sec, the atom residence times on average in the capillary tube and the storage cell are respectively, equation (3.13),

$$\begin{aligned}
\frac{\text{no. of atoms}_{\text{capillary}}}{\text{flowrate}} &= \frac{0.5\ [\text{Torr}] \cdot 1.0 \cdot \pi \cdot 0.1^2/4\ [\text{cm}^3]}{1.2 \times 10^{17}\ [\text{atoms/sec}]}\ 3.22 \times 10^{16}\ [\frac{\text{atoms}}{\text{Torr cm}}] \\
&= \frac{6 \times 10^{13}\ [\text{atoms}]}{1.2 \times 10^{17}\ [\text{atoms/sec}]} \\
&= 0.5\ [\text{msec}]
\end{aligned}$$

and

$$\begin{aligned}
\frac{\text{no. of atoms}_{\text{cell}}}{\text{flowrate}} &= \frac{1.4 \times 10^{15}\ [\text{atoms cm}^{-2}]}{1.2 \times 10^{17}\ [\text{atoms/sec}]}\ 1.2 \times 1.4\ [\text{cm}^2] \\
&= \frac{1.7 \times 10^{15}\ [\text{atoms}]}{1.2 \times 10^{17}\ [\text{atoms/sec}]} \\
&= 14\ [\text{msec}]\ .
\end{aligned} \tag{3.30}$$

Therefore, any depolarization due to the field gradient mechanism is negligibly small. However, when there is a gradient in the magnetic field, particularly when the holding field direction varies along the cell, the effective polarization of the gas is lowered as the field direction is followed by the spin of the ^{3}He atoms. If there is a deviation of 5° from the vertical, the polarization is reduced by a fractional amount of 0.4%.

Secondly, once the atoms are in the storage cell, they can be depolarized with some probability on each bounce off the Aluminum cell surface. In the following, the "probability of depolarization" on each bounce and the average number of bounces per atom in the storage target cell are estimated. The first quantity can be estimated from the Caltech double cell target assuming that the depolarization

effect by copper surfaces is similar to that of Aluminum. It was known that when the copper cryogenic cell was not coated properly with N_2 gas, the relaxation time was short. Assuming that it was 100 sec long, the probability of depolarization per bounce can be estimated as

$$\begin{aligned}
\text{depolarization prob/bounce} &= \frac{\text{polarization decay rate}}{\text{surface flux}} \\
&= \left[\frac{\int \sqrt{kT/2\pi m_{^3He}}\rho dA\ \tau}{\int \rho dV}\right]^{-1} \\
&= \left[\frac{6.62\times10^3\ [\text{cm/sec}]\cdot 170\ [\text{cm}^2]\cdot 100\ [\text{sec}]}{100\ [\text{cm}^3]}\right]^{-1} \\
&= 8.9\times10^{-7}\ .
\end{aligned} \tag{3.31}$$

Next, the average number of bounces per atom in the storage target cell can be estimated as, extending the concept in equation (3.13),

$$\begin{aligned}
\text{no. of bounces/atom} &= \frac{\text{surface flux}}{\text{total no. of atoms}} \\
&= \frac{\int \sqrt{kT/2\pi m_{^3He}}\rho dA}{\text{flowrate}} \\
&= \left[\frac{3.6\times10^4\ [\text{cm/sec}]\cdot 3.5\times10^{13}\ [\text{atoms/cm}]\cdot 96\ [\text{cm}^2]}{1.2\times10^{17}\ [\text{atoms/sec}]}\right] \\
&= 1.0\times10^3\ .
\end{aligned} \tag{3.32}$$

The number of bounces per atom can be multiplied with the probability per bounce to obtain the "fractional depolarization" in the storage cell,

$$\begin{aligned}
\text{prob} &= 1-\exp\left[-(\text{no. of bounces/atom})\ (\text{depol. prob/bounce})\right] \\
&= 1-\exp\left[-(1.0\times10^3)\ (8.9\times10^{-7})\right] \\
&\approx 1\times10^{-3}\ .
\end{aligned} \tag{3.33}$$

The estimate shows that the polarized ^{3}He gas can lose its fractional polariztion by about 0.1% at the two ends and a negligible drop in polarization from the pumping cell value on average over the whole length of the storage cell.

3.4.5 Beam Depolarization

^{3}He atoms may be depolarized also by the beam from magnetic field and ionization of the beam. The magnetic field from the beam can be estimated using the expression

$$\mathbf{B} = \mu_\circ \cdot 10^6 \frac{\mathrm{I}}{2\pi \mathrm{r}} , \tag{3.34}$$

where I is in Amps, r the distance from the beam center in cm and B in Gauss. Assume that the beam has a Gaussian distribution radially with its σ = 1 mm. Then, the maximum B field generated is only 0.1 mGauss, and the gradients over the widths of the target cell becomes 0.2 mGauss/cm. In the holding field of 10 Gauss, equation (3.28) gives the longitudinal relaxation time T_1 = 25,000 sec. Therefore, any field gradient due to the 100 μA beam current is much too small to cause the atoms in the target cell to depolarize, and the depolarization effects due to the beam magnetic field are negligible.

In contrast, at close range from beam protons the ^{3}He atoms become ionized. The rate of ionization is given by the rate of average energy loss of the beam protons traversing the gas target

$$\mathrm{R} = \frac{3.13 \times 10^{-11}[\text{g atoms}]}{\mathrm{I_p}} \mathrm{I_{beam} s_{target}} \frac{\mathrm{dE}}{\overline{\rho}_{\mathrm{target}} \mathrm{dx}} , \tag{3.34}$$

where I_p, the ^{4}He singly charged ionization potential, is 24.6×10^{-6} MeV, I_{beam} the beam current in [μA], s_{target} the target thickness in [atoms/cm^2], and $dE/\overline{\rho}_{target}dx$ the stopping power in [MeV/g cm^{-2}]. It is assumed here that all the energy loss contributes to the formation of singly charged atomic ions. At 200 MeV proton beam energy, dE/overlineρ_{target}dx is 5.7 MeV/g cm^{-2} for ^{3}He [3.44]. Then the rate of ionization is 1.0×10^{12} ions/sec. Assuming that each ionized atom becomes completely depolarized, the "fractional depolarization" can be estimated as

$$\begin{aligned} \text{prob} &= \frac{\text{ionizationrate}}{\text{flowrate}} \\ &= \frac{1.0 \times 10^{12} \text{ [ions/sec]}}{1.2 \times 10^{17} \text{ [atoms/sec]}} \approx 10^{-5} , \end{aligned} \tag{3.35}$$

showing that the estimated fractional loss of the polarization is negligibly small from beam ionization of the ultra thin target gas.

In an ultra thin target gas where the target density is $\sim 10^{13}$ atoms/cm^3, the mean free path is limited by the dimensions of the target cell. In a thicker target gas, the ionization rate becomes higher. In contrast, when the mean free path is

small compared to the dimensions of the target cell where the target density is $> 10^{15}$ atoms/cm^3, the atomic ions have a significant probability to undergo three body collision forming diatomic ions [3.45]. Collision of the atoms with the diatomic ions constitue the dominant source of depolarization where it is assumed that upon collision the atom becomes completely unpolarized. This mechanism does not exist in the ultra thin internal gas target while it is the dominant source of beam depolarization in the thicker external gas target. Note also that depolarization from two body collision in the internal gas target is negligible for the same reason. Finally, the negligible depolarization from the mechanisms considered above is consistent with the null evidence for depolarization in the storage cell from the nuclear scattering asymmetry result at 45 MeV (*see section* 6.2).

3.5 Target Operation and Performance

When the entire target apparatus was assembled together, the gas manifold and the glass system were pumped out by opening an electro-pneumatic valve on the feedline to an Alcatel 100 liter/sec turbo molecular pump. For pump out, the feedline and the glass system were heated to slightly above 100° C with the exception of all the valves. Initially, the base vacuum rose to 10^{-5} Torr indicating outgassing of mainly water from the inner surfaces. The baking was maintained for three to four days until the base vacuum improved to low 10^{-6} Torr. At this point, the base vacuum could reach low 10^{-8} Torr near the Alcatel pump when the gas system was allowed to cool down to room temperature.

After the system was allowed to cool back to lower temperature, usually high power RF discharge cleaning was applied on the target glass cell for two to six more hours while flowing ^{3}He gas at approximately 1×10^{16} atoms/sec or less. In the initial minute, it was normal to observe a violet hue in the discharge, presumably from discharge of the hydrogen gas outgassing from surfaces. After a few minutes, the gas flow was usually interrupted to pump out the glass cell and was resumed again repeating for several cycles. In the second cycle, the discharge usually appeared to have less violet hue. After a few cycles, the discharge already turned to bluish-white. At this point, the discharge was spectroscopically pure, having only six distinct bright lines as visible in a small hand-held spectroscope.

After allowing the system cooled back to room temperature, the base vacuum was normally in the low 10^{-8} Torr. However, due to finite conductances in the gas system, the vacuum at the glass cell was estimated to be $\approx 10^{-6}$ Torr. Compared to the estimates of allowable impurity density given in table 3.9, the 10^{-6} Torr (3×10^{10} atoms/cm^3) was two orders of magnitude less. These estimates can only regarded with a grain of salt as no systematic understanding exists of the effects of impurity types and levels on metastability exchange optical pumping.

For accurate monitoring of the discharge polarization, it was important to have the polarimeter see only light from a direct line of sight. Reflected light from metal surfaces would usually decrease the measured polarization of 668 nm discharge line. Therefore, the cylindrical glass cell was wrapped carefully around on the side with black electrical tapes to allow only the discharge radiation to exit at the top. The surrounding metal surfaces were also covered to minimize light reflection. Furthermore, the target area was generally shaded to minimize background light at the same wave length.

Four cell length long and $\approx$1 cm wide aluminum or copper electrodes were taped

on the outside of the 7 cm diameter × 13 cm long cylindrical glass cell to achieve a uniform discharge of the ^{3}He gas. From 0.1 to 1 Torr pressure, the discharge was seen to be fairly uniform. In tests using a larger size sealed ^{3}He Pyrex cell, it was found that the polarization and pumping rate were higher when four evenly placed electrodes were used instead of two.

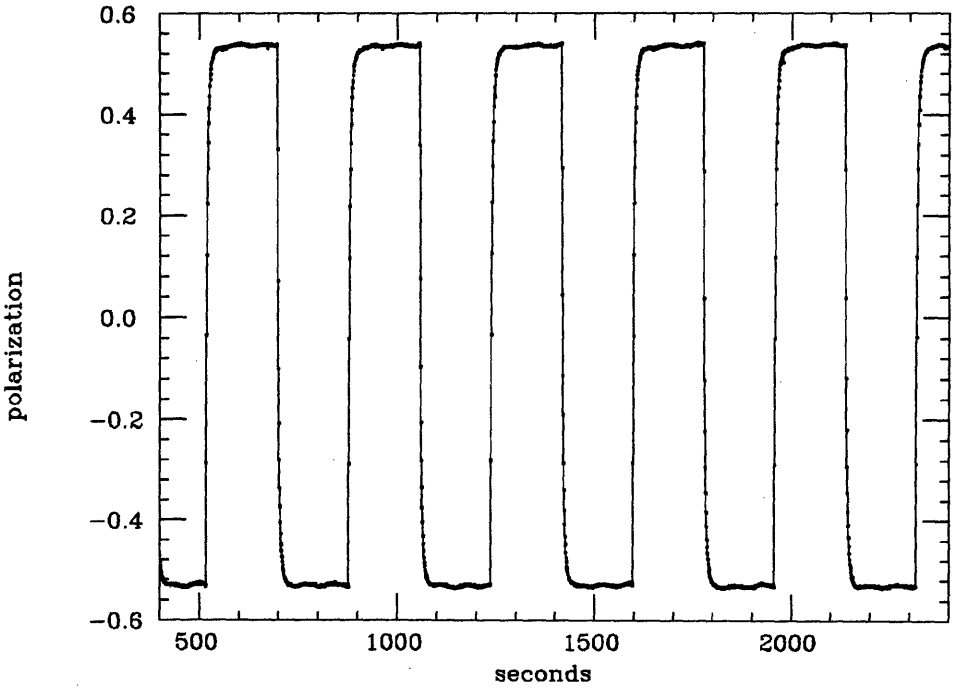

Figure 3.22. Target polarization as a function of time, flipped every 180 sec.

The target operation was marked by stability and reproducibility during each of the series of CE-25 experimental runs. The simple gas flow system was trouble free, and gas was switched from the ^{3}He gas to the ^{2}H gas for detector system calibration whenever beam energy was changed and back to ^{3}He gas for data production. Typically, the target polarization was flipped every 180 sec as shown in figure 3.22. The LNA laser system maintained output powers greater than 3 Watts at the C_8 or the C_9 transition with only a steady decrease from 4 to 3 Watt over the period of two to three days. Correspondingly, the target polarization decreased slowly from 55% to 45%.[1]

[1] To our dismay before the first test measurement, we saw a huge background noise in the silicon detector signals due to the laser light leaking into the target chamber via the exit capillary of glass pumping cell. Putting a penny on the top center of the glass cell reduced the noise and also the polarization. A penny was replaced with a smaller diameter aluminum collimator in later measurements.

Chapter 4

Description of The Experiment

4.1 Overview

The experiment measured the analyzing powers of the spin dependent cross-section for both $^3\overrightarrow{He}(\overrightarrow{p},2p)$ and $^3\overrightarrow{He}(\overrightarrow{p},pn)$ quasielastic scattering over a large kinematic range. In the framework of plane wave impulse approximation in figure 4.1, the experiment probed the spin-dependent momentum distribution of the nucleons in the ground state of ^{3}He. The incident proton with a momentum $\mathbf{p}_{inc}$ knocks out a nucleon having an initial momentum $\mathbf{p}_0$ without involving the remaining nucleons which recoil as a spectator system with momentum $\mathbf{p}_{A-1}$. In the final state the spectator system can either be a bound particle as in 2-body breakup or two individual nucleons as in 3-body breakup.

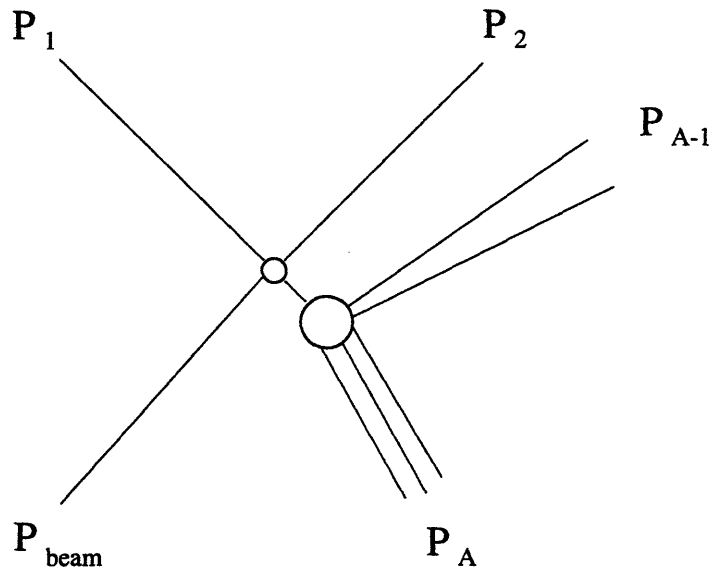

Figure 4.1. Quasielastic nucleon knockout by an incident proton with momentum $\mathbf{p}_{inc}$ resulting in the outgoing nucleons with momenta $\mathbf{p}_1$ and $\mathbf{p}_2$ and the recoilings systemt with momentum $\mathbf{p}_{A-1}$.

The experiment was carried out at the IUCF cooler storage ring using a high duty factor and high intensity polarized proton beam, and the polarized ^{3}He internal gas target described in chapter 3. Two large acceptance nonmagnetic detector

arms were employed one on each side of the beam for coincidence measurements over a range of angles from 36° to 67° on the left and from 21° to 47° on the right. The asymmetric configuration was chosen to optimize the angular range with available detectors covering a much larger kinematic range than the previous TRIUMF experiments [1.29, 1.31]. Data were taken at three incident proton energies: 197, 300 and 414 MeV to look for beam energy dependence of the analyzing powers. Each detector arm consisted of one thin plastic scintillators, wire chambers, and six large position-sensitive scintillator bars to reconstruct the trajectory and momenta of detected particles from the wire chambers and the scintillator bars and from time-of-flight information, respectively. See the layout of the experiment in figure 4.2. The detectors also triggered on scattered deuterons and pions thus allowing detection of various other reactions.

Because the target was ultra-thin, low energy recoil particles, *e.g.* sub-MeV ^{3}He, could exit the target with sufficient energy to be detected. Such particles were detected by large area silicon detectors located near the target. In this way ^{3}He(p,p^{3}He) elastic scattering was measured. Moreover, these detectors also allowed a separation of ^{3}He(p,2p)pn and ^{3}He(p,2p)d final states by detecting slow recoiling deuterons.

The data production runs with the above configuration were realized only in the last months of 1992 and the early months of 1993. The 197 MeV data reported here were recorded in March of 1993. Preceding the data production runs were many test runs during which the Cooler beam development was carried out to obtain high stored beam currents and polarizations; beam currents ranged only from 10 to 30 μA initially and were greatly improved to maximum beam currents over 100 μA. In the final production phase of the experiment, the data taking rate was limited by the data acquisition system. Prior to the quasielastic experiment, measurements of the target asymmetry in elastic scattering at 45 MeV were taken in April of 1992.

4.2 Polarized Proton Beam in the IUCF Cooler Ring

Storage rings offer a new precision tool for nuclear physics and recently, several of these rings have come into operation, such as the Bates South Hall Ring, the Nikhef Amps Ring, and the IUCF Cooler Ring. The Cooler ring successively stored its first beam for a full turn in October of 1987 and for a few seconds in early 1988 [4.1]. The storage rings at the facilities mentioned above make use of existing low duty cycle accelerators to produce beams of high duty cycle, high beam current, and good energy resolution. Macroscopic structures of the injected μsec beam

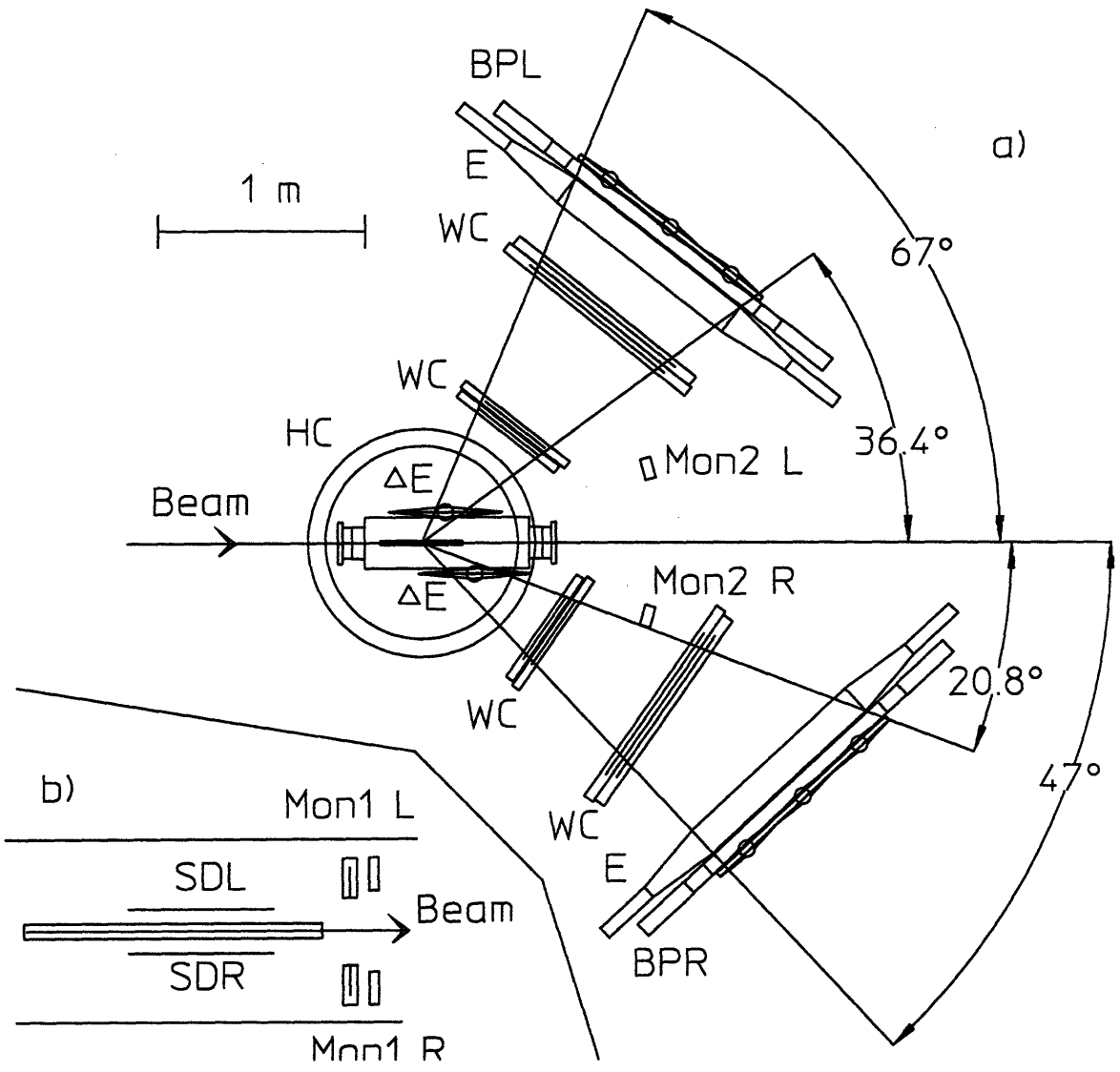

Figure 4.2. (a) A schematic layout of the experiment. In each detector arm, there are the start ΔE scintillator, two pairs of wire chamber planes labelled WC, stack of scintillator bars labelled E, and two layers of backing scintillators BPL(R). The external luminosity monitors are labelled Mon2L(R). (b) An expanded view of the target region. The target cell has 3 large area silicon detectors labeled SDL/SDR on each side for recoil detection. A silicon detector and plastic scintillator labeled Mon1 are placed just downstream of the target on each side and used for luminosity monitoring.

pulses from a low duty cyle machine are removed once stored in the ring with circumferences of about 100 m creating an almost continuous beam. Beam can be accumulated over a short time with repeated injection of the beam pulses and cooling of stored beam to give high stored beam currents. From a knowledge of the storage ring circumference and storage radio frequency, beam energies are known to very high precision, *e.g.* a few hundred keV. At IUCF, developments have been carried out to store beams with high polarizations in different directions, beams of different light ions, and beam with energies up to the maximum. In 1992, polarized proton beams at energies of 197, 290, and 414 MeV were stored in the Cooler ring with stable beam currents of 50 μA or greater. During the experiment, typical beam currents were 50-60 μA and the target thickness was 1.5×10^{14} atoms/cm^2, corresponding to luminosities of about 5×10^{28} events/cm^2 sec. At the energies of the experiment, the stored beam lifetimes were 1000-2000 sec without gas in the target cell and 600-900 sec with gas in the target cell.

4.2.1 IUCF Cooler Ring

The Cooler Ring is a zero gradient synchrotron that can accelerate light ions of charge q and atomic number A to about $500 \cdot q^2 \cdot A^{-1}$ MeV (maximum magnetic rigidity 3.6 T m). The ring is hexagonal in shape with four straight sections alloted for experiments. See figure 4.3. This experiment was carried out in the A section occupied partially by an RF cavity for beam acceleration. Cooling of the beam phase space is a continuous action accomplished in a straight section, called the C section by an intense beam of nearly monoenergetic electrons travelling together with the ions. In the rest frame of the electrons, a dissipative force is exerted on ions in motion bringing the stored ions to rest. The acceptance is 35π *mm mrad* at the most restricted part of the ring.

The stored beam is injected from the Main Stage cyclotron in strip injection mode (only unpolarized beam currently) or in stack injection mode. In strip injection mode, a beam of ions from the cyclotron is injected through a thin Carbon foil removing remaining electrons from the ions. For example, a 90 MeV beam of H_2^+ ions is strip injected, resulting on average 1.8 of 45 MeV protons and 0.2 Hydrogen neutrals for each dissociation [4.2]. Beam is accumulated by moving the closed orbit of the stored, cooled beam to the edge of the foil, injecting more beam through the foil, and then cooling the beam. The action is continued until the beam accumulation rate is equal to the beam loss rate from heating and interaction with the foil and other beam loss mechanisms. In stack injection mode, a low emittance beam of

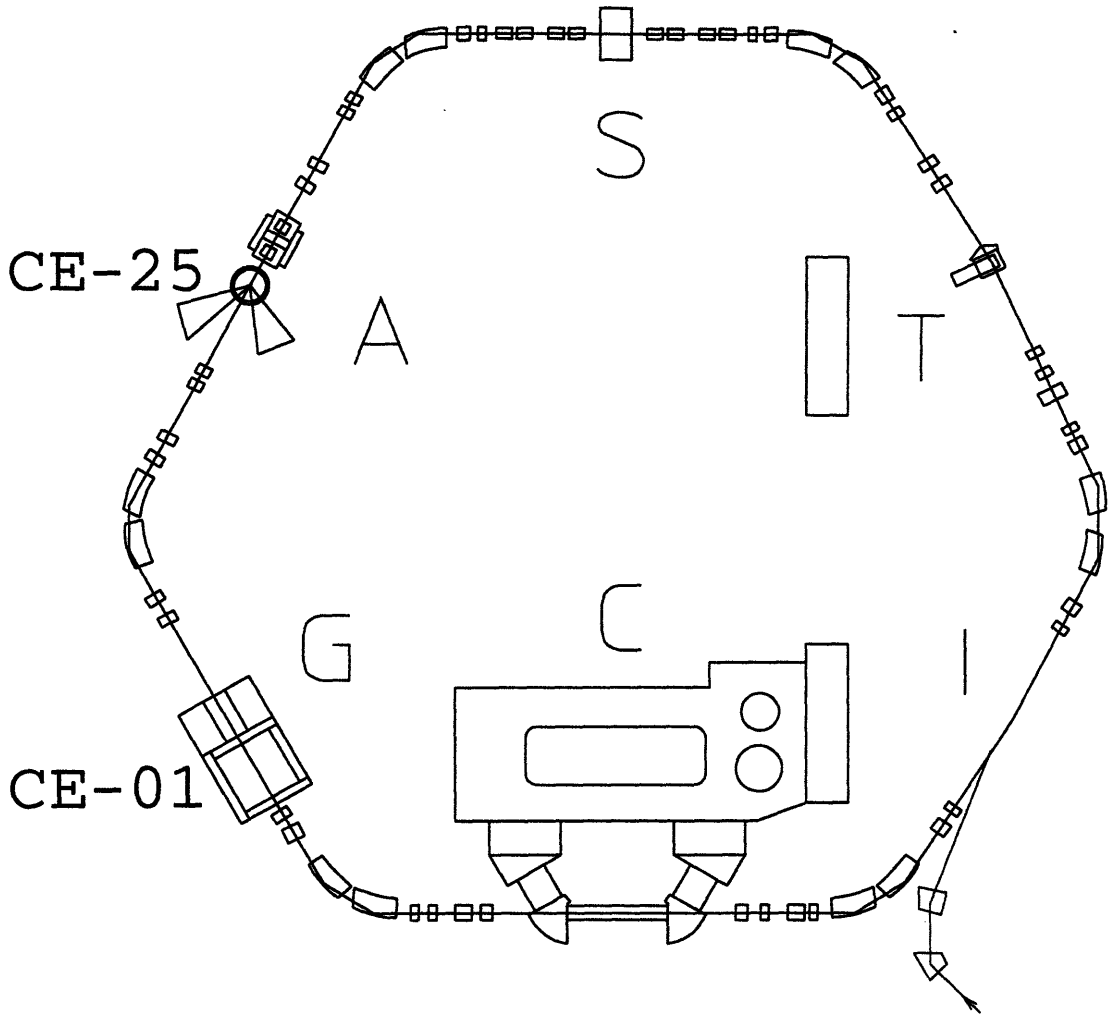

Figure 4.3. A schematic layout of the IUCF Cooler Ring. The stored beam is injected in Section I and the electron cooling occurs in Section C. Section A contains the apparatus for the CE-25 experiment. Section G contains the CE-01 apparatus where additional ^{1}H(p,2p) measurements were made to calibrate the luminosity monitors of the main experiment.

protons from the cyclotron is injected into the large longitudinal phase space of the ring. Beam accumulation is accomplished by repeating the process of kick injection followed by RF stacking and cooling until the beam accumulation rate equals the rate of loss to the stored beam from kick injection. Cooling reduces the emittance of the stored beam allowing an increased number of protons to be in the available phase space.

A parametric current transformer (PCT) installed in the T straight section was

used to monitor the DC beam current in the ring. A voltage signal proportional to the beam current is generated at the output of the Cooler PCT amplifier [4.3] and is converted to a frequency of electrical pulses that can be integrated with scalers to give integrated charges. The output voltage was calibrated by sending a known current through the toroid cores. Linearity of the PCT output voltage to input test current values through the wire is shown in figure 4.4. Calibration current pulses of 20 μA were sent through the wire at regular intervals during data taking. The offset of the PCT output drifted to $\pm$ 10 μA in a few hours and regularly required resetting to positive 10-20 μA since negative voltages were not registered by the frequency converter.

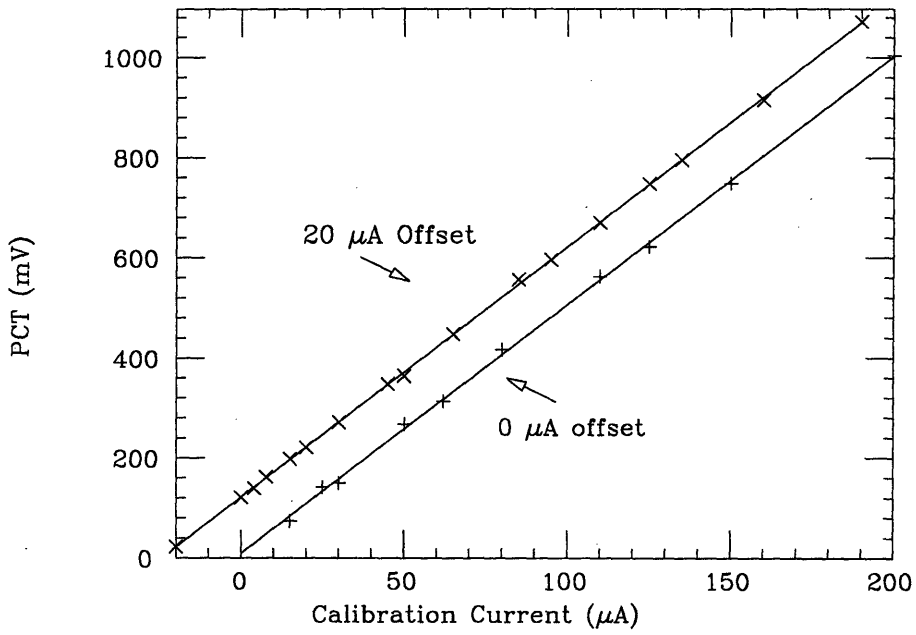

Figure 4.4. Calibration of PCT output voltage to wire current values.

4.2.2 Synchronization with the Cooler

Experiments with the Cooler have a macroscopic time structure that consists of cycles. This is shown schematically in figure 5.20 where the stored current in the ring as measured by the PCT is plotted as a function of time. The polarized protons are injected, accelerated to an experimental energy, and cooled. The data taking then commences as the intensity of the stored beam decays because of loss mechanisms. When the stored beam has decayed to about one half of its initial

is kicked from the ring. This constitutes one cycle. The duration was chosen to optimize the integrated luminosity based on the fill time and lifetime of the stored beam.

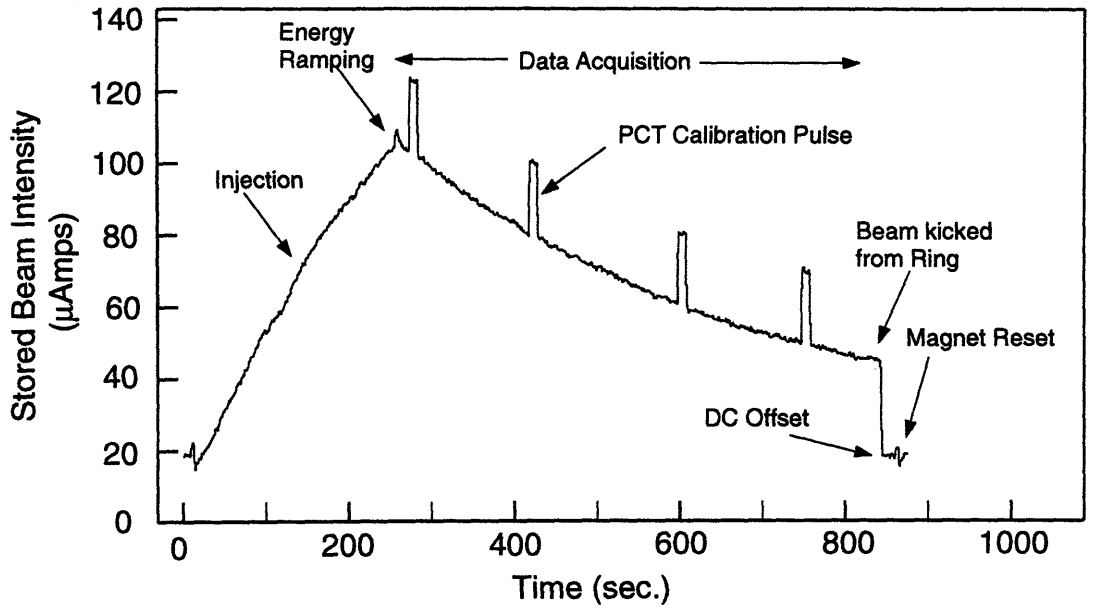

Figure 4.5. A schematic figure of the time structure of the experiment.

The Cooler was filled to 100 μA of polarized beam using the method of RF-stacking [4.1]. The beam was then accelerated to the final energy and cooled. At this point a start pulse was sent from the Cooler controls computer to the experiment. The start pulse was used to trigger a programmable timing and sequencing module (Jorway). The Jorway issued the command to ramp the wire chamber voltages from the quiescent level at injection to their plateau voltage, to clear CAMAC modules at the begmnning of each cycle and to enable data taking. 20 μA calibration pulses to the PCT were triggered by the Jorway several times throughout the cycle. After 600-900 sec, the data taking was stopped and the wire chambers were reset to the quiescent voltage levels. The residual beam was kicked from the Cooler, the ring magnets were reset and the ring was then filled with beam of the opposite spin state.

4.2.3 Impact on the Cooler ring

With conventional external target experiments the accelerator and experiment are essentially unconnected. In this experiment, where the target was internal to the storage ring, there were several new considerations. The apertures, vacuum properties and magnetic field of the target, in addition to the presence of gas target atoms in the path of the stored beam, all directly influenced operation of the storage ring.

The transverse dimensions of the target cell were carefully chosen based on several considerations. The thickness of the target increases rapidly as the transverse dimensions of the cell are decreased. The effectiveness of the flow limiters also improves rapidly with decreased radius. However, sufficiently small apertures can intersect the beam halo and produce backgrounds. In addition, small apertures can lower the geometrical acceptance of the accelerator thus impacting the beam lifetime and making it more difficult to inject beam into the ring. The target cell and pumping aperture dimensions were chosen to be approximately equal to the machine design acceptance 35 π mm mrad. The best performance seen in previous experiments was half this value [4.2]. By choosing the target acceptance to be larger than the operating machine acceptance it was straightforward to tune the stored beam through the target. In addition, the scattering of beam halo from the target cell was minimized.

The presence of target gas reduced the stored beam lifetime. This directly influenced the time required for data taking and refilling the ring. With no target gas in the cell the beam lifetime was typically 2000 sec and depended on the tune of the Cooler. With the target gas flowing this value was reduced to 500-900 sec. It took about 100-200 sec to fill the ring to 100 μA.

The polarized target required a holding magnetic field of about 10 G (1 mT) both to orient the ^{3}He atoms by optical pumping and to define the direction of polarization. The field was present over about 1 m along the beam line resulting in a maximum field integral of 1 mT m. This was sufficiently large to produce a nonnegligible deviation in the trajectory of the stored beam. Without correction, the stored beam lifetime and the rate of background events in the detectors would be different for the two field directions. Further, any change in the magnetic holding field would disrupt beam injection. To correct for the effect of the target holding field two additional magnets were added to the straight section immediately following the target. These magnets were controlled using a shunt across the power supply which provided current to the target magnetic field coils. This combination of three

magnets then allowed for a local motion of the beam without affecting the closed orbit elsewhere in the ring. With this configuration deflections of the beam in the target cell were less than $\pm 0.1\ mm$, and operation of the ring could be made independent of the field in the target.

4.2.4 Polarized Proton Beam

The injected polarized proton beam is produced in three stages: the Preinjector, the Injector cyclotron, and the Main Stage cyclotron. See the complete accelerator floor plan of the IUCF in figure 4.6. Protons from the source are accelerated to 0.6 MeV and then injected into the first cyclotron. The injector cyclotron has four separated magnet sectors operating at fields up to 1.5 T and RF cavities in two opposing regions between magnet sectors operating typically at 35 kV and frequencies from 26-35 MHz to accelerate ions to energies up to 15 MeV for injection into the Main Stage. The Main Stage cyclotron, similar in design and three times larger in size, also has four magnet sectors operating at fields up to 1.7 T. RF cavities in two opposing regions between magnet sectors operate at voltages from 60 kV to 200 kV increasing radially out and frequencies from 25.4 MHz up to 35.2 MHz to accelerate protons to energies up to just over 200 MeV [4.2]. The beam pulses from the Main Stage cyclotron can be directed to the Cooler ring or to one of the experimental areas in the top right section of figure 4.6. It is interesting to note that whenever Cooler injection energies matches the beam specifications of an experiment in one of these experimental areas, the cyclotron can run in a time sharing mode where beam pulses can be injected into the Cooler ring for a time and then directed to the second experiment while the ring is in data taking mode.

There are two Preinjectors in figure 4.7, and in the larger Preinjector is an atomic-beam polarized hydrogen ion source sitting on a high voltage platform with which protons are accelerated before injection into the Injector Cyclotron. Components in the polarized hydrogen ion source are an RF dissociator to form hydrogen atoms, a sextupole selection magnet, a transition polarizer, and an ionizer. See figure 4.7.

From the hyperfine interaction between the electron spin S=$\frac{1}{2}$ and the nuclear spin I=$\frac{1}{2}$ the ground state hydrogen atoms in the levels F=0,1 are separated by 1420.4 MHz. In the presence of a small external magnetic field, the ground state levels split into magnetic hyperfine levels, labelled as magnetic states 1,...,4, and and at field strengths greater than the nuclear spin field on the electron field, coupling between the external field with each of the spins becomes stronger than the

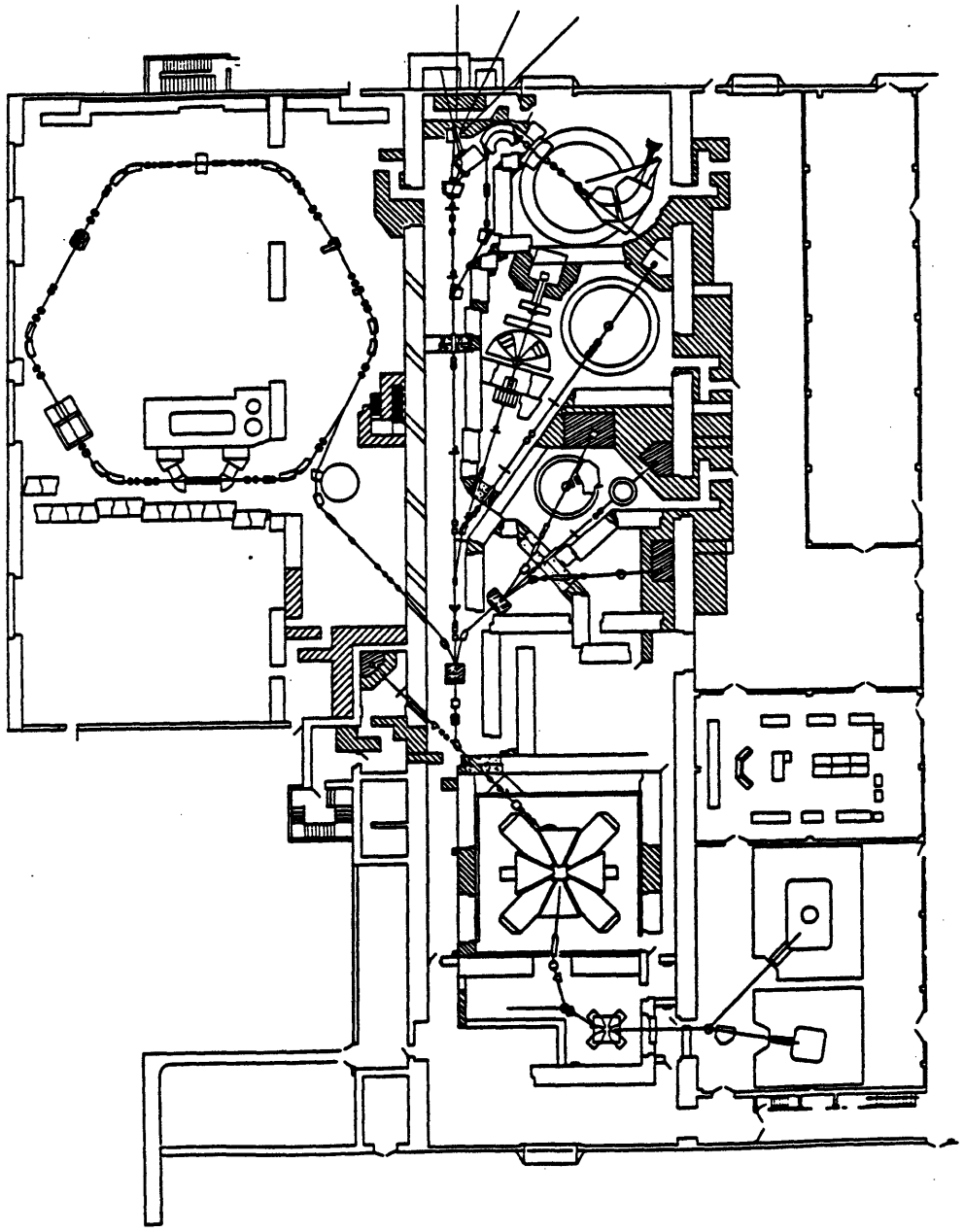

Figure 4.6. The IUCF acclerator floor plan.

hyperfine coupling, changing the quantum numbers of the atom from F to m_S and m_I as in figure 4.8. Note that the magnetic field due to the electron spin on the nuclear spin is $\sim 10^5$ G (10 T) while the field on the electron spin due to the nuclear spin is only $\sim 10^2$ G (0.01 T). The force acting on the atoms in the presence of a gradient field is given by the slope of the magnetic energy levels,

$$\mathrm{F} = -\frac{\mathrm{dE}}{\mathrm{dH}} \cdot \frac{\mathrm{dH}}{\mathrm{dx}} \,. \tag{4.1}$$

Atoms passing through the gradient field of a Stern Gerlech type magnet then become separated according to magnetic states.

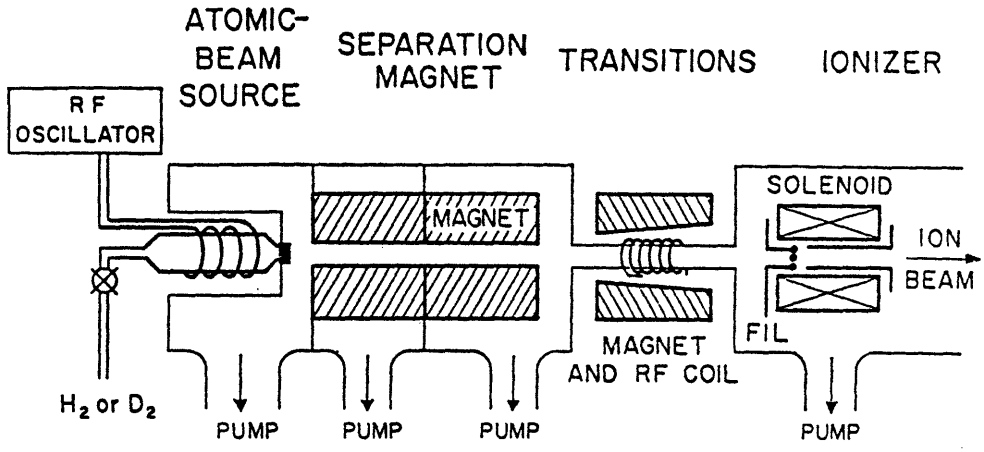

Figure 4.7. Schematic diagram of an atomic-beam polarized-ion source.

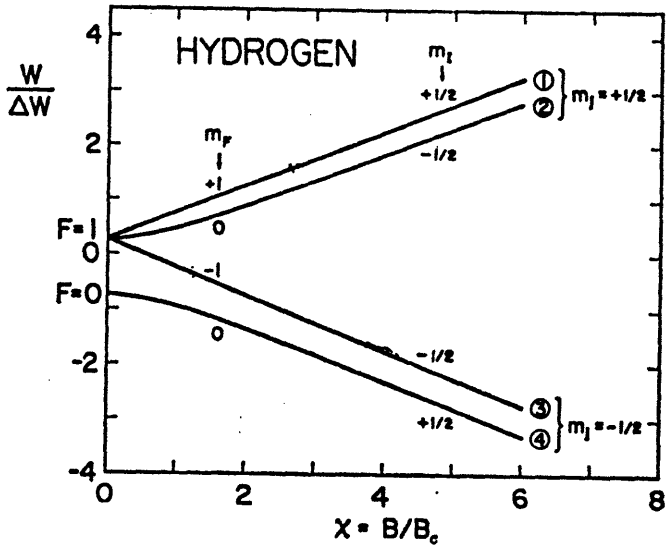

Figure 4.8. Energy level diagram of the hydrogen ground atom in a magnetic field.

Magnetic state 1 which has 100% nuclear polarization, can be selected by a small gradient field. However, in practice, the polarized atomic beam intensity is severely limited at small fields and most polarized hydrogen sources use strong fields that are greater than the nuclear spin field [4.4].

In the polarized source, the dissociator is a glass discharge tube where hydrogen

atoms are formed by a high power RF field generated by a solenoid wound around the tube. At the end of the tube is either a pin hole nozzle or a stack of capillary holes through which hydrogen atoms effuse out in the forward direction toward the selection sextupole magnet. A small opening collimator before the sextupole magnet further collimates the beam of atoms, and as the atoms move into the magnet, the gradient field of the sextupole magnet deflects out the $m_S=-\frac{1}{2}$ states and deflects in the $m_S=\frac{1}{2}$ states along the central axis focussing the atoms to a point on the central axis outside the magnet. The atoms exiting from the sextupole magnet are collimated further to keep the $m_S=\frac{1}{2}$ states as they enter into a transition field region where they become polarized in the direction of the transition field. The beam travels into the ionizer where the atoms lose an electron to form protons or pick up an electron to form H^- ions. The deflected or stopped atoms are pumped away at each stage maintaining a high vacuum inside the source.

4.3 The Detectors

The detectors consisted of three main subsystems designed to simultaneously record data from a number of different reactions: main detector arms to the left and the right of the target, recoil detectors inside the target vacuum chamber on each side of the target cell, and forward angle detectors. The quasielastic events, ^{3}He(p,2p), ^{3}He(p,pn), and ^{3}He(p,pd), were defined by a charged particle in one of the main detector arms and a charged or neutral particle (a neutron) in the other. The internal recoil detectors were used to detect low energy (sub-MeV) particles such as ^{3}He and ^{2}H in coincidence with either the main detectors or the forward angle detectors. The forward angle-recoil coincidence events originated from fast protons due to ^{3}He(p,p^{3}He) elastic scattering in coincidence with the ^{3}He recoil particles. These detectors were left-right symmetric to allow for separation of the luminosity from spin dependent quantities.

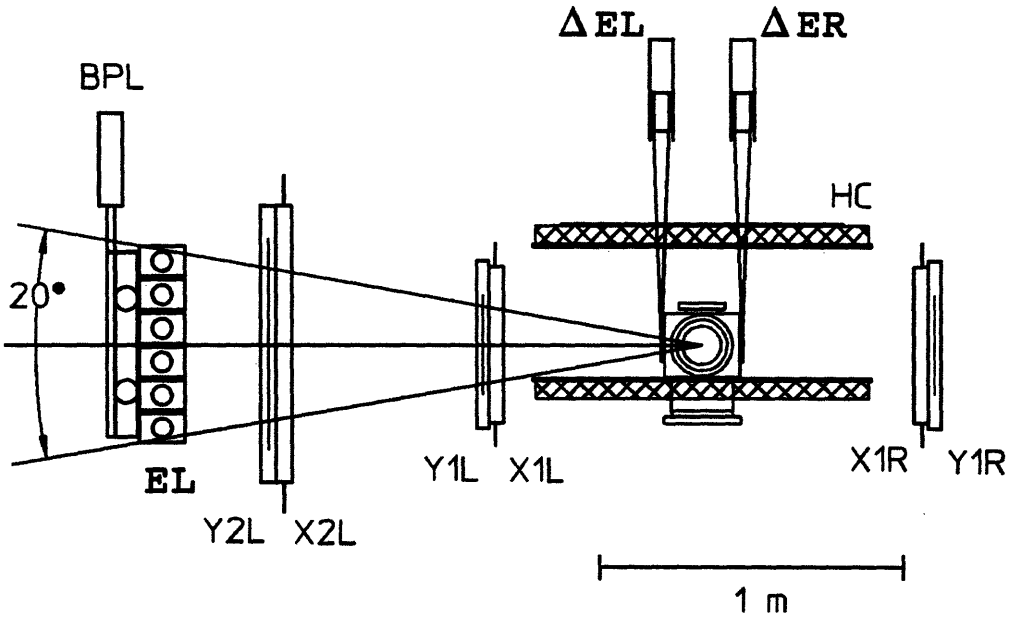

Figure 4.9. A side view of the main detector arm. The labels are as defined in the caption to figure 4.2.

4.3.1 The Main Detector Arms

Each main detector arm consisted of a ΔE-E scintillator pair with two planes of $x - y$ multi-wire proportional chambers positioned between them. A pair of thick backing scintillators were located behind the E scintillators. This is shown schematically in figure 4.10.

The ΔE detector was made of a thin BC400 scintillator [4.5], 3 mm thick, 54.7 cm wide, and 10.8 cm high. connected at the longer edge to a Burle 8575 photomultiplier tube with a 64.8 cm long tapered triangular light guide designed to emphasize direct rather than reflected photons. The ΔE detector was suspended from the optics platform on top of the target Helmholtz with the scintillator paddle positioned close against the exit window of the chamber on each side. The upstream edge of the paddle was aligned at 11.75 cm from the upstream edge of the chamber box for the left detector arm and at 26 cm for the right detector arm. The paddle area was larger than the acceptance of each detector arm so that exact positioning was not critical.

Each E detector consisted of a stack of six NE102 scintillator bars 102 cm long, 10 cm high and 15 cm thick. An Amperex 2240 photomultiplier tube was attached to each end with a ~32.4 cm long hyperbolic light guide to optimize the timing characteristics of the bars. Timing difference between the two PMT signals was used to determine particle intersections along the scintillator bar. Spacers were required between the bars to avoid stressing the light guides, resulting in a 65 cm high stack on the left and a 63 cm high stack on the right. Each stack was set on top of an Aluminum table and their locations were determined by measurement of the distance from the corners of the target chamber box to the corners of the detector stack.

The center points on the front plane of the left E detector stack and the right E detector stack were located 197.61 cm and 169.64 cm respectively from the center of the storage target cell. Angular acceptances were approximately $36° < \theta_L < 67°$, $21° < \theta_R < 47°$, and $-10° < \phi_{L(R)} < +10°$. The neutron detection efficiency at 197 MeV was approximately 15%.

Multi-wire proportional chambers (MWPC) [4.6] were used to reconstruct charged particle tracks and thus to determine the event vertex. They were arranged in two pairs: a large and a small set, located on each of the two major left-right detector arms. The first detector of each pair was positioned with its wires in a vertical direction (XnR, XnL chambers) and the second detector with its wires running horizontally (YnR, YnL chambers). The small forward chambers (X1, Y1)

had wire spacings of 1.92 mm and 2.54 mm respectively; the rear chambers' (X2, Y2) wire spacings were about twice as large, 4.36 mm and 5.45 mm respectively, giving an intrinsic angular resolution of about 0.2°. The LeCroy PCOSII readout system, employing model 7700 MWPC chamber boards (locally modified for noise reduction), and separate model 2700 CAMAC-based controllers, was used to record the MWPC hit patterns. Alternate odd and even wires were read out on separate chamber boards to minimize cross talk. The wire chamber information was not incorporated into the hardware trigger but was read out for every event generated by the main detector arms. Constraints on the MWPC hit patterns were incorporated in the replay software. The efficiency of the wire chambers was measured to be 99% with minimum ionizing particles. A large effort was required to reduce the noise level in the MWPC spectra. However, some chamber spectra always had one or two super noisy wires, not due to the wires in chambers but the electronics.

Although the present experiment was conducted in the Cooler A region, which is located approximately half way around the ring from the injection point (see figure 4.3), considerable background was present during injection of the polarized beam into the ring. For this reason the chamber voltages (nominally 3.1 kV for the small, and 2.8 kV for the large chambers) were reduced by 50% during the fill, ramp, and initial cooling phase of the Cooler cycle. This was accomplished by a logic level supplied to the bin gate of commercially available high voltage modules (with a slight internal modification to achieve the 50% voltage reduction) which then held the MWPC at full voltage for a period longer than the data acquisition time during each cycle. The chambers used an argon-ethane gas mixture (50%/50%) to which n-propyl alcohol vapor was added to reduce sparking. The MWPC trip circuit was integrated into the data "run gate" in order to guard against the effects of occasional sparking during the acquisition period.

Two scintillator planes were placed behind each E detector stack to provide additional energy information on high energy particles that did not stop in the E detectors. The first plane was 7.0 cm thick with two photomultiplier tubes attached at each end. The second was 2.54 cm thick with three PMT's attached along the upper edge. The total scintillator thickness was sufficient to stop the highest energy deuterons, thus allowing the separation of protons and deuterons at all energies.

4.3.2 Recoil Detectors

For recoil detection, three silicon microstrip detectors were mounted on each side of the target cell, 3 cm from the beam axis and slightly downstream of the target center. These were type I detectors from Micron Semiconductor [4.7] with an active area 4 cm high and 6 cm long. One was 500 μm thick, the others 300 μm. Although each detector was segmented into 7 strips, in this experiment the strips were read out in parallel and treated as a single large detector. To reduce noise due to the turbomolecular pumps on the target vacuum system, the detectors were mounted inside a Faraday cage connected to the electronic ground. The other main noise source was the infrared laser light that leaked down into the target chamber through the ^{3}He capillary. To block this light, an additional 0.2 μm of aluminum was evaporated onto the mylar target cell windows. In addition, a small opaque disk was placed on top of the pumping cell to prevent laser light from travelling directly down the capillary. The effective solid angle subtended by the recoil detectors for the entire target length, weighted by the triangular target density distribution, amounted to 3.1 Sr.

The microstrip detectors were calibrated continuously with a ^{228}Th alpha source mounted inside the Faraday cage. This source had resolvable lines at 5.38, 5.69, 6.29, 6.78, and 8.78 MeV. The recoil detector energy resolution was typically 200 keV (FWHM) with the laser beam shuttered. With the laser on the target, the light noise limited the resolution to about 300 keV and the energy threshold to 0.5 MeV.

4.3.3 The Luminosity Monitor Detectors

The luminosity is the product of the beam current and target thickness. This was monitored by measuring ^{3}He(p,p^{3}He) elastic scattering at forward angles outside the acceptance of the main detector arms. The forward scattered protons were detected in separately mounted plastic scintillators and the coincident ^{3}He nuclei were detected in the recoil detectors. There were two left-right symmetric sets of plastic monitor scintillators, one inside (Mon1) and one outside (Mon2) the target vacuum chamber. The Mon1 detectors were 6.35 cm high, 4.45 cm wide, 1.27 cm thick, and centered at 27.8 cm on a line 16.1° from the target center. The angular acceptance of the scintillators was centered near the forward maximum in the analyzing power of the ^{3}He(p,p^{3}He) reaction at all incident beam energies. The Mon2 scintillators were 10.2 cm wide, 25.4 cm tall, and 5.1 cm thick, were centered at 115.1 cm on a line 18.0° from the center of the cell.

The scintillator material for the Mon1 detectors located in the Cooler vacuum was Bicron BC-400 plastic scintillator [4.5]. A polystyrene light guide, chosen due to its lower outgassing rate compared to plexiglass, brought the light from the scintillator to an optical viewport. The scintillator and light guide were loosely wrapped in one layer of 12.7 μm thick aluminum foil, which had a slit to allow easy escape of the gas load from the plastic. The additional gas load and reduced bakeout temperature due to the Mon1 detectors did not significantly affect the quality of the ring vacuum.

4.4 Electronics and Data Acquisition

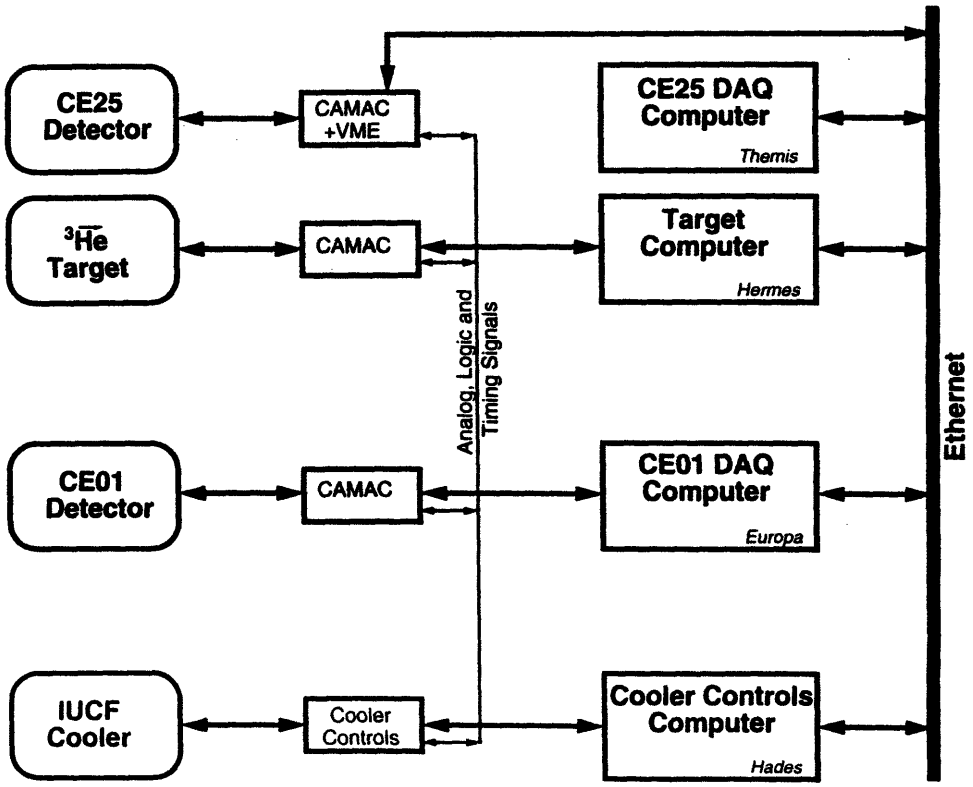

Figure 4.10 Schematic block diagram of the electronics and data acquisition system used in the experiment.

4.4.1. Data acquisition and readout

Online data were processed using a network of 4 computers plus one VME crate for CAMAC readout. A schematic block diagram of this arrangement is shown in figure 4.10. The main data acquisition and control computer of the system was linked to the other computers via an Ethernet network. Four CAMAC crates were

read out through the VME crate which sent buffered data by Ethernet to the main computer, where the data were written to disk (later archived to 8 mm tape) and sorted into histograms that could then be used for online analysis. The control computer for the polarized target transmitted updates of the target status in five minute intervals to the main computer.

4.4.2 Trigger

The utilization of a windowless internal target with a cooled proton beam provided a relatively background free environment. In addition, a high duty cycle beam provided a low event rate with less than 0.1% accidental coincidence. To take advantage of the low background, the low accidental coincidence, and the large kinematic acceptance provided by the various detectors, the electronic trigger system was designed with the flexibility to accommodate all possible coincidence combinations. See the schematic layout in figure 4.12 for an overview of the trigger system.

In the first level, there are the "fast" and the "slow" trigger. To initiate the fast trigger logic a coincidence between the ΔE and E detectors on one side was required, indicating the passage of a charged particle or a coincidence between all the six scintillator bars in the E detector on either side was required, indicating the passage of a charged particle vertically through the stack of E detector.

The slow trigger logic is initiated by a coincidence between the any of the side silicon microstrip recoil detectors and one of the forward scintillators on the other side of the beam to detect mainly elastic events for luminosity and beam polarization measurements. The OR signal from each trigger circuit along with the computer BUSY logic signal are then used to gate the output logic signals of the other trigger circuit.

The output logic signals of the fast trigger were put through a long delay line before combining with each other and with the slow logic signals from the side silicon microstrip dectectors and the forward scintillators. A coincidence was sought between the ΔE and E detectors on one side and the E detector on the opposite side of the beam to detect quasielastic events (p,2p), (p,pn), and (p,pd). A coincidence between the ΔE and E detectors on one side and one of the side silicon microstrip detectors on the opposite side of the beam was sought to detect the elastic events (p,p^3He). Further, a coincidence between the ΔE and E detectors on one side and a forward silicon microstrip detector on the opposite side of the beam was used to detect (p,$\pi^+{}^4$He) events which has a target anayzing power of -1. As mentioned

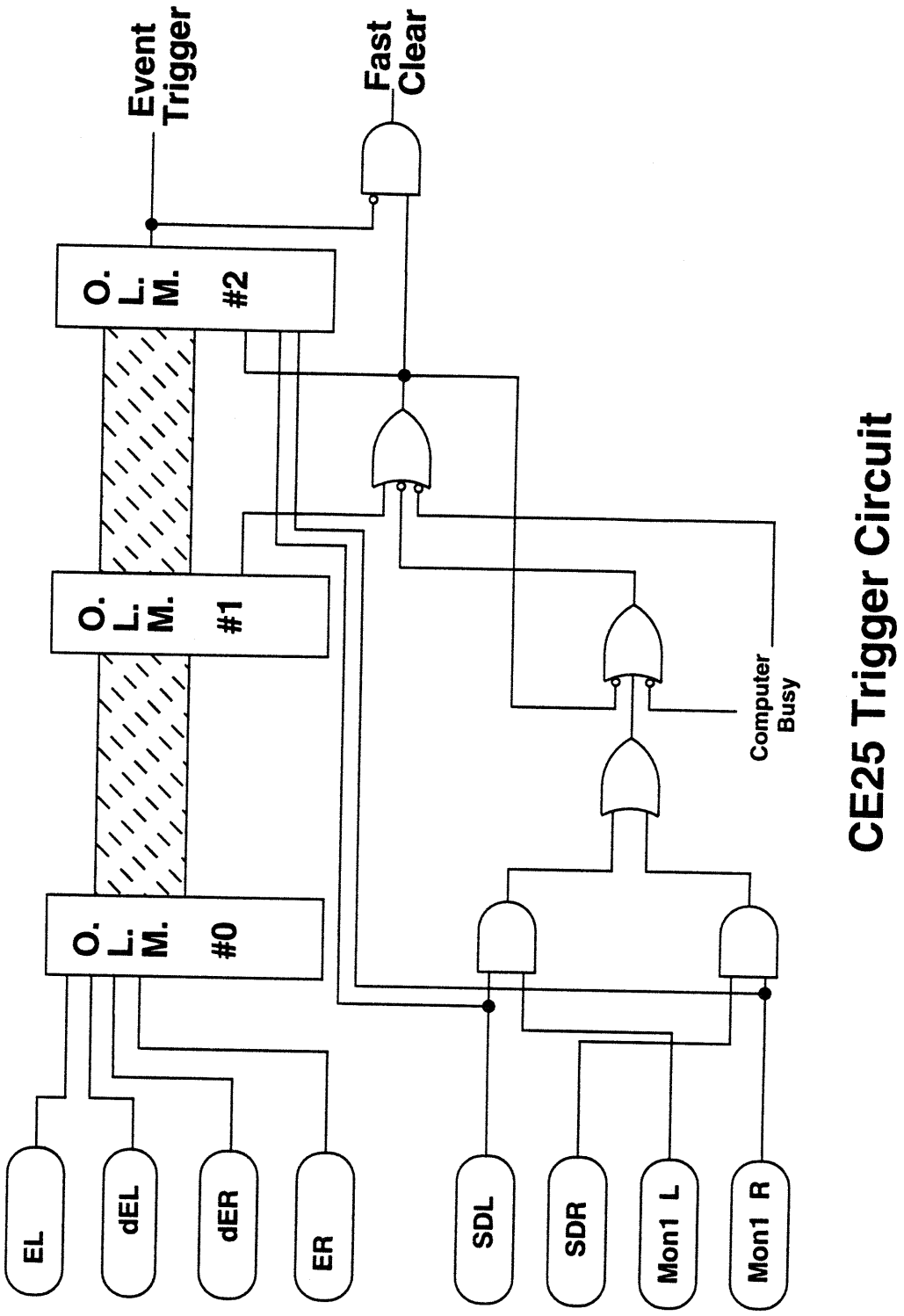

Figure 4.11. Schematic diagram of the trigger system used in the experiment.

above, these signals have been gated with the OR signal from the slow trigger circuit and the computer busy signal.

The coincidence signals that involve the main detector arms are called event 5's, and the coincidence signals that involve only the side silicon microstrip detectors and forward luminosity scintillators are called event 6's. The event 5 logic signal, when triggered, is used to start the readout of the coincidence register signals which had the detector hit patterns and the status bits for the beam and target polarization and the target holding field direction. Also, either the event 5 or the event 6 logic signal, when triggered, is used to start the conversion of the slow ADC and TDC analog signals of the silicon microstrip detectors and the forward scintillators and the wire chamber PCOSII signals, and the ADC analog signals of the target polarization and pressure. Other than the mutual inhibit, the event 5 and event 6 triggers operated independently. The event 5 and event 6 coicidence triggers are summarized in Table 4.1 and 4.2.

Trigger	
C-single	$[\mathrm{CL} \cup \mathrm{CR}] \cap \overline{\mathrm{busy}}$
pLnR	$(\mathrm{dEL} \cap \mathrm{EL}) \cap \mathrm{ER} \cap \overline{\mathrm{busy}}$
pRnL	$(\mathrm{dER} \cap \mathrm{ER}) \cap \mathrm{EL} \cap \overline{\mathrm{busy}}$
p-single	$[(\mathrm{dEL} \cap \mathrm{EL}) \cup (\mathrm{dER} \cap \mathrm{ER})] \cap \overline{\mathrm{busy}}$
pLMR	$(\mathrm{dEL} \cap \mathrm{EL}) \cap \mathrm{MR} \cap \overline{\mathrm{busy}}$
pRML	$(\mathrm{dER} \cap \mathrm{ER}) \cap \mathrm{ML} \cap \overline{\mathrm{busy}}$
pLFMR	$(\mathrm{dEL} \cap \mathrm{EL}) \cap \mathrm{FMR} \cap \overline{\mathrm{busy}}$
pRFML	$(\mathrm{dER} \cap \mathrm{ER}) \cap \mathrm{FML} \cap \overline{\mathrm{busy}}$
$\overline{\mathrm{busy}}$	computer and electronics not busy
dEL/dER	start scintillator (Left/Right)
CL/CR	no dE and all six E bars in the stack
EL/ER	at least one of the six E bars in the stack
ML/MR	at least one of the three transverse μ detectors
FML/FMR	forward μ detector

Table 4.1. The event 5 triggers.

Trigger	
ML-FSR	transverse μ detector left and forward scintillator right and $\overline{\text{busy}}$
MR-FSL	transverse μ detector right and forward scintillator left and $\overline{\text{busy}}$
ML-FSR2	transverse μ detector left and forward externalscintillator right and $\overline{\text{busy}}$
MR-FSL2	transverse μ detector right and forward external scintillator left and $\overline{\text{busy}}$
$\overline{\text{busy}}$	computer and electronics not busy

Table 4.2. The event 6 triggers.

The conversion of analog scintillator signals in fast encoding ADC and TFC modules was initiated by the gated fast OR logic signal. In the absence of an event 5 logic signal, a delayed version of the gated fast OR trigger provided a fast clear to the ADC and TDC modules. The total electronic processing time (dead time) for each event was about 2.6 μsec.

A periodic trigger was generated every 0.1 sec by a clock to initiate scaler reads. These scalers monitored rates at various stages of the electronics—namely logic signals at every detector including the MWPC's, first level triggers, the fast OR and the slow OR triggers, the gated fast OR and the slow OR signals, the output event 5 and event 6 triggers, and so on. Also, it monitored the PCT signal of the beam current, and the 60 cycle AC signal for a possible use in the analysis for control of the AC signal background. The scaler events are summarized at the end of appendix D.

Due to the time structure of the cooler beam it was possible to make a direct measurement of the quasielastic accidental rate. The time separation between the cooler beam pulses was typically about 100 nsec, and so it was possible to delay a copy of the first level trigger into the next beam burst, and then look for coincidences with the undelayed first level trigger from the other side of the beam. The accidental coincidence rate measured in this manner was typically about 0.1% of the total quasielastic trigger rate at the luminosities attained during the experiment.

Chapter 5

Data Analysis

5.1 Introduction

As discussed in section (4.4.2), coincidence signals of the quasielastic reactions (p,pn), (p,2p), (p,pd), the elastic reaction (p,p^3He), the pion production (p,π^+ ^{4}He), and cosmic ray muons were recorded as event 5 data in the experiment. For relative luminosity monitoring, the experiment also recorded (p,p^3He) coincidence events with symmetrically configured detectors in the target chamber. These events were named event 6. Moreover, the target polarization and target input gas pressure at the optical pumping glass cell were read out for each data event. Cumulative counts, *i.e.* scalers, detector logic signal pulses at various points in the trigger system, clock pulses, and beam current signal pulses from the PCT (*see section* 4.2.1) were recorded as events every 0.1 sec in the data stream. These scaler events were named event 9. In addition, a large amount of target diagnostic data were recorded at 10 min intervals. Finally, these diagnostic events were named event 10.

The data were written continuously to hard disks in files of approximately one hour long, typically segmented into four experimental cycles (*see section* 4.2.1), and were later copied to 8 mm video tapes for portability and backup.

Analysis of the data were carried out at five different locations among the experimental collaborators. At IUCF, the data were recorded and analyzed using XSYS data acquisition; at the University of Wisconsin—Madison (UW) and at MIT, the data files were first processed and then converted to HBOOK files for analysis using PAW (Physics Analysis Workstation); at the University of Louisville (UL) and Ohio State University (OSU) analyses were carried out using XSYS.

Analysis steps for the data presented in the thesis are shown in the flowchart in figure 5.1. There were two steps in the analysis of both event 5 and event 9 data before asymmetries were computed. For each event 5, reconstruction of the kinematic quantities was carried out in the first step, such as the particle trajectory, kinetic energy, and momentum in each detector arm, the missing momentum, and the missing energy of the quasielastic reactions (p,pn) and (p,2p). Results were then written as an ntuple 5 into HBOOK files to be analyzed in PAW in the second step. Here, conditions were applied to filter and sort the data into histograms of missing momentum or momentum transfer for different combinations of beam and target spin states for (p,pn) and (p,2p) reactions. As the first step in event 9 analysis,

computer and electronics livetime and beam current spectra as a function of the experimental cycle time were generated. Results were then written as an ntuple 9 into HBOOK files. In the second step, the beam charges for all beam and target spin configurations were computed from the beam current time spectra. Finally, the asymmetries of the quasielastic reactions (p,pn) and (p,2p) of the 197 MeV data were calculated.

5.2 Reduction of the Event 5 Data

There were eight different coincidence triggers in the event 5 data stream (*see table* 4.1). In the quasielastic analysis, only the event triggers, pLnR and pRnL, were selected. These events were formed by a coincidence between the dE and the E detector triggers on the same side of the beam and the E detector trigger on the opposite side of the beam. The first coincidence indicated a possible passage of a leading charged particle, often a proton, and the E trigger in the second coincidence indicated a possible passage in the second detector arm of a charged particle or a neutron, identified by the presence or absence of a coincidence dE detector trigger. Therefore, the quasielastic coincidence triggers, pLnR and pRnL, consisted of (p,2p), (p,pd), and (p,pn) events. However, the identification of a charged particle required additional conditions including the wire chamber signals as the dE and E detectors were not 100% efficient. This will be discussed further in section 5.4. In the subsections below, the reconstruction of the trajectory, the time of flight calculation, and the calculation of the kinematic quantities, such as kinetic energy, momentum, and missing momentum are discussed.

5.2.1 Trajectory Reconstruction

The reconstruction of particle trajectories in each detector arm required a minimum of two points along each trajectory in space. For charged particles, the two points were determined by two pairs of standard MWPC wire chamber planes separated by some distance. For the neutron, one of the points was determined by the position sensitive scintillator arrays in the E detector, and the second point was the vertex of the coincident charged particle on the opposite side of the beam.

5.2.1.1 Charged Particles

The first of the two trajectory points was determined by the intersection point on the (X1n, Y1n) pair of small wire chambers located next to the holding magnetic field coils pair, and the second was given by intersection point on the (X2n, Y2n) pair of larger wire chambers located downstream from the first pair, before the E

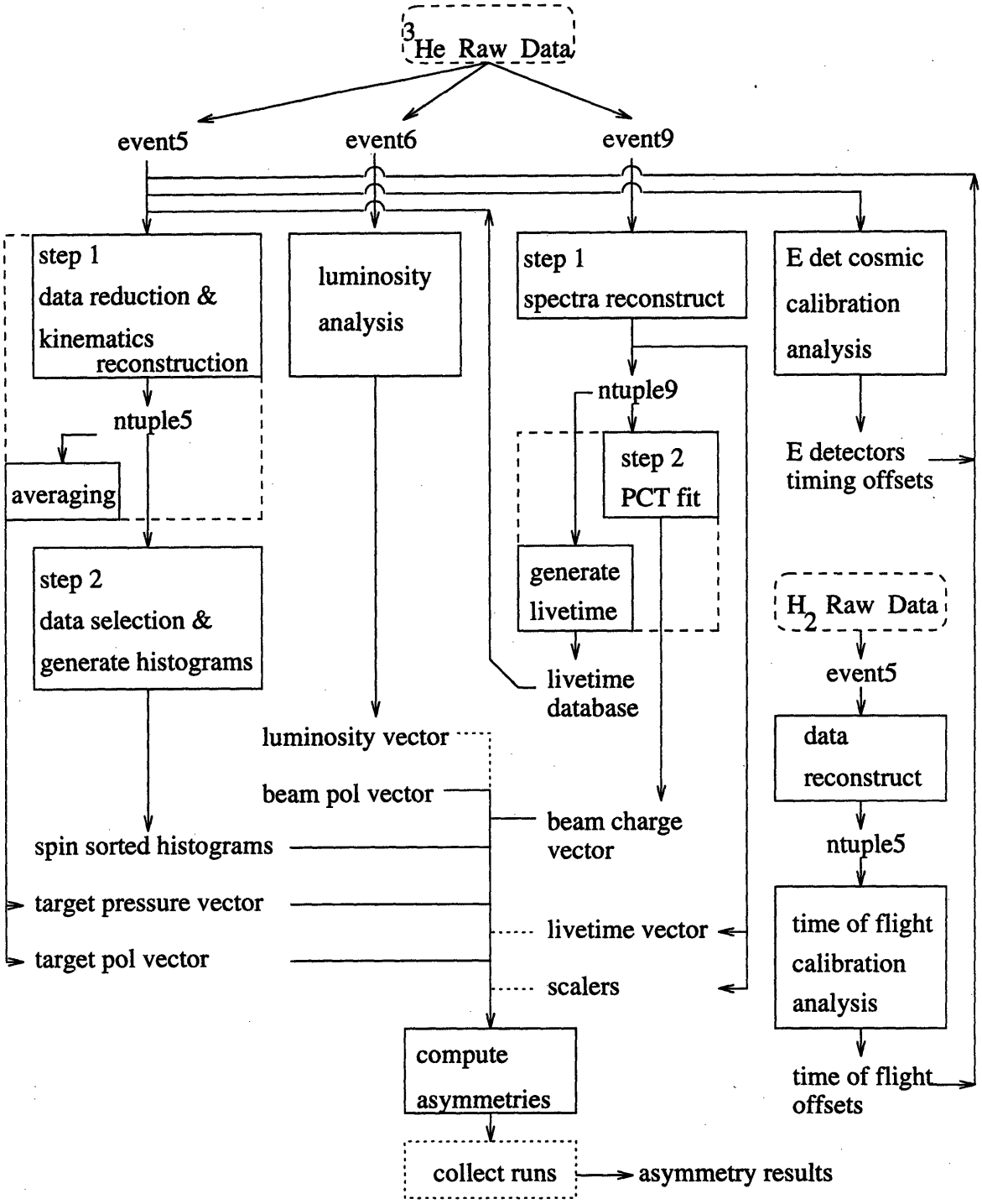

Figure 5.1. Flowchart for the analysis of the 197 MeV data.

detector, approximately 65 cm (70 cm) in the left (right) detector arm. The index n (=L or R) indicates the left and the right hand side of the beam.

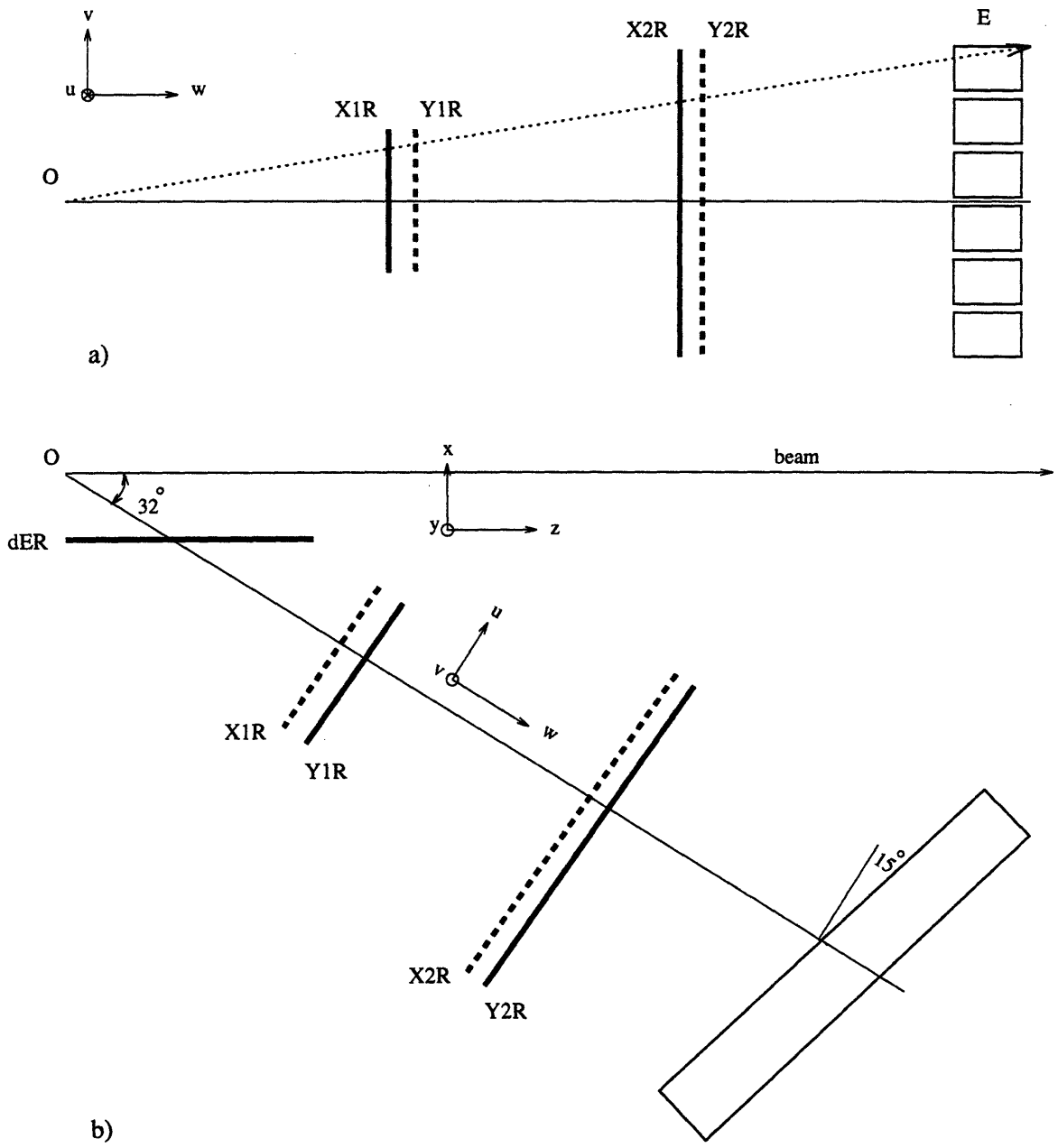

Figure 5.2. (a) Particle trajectory traversing the two sets of MWPC and the E detector and (b) rotation from detector coordinates to lab coordinates.

The two intersection points were measured in the detector arm coordinate system, (u, v, w). The *ith* intersection point was by convention on the second

chamber plane of the *ith* pair and was determined as

$$\begin{aligned} u_i &= x_i + d_i\,(x_2 - x_1)\,/\,(w_2 - w_1) \\ v_i &= y_i \\ w_i &= D_i\ , \end{aligned} \tag{5.1}$$

where x_i was the horizontal intersection position measured at the Xin chamber, d_i the separation between chamber planes in each pair, y_i the vertical intersection position measured at the Yin chamber, and D_i the central line of sight distance from the center of the target cell to the center of the second plane of the *ith* chamber pair.

The detector arm coordinates were then transformed into the laboratory coordinates having a common origin. The transformation can be written as

$$\begin{pmatrix} x_i \\ y_i \\ z_i \end{pmatrix} = \begin{pmatrix} \cos\theta_d & 0 & \sin\theta_d \\ 0 & 1 & 0 \\ -\sin\theta_d & 0 & \cos\theta_d \end{pmatrix} \begin{pmatrix} u_i \\ v_i \\ w_i \end{pmatrix}\ , \tag{5.2}$$

where the angle θ_d was the angle orientation of the chamber planes in the lab coordinates. Finally from the two intersection points in the lab coordinate system, the polar and azimuthal angles of the trajectory in the lab coordinate system were calculated as

$$\begin{aligned} \theta &= \cos^{-1}\left(\frac{z_2 - z_1}{\sqrt{(x_2 - x_1)^2 + (y_2 - y_1)^2 + (z_2 - z_1)^2}}\right) \\ \phi &= \tan^{-1}\left(\frac{y_2 - y_1}{x_2 - x_1}\right) \end{aligned} \tag{5.3}$$

The angles θ, ϕ, and one of the two intersection points then completely determined the trajectory.

5.2.1.2 The Neutron (p,pn)

The MWPC's were sensitive to charged particles and high energy photon, but not to neutral particles, such as a neutron. Thus, the E detector was used to measure the first of the two intersection points of the neutron trajectory. The vertex of the coincident proton on the opposite side of the beam determined the second point. Each scintillator bar in the E detector was equipped with a photomultiplier tube

at each end to measure the intensity and arrival time of the light signal from the particle intersection, and in turn, to measure the time difference between light signal arrival at the photomultiplier tubes. This technique yielded a position resolution of ± 3 cm along the scintillator bar. In addition, the six scintillator bars were uniformly stacked to give the vertical position with ± 5.5 cm resolution (*see section* 4.3.1). With the center of the EL (ER) detector 169.64 cm (197.61 cm) away from the center of the target cell, the estimated angular resolutions were $\Delta\theta_{\rm L} = \pm 1.0°$ ($\Delta\theta_{\rm R} = \pm 0.9°$) and $\Delta\phi_{\rm L} = \pm 1.7°$ ($\Delta\phi_{\rm R} = \pm 1.5°$).

The intersection point at the E detector was then transformed from the detector arm coordinates to the laboratory coordinates by a similar rotation as above in equations (5.2). Construction of the vertex will be discussed in the next subsection. Once the two intersection points were determined in the lab coordinate system, the neutron trajectory angles θ and ϕ were immediately given by equations (5.3).

5.2.1.3 Vertex

After the trajectory of a charged particle was determined, its vertex could be computed as the point along the trajectory of shortest separation from the beam axis. For two charged particle trajectories, one on the left and one on the right, the vertex could be computed as the average position along shortest separation between the trajectories. The procedure used was simply to find the minimum with respect to two parameters of the trajectory lines. It could be written in analytical form as

$$\begin{aligned} \frac{d|\mathbf{l}_1 - \mathbf{l}_2|^2}{d\lambda_1} &= 2\,(\mathbf{l}_1 - \mathbf{l}_2)\cdot\hat{\mathbf{n}}_1 = 0 \\ \frac{d|\mathbf{l}_1 - \mathbf{l}_2|^2}{d\lambda_2} &= 2\,(\mathbf{l}_2 - \mathbf{l}_1)\cdot\hat{\mathbf{n}}_2 = 0\,, \end{aligned} \tag{5.4}$$

where

$$\begin{aligned} \mathbf{l}_1 &= \lambda_1\,\hat{\mathbf{n}}_1 + \mathbf{r}_1 \\ \mathbf{l}_2 &= \lambda_2\,\hat{\mathbf{n}}_2 + \mathbf{r}_2 \end{aligned}$$

and where $\mathbf{r}_1$ and $\mathbf{r}_2$ were the reference points of trajectories 1 and 2. The resulting minimum equation could be rewritten as a 2×2 matrix equation,

$$\begin{pmatrix} (\mathbf{r}_1 - \mathbf{r}_2)\cdot\hat{\mathbf{n}}_1 \\ (\mathbf{r}_1 - \mathbf{r}_2)\cdot\hat{\mathbf{n}}_2 \end{pmatrix} = \begin{pmatrix} -1 & \hat{\mathbf{n}}_1\cdot\hat{\mathbf{n}}_2 \\ -\hat{\mathbf{n}}_1\cdot\hat{\mathbf{n}}_2 & 1 \end{pmatrix} \begin{pmatrix} \lambda_1 \\ \lambda_2 \end{pmatrix}. \tag{5.4a}$$

This was then solved to obtain the parameters,

$$\begin{pmatrix} \lambda_1 \\ \lambda_2 \end{pmatrix} = \frac{1}{1 - (\hat{\mathbf{n}}_1 \cdot \hat{\mathbf{n}}_2)^2} \begin{pmatrix} -1 & \hat{\mathbf{n}}_1 \cdot \hat{\mathbf{n}}_2 \\ -\hat{\mathbf{n}}_1 \cdot \hat{\mathbf{n}}_2 & 1 \end{pmatrix} \begin{pmatrix} (\mathbf{r}_1 - \mathbf{r}_2) \cdot \hat{\mathbf{n}}_1 \\ (\mathbf{r}_1 - \mathbf{r}_2) \cdot \hat{\mathbf{n}}_2 \end{pmatrix} . \quad (5.4b)$$

The indices {1, 2} were for any combination of

{left trajectory, beam axis}
{right trajectory, beam axis}

or

{left trajectory, right trajectory} .

5.2.1.4 Intersection Point on Detector Planes

Once the trajectory had been reconstructed, the intersection position on any given detector plane could be computed, such as on the dE scintillator and the front or mid plane of the E detector. The intersection position at a given plane can be found by solving a linear vector equation and a nonparallel planar equation, which were given respectively as

$$\begin{aligned} \mathbf{l} &= \mathbf{r} + \lambda \hat{\mathbf{n}} \\ \mathbf{P} &= \mathbf{R} + \eta_1 \hat{\mathbf{u}} + \eta_2 \hat{\mathbf{v}} , \end{aligned} \quad (5.6)$$

where $\mathbf{r}$ was the intersection vector position on the reference, Y1n chamber plane, $\hat{\mathbf{n}}$ the unit vector of the trajectory direction, $\mathbf{R}$ the central point of a detector plane, and $\hat{\mathbf{u}}$ and $\hat{\mathbf{v}}$ the horizontal and vertical unit vectors on the specified detector plane. The unit vectors could be expanded in the unit vector basis of lab coordinate system ($\hat{\mathbf{x}}$, $\hat{\mathbf{y}}$, $\hat{\mathbf{z}}$) as

$$\begin{aligned} \hat{\mathbf{n}} &= \sin\theta\cos\phi\hat{\mathbf{x}} + \sin\theta\sin\phi\hat{\mathbf{y}} + \cos\theta\hat{\mathbf{z}} , \\ \hat{\mathbf{u}} &= \cos\delta_{\mathrm{d}}\hat{\mathbf{x}} - \sin\delta_{\mathrm{d}}\hat{\mathbf{z}} , \\ \hat{\mathbf{v}} &= \hat{\mathbf{y}} , \end{aligned} \quad (5.7)$$

where θ and ϕ were the direction angles of the trajectory and δ_d ($= \theta_{\mathrm{d}} + \alpha_{\mathrm{d}}$) the sum of the position angle and the tilt angle of the detector plane, *e.g.* $\theta_{\mathrm{d}} = +32°$ and $\alpha_{\mathrm{d}} = +15°$ in figure 5.2. Equation (5.6) was then re-expressed in the lab coordinate system as a 3×3 matrix equation

$$\begin{pmatrix} \mathrm{X}_0 - \mathrm{x}_0 \\ \mathrm{Y}_0 - \mathrm{y}_0 \\ \mathrm{Z}_0 - \mathrm{z}_0 \end{pmatrix} = \begin{pmatrix} \sin\theta\cos\phi & -\cos\delta_{\mathrm{d}} & 0 \\ \sin\theta\sin\phi & 0 & -1 \\ \cos\theta & \sin\delta_{\mathrm{d}} & 0 \end{pmatrix} \begin{pmatrix} \lambda \\ \eta_1 \\ \eta_2 \end{pmatrix} , \quad (5.8)$$

which can be solved to give

$$\begin{pmatrix} \lambda \\ \eta_1 \\ \eta_2 \end{pmatrix} = \frac{1}{\sin\theta\cos\phi\sin\delta_d + \cos\theta\cos\delta_d}$$
$$\times \begin{pmatrix} \sin\delta_d & 0 & \cos\delta_d \\ -\cos\theta & 0 & \sin\theta\cos\phi \\ \sin\theta\sin\phi\sin\delta_d & -\sin\theta\cos\phi\sin\delta_d - \cos\theta\cos\delta_d & \sin\theta\sin\phi\cos\delta_d \end{pmatrix} \begin{pmatrix} X_0 - x_0 \\ Y_0 - y_0 \\ Z_0 - z_0 \end{pmatrix} . \tag{5.9}$$

Either λ or η_1 and η_2 could be used to obtain the intersection point on a plane using equation (5.6). Intersection points on the dE and the E detector planes were used for determining the trajectory path length, which in turn was used for calculating the particle speed from the time of flight discussed in the next subsection.

5.2.2 Time of Flight

At the experimental beam energy 197 MeV and certainly at the higher energies, a large number of quasielastically scattered and recoil protons punched through the E detector and formed a reaction tail in the pulse height signals making direct energy determination difficult. Therefore, the time of flight (tof) technique was used to determine the energy of particles. The technique involved determining the flight path and the flight time of particle trajectories between two points in the detector arm. The ratio of the flight path to the flight time was the speed of the particle,

$$\beta c = \frac{\sqrt{(x_2 - x_1)^2 + (y_2 - y_1)^2 + (z_2 - z_1)^2}}{(t_2 - t_1)} , \tag{5.10}$$

from which the particle's kinetic energy and momentum were calculated as follows

$$\begin{aligned} \gamma &= \frac{1}{\sqrt{1 - \beta^2}} , \\ T &= (\gamma - 1) m_N c^2 , \\ \mathbf{P} &= \gamma m_N \beta c \left[\sin\theta\cos\phi\ \hat{\mathbf{x}} + \sin\theta\sin\phi\ \hat{\mathbf{y}} + \cos\theta\ \hat{\mathbf{z}} \right] , \end{aligned} \tag{5.11}$$

where m_N was the particle mass and θ and ϕ were the trajectory angles.

The two referenced points along a trajectory were determined slightly differently for a charged particle and the neutron. For a charged particle, the first

reference point was measured at the dE start scintillator and the second at the E detector. In the case of the neutron, the first point was the vertex of its coincident proton on the other side of the beam and the second was measured at the E detector. See the previous section for a discussion of calculating the intersection position on a detector plane. At the vertex, the time t_{vertex} was obtained by projecting backward along its trajectory from the dE start time of a coincident proton as

$$t_{vertex} = t_{dE} - \frac{|\mathbf{r}_{dE} - \mathbf{r}_{vertex}|}{\beta c}, \tag{5.12}$$

where t_i and $\mathbf{r}_i$ were the time and position at corresponding points and βc was the charged particle speed at the vertex. The time projection was complicated by the loss of kinetic energy by the proton from ionization on its exit through the target chamber aluminum window and one of the silicon microstrip detectors.

In fact, each detected charged particle on its exit passed through one of the silicon microstrip detectors, the target chamber window, the dE detector, the wire chambers, and the surrounding air. Thus, it lost kinetic energy by a number of mechanisms in each medium, such as ionization and excitation. The mean energy loss per unit length is given by the Bethe-Bloch equation [5.1]

$$-\frac{dE}{dx} = 4\pi N_A r_e^2 m_e c^2 \frac{Z_{med}\rho_{med}}{A_{med}} \frac{Z^2}{\beta^2} \left[\ln\left(\frac{2m_e c^2 \gamma^2 \beta^2 T_{max}}{I_{adj}^2}\right) - \beta^2 - \frac{\delta}{2} - \frac{C}{Z_{med}} \right]. \tag{5.13}$$

where Z_{med} is the charge of the medium, ρ_{med} the density, A_{med} the atomic mass, I_{adj} an adjusted ionization potential, δ a density correction applicable at high energy, C for shell corrections, T_{max} the maximum energy transferred to an electron given as

$$T_{max} = \frac{2m_e c^2 \gamma^2 \beta^2}{1 + 2\gamma\frac{m_e}{M} + \left(\frac{m_e}{M}\right)^2}.$$

Although the ionization energy loss could be calculated using the Bethe-Bloch equation, the energy-range empirical formula [5.2]

$$\rho_{med}\, d_{range} = c_1\, T^{c_2}\, [\frac{gm}{cm^3}], \tag{5.14}$$

was found to be more useful. It gives the range d [cm] of a charged particle travelling with a kinetic energy T [MeV] in a medium with density ρ_{med} [gm/cm^3]. If the energy-range formula correctly calculates the average range of travel, then a given kinetic energy T_0 corresponds to a distance d_{range0} and a smaller kinetic energy T_1

corresponds to a shorter distance d_{range1}. The difference between the two distances Δd then was related to the energies T_0 and T_1 as,

$$\rho_{med}\ \Delta d\ =\ c_1\ T_0^{c_2}\ -\ c_1\ T_1^{c_2}\ . \tag{5.15}$$

Conversely, the distance Δd can be identified as the thickness of a medium into which a charged particle enters with an initial kinetic energy T_0 and exits with a final kinetic energy T_1. In the analysis, the tof calculated kinetic energy loss in each medium was corrected backward along the particle's trajectory to obtain its kinetic energy at the vertex. Given a final kinetic energy T_1, the corresponding initial kinetic energy T_0 was calculated for each medium. However, the tof calculation gave only some weighted average kinetic energy across the air medium, not the final kinetic energy. Figure 5.3 (a) and (b) show an average energy loss by the protons in each detector arm calculated using the dE/dx Bethe-Bloch equation. The dominant energy losses of the protons occured in the the dE start scintillators.

After the kinematic variables had been determined for both detector arms, the missing momentum and missing energy of the quasielastic scattering events were calculated as

$$\mathbf{P}_m\ =\ \mathbf{P}_{beam}\ -\ \mathbf{P}_R\ -\ \mathbf{P}_L\ , \tag{5.16a}$$

$$\begin{aligned} E_m\ &=\ m_L\ +\ m_R\ +\ m_{A-1}\ -\ m_{^3He}\ -\ m_{beam} \\ &=\ T_{beam}\ -\ T_L\ -\ T_R\ -\ T_{A-1}\ , \end{aligned} \tag{5.16b}$$

where

$$m_{A-1}\ =\ \sqrt{\left(E_{beam}\ +\ m_{^3He}\ -\ E_L\ -\ E_R\right)^2\ -\ \left(|\mathbf{P}_m|^2\right)^2}\ , \tag{5.17a}$$

$$\begin{aligned} T_{A-1}\ &=\ E_{beam}\ +\ m_{^3He}\ -\ E_L\ -\ E_R\ -\ m_{A-1} \\ &\approx\ \frac{|\mathbf{P}_m|^2}{2\ m_{A-1}}\ . \end{aligned} \tag{5.17b}$$

5.3 Detector Calibrations

The essential functions of the detector arms were to measure the trajectory angle, path length, and time-of-flight (tof) of detected particles. Below, a calibration of the detector arms is discussed. The calibration relied on measurements of detector

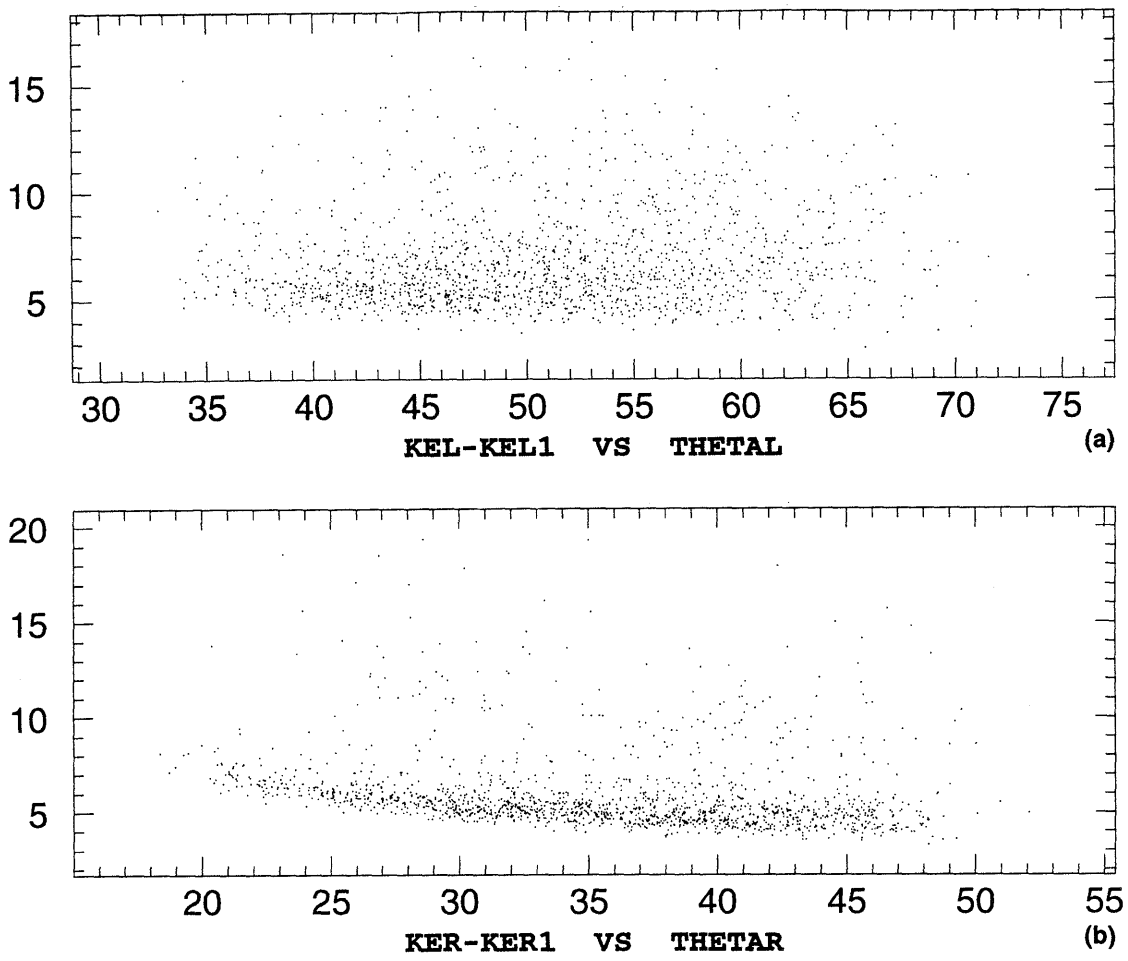

Figure 5.3. The 197 MeV ^{3}He target proton dE/dx total energy loss for traversing the silicon microstrip detector, the aluminum window, the dE scintillator, and the $\approx$1.5 m of air in the left detector arm (a) and in the right detector arm (b) as a function of the trajectory angle in the laboratory.

positions, involved comparison between the end photomultiplier time signals for each scintillator bar using the cosmic ray muon trajectories formed in the E detector stack, and required comparison of the tof in the detector arm to that expected from kinematics for the ^{1}H(p, 2p) data. The angular separations between the two energetic protons were also compared to that expected from theory. During the experiment, cosmic ray data were continuously recorded in the event data stream and ^{1}H(p, 2p) elastic scattering data were collected by flowing hydrogen gas in the target cell at each beam energy. The calibration results of the cosmic ray analysis were provided by the OSU analysis, and the detector positions and angles were provided by the IUCF group who also analyzed the ^{1}H(p, 2p) elastic data for fine

adjustment of the wire chamber angular positions.

5.3.1 Determination of Detector Position and Angle

The absolute position and orientation of the detector components were required in the reconstruction of the trajectory angles (*see section* 5.2.1). To determine the position and orientation of the detector components, *i.e.* with respect to the target cell center and beam direction, measurements were carried out between a number of locations in both detector arms and the target chamber. In each detector arm, distances between corners of the target chamber and the center marks on the front of the nearest pair of wire chamber planes were first measured, followed by measurements of distance between detectors. Also in some cases measurements from fixed points on the target chamber to the E detector ends were possible. Thus not only were positions of other detectors relative to front chamber planes measured, but also some measured relative to target chamber. The measurements were then entered into a CAD drawing of the experimental layout to determine the absolute position and orientation of each detector component with respect to the target cell center and the beam direction. In general, there were sufficient measurements to overconstrain the position. On the CAD drawing, the detector position and orientation were determined with an accuracy of ± 0.2 cm and $\pm 0.3°$ respectively [1.19]. However, the uncertainties of the measurements were small compared to the resolution of the experiment.

The angular separation of the pair of outgoing protons in the elastic reaction ^{1}H(p, 2p) provided a necessary calibration of the relative angular position between the two detector arms. First, the difference of the azimuthal angle between the pair of outgoing elastic protons is

$$\begin{aligned} \Delta\phi &= \phi_R - \phi_L \\ &= 180° , \end{aligned} \tag{5.18a}$$

thus, allowing a check on the ϕ angle defined by vertical position of each wire chamber plane. A large offset from 180° could be seen when the vertical positions of one or more of the wire chamber planes were incorrect. In figure 5.4 (a), a histogram of the $\Delta\phi$ was made showing the center of the peak to be at 180° with a spread of $\pm 1.6°$.

Second, the opening angle between the protons pair is

$$\begin{aligned} \theta_{open} &= \cos^{-1} \left(\sin\theta_L \sin\theta_R \cos(\phi_L - \phi_R) + \cos\theta_L \cos\theta_R \right) \\ &\approx 90° , \end{aligned} \tag{5.18b}$$

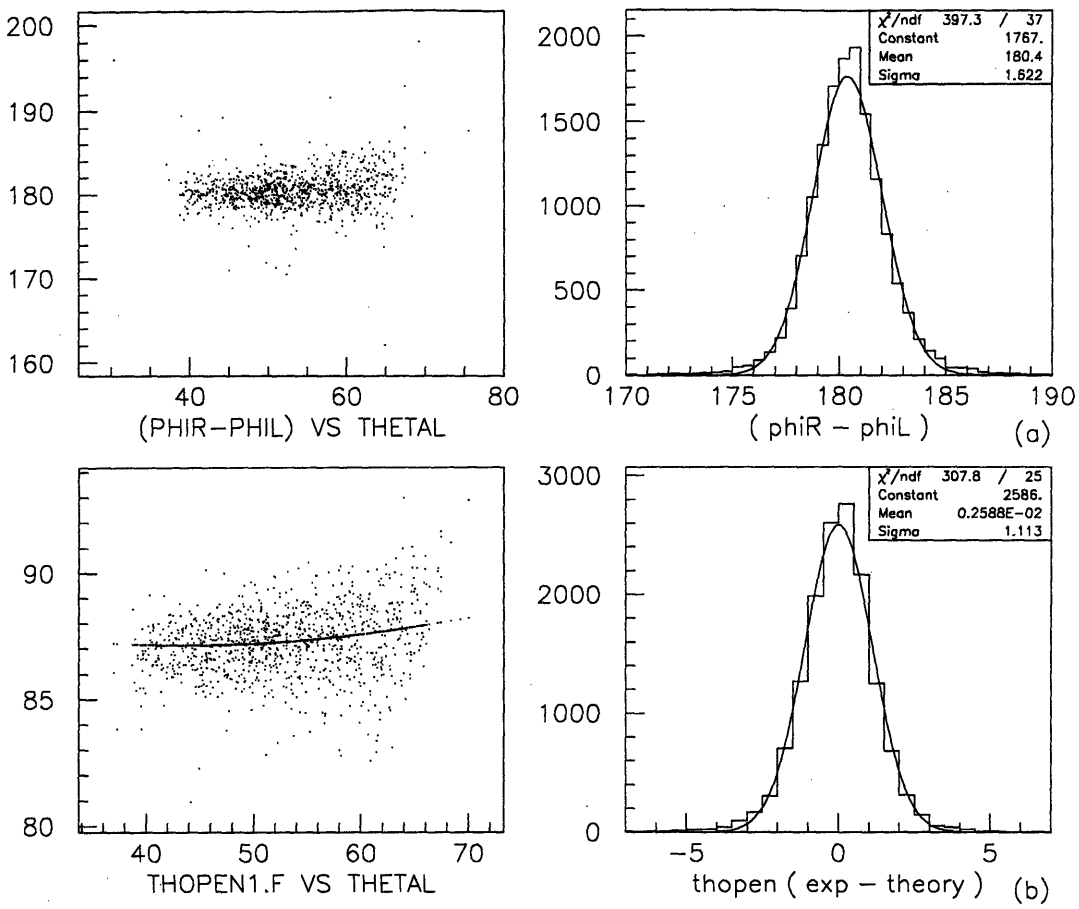

Figure 5.4. (a) ϕ_R - ϕ_L as a function of θ_L; The difference angle was independent of θ_R and was centered at 180.4° ± 1.6°, (b) θ_{open} is plotted as a function of θ_L; the calculated θ_{open} as a function of θ_L is the heavy line. The difference between the two shown in the histogram is only 0.1° ± 1.2°.

which can be exactly calculated as a function of the beam kinetic energy and angle of one of the particles, thus, allowing a check of the relative angular position of the two detector arms. In figure 5.4 (b), the opening angle of the two elastic protons is compared with that obtained as a function of θ_L at 197 MeV beam energy. The histogram shows the difference to be centered within the resolution spread of ±1.1°. However, these two comparisons did not provide an absolute determination of the wire chamber positions.

A third comparison was made in the IUCF analysis to determine the absolute angle orientation of each detector arm. The beam related asymmetry of the $^1H(\overrightarrow{p}, 2p)$ reaction is zero at the 90° scattering angle in the center of mass frame. See the discussion in section 2.3 and figure 2.4. Thus, the zero crossing of the measured beam asymmetry in the c.m. angle θ was used for fine adjustment of the wire chamber angular positions in each detector arm.

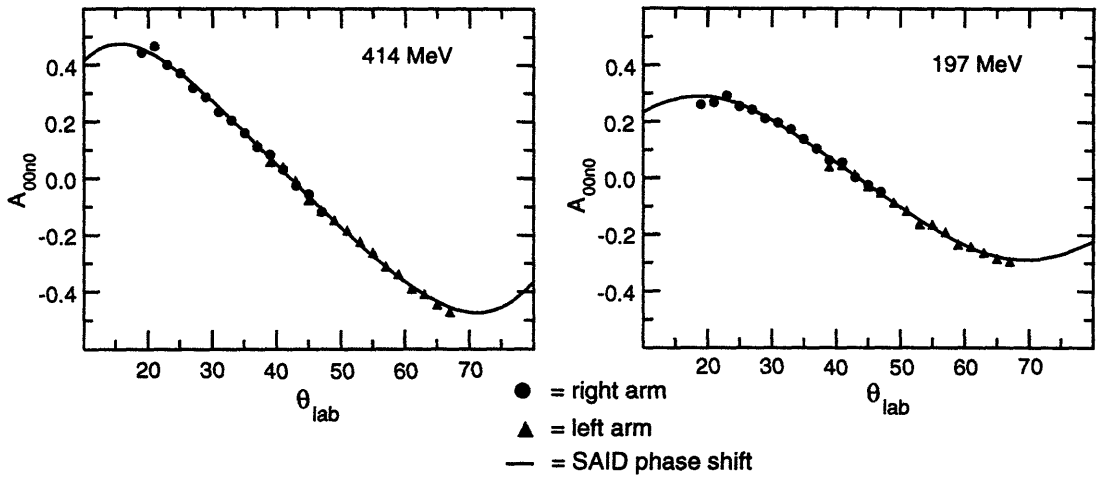

Figure 5.5. Elastic asymmetry of $^1H(\overrightarrow{p}, 2p)$ data for 414 MeV and 197 MeV as a function of laboratory angle. The solid curves are SAID SM89 phase shift solutions [1.18].

5.3.2 Cosmic Ray E Detector Calibration

The time difference between the light signal arriving at the photomultiplier tubes was related to the intersection position of the particle along each scintillator bar as,

$$x_i = \frac{c}{n}\left((tfc_{i-} - tfc_{i+})7.6 + t_{offset_i} \right) [cm] , \qquad (5.19)$$

where c was the speed of light, n the index of refraction = 1.6, and i the detector index number (= 0-5 from top to bottom). The quantity $tfc_{i\pm}$ was the time recorded by a time-to-FERA-converter (tfc) module from the arrival time at the module of a start dE scintillator signal pulse to the arrival time of a pulse from the $\pm$ end of an E detector scintillator bar. In an ideal situation, when a particle intersects the midpoint of the bar, the scintillated light signal travels in both directions toward the ends, arrives at the same time at the photomultiplier tubes and is converted to two electrical pulses that travel through electronic modules and cables and reach the tfc module at the same time. Due to varying cable lengths and different delay times of electronic modules, there was a difference between the arrival times which was adjusted by a time offset, t_{offset_i}, obtained from the calibration.

Cosmic rays that penetrated vertically through all six E detector scintillator bars were used to calibrate the offsets. See figure 5.6. At sea level, almost all the penetrating component of the cosmic ray flux are the muons [1.3]; only $\approx$ 3.5 % are protons. Further, the muon flux has a mean energy of 2 GeV, and therefore, the muons were minimally ionizing and formed a linear trajectory through stack. The recorded cosmic events were then fit to linear trajectories to obtain the time offsets t_{offset_i} for each bar. This part of the analysis was carried out by the collaborators at Ohio State University who had used the scintillator bars in previous experiments. Results of the calibrations are summarized below in table 5.2 for the 197 MeV runs that have been analyzed. The quantity summarized is the position offset, an equivalent of the time offset mentioned above.

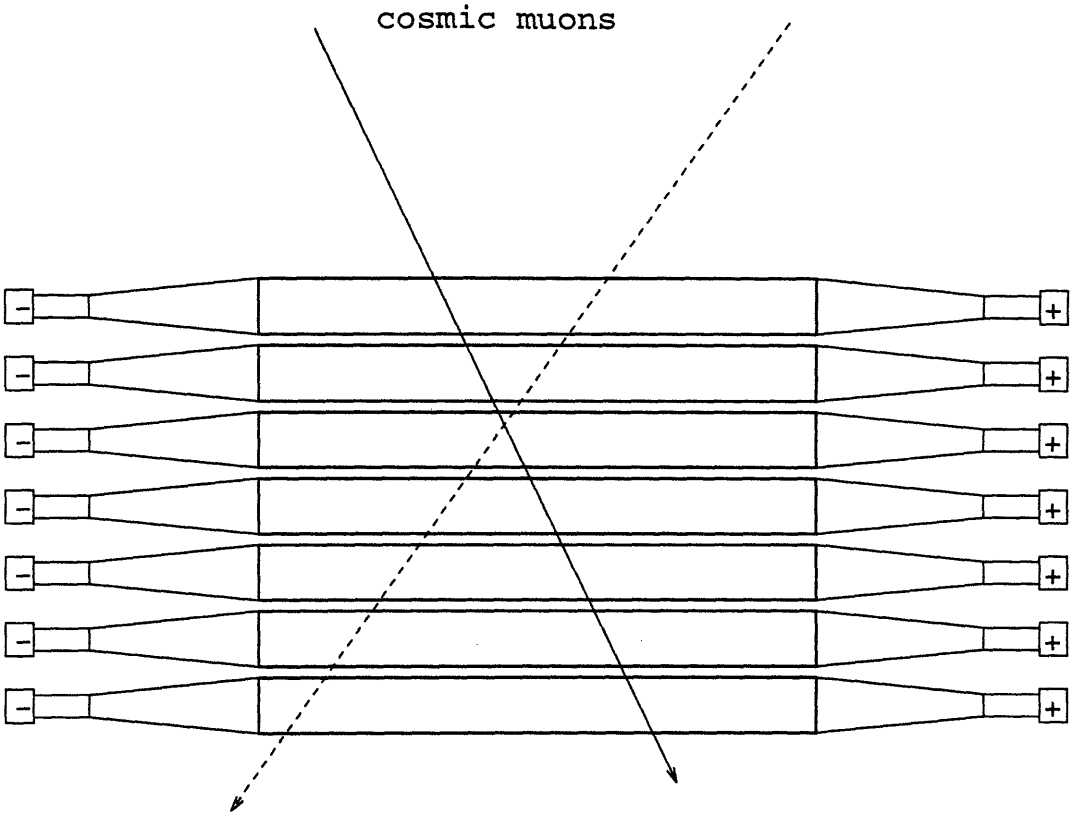

Figure 5.6. Events that triggered all six scintillator bars were recorded as cosmic muons. Due to the $\cos^2\theta$ distribution in the zenith direction, most cosmic events pass through the stack at slight angles.

	Left (cm)	Right (cm)
bar 0	12.22 ±0.16	11.42 ±0.13
bar 1	5.83 ±0.13	10.39 ±0.15
bar 2	-1.75 ±0.17	6.08 ±0.15
bar 3	4.08 ±0.11	-13.56 ±0.05
bar 4	-9.89 ±0.08	24.35 ±0.09
bar 5	-24.86 ±0.09	6.90 ±0.09

Table 5.1. The average and the rms values of the E detector scintillator bar tfc-position offsets of the analyzed 197 MeV data.

5.3.3 Time of Flight Calibration

For charged particles, the tof was measured as the difference between the particle arrival times at the E detector and the dE detector on the same side of the beam. The charged particle tof was then given as

$$\mathrm{tof}^{q} = (\mathrm{tfc}_{E_i} - \mathrm{tdc}_{dE})7.6 + \mathrm{tof}^{q}_{\mathrm{offset}_i}\ [\mathrm{nsec}]\ , \tag{5.20a}$$

where tfc_{E_i} and tdc_{dE} were respectively the digitized time signals of the E detector scintillator bar i and the dE detector on the same side of the beam and $\mathrm{tof}^{q}_{\mathrm{offset}_i}$ the tof offset of scintillator bar i for a particle of charge q.

In the case of the neutron, since it was not detected by the dE detector its tof was measured using the E detector time signal and the dE detector time signal of the coincident proton on the opposite side of the beam. The time signal at the dE detector was projected back to the time at the vertex using the proton speed and the pathlength from the dE detector to the vertex. The proton speed was corrected for the energy loss due to ionization as it traversed through the 3 mm thick dE start scintillator, the 0.012 in thin aluminum window, and the 300 μm thin silicon microstrip detector. The neutron tof was then given as

$$\mathrm{tof}^{n} = (\mathrm{tfc}_{E_i} - \mathrm{tdc}_{dE})7.6 - \Delta t' + \mathrm{tof}^{n}_{\mathrm{offset}_i}\ [\mathrm{nsec}]\ , \tag{5.20b}$$

where the tfc_{E_i} and tdc_{dE} were the digitized time signals of the E detector scintillator bar i and the dE detector on opposite sides of the beam, the $\Delta t'$ the tof (positive quantity) from the dE detector to the vertex, and the $\mathrm{tof}^{n}_{\mathrm{offset}_i}$ was the tof offset of scintillator bar i for the neutron.

To calibrate the tof system, ^{1}H(p, 2p) data were taken at 197 MeV, 300 MeV, and 414 MeV beam energies. The data were fit to a calculation to obtain the offset constants, $\mathrm{tof}^{q}_{\mathrm{offset}_i}$ and $\mathrm{tof}^{n}_{\mathrm{offset}_i}$, at each energy. The calculation of the tof involved the determination of the particle trajectory, the computation of the initial speed from the elastic scattering reaction, and the correction of the particle's speed due to energy loss in each medium of the detector arm—the 300 μm thin silicon microstrip detector, the 0.012 in (0.305 mm) thin aluminum window, the 3 mm thick scintillator, and approximately 1.5 m thick air. The wire chamber gases and the mylar windows on the wire chambers were assumed to cause approximately the same amount of energy loss as air. See figure 5.7 for a fit of the proton tof data to a calculation.

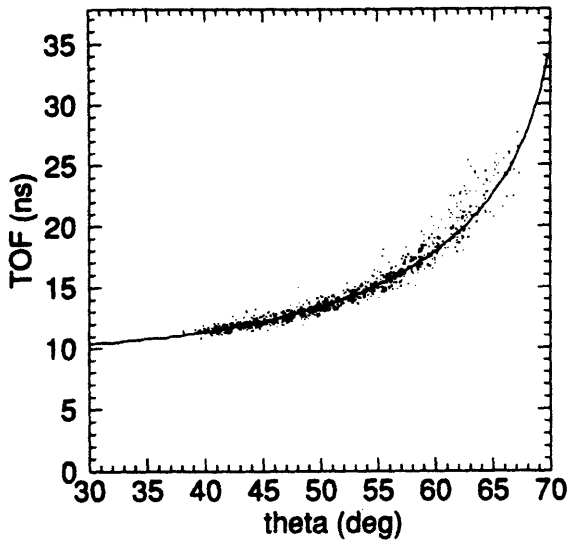

Figure 5.7. Proton time-of-flight ^{1}H(p,2p) data fit to a calculation for 197 MeV beam kinetic energy.

5.3.4 Missing Momentum and Missing Energy Resolution

Once the momentum and energy of the coincident particles were determined, the missing momentum and energy were obtained using equation (5.16). The resolution of the missing momentum and the missing energy were approximately 10-20 MeV and was due to the limited resolution of the electronics timing and the trajectory determination. For the (p,2p) coincidence detection, the missing momentum p_{m_x}, p_{m_y}, and p_{m_z} and the missing energy E_m are shown respectively in figures 5.8 and 5.9, prepared at the University of Wisconsin—Madison.

The mechanism for the coincidence detection of (p,pn) required that the E detector time signal in one detector arm be measured with respect to the dE time signal in the detector arm on opposite side of the beam. Due to the zero energy loss from ionization by the neutron, it was not clear as to the use of protons in ^{1}H(p, 2p) elastic scattering reaction for calibration of this (p,pn) detection mechanism. The approach chosen was to calibrate the time offsets of this (p,pn) mechanism to obtain a similar missing momentum p_m distribution for the ^{3}He neutron as for the ^{3}He proton. See figure 5.8. Also, in Appendix E, a different calibration of the neutron and the proton missing momentum distributions is presented.

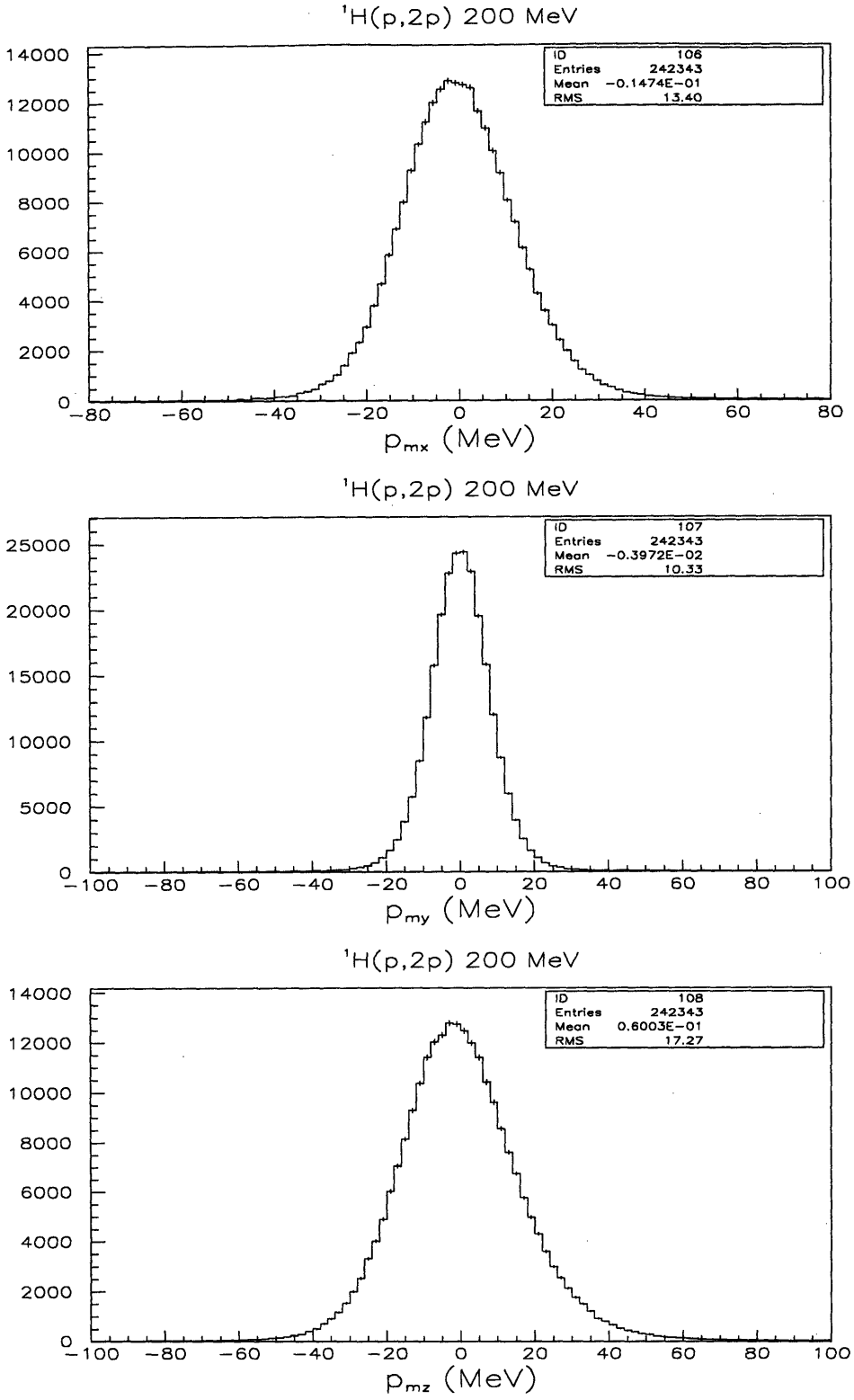

Figure 5.8. Missing momentum $\mathbf{p}_{m_x}$, $\mathbf{p}_{m_y}$, and $\mathbf{p}_{m_z}$ plots of 197 MeV ^{1}H(p,2p) data for protons.

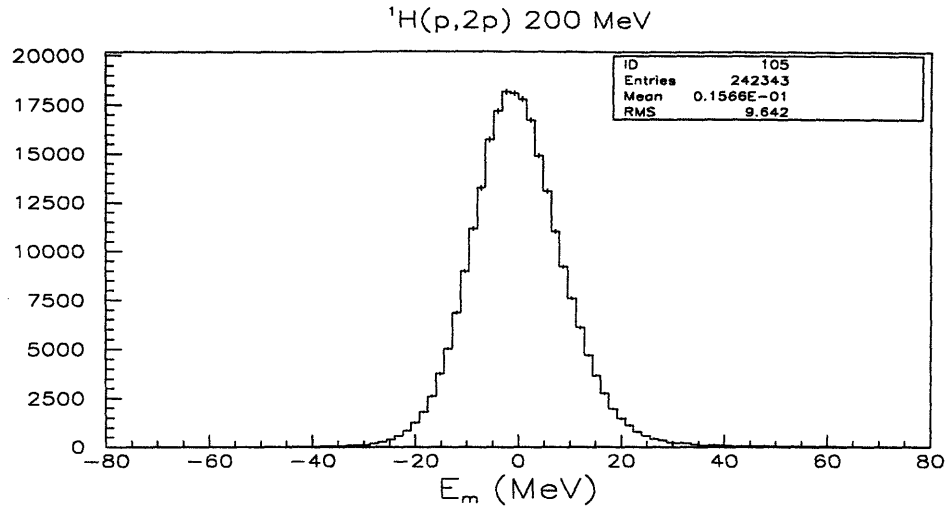

Figure 5.9. Missing energy E_m plot of 197 MeV ^{1}H(p,2p) data for protons.

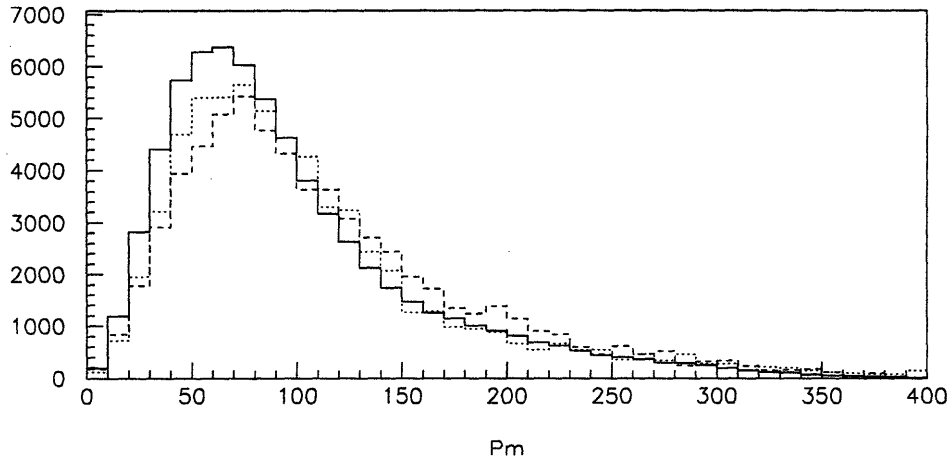

Figure 5.10. Missing momentum p_m plots of 197 MeV ^{3}He(p,2p) and ^{3}He(p,pn) data. The solid curve is for pp, the dashed for LnRp, and the dotted for LpRn.

5.4 Selection of the Event 5 Data

After the construction of kinematic variables for the quasielastic (p,pn) and (p,2p) event 5 data as ntuple 5 data, cut conditions were then applied to sort the events into histograms of the missing momentum, p_m, and the 3-momentum transfer, q according to beam and target spin state and reaction type. There were five different reaction types: pp, LpRn, LnRp, LpRd, and LdRp; the deuterons were not analyzed for this thesis. Also, for each reaction there were four different beam and target spin states namely: beam-up-target-up, beam-up-target-down, beam-down-target-up, and beam-down-target-down.

For the 197 MeV data, there was no pion recorded since its production threshold was at 290 MeV proton beam kinetic energy, and there was a small number of quasielastic deuteron events recorded along with the proton events. The deuterons had a longer tof than the protons for the same kinetic energy and were stopped in the E detector 15 cm thick scintillator bars. Therefore, the deuteron events could be separated from the protons in the plots of E detector pulse height *vs.* tof as in figure 5.11. However, the deuteron events were diluted with the protons of bad tdc timing. In order to see clearly the events with bad tdc timing, data from a hydrogen target run were plotted similarly in figure 5.12. Although it was not done in the analysis of the neutron and the proton data, the events with bad tdc timing could be rejected from the tdc plots below in figures 5.13 and 5.14.

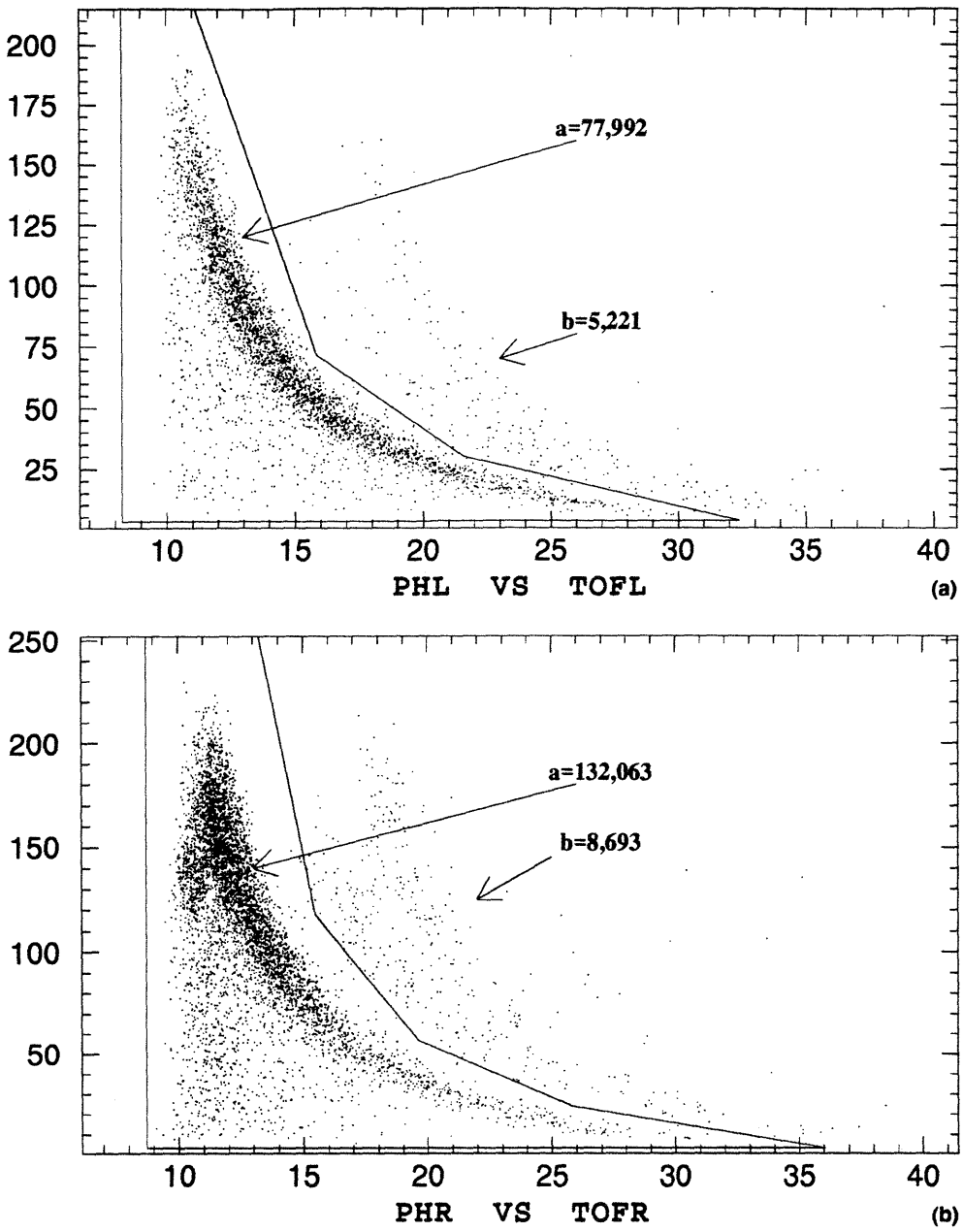

Figure 5.11. The 197 MeV ^{3}He target data E detector pulse height *vs.* tof plot for protons and deuterons in the left detector arm in (a) and the right detector arm in (b). The protons are located in the main loci of events enclosed inside the 2-d cut regions. A small amount of deuterons located just above the protons are diluted with protons that have bad tdc timing. All the deuterons are stopped in both detector arms while the most energetic protons in the right detector arm were not stopped in the E detector as indicated by the sharp bent in the distribution in (b).

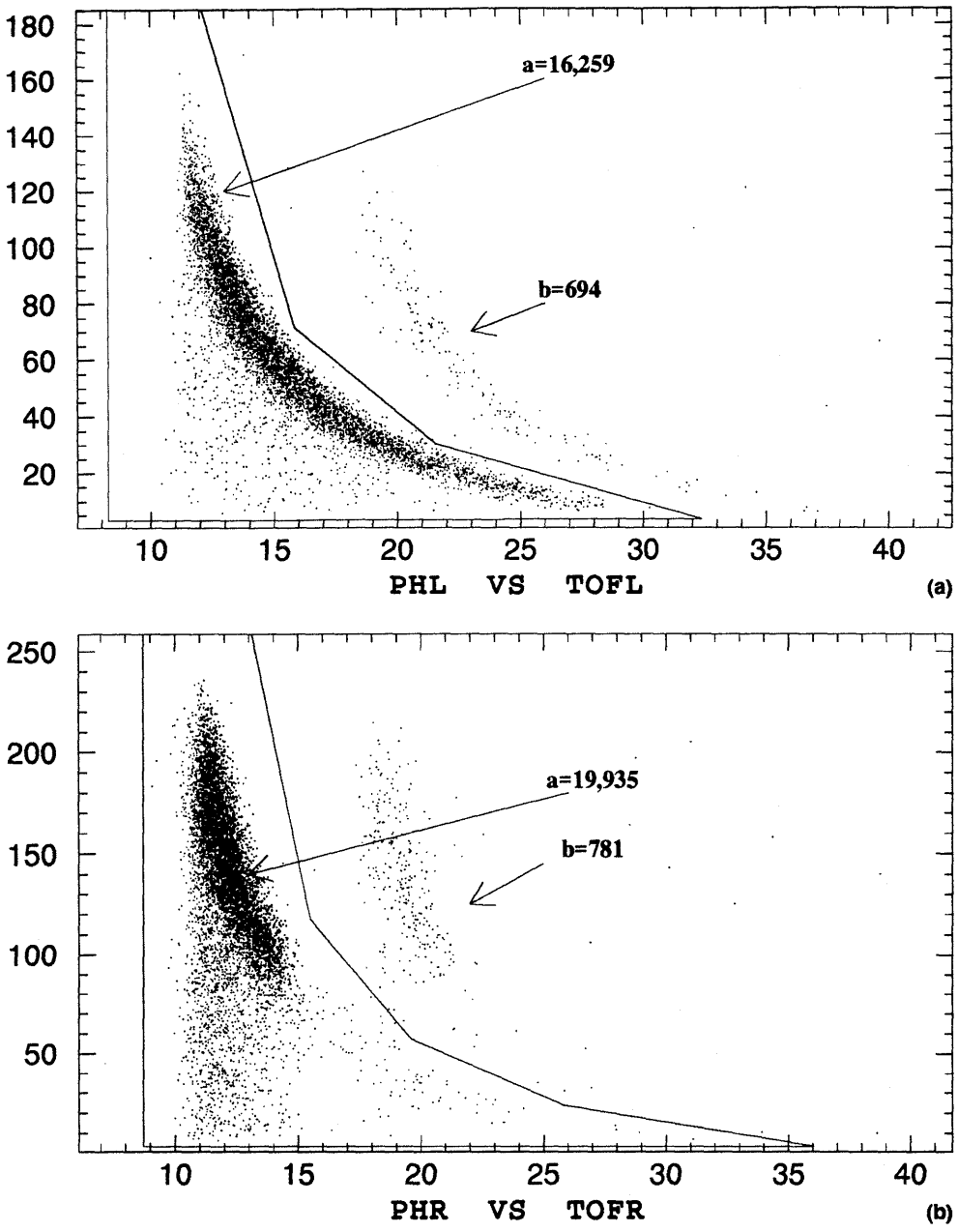

Figure 5.12. The 197 MeV hydrogen target data E detector pulse height *vs.* tof plot for protons in left detector arm in (a) and the right detector arm in (b). The protons are located in the main loci of events enclosed inside the 2-d cut regions. A small number of events located above the cut regions are protons with bad tdc timing.

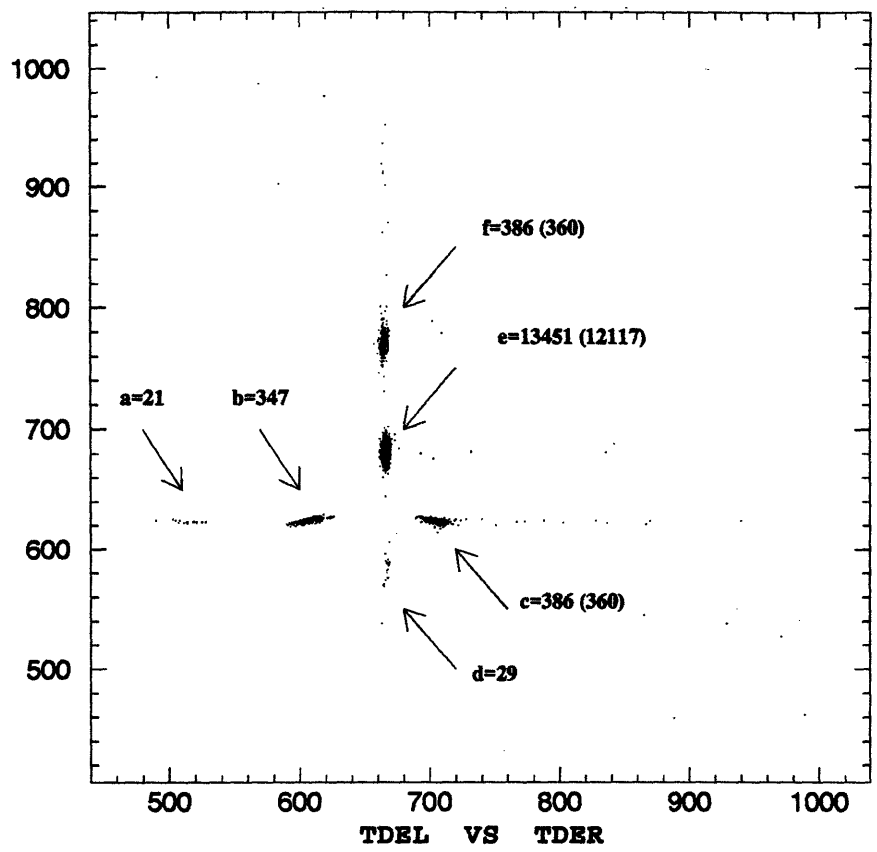

Figure 5.13. The 197 MeV hydrogen target data tdc_{dEL} *vs.* tdc_{dER} scatter plot. There were six loci of scatter points labelled a through f indicated also by the corresponding number of events. The numbers inside parentheses were results of changing the cut conditions from requiring only the four wire chambers in each detector arm to trigger once to requiring also the E detector in each detector arm to trigger once. With the E detector cut condition, the loci a, b, and d reduced to zero number of events.

About 6-7% of the data were degraded from bad tdc timing. In figure 5.13, there were six loci of events on the plot of tdc_{dEL} *vs.* tdc_{dER}. When the cut condition required that the E detector triggered once in addition to each of the four wire chambers, the loci labelled a, b, d reduced to zero and the loci labelled c, e, and f reduced in number—indicated in parantheses. The loci c and f respectively had a delay of about 100 channels (7-8 nsec) from the locus d. The delay also occured in the tfc signals of the EL and ER detectors by the same amount. Note that the events in loci e and f had almost a constant value of tdc_{dER}, *i.e.* they were started by the dER scintillator, while the events in locus c had approximately also a constant value of tdc_{dEL}. Due to the way the delays occured in different signals,

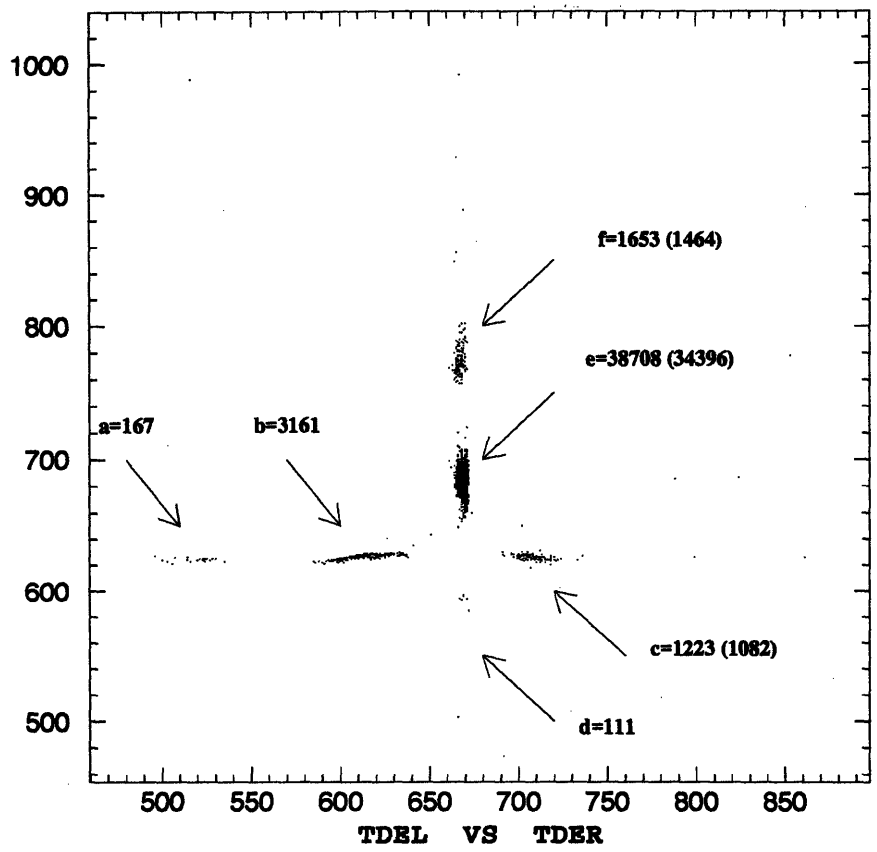

Figure 5.14. The 197 MeV ^{3}He target data tdc_{dEL} *vs.* tdc_{dER} scatter plot. There are six loci of scatter points labelled a through f indicated also by the corresponding number of events. The numbers inside parentheses are results of changing the cut conditions from requiring only the four wire chambers in each detector arm to trigger once to requiring also the E detector in each detector arm to trigger once. With the E detector cut condition, the loci a, b, and d reduced to zero number of events.

the events in locus c resulted a 7-8 nsec shift in the tof of the left detector arm while the events in locus f resulted a 7-8 nsec shift in the tof of the right detector arm.

In figure 5.14, the scatter plot of tdc_{dEL} *vs.* tdc_{dER} for the 197 MeV ^{3}He data show similar characteristics seen in the hydrogen data in figure 5.13. When the cut condition required also to trigger the E detector once in each detector arm, the loci labelled a, b, and d reduced to zero and the loci labelled c, e, and f reduced in number. The loci c and f had delays of 7-8 nsec respectively in tdc_{dEL} and tdc_{dER} values. The tdc timing degradation is given approximately by the ratio of the number of events in loci c and f and the number of events in loci b and e. Therefore, the small number events in loci c and f in figures 5.13 and 5.14 could be thrown out although it was not done in the analysis for this thesis.

From the numbers shown in figures 5.13 and 5.14, charge particle detection efficiency of the E detectors were calculated to be approximately 90%. Similarly, the dE detectors were not 100% efficient. Therefore, it was not sufficient to use only the dE and E detectors for particle identification. By requiring no trigger for all wire chambers in the detector arm, a detected particle was identified as a neutron. In the analysis, particle identification for the neutron, the proton, and the deuteron were defined as

$$\text{neutron} = \overline{\text{dE}} \cdot \text{E} \cdot \prod_i \overline{\text{WC}_i} \cdot \text{mask}$$

$$\text{proton} = (\text{proton cut}) \cdot \text{dE} \cdot \text{E} \cdot \prod_i \text{WC}_i \cdot \text{mask}$$

$$\text{deuteron} = (\text{deuteron cut}) \cdot \text{dE} \cdot \text{E} \cdot \prod_i \text{WC}_i \cdot \text{mask}$$

where the proton cut is shown in figure 5.11, the deuteron cut to be defined around the upper loci of the events in the figure, and the mask was set to reject the data when one of the wire chambers was tripped.

5.5 Background

There was very little background in the 197 MeV ^{1}H(p,2p) elastic scattering data as indicated by the less than 1% signal to background ratio shown in figure 5.15. As discussed in section 5.3.1, the opening angle between the two elastic protons was

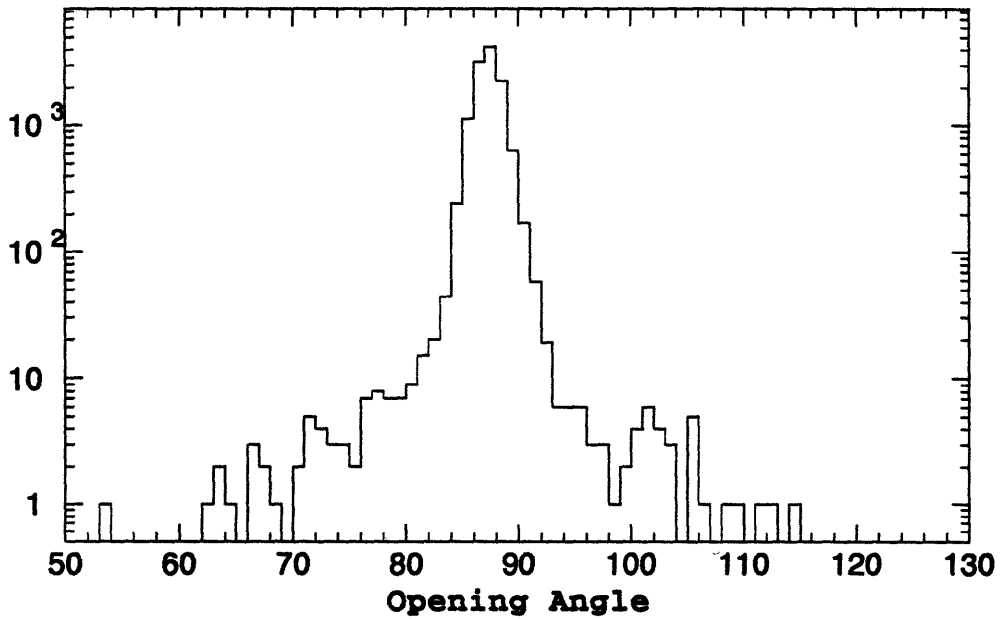

Figure 5.15. Opening angle distribution of ^{1}H(p,2p) elastic scattering events.

around 89° given from kinematics. Any deviation was then a result of a combination of the detector angle resolution and quasielastic events which have with a larger spread in the opening angle distribution.

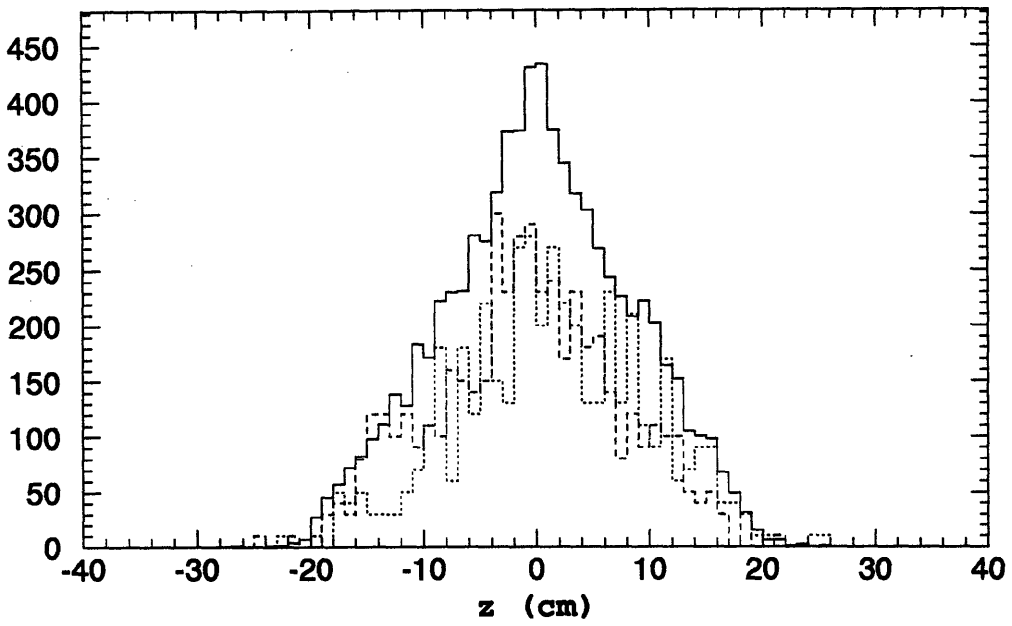

Figure 5.16. The vertex distributions of the 197 MeV data along the cell length for the ^{3}He(p,2p) reaction in continuous line, the ^{3}He(p,pn) LpRn reaction in dashed line ($\times$10), and the ^{3}He(p,pn) LnRp reaction in dotted line ($\times$10).

Moreover, the distribuitons of the vertex positions along the target cell length shown in figure 5.16for the quasielastic data are close to the expected triangle distribution of the target gas density in figure 3.7. Cuts on θ_L and θ_R were applied to remove angle dependence of the vertex distributions.

In figure 5.17 (a), the 197 MeV hydrogen data were sorted for a proton in the left in coincidence with a neutron in the right detector arm, and in 5.17 (b), for a neutron in the left in coincidence with a proton in the right detector arm. The events were binned in histograms respectively as functions of $\mathrm{tdc_{dEL}}$ and the $\mathrm{tdc_{dER}}$. Both of these histograms contained very little (p,pn) events compared to the number of (p,2p) events in 5.17 (c). The small number of events recorded as (p,pn) could have resulted from interaction of target walls with beam halo, scattering from a small trace of ^{3}He gas that was leaking out from its source, accidental triggering or even neutron conversion of the proton on its exit trajectory from interaction with the silicon microstrip detector, the thin aluminum window and the thin dE detector.

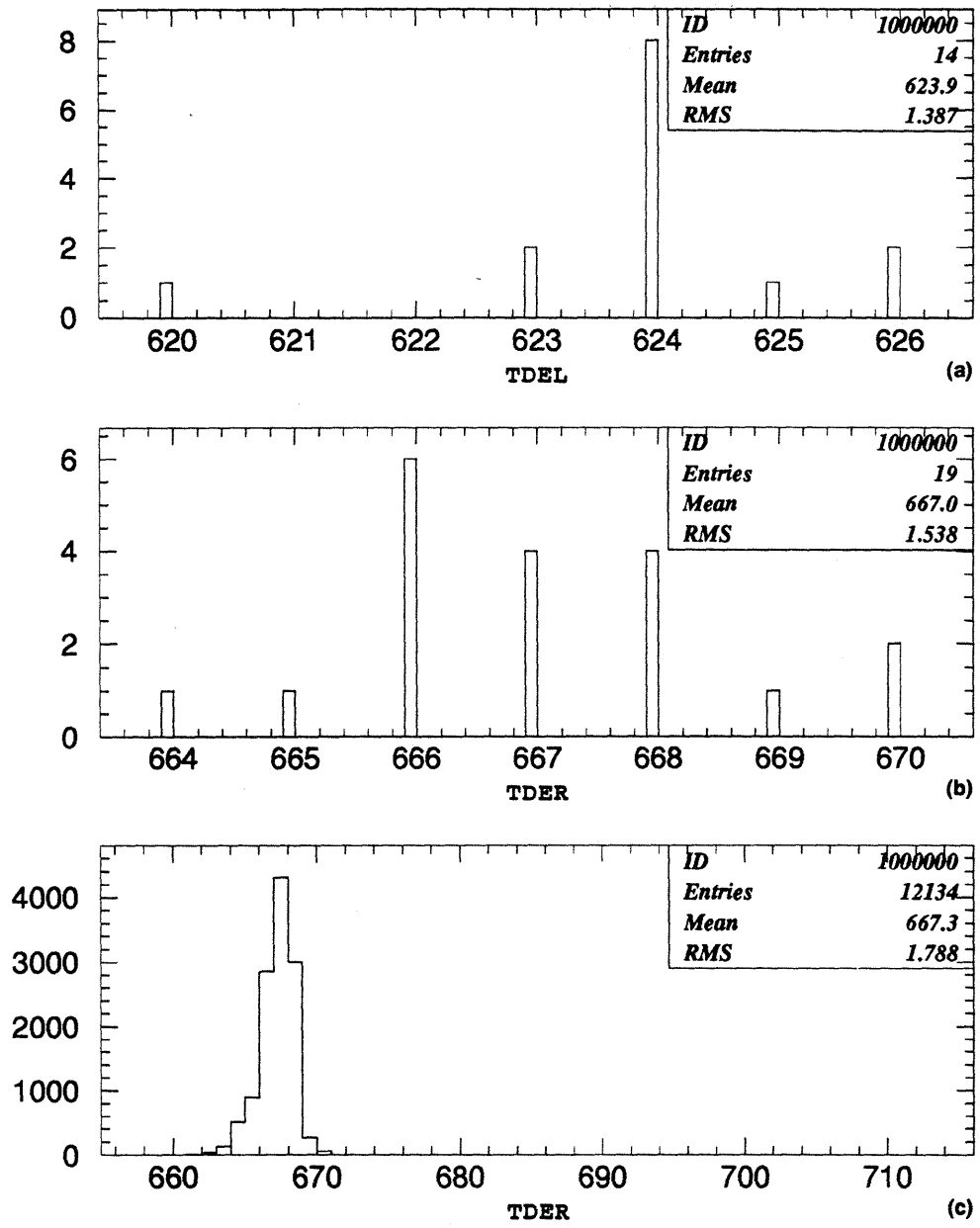

Figure 5.17. The 197 MeV hydrogen target data. Events were sorted in (a) left proton and right neutron; in (b) left neutron and right proton; and in (c) left proton and right proton.

In figure 5.18 (a), the 197 MeV ^{3}He data were sorted for a proton in the left in coincidence with a neutron in the right detector arm. In 5.18 (b), the events were sorted for a neutron in the left in coincidence with a proton in the right detector arm. The events were then binned in histograms respectively as functions of $\mathrm{tdc_{dEL}}$ and the $\mathrm{tdc_{dER}}$ channel numbers. Furthermore in 5.18 (c), the events were sorted for coincident protons in the detector arms. The ratios of the (p,pn) to the (p,2p)

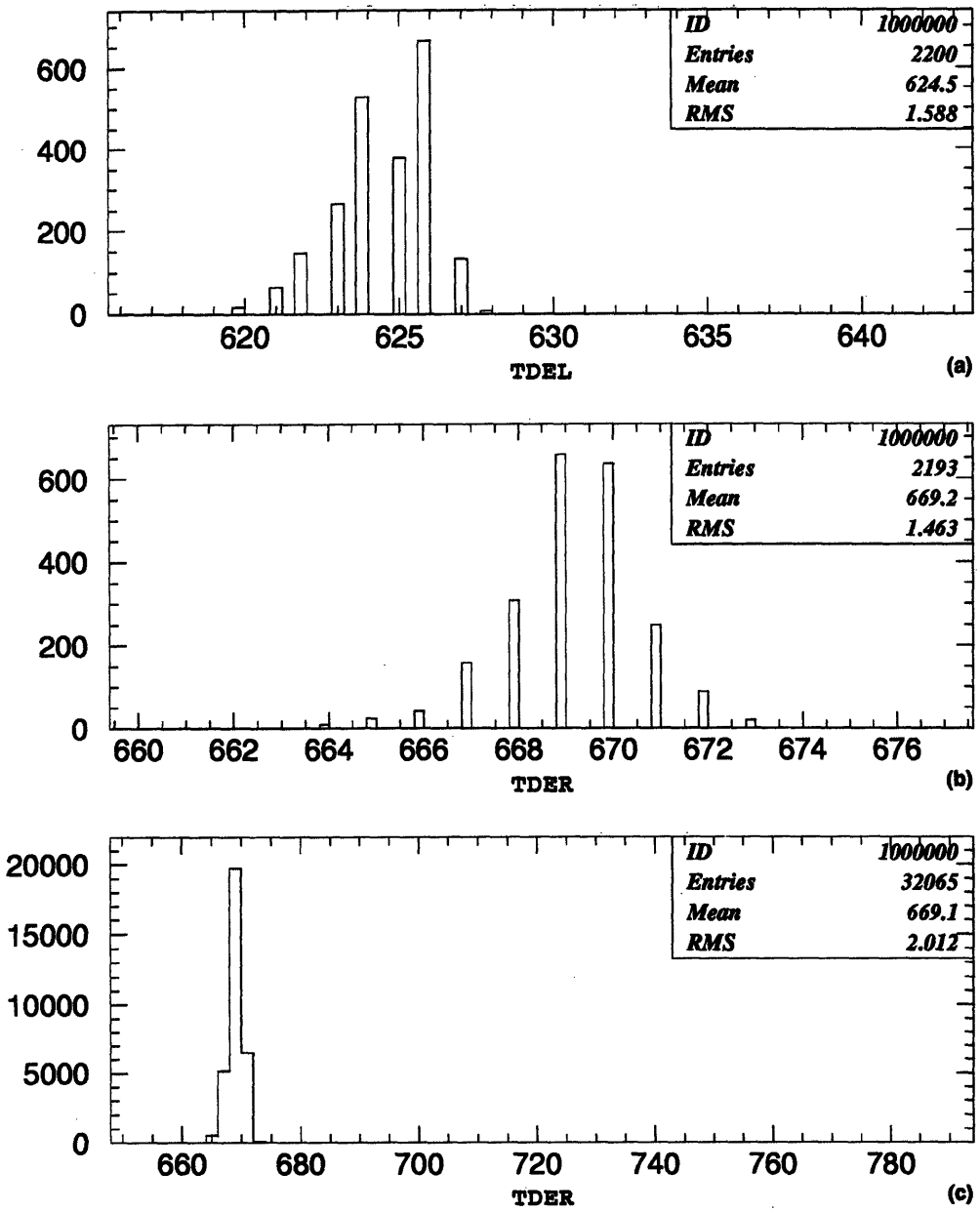

Figure 5.18. The 197 MeV ^{3}He target data. Events were sorted in (a) left proton and right neutron; in (b) left neutron and right proton; and in (c) left proton and right proton.

events with the neutron in the left and the right detector arms were respectively 0.0686 and 0.0684. The ratios were then multiplied by a factor 2, the ratio of the neutrons to the protons the in ^{3}He, resulting in both cases 13.7%. This number can be interpreted as the neutron detection efficiency given the proton detection efficiency was 100%. In addition, the number was close to the expected neutron detection efficiency of 15% for 15 cm thick plastic scintillators.

5.6 Analysis of the Event 9 Data

In the analysis, only a few of the recorded scalers were used. See Appendix D for a complete list of the event 9 scalers. These were the scalers used to obtain the spin sorted averaged deadtimes and beam charges for normalization in the asymmetry cross sections. In addition, the wire chamber scalers were used for generating time masks to reject the data when the wire chambers were tripped off during the experimental cycles.

One or two wire chambers were tripped off frequently during the experiment, suspending the data acquisition temporarily while the scalers in their counting mode continued counting triggers from the other detectors and wire chambers. In the time spectra of a wire chamber scaler, then, large gaps appeared corresponding to the time when the chamber was tripped off and the data acquisition suspended. Since the deadtime scaler counts and beam charge counts were used in the normalization, proper counting of these scalers was done by using, for every second in the experimental cycles, time mask bits which equal to 1 or 0 to exclude the counts whenever a wire chamber was tripped off. The time mask files for the experimental runs were generated by looking at the wire chamber time spectra and setting the mask bits to zero from the time 5 sec before the gap and to the time 5 sec after the gap. Also, the time mask bits were set to zero for 10 sec into the beginning of every cycle to wait for the chamber voltages to stabilize. The time mask files were generated by the analysis at IUCF and were used as an input to this analysis.

The event 9 scalers were recorded at 0.1 sec intervals. In the first step of the event 9 analysis, time spectra of the scalers were then generated by plotting the difference between consecutive scaler counts as a function of the experimental run time. In figure 5.19 are time difference plots of the fastOR and fastTrig scalers.

The triggers fastOR and fastTrig were defined in table 4.1. FastTrig was just the fastOR trigger gated with computer and electronics busy. The ratio of fastOR to fastTrig was used as a correction factor for the electronics and data acquisition deadtime. See in section 5.7 for the use of the correction factor in calculating asymmetries.

The PCT time spectra were fit to a functional form given below, which was the sum of a smooth decay, the calibration pulses, and a background term with a linear time dependence,

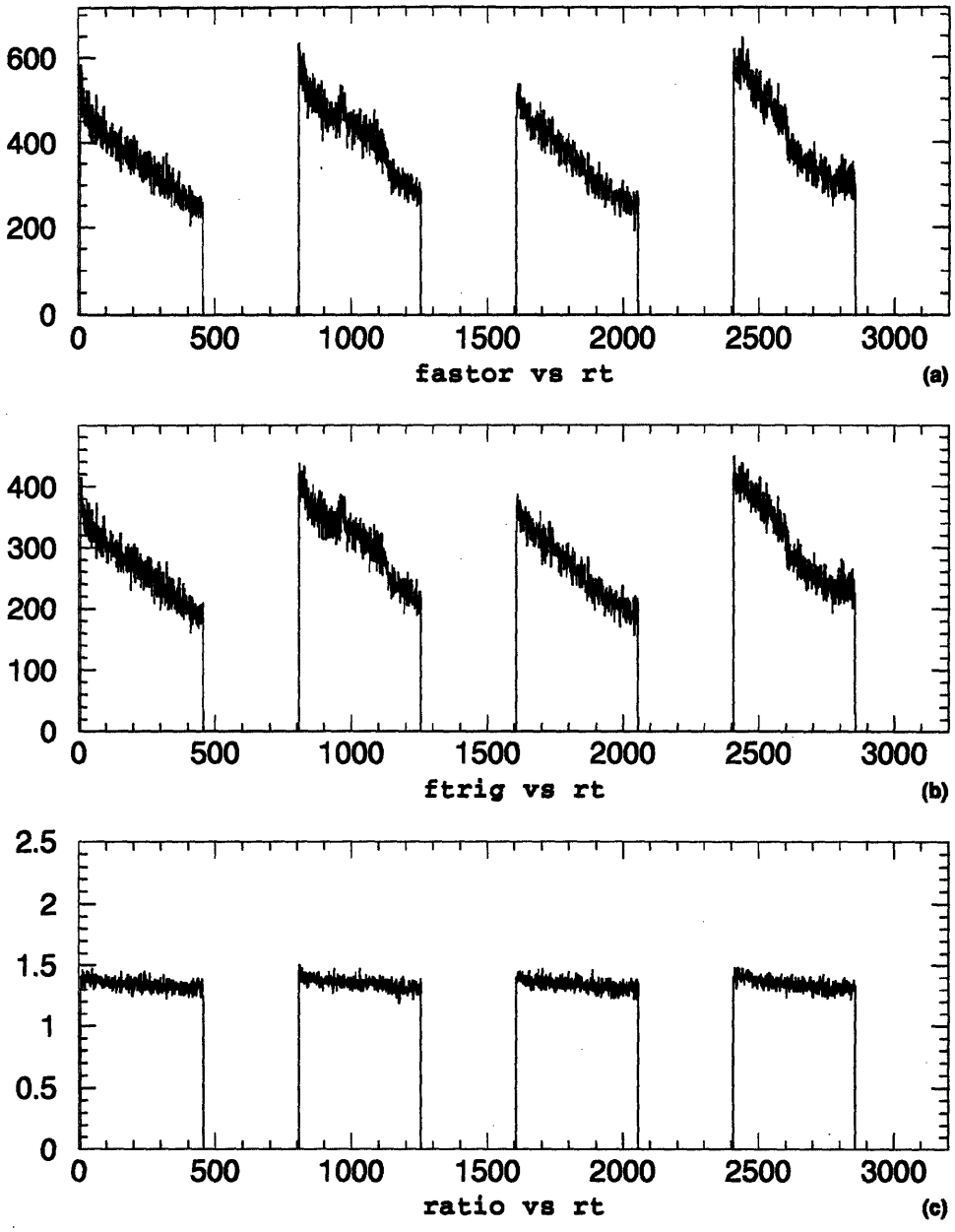

Figure 5.19. In (a) and (b), respectively the time difference scaler spectra of fastOR and fastTrig triggers as functions of the cycle time. In (c), the ratio of fastOR to fastTrig used in the correction of the electronics and the data acquisition deadtime. The cycle length of 800 sec is used only for display purposes.

$$\mathrm{PCT(t)} \;=\; \mathrm{beam(t)} \;+\; \mathrm{calibration(t)} \;+\; \mathrm{background(t)}$$

where

$$\mathrm{beam(t)} = \begin{cases} A_i \; e^{-t_i/\tau_i} & t_i \;<\; t_{i_{cutoff}} \\ 0 & t_i \;>\; t_{i_{cutoff}} \end{cases} ,$$

$$\mathrm{calibration(t)} =$$

$$\begin{cases} \frac{(t_i \;-\; t_{i_0})}{t_{rise}} & t_{i_0} \;<\; t_i \;<\; t_{i_0} \;+\; t_{rise} \\ 1.0 & t_{i_0} + t_{rise} \;<\; t_i \;<\; t_{i_0} + \Delta t - t_{rise} \\ \frac{(t_{i_0} \;+\; \Delta t \;-\; t_i)}{t_{rise}} & t_{i_0} + \Delta t - t_{rise} \;<\; t_i \;<\; t_{i_0} + \Delta t \end{cases} , \qquad (5.21)$$

$$\mathrm{background(t)} = \; B_0 \;+\; B_1 \; t \quad .$$

See figure 5.20. There were local and global parameters in the fitting procedure. The parameters for the exponential decay beam component were adjusted for each cycle while the parameters such as the start time and the width of the calibration pulses and the slope of its edges were adjusted for all cycles. Similarly, the two parameters of the background linear component were adjusted for all cycles. Note that the beam fill and ramp in the experimental cycle were not included in the fit in figure 5.20. Thus, the background linear component deviated slightly from the actual PCT offset over most of each cycle time.

From the functional form obtained, beam charge was calculated for each beam and target spin state. The uncertainty of the beam charge in each spin state was estimated using

$$\delta Q_{ij} \;=\; Q_{ij} \cdot \sqrt{\chi^2_{ij}} \; , \qquad (5.22)$$

where the indices $\{i,j\}$ were for the beam and the target spin states respectively, and the quantity χ^2_{ij} was the relative fluctuation of the PCT data from the fit function. Uncertainty associated with the absolute measurement of the beam charge was not included as it was not pertinent to the calculation of asymmetries. Lastly, the uncertainty due to the difference between the background term and the actual PCT

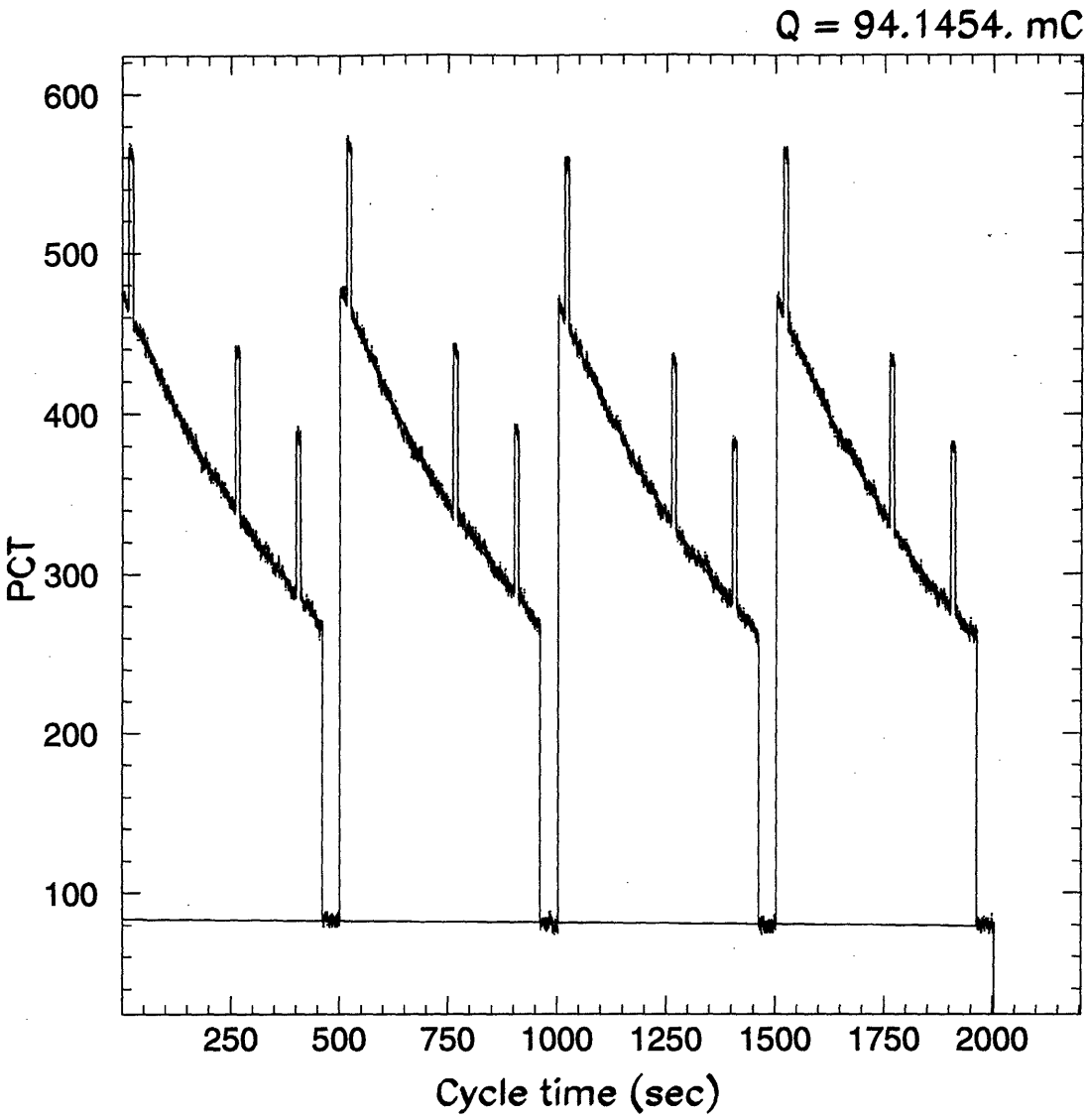

Figure 5.20. Fit to the PCT data to determine the total charge of each beam and target spin configuration in an experimental run. The total beam charge accumulated is 94.1 mC.

offset was expected to be relatively small because the total drift in the PCT offset was less than the fluctation width over the course of four experimental cycles as seen in figure 5.20. Furthermore, the PCT offset appeared not to fluctuate greatly as indicated by the good fit to the data in the interims between PCT offsets.

5.7 Analysis of the Event 6 Data

Data from the luminosity monitors were analyzed at University of Louisville, and a discussion on the calibration and operation of the luminosity monitors can be found in the reference C. Bloch *et al.* [3.10]. In figure 5.21, a comparison of the product Q×pressure×livetime efficiency is made with the luminosity results for the four beam and target spin states.

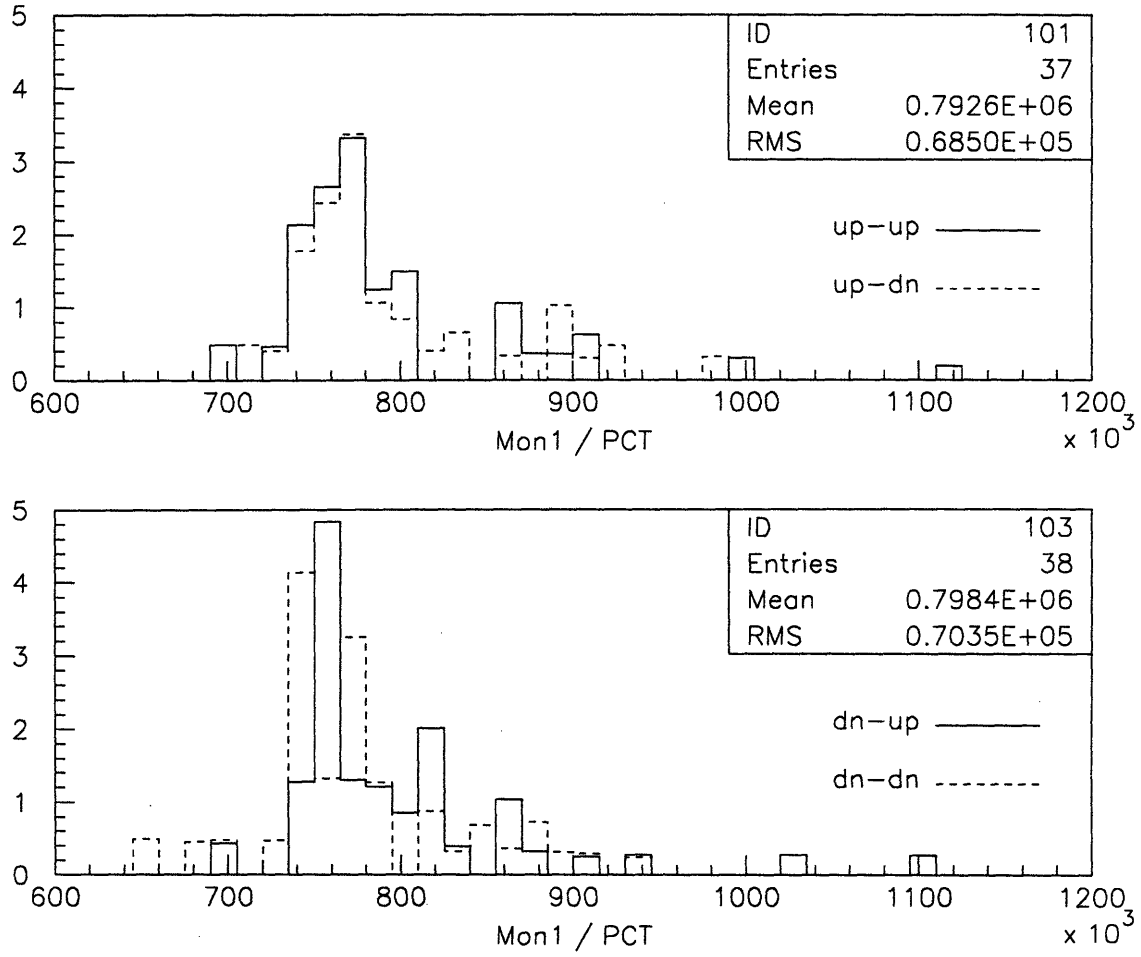

Figure 5.21. Histogram of the ratio of the luminosity monitor1 to PCT normalizations for the different beam-target spin configurations at 197 MeV. The rms values are 3-4 times larger than the statistical uncertainties of the monitor1 normalizations.

The beam polarizations were also extracted from the event 6 data [3.10]. Data were taken with the CE-01 experiment and the CE-25 experiment simultaneously to calibrate the beam asymmetry of the $^3\overrightarrow{He}(\overrightarrow{p},p^3He)$ elastic data of the CE-25 luminosity monitors. The CE-01 experiment was situated in the G section of the Cooler Ring, and H_2 gas was flowed in the experiment to measure the beam polarization using the $^1H(\overrightarrow{p},2p)$ reaction. As the beam polarization was stable around $\pm$70value at each beam energy was sufficient. Thus, the elastic beam asymmetries obtained with the luminosity monitors could be converted to beam polarizations even though the data included breakup channels. In table 5.2 below, a summary of the beam polarization measured in the CE-01 experiment.

MeV	Beam Polarizations
197	0.771 ± 0.028, -0.675 ± 0.027
414	0.724 ± 0.029, -0.645 ± 0.029

Table 5.2. Beam polarization measured with the CE-01 experiment at 197 and 414 MeV beam energies [3.10].

5.8 Extraction of the Asymmetries

The experiment measured the quasielastic events of the ^{3}He(p,2p), ^{3}He(p,pn), or ^{3}He(p,pd) reactions which were binned in histograms as yields as a function of a given parameter, such as the missing momentum. The yield of a particular reaction of quasielastic events for a given beam and target polarizations combination can be expressed as follows, as the quasielastic scattering cross section equation from equation (2.30) integrated over time, the extended target, and the angle acceptances of the detector arms:

$$Y_{ij} = L_{ij}\epsilon_{ij}\sigma_\circ \left\{ 1 + \overline{P}_{b_i}\mathcal{A}_{00n0} + \overline{P}_{t_j}\mathcal{A}_{000n} + \overline{P_{b_i}P_{t_j}}\mathcal{A}_{00nn} + \overline{P_{b_i}P_{t_j}}\mathcal{A}_{00ss} \right\}, \tag{5.23a}$$

where

$$\sigma_\circ = \frac{1}{s_{ij}} \int \rho_{target_{ij}}(z)dz \int_{\Omega_1(z)\Omega_2(z)} \frac{d\sigma_\circ}{d\Omega_1 d\Omega_2 dp_{A-1}}\, d\Omega_1\, d\Omega_2 \tag{5.23b}$$

$$\mathcal{A}_{00ij}\,\sigma_\circ = \frac{1}{s_{ij}} \int \rho_{target_{ij}}(z)dz \int_{\Omega_1(z)\Omega_2(z)} \frac{d\sigma_\circ}{d\Omega_1 d\Omega_2 dp_{A-1}}\, A_{00ij}\, (\hat{\imath}\cdot\hat{\mathbf{P}}_b)(\hat{\jmath}\cdot\hat{\mathbf{P}}_t)\, d\Omega_1\, d\Omega_2 \tag{5.23c}$$

$$L_{ij} = \int_{\{T_{ij}\}} \mathcal{L}_{ij}(t)\cdot\epsilon_{ij}\, dt \tag{5.23d}$$

$$s_{ij} = \int \rho_{target_{ij}}(z)dz \tag{5.23e}$$

$$\overline{P}_{\{b_i,\,t_j\}}\, L_{ij} = \int_{\{T_{ij}\}} P_{\{b_i,\,t_j\}}\, \mathcal{L}_{ij}(t)\, \epsilon_{ij}\, dt \tag{5.23f}$$

and

$$\overline{P_{b_i}P_{t_j}}\, L_{ij} = \int_{\{T_{ij}\}} P_{b_i}P_{t_j}\, \mathcal{L}_{ij}(t)\, \epsilon_{ij}\, dt\ . \tag{5.23g}$$

The index i (j) stands for the beam (target) polarization state, and there are a total of four possible different spin states when both the beam and target particles are polarized. The quantities $\overline{P}_{\{b_i,\,t_j\}}$ and $\overline{P_{b_i}P_{t_j}}$ are the luminosity and efficiency averaged polarizations. The overall detection efficiency ϵ_{ij} can be separated into particle interaction efficiency and electronics efficiency due to electronics or computer busy. The particle interaction efficiency was expected to be constant for each

experimental run while the electronics efficiency was expected to be rate dependent. The particle interaction efficiency, however, could vary over long periods of time. Finally, the luminosity $\mathcal{L}_{ij}(t)$ is a product of the beam current and target thickness, which can be expressed as

$$\mathcal{L}_{ij}(t) = \frac{I_{b_{ij}}(t)}{1.602 \times 10^{-13}} \cdot s_{ij}(t) \ , \tag{5.24}$$

where I(t) is the beam current in units of μA, typically 60 μA; s(t) the target thickness, typically 1.5×10^{14} atoms sec^{-1}; and $\mathcal{L}_{ij}(t)$ the luminosity, typically 6×10^{28} events cm^{-2} sec^{-1}. Therefore the integrated luminosity L_{ij} is in units of events sec^{-1}.

Comparing the above equation (5.23a) with equation (2.30), one finds that in equation (5.23a) the terms containing the longitudinal polarization have been neglected since both the beam and the target particles were polarized along the laboratory vertical direction. To a good approximation, the beam and the target polarizations were normal with respect to the horizontal plane. Due to the small transverse dimensions of of the target cell, the maximum deviation of the beam was $\pm 2°$ vertically or horizontally. In addition, any nonvertical component to the beam polarization would rapidly average to zero due to g$-$2 precession. Moreover, the alignment tolerance of target polarization allowed only a maximum of 1-2° deviation from the vertical direction; the target chamber was close to perpendicular to the uniform, vertical B field.

In the yield expression in equation (5.26), the term A_{00ss} contributed only as a small correction since the factor

$$(\hat{\mathbf{s}} \cdot \hat{\mathbf{P}}_{b_i})(\hat{\mathbf{s}} \cdot \hat{\mathbf{P}}_{t_j}) \ = \ \sin^2(\phi_{scat}) \tag{5.25}$$

was small due to the limitation of the acceptance in the azimuthal angle ϕ_{scat} to $\pm 15°$. In figure 5.22, a comparison using the Monte Carlo simulation with the experimental acceptance was made of the weightings by $\cos^2(\phi_{scat})$ and by $\sin^2(\phi_{scat})$, showing that any observables multiplied with the weighting $\sin^2(\phi_{scat})$ was expected to contributed at the small values of 2-3%.

Next, the yield of the four different beam and target polarization combinations

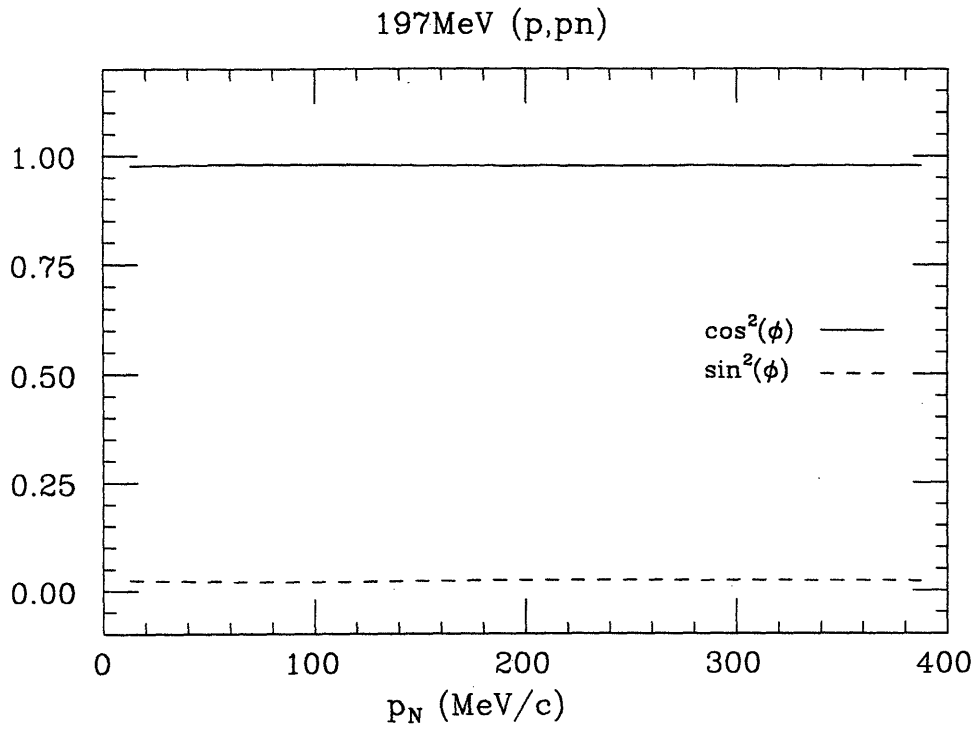

Figure 5.22. A 197 MeV beam kinetic energy, Monte Carlo simulation of the weightings by $\cos^2(\phi_{\rm scat})$ and by $\sin^2(\phi_{\rm scat})$.

can be written as

$$\begin{pmatrix} Y_{\uparrow\uparrow} \\ Y_{\uparrow\downarrow} \\ Y_{\downarrow\uparrow} \\ Y_{\downarrow\downarrow} \end{pmatrix} = \begin{pmatrix} L_{\uparrow\uparrow} & L_{\uparrow\uparrow}\overline{P}_{b\uparrow} & L_{\uparrow\uparrow}\overline{P}_{t\uparrow} & L_{\uparrow\uparrow}\overline{P}_{b\uparrow}P_{t\uparrow} \\ L_{\uparrow\downarrow} & L_{\uparrow\downarrow}\overline{P}_{b\uparrow} & L_{\uparrow\downarrow}\overline{P}_{t\downarrow} & L_{\uparrow\downarrow}\overline{P}_{b\uparrow}P_{t\downarrow} \\ L_{\downarrow\uparrow} & L_{\downarrow\uparrow}\overline{P}_{b\downarrow} & L_{\downarrow\uparrow}\overline{P}_{t\uparrow} & L_{\downarrow\uparrow}\overline{P}_{b\downarrow}P_{t\uparrow} \\ L_{\downarrow\downarrow} & L_{\downarrow\downarrow}\overline{P}_{b\downarrow} & L_{\downarrow\downarrow}\overline{P}_{t\downarrow} & L_{\downarrow\downarrow}\overline{P}_{b\downarrow}P_{t\downarrow} \end{pmatrix} \begin{pmatrix} \sigma_o \\ \sigma_o A_{00n0} \\ \sigma_o A_{000n} \\ \sigma_o(A_{00nn} + A_{00ss}) \end{pmatrix} . \quad (5.26)$$

In practice, the target thickness was known only with a relative precision, and only the asymmetry cross sections A_{00ij} can be measured and not the unpolarized cross section σ_o. As described in section (3.3.4) on the target storage cell, the target thickness depended on the target cell geometric conductance and gas flow rate, neither of which was known to better than $\pm 10\%$ in the experiment. In the analysis, the luminosity and integrated luminosity for each beam and target polarizations

combination were then replaced by their corresponding relative quantities,

$$\begin{aligned} \mathcal{L}' &= \int\limits_{\{T_{ij}\}} I_{b_{ij}}(t)\, P_{cell_{ij}}(t) \\ L'_{ij} &= \int\limits_{\{T_{ij}\}} I_{b_{ij}}(t)\, P_{cell_{ij}}(t)\, \epsilon_{E_{ij}}\, dt \end{aligned} \tag{5.27}$$

where $I_{b_{ij}}(t)$ was the beam current in μA, $P_{cell_{ij}}(t)$ the gas pressure in Torr in the optical pumping glass cell, and $\epsilon_{E_{ij}}(t)$ efficiency due to the computer and trigger electronics deadtime. The overall detection efficiency ϵ_{ij} was replaced by the electronics efficiency $\epsilon_{E_{ij}}$ since the particle interaction efficiency was expected to be constant in each experimental run. Moreover, since the pumping cell pressure was constant on the time scale of the experimental cycle, it could be replaced in the above expression with its time averaged constant

$$\begin{aligned} \overline{P}_{cell_{ij}} &= \frac{1}{T_{ij}} \int P_{cell_{ij}}(t)\, dt \\ &= \frac{1}{\mathcal{N}_{ij}} \sum_{t=1}^{\mathcal{N}_{ij}} \sum_{k=1}^{n_t} \frac{P_{cell_{ij}k}}{n_t}\ , \end{aligned} \tag{5.28}$$

where the first summation over k was for all events in a 0.1 sec time interval and the second summation over t was for the 0.1 sec intervals in the total time T_{ij} of spin state $\{i,j\}$. The averaged results for each run were stored as a vector of spin states to be used in calculating the asymmetries.

The electronics efficiency $\epsilon_{E_{ij}}$, on the other hand, was rate dependent and thus also time dependent through the beam current, and it could be integrated together with the beam current to get

$$L'_{ij} = \overline{P}_{cell_{ij}} \int\limits_{\{T_{ij}\}} I_{b_{ij}}(t)\, \epsilon_{E_{ij}}\, dt\ , \tag{5.29}$$

or could be incorporated in the deadtime corrected yield as

$$Y'_{ij} = \int\limits_{T_{ij}} R_{ij}(t) \cdot \epsilon_{E_{ij}}^{-1}\, dt\ , \tag{5.30}$$

where $R_{ij}(t)$ was the rate of detected quasielastic events. This redefined the time integrated luminosity as

$$\begin{aligned} L'_{ij} &= \overline{P}_{cell_{ij}} \int\limits_{\{T_{ij}\}} I_{b_{ij}}(t)\, dt \\ &= \overline{P}_{cell_{ij}} Q_{ij} \end{aligned} \tag{5.31}$$

The deadtime correction to the yield was used in our analysis although in hind sight it would have been simpler to incorporate the deadtime efficiency into the luminosity as in equation (5.29).

As mentioned previously, the beam polarization P_{b_i} was obtained by the luminosity monitors averaged over at least one experiment cycle. Therefore, as it has no time dependence in each experimental run, it could be taken outside the average of the double polarization as

$$\begin{aligned} \overline{P_{b_i} P_{t_j}} &= \frac{P_{b_i}}{L_{ij}} \int_{\{T_{ij}\}} P_{t_j}\, \mathcal{L}(t)\, \epsilon_E \, dt \\ &= P_{b_i} \overline{P}_{t_j} \, . \end{aligned} \tag{5.32}$$

The luminosity weighted average of the target polarizations could be simply computed as

$$\overline{P}_{t_j} = \frac{1}{N_{ij}} \sum_{k=1}^{N_{ij}} P_{t_j k} \tag{5.33}$$

However, in the analysis it was averaged over time as below,

$$\begin{aligned} \overline{P}_{t_j} &= \frac{1}{T_{ij}} \int_{T_{ij}} P_{t_i}(t) dt \\ &= \frac{1}{\mathcal{N}_{ij}} \sum_{t=1}^{\mathcal{N}_{ij}} \sum_{k=1}^{n_t} \frac{P_{t_j k}}{n_t} \end{aligned} \tag{5.34}$$

where the first summation over k was for all events in a 0.1 sec time interval and the second summation over t was for the 0.1 sec intervals in the total time T_{ij} of spin state $\{i,j\}$. Also, the averaged results for each run were stored as a vector of spin states to be used in calculating the asymmetries. The time averaged target polarization was not expected to be different from the luminosity averaged value as the target polarization was constant. However, differences arose from a period of 10-20 sec in the beginning of the 300 sec period of the target cycle when the polarization was still rising 10 sec after it was reversed and also from variation of the gas pressure in the pumping cell.

The yield matrix equation (5.26) can then be re-expressed in terms of the

redefined quantities as

$$\begin{pmatrix} Y'_{\uparrow\uparrow} \\ Y'_{\uparrow\downarrow} \\ Y'_{\downarrow\uparrow} \\ Y'_{\downarrow\downarrow} \end{pmatrix} = \begin{pmatrix} L'_{\uparrow\uparrow} & L'_{\uparrow\uparrow}P_{b\uparrow} & L'_{\uparrow\uparrow}P_{t\uparrow} & L'_{\uparrow\uparrow}P_{b\uparrow}P_{t\uparrow} \\ L'_{\uparrow\downarrow} & L'_{\uparrow\downarrow}P_{b\uparrow} & L'_{\uparrow\downarrow}P_{t\downarrow} & L'_{\uparrow\downarrow}P_{b\uparrow}P_{t\downarrow} \\ L'_{\downarrow\uparrow} & L'_{\downarrow\uparrow}P_{b\downarrow} & L'_{\downarrow\uparrow}P_{t\uparrow} & L'_{\downarrow\uparrow}P_{b\downarrow}P_{t\uparrow} \\ L'_{\downarrow\downarrow} & L'_{\downarrow\downarrow}P_{b\downarrow} & L'_{\downarrow\downarrow}P_{t\downarrow} & L'_{\downarrow\downarrow}P_{b\downarrow}P_{t\downarrow} \end{pmatrix} \begin{pmatrix} \sigma'_\circ \\ \sigma'_\circ \mathcal{A}_{00n0} \\ \sigma'_\circ \mathcal{A}_{000n} \\ \sigma'_\circ(\mathcal{A}_{00nn} \\ +\mathcal{A}_{00ss}) \end{pmatrix}, \tag{5.36}$$

where the unpolarized cross section $\sigma_\circ$ is replaced with some uncorrected cross section $\sigma'_\circ$. The above matrix equation can be inverted to give,

$$\begin{pmatrix} \sigma'_\circ \\ \sigma'_\circ \mathcal{A}_{00n0} \\ \sigma'_\circ \mathcal{A}_{000n} \\ \sigma'_\circ(\mathcal{A}_{00nn} \\ +\mathcal{A}_{00ss}) \end{pmatrix} = \begin{pmatrix} M_{11} & M_{12} & M_{13} & M_{14} \\ M_{21} & M_{22} & M_{23} & M_{24} \\ M_{31} & M_{32} & M_{33} & M_{34} \\ M_{41} & M_{42} & M_{43} & M_{44} \end{pmatrix} \begin{pmatrix} Y'_{\uparrow\uparrow}/L'_{\uparrow\uparrow} \\ Y'_{\uparrow\downarrow}/L'_{\uparrow\downarrow} \\ Y'_{\downarrow\uparrow}/L'_{\downarrow\uparrow} \\ Y'_{\downarrow\downarrow}/L'_{\downarrow\downarrow} \end{pmatrix}, \tag{5.37}$$

where $\sigma'_\circ$ is a polarization weighted average over the four spin states of the normalized yield Y'_{ij}/L'_{ij}, $\sigma'_\circ\ \mathcal{A}_{00ij}$ some polarization weighted combination of the the normalized yield, and M_{ij} matrix element some function of the beam and target polarizations. If the beam and target polarizations were 100%, then the above matrix equation becomes

$$\begin{pmatrix} \sigma'_\circ \\ \sigma'_\circ \mathcal{A}_{00n0} \\ \sigma'_\circ \mathcal{A}_{000n} \\ \sigma'_\circ(\mathcal{A}_{00nn} \\ +\mathcal{A}_{00ss}) \end{pmatrix} = \frac{1}{4} \begin{pmatrix} 1 & 1 & 1 & 1 \\ 1 & 1 & -1 & -1 \\ 1 & -1 & 1 & -1 \\ 1 & -1 & -1 & 1 \end{pmatrix} \begin{pmatrix} Y'_{\uparrow\uparrow}/L'_{\uparrow\uparrow} \\ Y'_{\uparrow\downarrow}/L'_{\uparrow\downarrow} \\ Y'_{\downarrow\uparrow}/L'_{\downarrow\uparrow} \\ Y'_{\downarrow\downarrow}/L'_{\downarrow\downarrow} \end{pmatrix}. \tag{5.38}$$

The above inverted 4×4 matrix in analytical form was not simple to solve. So the equation was solved using Maple, a symbolic algebra program. Later, it was replaced with a small subroutine for matrix inversion, and the two codes were found to agree with each other.

In figures 5.23 and 5.24, the unpolarized "cross section" yields were scaled to the size of the PWIA cross section convoluted with the target and the detectors acceptance geometry. As mentioned earlier, no absolute cross section of any reaction was measured by the experiment. Therefore, only qualitative comparison of the shapes of the data distributions and the PWIA calculations are shown in the figures. The asymmetries will be presented in the results and summary chapter.

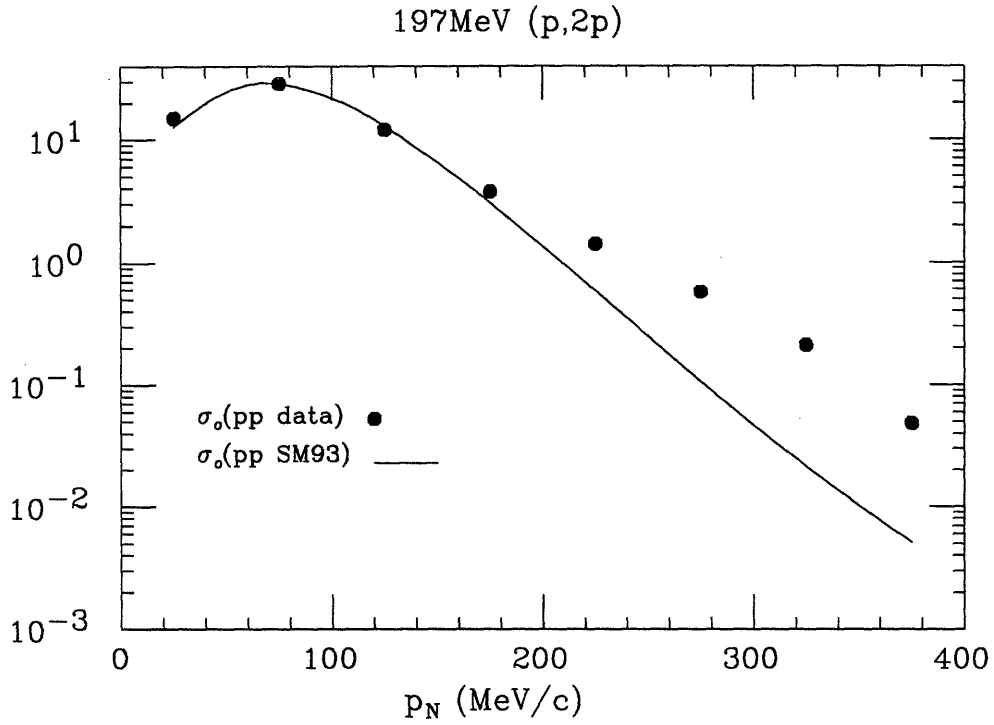

Figure 5.23. Unpolarized "cross section" yield for ^{3}He(p,2p) reaction scaled to a PWIA calculation using the SM93 phase shift solution.

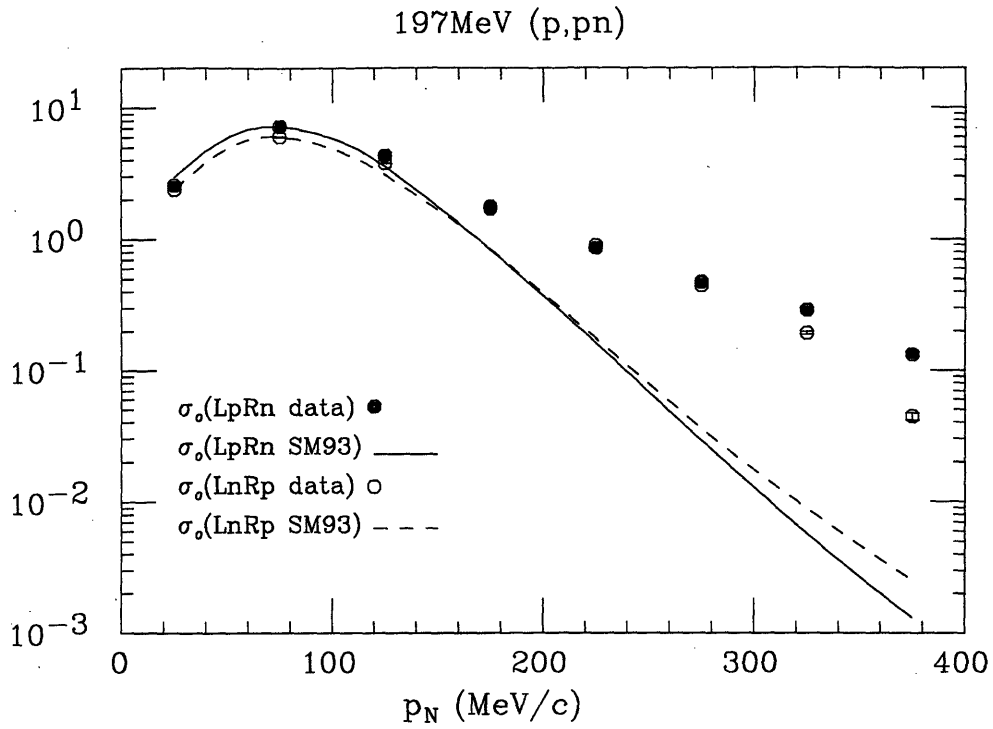

Figure 5.24. Unpolarized "cross section" yield for ^{3}He(p,pn) reaction in solid circles (open circles) for left proton and right neutron (left neutron and right proton) scaled at the peak to PWIA calculations using the SM93 phase shift solution.

5.9 The Experimental Uncertainties

To evaluate the error propagation of the matrix equation (5.37) in analytic form would have been an enormous task. Instead, it was chosen to perform the error propagation numerically, *i.e.* taking numerical partial derivatives of the solution with respect to observables on the right side of the matrix equation and using the partial derivatives as weightings to the uncertainties of the observables as in standard error propagation.

There were four pieces of information used in obtaining the experimental asymmetries, namely total event counts, luminosity, beam polarization, and target polarization. The latter three quantities have systematical uncertainties and are listed in table 5.3 with the resulting uncertainties on the asymmetries in table 5.4 following.

The uncertainty in the target glass cell pressure resulted from a calibration to extract the cell pressure from the input pressure combined with the precision of the baratrons used, which contributed only a small uncertainty. The resulting uncertainty in the cell pressure was then used along with other items listed in ta-

Quantity	X	δX/X	Source
number of events	N	$1/\sqrt{N}$	p-^{3}He elastic, (p,2p) and (p,pn)
			1. quasielastic events
glass cell pressure	P_{cell}	± 0.02	2. flow-pressure calibration
		± 0.002	3. Baratron precision
pressure factor	F_p	± 0.004	propagated error of items 2,3
		± 0.02	4. Caltech calibration
polarimeter angle	$\cos\theta$	± 0.009	5. alignment and angular acceptance
	V_{AC}	$\approx \pm 0.001$	lockin amplifier precision, phase
			6. adjustment and offset
	V_{DC}	± 0.002	7. DC amplifier precision and offset
target polarization	P_t	———	8. polarimeter optics
		± 0.001	9. data acquistion CAMAC's
		± 0.025	total effect of items 2-9
beam polarization	P_b	± 0.01	statistical and cross clibration with CE-01
beam charge	Q	± 0.02	10. PCT fit error and noise
glass cell pressure	P_{cell}	± 0.001	11. pressure fluctuation
livetime efficiency	LT	± 0.0015	12. statistical precision
Effective luminosity	$Q \cdot P_{cell}$	± 0.028	total effect of items 10,11

Table 5.3. The Systematic uncertainties.

ble 5.3 to compute the uncertainty in the target polarization measured by the optical polarimeter. The uncertainty in the calibration factor can be found in the paper by Lorenzon *et al.* [3.18]. The uncertainty in the angle of polarimeter was estimated to be $\pm 2°$. See section 3.3.7.2 for a calibration of the DC and the lockin amplifiers. The uncertainties of the optical analyzer, a $\frac{\lambda}{4}$ wave plate and a plastic sheet linear polarizer, were not determined as attempts to construct a circular polarizer for calibration using good optical equipments were not successful. Calibration data taken with a plastic sheet circular polarizer indicated an approximately 97% measured polarization for a 100% circularly polarized light (*see section* 3.3.7.2). If the calibration was correct, then the asymmetries presented in chapter 6should be decreased by a factor 0.97 to account for the reduced measured value of the polarimeter. If the discrepancy 0.03 were included in the systematics, target polarization uncertainty would be increased from ± 0.025 in table 5.3 to ± 0.04.

The uncertainty in the beam polarization was due to the calibration with the CE-01 experiment and the statistical precision of the monitors for each data run. The calibration also inherently contained both systematic and statistical uncertain-

ties. The resulting uncertainty in the beam polarization for each data run was treated as a systematical uncertainty in the measurement of the quasielastic events.

Lastly, the uncertainty in the relative luminosity of the analysis included only the uncertainties in the beam charge and the precision of the Baratron that monitored the input gas pressure. The uncertainty of the cell pressure from the calibration did not depend on the spin state of the beam and thus, was *not* used to determine the uncertainty of the relative luminosity. However, the input gas pressure fluctuated at 2.5% with a regular period of 110 sec in each data run of one hour long. The 2.5% was reduced by a factor of 0.35 due to the cumulative averaging effect in each of the four different spin states that were approximately 15 min long and further, by a factor of 0.125 (sees 3.8) due to the damping on the pressure oscillation by the glass cell volume. The resulting spin dependent uncertainty was estimated to be 0.1%. The uncertainty of the beam charge resulted from the fit to the PCT data. Only the uncertainties of the Baratron precision and the beam charge were included in the uncertainty of the relative luminosity since the live-time efficiency was incorporated as a weighting factor to the histogramming of the quasielastic events, *c.f.* equation (5.30). Furthermore, the uncertainty in the live-time efficiency was negligibly small due to the high count rate of the scalers when the efficiency was calculated in intervals of 10 sec.

Quantity X	δX	Source
beam asymmetry $\mathcal{A}^{pN}_{00n0}$	$\pm$0.029, $\pm$0.029, $\pm$0.029	(p,2p), (p,LpRn), (p,LnRp)
target asymmetry $\mathcal{A}^{pN}_{000n}$	$\pm$0.019, $\pm$0.019, $\pm$0.019	(p,2p), (p,LpRn), (p,LnRp)
spin correlation parameter $\mathcal{A}^{pN}_{00nn}$	$\pm$0.04, $\pm$0.04, $\pm$0.04	(p,2p), (p,LpRn), (p,LnRp)

Table 5.4. The result systematic uncertainties.

Chapter 6

Summary of the Results and Discussion

The results of the 197 MeV quasielastic data are summarized here. In addition, previous experimental results are compared to the elastic beam asymmetry for the unpolarized H_2 target at 197 MeV and 415 MeV beam energies and the target asymmetry for the polarized ^{3}He target at 45 MeV. The H_2 asymmetry data allowed calibration of the wire chamber positions in both detector arms to high precision, and the ^{3}He asymmetry data provided the first measurement to prove the feasibility of the ^{3}He internal gas target in the Cooler Ring. Moreover, the 197 MeV quasielastic data are discussed in the kinematic regions where the PWIA is valid in which case an extraction is made of the nucleon polarization in the ^{3}He nucleus at low p_m. Finally, future measurements using polarized ^{3}He are discussed.

6.1 The 197 MeV and 414 MeV Beam Asymmetry with Unpolarized Hydrogen Target

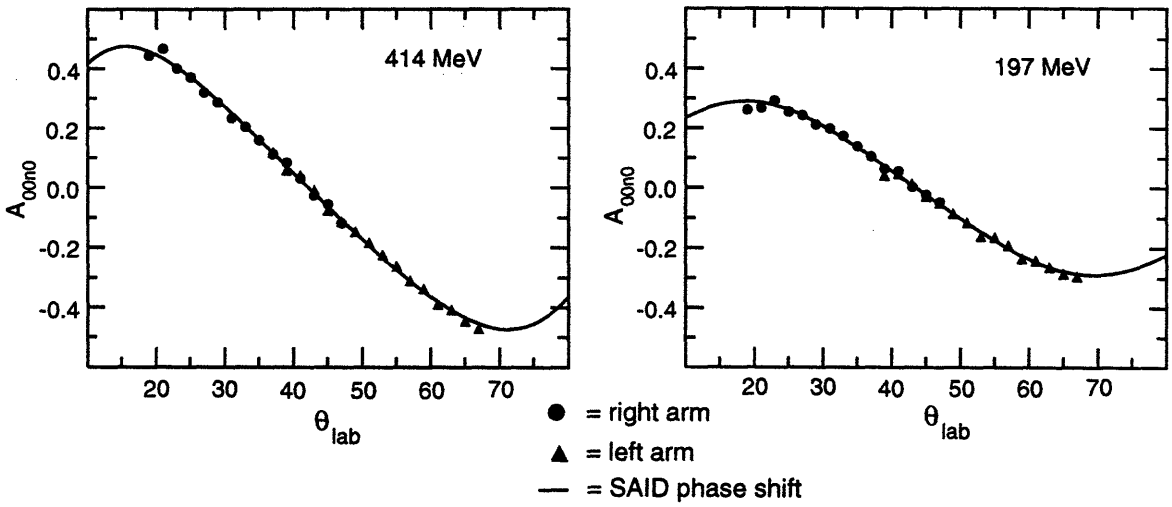

Figure 6.1. Elastic asymmetry of $1H(\vec{p}, 2p)$ data for 414 MeV and 197 MeV. The solid curves are SAID SM89 phase shift solutions [1.18].

Elastic scattering of polarized proton from unpolarized hydrogen has been compared with the phase shift solution of the proton-proton normal asymmetry A^{pp}_{00n0} from SAID. Since A^{pp}_{00n0} has a zero crossing right at 90° c.m. angle, wire chamber positions were adjusted slightly (0.6°) to center the data zero crossing at the 90°.

The normal asymmetry at both the 414 MeV and 197 MeV beam energies, after the detector angle adjustment, was in good agreement with the SAID FA89 phase shift solutions as shown in figure 6.1.

6.2 The Elastic Results

The first result using the polarized ^{3}He internal gas target were obtained at the 45 MeV beam energy [1.20]. This allowed a comparison with previous measurements of the target asymmetry. Although there were no data at exactly this energy, there was no indication of significant beam energy dependence at lower energies [6.1]. Therefore, a phase shift analysis was carried out on the previous data [6.1, 6.2, 6.3] at 35 MeV for the cross section, and the beam and target asymmetries.

In figure 6.2, the target asymmetry at 45 MeV, analyzed at the University of Wisconsin-Madison, is compared to a curve from the phase shift analysis and agrees to within 10%. The curve is shifted slightly from the data to the forward angles, but lack of previous data at the same energy does not allow any better comparision. There is, therefore, no evidence for target depolarization in the storage cell at room temperature.

A primary concern with the internal target was the possible depolarization of the ^{3}He gas after it leaves the optical pumping cell from effects due to magnetic field gradients, due to interaction with the storage cell wall, and due to interaction with the proton beam in the storage cell. It was estimated in section 3.7 that all three mechanisms caused no depolarization to the atoms in the exit capillary, the transition region, and the storage target cell. Therefore, the agreement of the target asymmetry with the previous data proved that the short dwell time of the ^{3}He atoms in all three regions mentioned was too small for depolarization to be significant in this experiment.

The 197 MeV elastic data analyzed at IUCF are also shown here in figure 6.3 and compared with the 200 MeV data from TRIUMF. There is a good agreement between the two data sets in the forward c.m. angles but the CE-25 data deviates from the TRIUMF at large c.m. angles. The disagreement at large angles has been explained as dilution due to nonelastic reaction background.

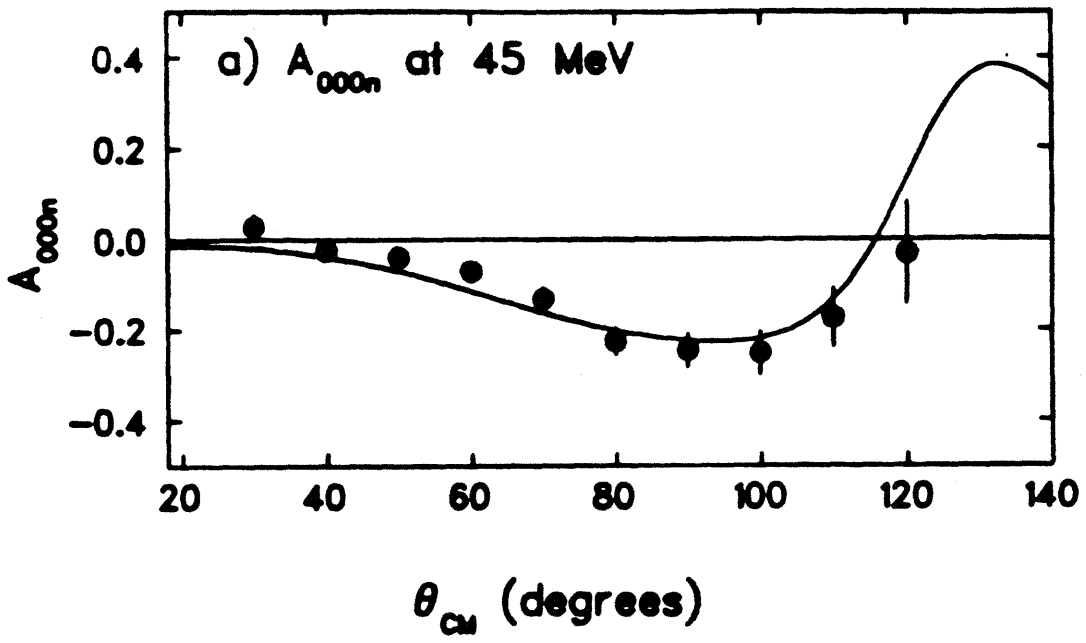

Figure 6.2. Target asymmetry A_{000n} of p-^{3}He elastic scattering at 45 MeV.

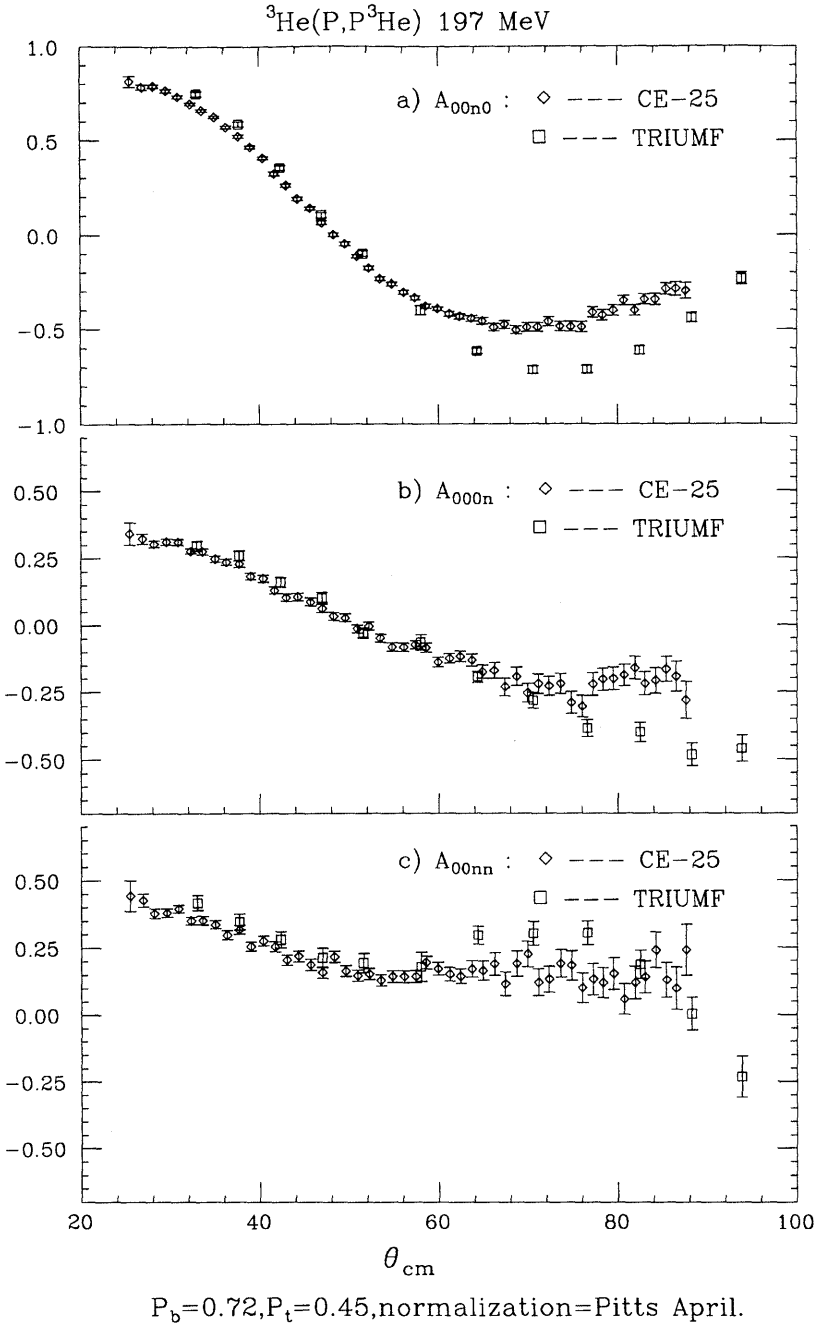

Figure 6.3. Beam asymmetry $\mathcal{A}_{00n0}$ (a), target asymmetry $\mathcal{A}_{000n}$ (b), and spin-correlation parameter $\mathcal{A}_{00nn}$ (c) of p-^{3}He elastic scattering at 197 MeV beam proton energy compared with the TRIUMF data at 200 MeV energy [6.4].

6.3 The 197 MeV Quasielastic Results

6.3.1 The ^{3}He(p,pn) Results

The PWIA model in section 2.4 predicts that in ^{3}He(p,pn) scattering, the target asymmetry $\mathcal{A}^{pn}_{000n}$ is identical to the beam asymmetry $\mathcal{A}^{pn}_{00n0}$ at low missing momentum p_m values. From Fadeev calculations, the neutron spin is aligned 100% along the direction of ^{3}He spin at low p_m values, and from charge symmetry, the asymmetry in scattering a polarized proton from an unpolarized neutron is identical to that of the unpolarized proton scattering from a polarized neutron. Deviations between the asymmetries would indicate that the PWIA is not a good model due to effects such as initial and final state interactions. In fact, the results of the 197 MeV ^{3}He(p,pn) data show a strong 3-momentum transfer q dependence of the target asymmetry. When the protons scattered to the right detector arm in figure 6.4, *i.e.* to small angles, the asymmetry $\mathcal{A}^{pn}_{000n}$ is strongly suppressed from the asymmetry $\mathcal{A}^{pn}_{00n0}$. When the protons scattered to larger angles in figure 6.4(b), the left detector arm, the asymmetry $\mathcal{A}^{pn}_{000n}$ is similar to the asymmetry $\mathcal{A}^{pn}_{00n0}$. Further, when the protons scattered to larger angles in both figure 6.4(b) and (d), the data are much closer to the PWIA curves at low p_m.

In figure 6.5, the beam and target asymmetry data are binned as a function of the magnitude of the 3-momentum transfer q of the struck neutron. We see that there is a good agreement between the two asymmetries at q>500 MeV/c. In this region the neutron polarization, extracted by calculating the ratio of the target to beam asymmetries, is $0.94\pm0.8\pm0.12$, where the errors are statistical and systematic respectively. At q<500 MeV/c, there is a significant deviation between the two asymmetries, consistent with the TRIUMF data [1.29-1.31] taken at q$\approx$382 MeV/c and at $\approx$364 MeV/c respectively, *i.e.* at 220 MeV and 290 MeV incident kinetic energies.[1] The apparent q dependence is interpreted to be due to final-state spin-dependent interactions of the recoiling neutron at low q values. Such an effect has been predicted in calculations of spin-dependent quasielastic (e, e'n) scattering [6.5].

The beam asymmetry appears to follow closely the PWIA initial kinematics calculation, solid curve, using the SAID SM93 phase shift solution. At high q values, where the PWIA model was put forward as correct in the previous discussion, *the*

[1] The 220 and the 290 MeV TRIUMF (p,pn) data sets in the references [1.29-1.31] were averaged over the experiment kinematical ranges. The 290 MeV data was not available in a table and was read off from a plot. Note that the open cross-circle for the 290 MeV target asymmetry is greater than the CE-25 data.

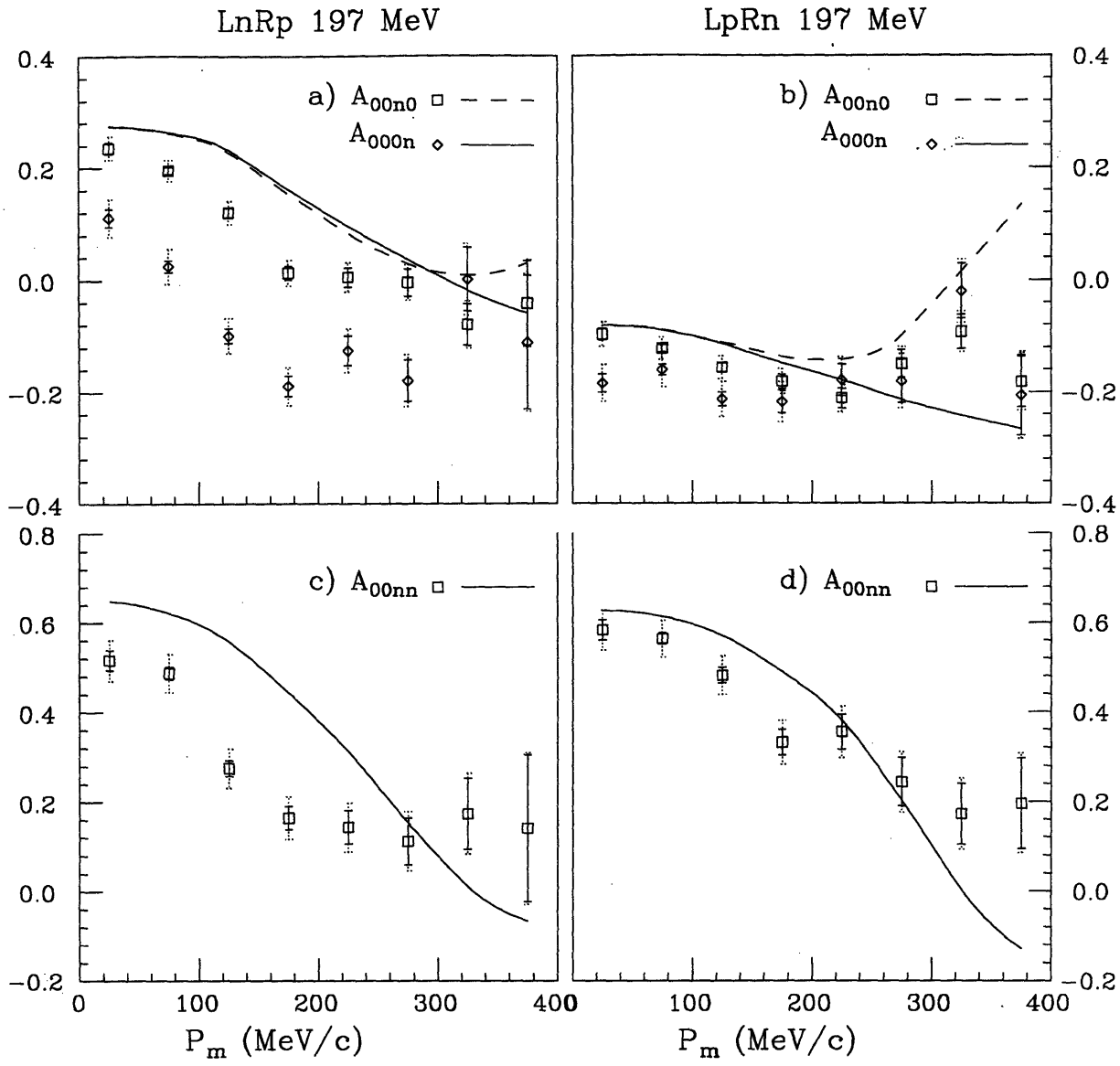

Figure 6.4. At 197 MeV incident energy target and beam asymmetries and spin-correlation parameter, $\mathcal{A}^{pn}_{000n}$, $\mathcal{A}^{pn}_{00n0}$, and $\mathcal{A}^{pn}_{00nn}$, respectively, for ^{3}He(p,pn) scattering as a function of missing momentum p_m: protons scatter to the right detector arm in (a) and (c); protons scatter to the left detector arm in (b) and (d). The curves are calculations of the PWIA model for initial kinematics using the Schulze and Sauer spectral function and the SAID SM93 phase shift solution. The solid error bars are for the statistical, and the dotted error bars are for the total.

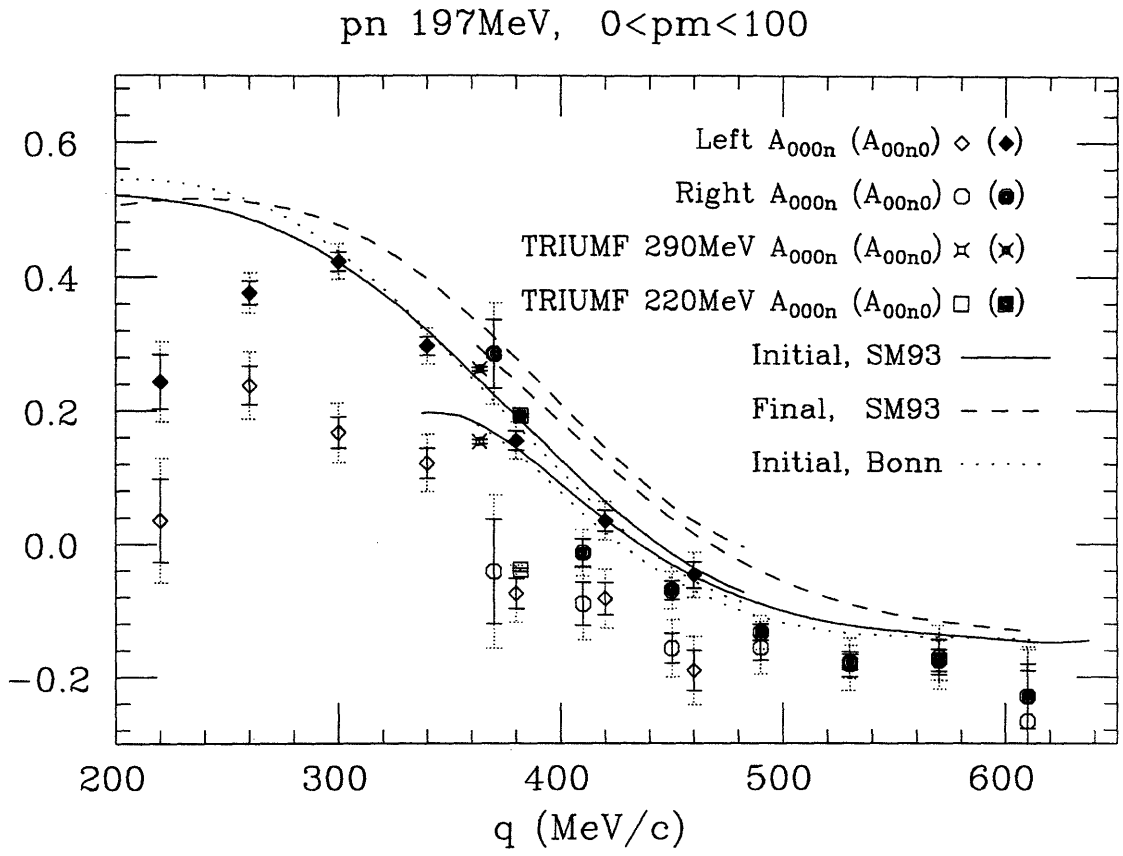

Figure 6.5. At 197 MeV incident energy the target (open symbols) and beam (filled symbols) asymmetries, $\mathcal{A}^{pn}_{000n}$ and $\mathcal{A}^{pn}_{00n0}$, respectively, for ^{3}He(p,pn) scattering at p_m <100 MeV/c as a function of the 3-momentum transfer to the struck neutron q. Data where the proton scattered to the right (left) detector and neutron to the left (right) detector are indicated by diamond (octagon) symbols. The TRIUMF data at 220 (290) MeV are shown at 364 (382) MeV/c in cross-circle (square) symbols. The curves shown are Monte Carlo calculations of the PWIA model for initial and final kinematics using the Schulze and Sauer spectral function and the SM93 and Bonn phase shift solutions. The solid error bars are for the statistical, and the dotted error bars are for the total.

data points are more negative than the solid curve. The PWIA final kinematics calculation, dashed curve, using the SAID SM93 phase shift solution is shifted to the right due to the nucleon binding energy in the ^{3}He. The dotted curve is the PWIA initial kinematics calculation using the Bonn phase shift solution available in SAID.

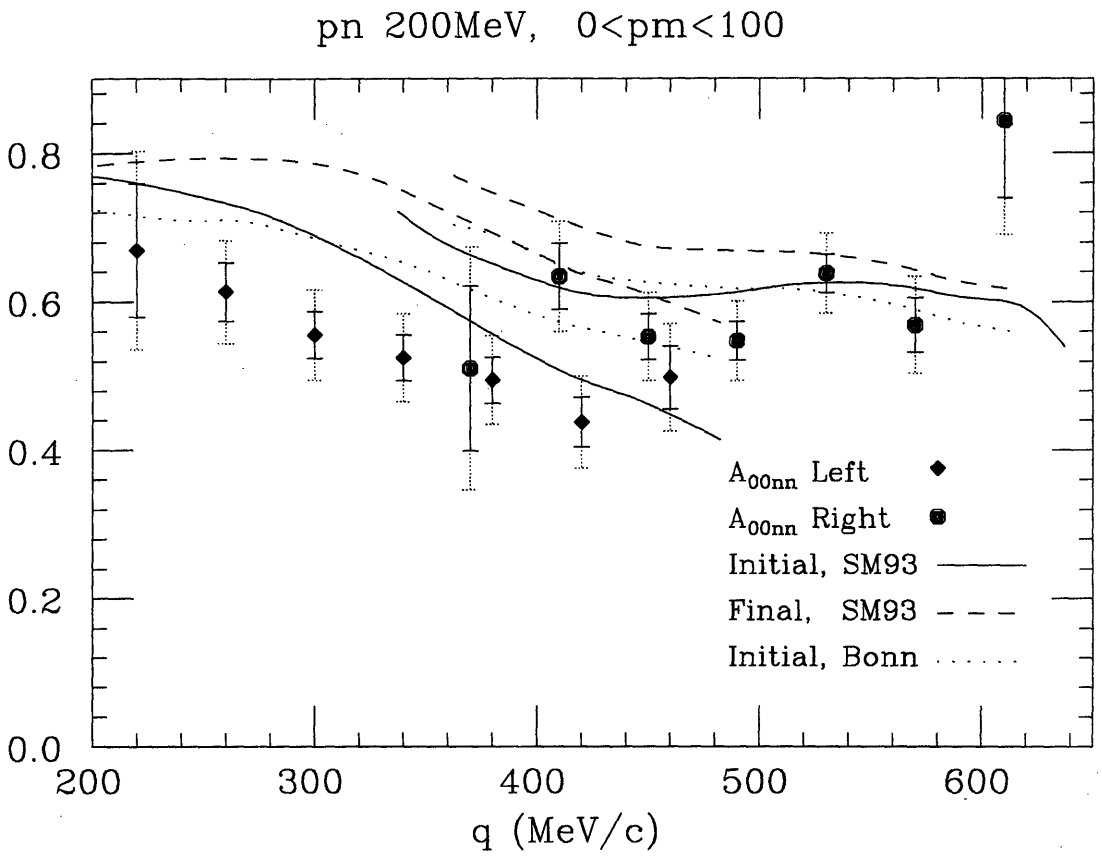

Figure 6.6. At 197 MeV incident energy the spin-correlation parameter for ^{3}He(p,pn) scattering at p_m <100 MeV/c as a function of the 3-momentum transfer to the struck neutron q. Data where the proton scattered to the right (left) detector and neutron to the left (right) detector are indicated by diamond (octagon) symbols. The curves are Monte Carlo calculations of the PWIA model using SM93 and Bonn proton-neutron phase shift solutions and initial and final kinematics. The solid error bars are for the statistical, and the dotted error bars are for the total.

In figure 6.6, the spin-correlation parameter $\mathcal{A}^{pn}_{00nn}$ data are binned as a function of the 3-momentum transfer q. We see that agreement between the data and the PWIA calculation is better at the high q values where the proton is scattered to the left. At the high q values, the data fall only about 5% below the PWIA initial kinematics calculation, solid curve. The PWIA final kinematics calculation, dashed curve, using the SAID SM93 phase shift solution is higher than the initial kinematics calculation by 5-10%. The dotted curve is the initial kinematics calculation using the Bonn phase shift solution.

6.3.2 The ^{3}He(p,2p) Results

In figure 6.7, the curves are PWIA calculations with detector resolution effects included. The small target asymmetry $\mathcal{A}^{2p}_{000n}$ agrees with the PWIA calculation at low p_m values. However, the beam asymmetry $\mathcal{A}^{2p}_{00n0}$ and the spin-correlation parameter $\mathcal{A}^{2p}_{00nn}$ differ significantly from the calculations; the asymmetry $\mathcal{A}^{2p}_{00n0}$ is overpredicted and the asymmetry $\mathcal{A}^{2p}_{00nn}$ is underpredicted by the PWIA calculations at low p_m values. All the solid curves are calculated by turning off the events when the third or fourth nucleon were detected by either detector arm. In the model, the recoiling system of the 3-body channel is assumed to decay into a pair of nucleons uniformly in angle in the c.m. frame. Approximately, 8% of the events in the 3-body channel are rejected. The dashed curves are calculated with only the detector resolutions.

The proton polarization in the nucleus (*see section* 1.2.2) is the sum of the 2-body and the 3-body breakup channels; the former has $\approx -25\%$ and the latter $\approx +13\%$ at low p_m values. When the reaction goes into the 3-body channel, the third proton can also be detected as in (p,3p). However, the analysis was capable of only reconstructing single trajectories in each detector arm. Therefore, the analyzed data are biased to omit events where the third proton was detected. The consequences are that there is more strength for the 2-body than for the 3-body channel, thus possibly bringing down the asymmetry to -16% and that the zero crossing of the proton polarization is also moved farther out from p_m $\approx$90 MeV/c as expected from the sum of the two channels to p_m $\approx$150 MeV/c. The Monte Carlo calculation that omitted events with detection of three or four nucleons, solid curve, has better agreement in figure 6.7(c) with the data than the calculation without the event rejection, lending some support for the above argument. The discrepancy remains to be understood. Morever, such weighting between the 2-body and the 3-body channels does not have any effect on the beam asymmetry $\mathcal{A}^{2p}_{00n0}$ as in figure 6.7(b), and the effect on the target asymmetry $\mathcal{A}^{2p}_{000n}$ is not dramatic since the target asymmetry itself is a small quantity as in figure 6.7(a).

For the (p,2p) reaction, the 3-momentum transfer $q=|\mathbf{p}_0 - \mathbf{p}_1|$ defined as the magnitude of the difference of the beam proton momentum and the momentum of the proton scattered into the left detector arm is not as good a kinematic quantity as for the (p,pn) reaction due to indistinguishability of the two protons. As a result, the 3-momentum transfer q of the (p,2p) data cannot be used to select a region where the PWIA is valid. In figure 6.8, the 197 MeV data, when plotted at p_m <100 MeV/c as a function of the 3-momentum transfer q, show good agreement with the asymmetry

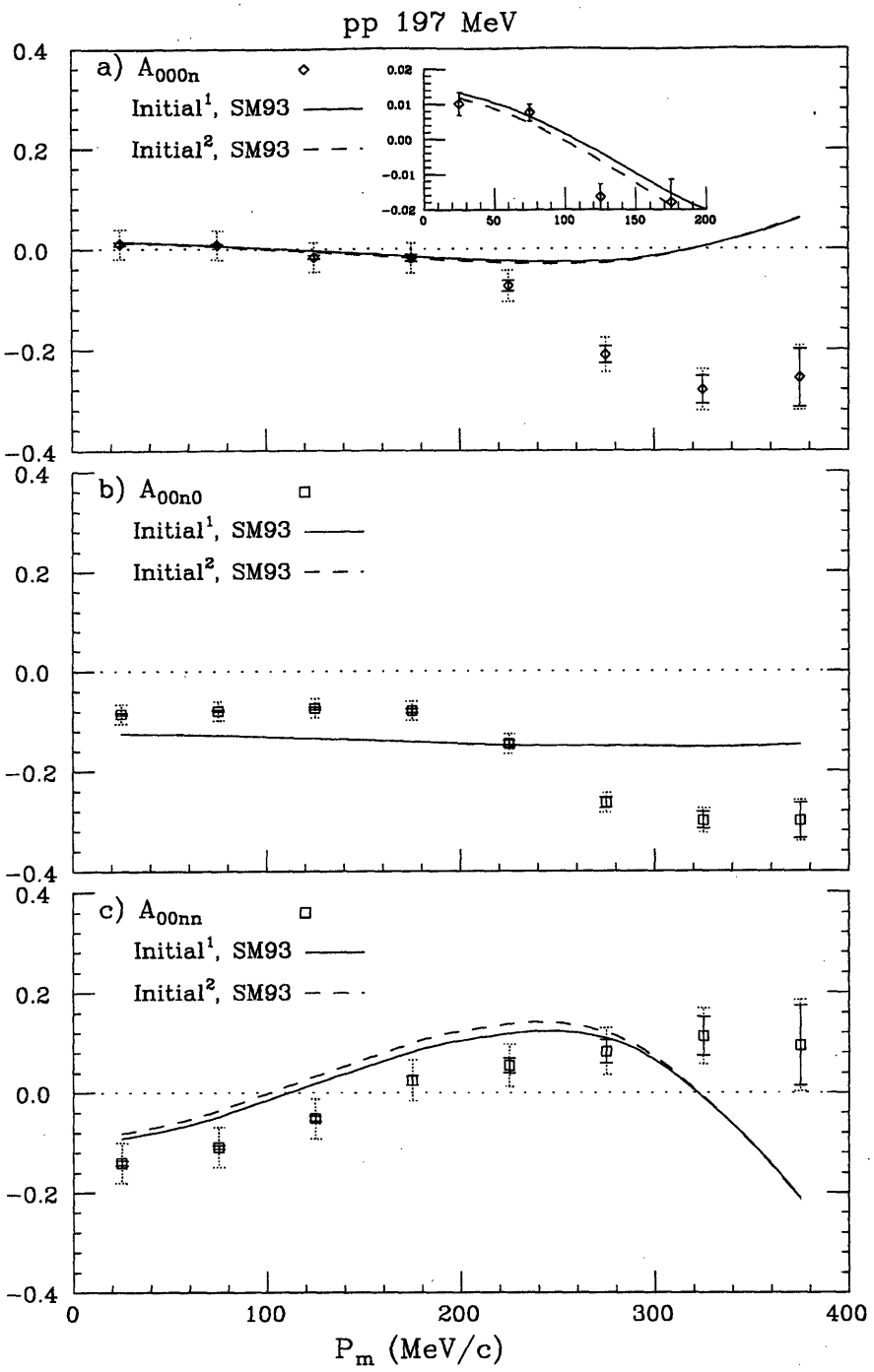

Figure 6.7. At 197 MeV incident energy the target and beam asymmetries and spin-correlation parameter: respectively $\mathcal{A}^{2p}_{000n}$ (a), $\mathcal{A}^{2p}_{00n0}$ (b), and $\mathcal{A}^{2p}_{00nn}$ (c) for ^{3}He(p,2p) scattering as a function of missing momentum p_m. The solid curves are resolutions built in PWIA calculations for initial kinematics using the Schulze and Sauer spectral function and the SAID SM93 phase shift solution and with rejection of triple or quadruple coincidence. The dashed curves has no rejection of the multi-nucleon events. The solid error bars are for the statistical, and the dotted error bars are for the total.

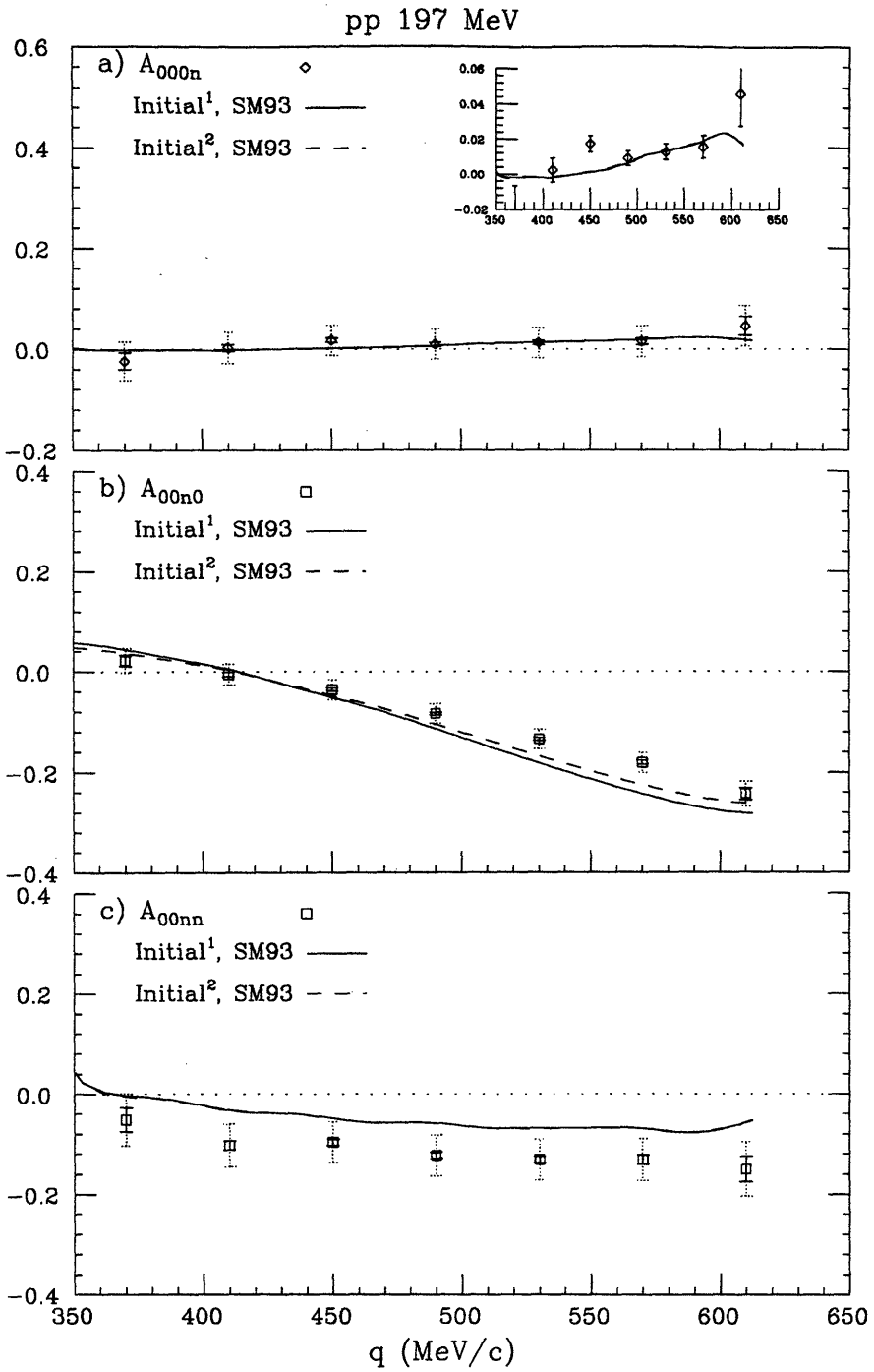

Figure 6.8. At 197 MeV incident energy the target and beam asymmetries and spin-correlation parameter: respectively $\mathcal{A}^{2p}_{000n}$ (a), $\mathcal{A}^{2p}_{00n0}$ (b), and $\mathcal{A}^{2p}_{00nn}$ (c) for ^{3}He(p,2p) scattering at p_m <100 MeV/c as a function of 3-momentum transfer q. The solid curves are resolutions built in calculations of the PWIA model for initial kinematics using the Schulze and Sauer spectral function and the SAID SM93 phase shift solution and with rejection of triple or quadruple coincidence. The dashed curves has no rejection of the multi-nucleon events. The solid error bars are for the statistical, and the dotted error bars are for the total.

$\mathcal{A}^{2p}_{000n}$ calculation in figure 6.8(a), overprediction of the asymmetry $\mathcal{A}^{2p}_{00n0}$ calculation at high q values in figure 6.8(b), and underprediction of the asymmetry $\mathcal{A}^{2p}_{00nn}$ calculation at all q values in figure 6.8(c). The agreement seen in figure 6.8(b) of the asymmetry $\mathcal{A}^{2p}_{00n0}$ at a low q value is only due to the zero crossing of the proton-proton scattering asymmetry A^{pp}_{00n0}.

The (p,2p) data are known to have less final state interaction [1.31-1.30] than the (p,pn) data since the spectral function predicts the (p,2p) to go via the 2-body channel 74% of the time and the 3-body channel 26% of the time at low p_N values (*see section* 1.2.2). A plausible hypothesis is that the final state interactions in the 3-body channel induce the nucleons to come out with higher probability in the directions of the scattered or ejected nucleon, thus, decreasing the weight of the 3-body channel in the analysis— more than that allowed in simple uniform decay of the recoiling system. However, *the recorded data lack any supporting evidence.* Most of the double hit events in the E detector plane were detected by neighboring scintillator bars, over 90% in either detector arm, and were recorded as single trajectories triggering all four wire chamber planes once, 82% in the right detector arm and 68% in the left detector arm. Moreover, the number of double hit events were respectively only 1.3% and 2.7% relative to the total number of single hit events in the left and the right E detector plane.

Although the 3-momentum transfer q could not be used as a kinematic variable for the (p,2p) data, the kinetic energy of the outgoing protons could be limited to regions with less final state interaction [6.6]. Preliminary analysis showed that when the proton kinetic energies were limited to above 100 MeV the PWIA calculation agreed with the data at p_m <200 MeV/c. Both the data and calculation for the spin-correlation parameter $\mathcal{A}^{2p}_{00nn}$ were more negative than without the kinetic energy cuts while they were closer to zero for the beam asymmetry $\mathcal{A}^{2p}_{00n0}$. Even though the statistics were reduced significantly due to the energy cuts and having analyzed less than half the number of runs presented in this thesis, the statistical uncertainties at low p_m values, out to 200 MeV/c, were increased only by a factor of four. The kinematical cuts removed most of the data at p_m >250 MeV/c as also confirmed by the Monte Carlo calculation. Thus, the final state interaction is a likely hypothesis to explain the discrepancy. As the spin-correlation parameter $\mathcal{A}^{2p}_{00nn}$— for both the data and the calculation—was more negative when the proton kinetic energy T>100 MeV, the experimental acceptance must be biased more toward the two body channel, *i.e.* also less final state interaction.

6.4 Extraction of the Neutron and the Proton Spin-Dependent Momentum Distributions

Below are plots of the momentum distributions of the nucleon polarization for the (p,pn) and the (p,2p) reactions obtained from the ratio of the measured spin-correlation parameter and the Monte Carlo spin-correlation parameter $\mathcal{A}^{pN}_{00nn}(100\%)$ with the nucleon polarization in the nucleus 100%. The neutron and the proton data, respectively in figure 6.9 and 6.10, are overlayed with two Monte Carlo calculations of the nucleon polarization momentum distributions. For both reactions, the asymmetry $\mathcal{A}^{pN}_{00nn}(100\%)$ is not only large but also changing only slowly over the kinematic range of the experiment that it can be used to divide out the nucleon-nucleon spin-correclation to obtain the spin-dependent momentum distribution. The spin-correlation parameters $\mathcal{A}^{pn}_{00nn}(100\%)$ and $\mathcal{A}^{2p}_{00nn}(100\%)$ vary respectively from 90% to 50% and from 64% to 30% over the missing momentum p_m range of the experiment, from 0 to 400 MeV/c. In each figure of the nucleon spin-dependent momentum distribution, the solid curve is the result of the spectral function closure over missing energy acceptance of the experiment, and the dashed curve is the result extracted as the ratio described above. The good agreement between the two calculations lends support to the extraction of the nucleon spin-dependent momentum distribution in the kinematic regions where the PWIA is valid.

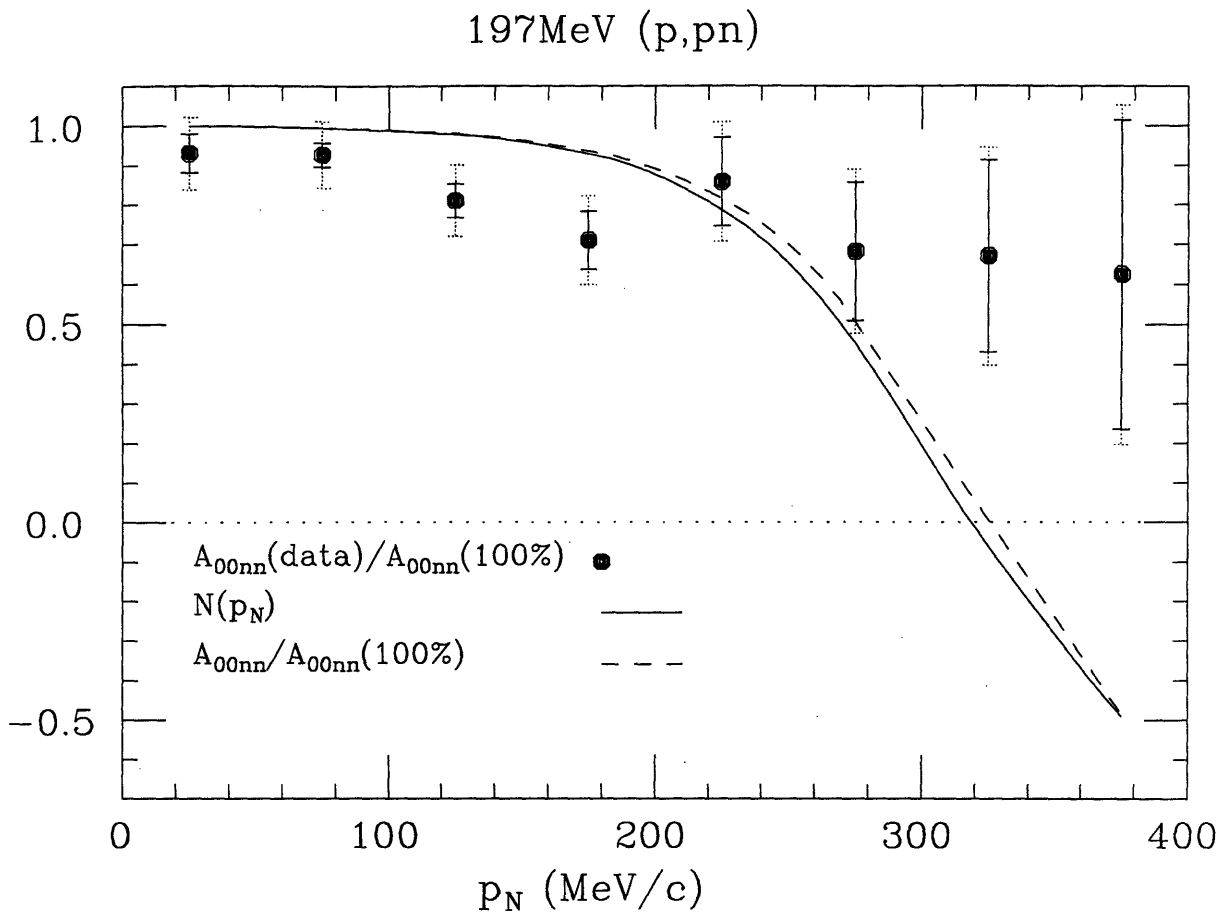

Figure 6.9. The neutron polarization in ^{3}He obtained from the ratio of the 197 MeV $\mathcal{A}^{pn}_{00nn}$ data and the asymmetry $\mathcal{A}^{pn}_{00nn}(100\%)$ from the SAID SM93 phase shift solution. The solid curve is an experimental weighted result of the Schulze and Sauer spectral function. The dashed curve is the ratio of the Monte Carlo results $\mathcal{A}^{pn}_{00nn}$ and $\mathcal{A}^{pn}_{00nn}(100\%)$ obtained from the Schulze and Sauer spectral function and the SAID SM93 phase shift solution. The solid error bars are only for the statistical. and the dotted error bars are for the total.

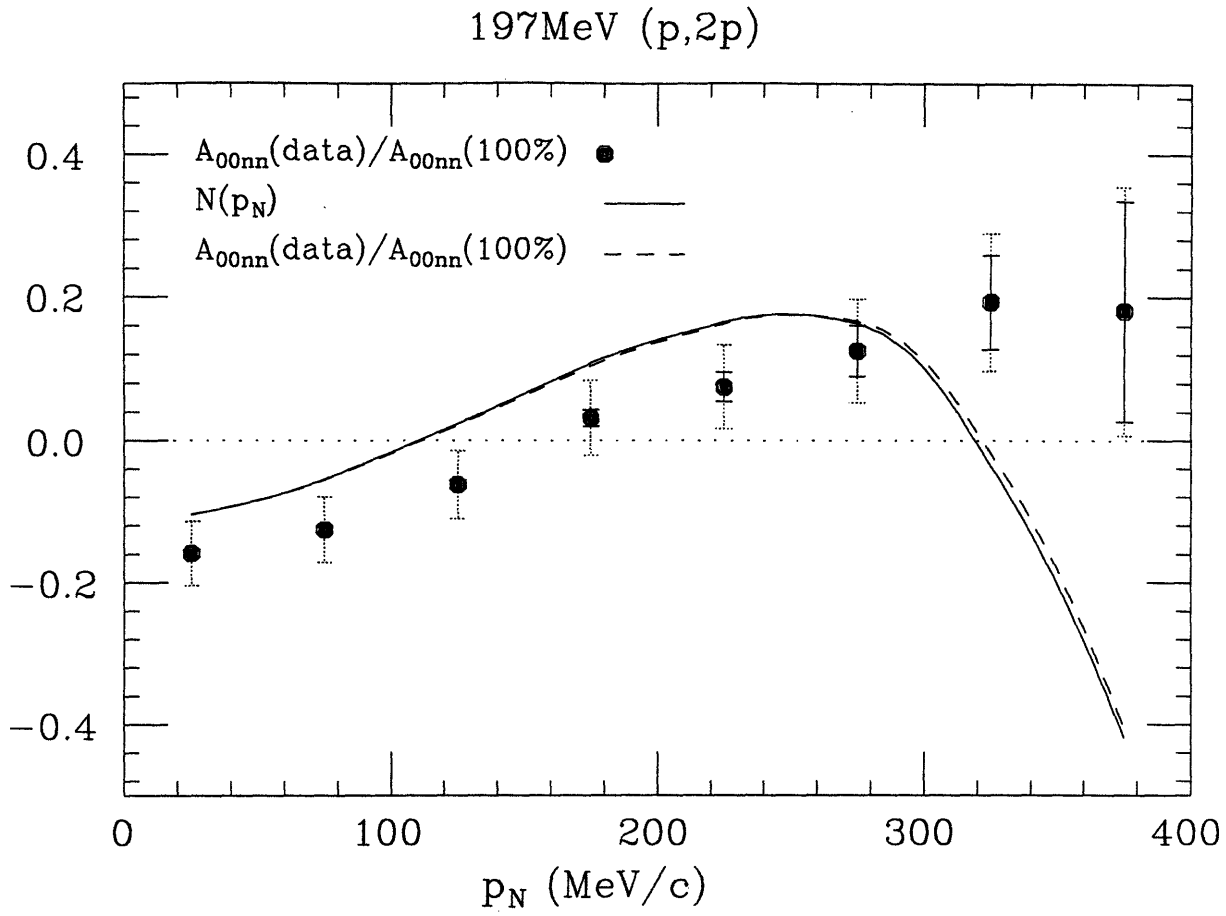

Figure 6.10. The proton polarization in ^{3}He obtained from the ratio of the 197 MeV $\mathcal{A}^{2p}_{00nn}$ data and the asymmetry $\mathcal{A}^{2p}_{00nn}(100\%)$ from the SAID SM93 phase shift solution. The solid curve is an experimental weighted result of the Schulze and Sauer spectral function. The dashed curve is the ratio of the Monte Carlo results $\mathcal{A}^{2p}_{00nn}$ and $\mathcal{A}^{2p}_{00nn}(100\%)$ obtained from the Schulze and Sauer spectral function and the SAID SM93 phase shift solution. The solid error bars are only for the statistical, and the dotted error bars are for the total.

6.5 Summary

The (p,pn) data for q<500 MeV/c are seen to agree at 350 and 300 MeV/c respectively with the TRIUMF data at 220 and 290 MeV proton beam energies. An advantage of using a large acceptance detector is that it allowed a simultaneous measurement over a large q range. In the CE-25 experiment, this was crucial to uncover the kinematic region where the PWIA is in good agreement with the (p,pn) data. Specifically, the target asymmetry $\mathcal{A}^{\mathrm{pn}}_{000\mathrm{n}}$ agrees with the beam asymmetry $\mathcal{A}^{\mathrm{pn}}_{00\mathrm{n}0}$ as in PWIA at q>500 MeV/c. In this region, the neutron polarization in polarized ^{3}He has been extracted and is close the 100% polarization expected from both the Blankleider and Woloshyn spin-dependent momentum distribution and the Schulze and Sauer spin-dependent spectral function. Therefore, the S-state was clearly observed in the (p,pn) data.

The (p,2p) data were expected to have less final state interaction as from the TRIUMF data. The target asymmetry $\mathcal{A}^{\mathrm{2p}}_{000\mathrm{n}}$ was small and consistent with the PWIA model while the beam asymmetry $\mathcal{A}^{\mathrm{2p}}_{00\mathrm{n}0}$ was over predicted by the PWIA model. Moreover, the spin-correlation parameter $\mathcal{A}^{\mathrm{2p}}_{00\mathrm{nn}}$ was under predicted by the calculations. The spin-correlation parameter $\mathcal{A}^{\mathrm{2p}}_{00\mathrm{nn}}$ data were -14% at low $\mathrm{p_m}$ and crosses the zero at $\mathrm{p_m} \approx 170$ MeV/c. The discrepancy remains to be understood. Even though the data are underpredicted by the curves for the spin-correlation parameter $\mathcal{A}^{\mathrm{2p}}_{00\mathrm{nn}}$. The extracted proton polarization was -16%, greater than the -9% polarization expected from calculations. In any case, the S'-state was clearly observed at the low $\mathrm{p_m}$ values in the (p,2p) data.

The 300 MeV and 414 MeV proton beam energy quasielastic data have been analyzed at IUCF [1.19]. Although less final state interactions is expected at these energies, the (p,pn) data indicate that the region where the PWIA begins to be valid depends on the scattered angle rather than the q value. At a higher proton beam energy, the agreement between the target and the beam asymmetries begins at a higher q value while at roughly a constant scattered angle. Such a running condition remains to be understood as coming from reaction mechanisms.

Although the Cooler ring had energy resolutions of a few hundred keV for hundreds of MeV beam kinetic energy, the missing momentum resolution obtained was $\pm$ 20 MeV/c from using time-of-flight technique on approximately 1.5 m long trajectory pathlengths in the nonmagnetic detector arms. The momentum and energy resolution was poorer at higher beam energy data as the tof decreased from 10 nsec to 6-7 nsec.

The first polarized ^{3}He internal gas target for use in storage rings was demon-

strated at the IUCF Cooler proton ring. Large acceptance detection allowed measurement of extensive kinematic regions to be observed in one experiment. The essentially 100% duty cycle beam of the Cooler ring allowed detection of coincidence particles with only a negligible amount of accidental events even for a large acceptance detector. Furthermore, the use of an ultra thin gas target and thin target cell window also allowed detection of sub-MeV particles such as the deuteron and ^{3}He. This opens up the possibility of future interesting measurements of multi-particles coincidence using storage rings and internal gas targets. There are approved experiments at Bates to perform such measurements using the ^{3}He internal gas target in the South Hall Ring with the proposed BLAST detector [1.13]. Recoil detection will be used to separate the 2-body and the 3-body channel of the proton knockout reaction. The use of electron probe will provide measurement with less initial and final state interaction the ^{3}He spin-dependent nucleon momentum distribution of the S' and D-state. In addition, there are experiments planned at NIKHEF and CEBAF. Finally, a systematic measurement of the ^{3}He nucleon momentum distribution is needed for proper interpretation of data on the deep inelastic scattering from polarized ^{3}He to extract the neutron spin structure function and for correction to quasielastic data to extract G_E^n at low Q^2 values.

References

[1.1] A measurement of the spin asymmetry and determination of the structure function g_1 in deep inelastic muon-proton scattering, European Muon Collaboration, J. Ashman *et al.* , Phys. Lett. **B 206**, 364 (1988); An Investigation of the spin structure of the proton in deep inelastic scattering of polarised muons on polarised protons, The European Muon Collaboration, J. Ashman *et al.* , Nucl. Phys. **B 328**, 1 (1989).

[1.2] Measurement of the spin-dependent structure function $g_1(x)$ of the deuteron, Spin Muon Collaboration, B. Adeva *et al.* , Phys. Lett. **B 302**, 533 (1993); Measurement of the spin-dependent structure function $g_1(x)$ of the proton, Spin Muon Collaboration, D. Adams *et al.* , D. Adams *et al.* , Phys. Lett. **B 329**, 399 (1994).

[1.3] Review of Particle Properties, Particle Data Group, Phys. Lett. **B 239**, (1990).

[1.5] HERMES proposal to DOE (1993).

[1.4] Determination of the neutron spin structure function, E142 Collaboration, P.L. Anthony *et al.* , Phys. Lett. **71**, 959 (1993); SLAC measurements of the neutron spin-structure function, SLAC E142 Collaboration, presented by G.G. Petratas, Nuovo Cimento **107 A** 2197 (1994).

[1.6] C.E. Jones, E.J. Beise, J.E. Belz, R.W. Carr, B.W. Filippone, W. Lorenzon, R.D. McKeown, B.A. Mueller, T.G. O'Neill, G.W. Dodson, K. Dow, M. Farkhondeh, S. Kowalski, K. Lee, N. Makins, R. Milner, A. Thompson, D. Tieger, J.F.J. van den Brand, A. Young, X. Yu, and J.D. Zumbro; Phys. Rev. **C 47** 110 (1993); Phys. Rev. Lett. **65**, 698 (1990).

[1.7] Cathleen Elaine Jones Ph.D. Thesis, Caltech (1992);

[1.8] A.K. Thompson, A.M. Bernstein, T.E. Chupp, D.J. DeAngelis, G.E. Dodge, G. Dodson, K.A. Dow, M. Farkhondeh, W. Fong, J.Y. Kin, R.A. Loveman, J.M. Richardson, H. Schmieden, D.R. Tieger, T.C. Yates, M.E. Wagshul, and J.D. Zumbro. Quasielastic scattering of polarized electrons from polarized ^{3}He and measurement of the neutron's from factors. Phys. Rev. Lett. **68**, 2901 (1992); Alan Keith Thompson Ph.D. Thesis, MIT (1991).

[1.9] H. Gao, J. Arrington, E.J. Beise, B. Bray, R.W. Carr, B.W. Filippone, A.F. Lung, R.D. McKeown, B. Mueller, M.L. Pitt, C.E. Jones, D. DeSchepper, G. Dodson, K. Dow, R. Ent, M. Farhondeh, J.-O. Hansen, W. Korsch, L.H. Kramer, K. Lee, N. Makins, R.G. Milner, D.R. Tieger, T.P. Welch, E. Candell, J. Napolitano, B.B. Wojtsekhowski, C. Tripp, W. Lorenzon. Measurement

of the neutron magnetic form factor from inclusive quasielastic scattering of polarized electrons from polarized ^{3}He. Phys. Rev. **C 50**, R546 (1994).

[1.10] J.-O. Hansen, M.A. Titko, D. DeSchepper, G. Dodson, T.W. Donnelly, K. Dow, R. Ent, M. Farhondeh, W. Korsch, L.H. Kramer, K. Lee, N.C.R. Makins, R.G. Milner, D.R. Tieger, T.P. Welch, C.E. Jones, J. Arrington, E.J. Beise, B. Bray, R.W. Carr, B.W. Filippone, H. Gao, A.F. Lung, R.D. McKeown, B. Mueller, M.L. Pitt, R.-W. Schulze, P.U. Sauer, E. Candell, J. Napolitano, C. Tripp, B.B. Wojtsekhowski, W. Lorenzon. The transverse-longitudinal asymmetry in the quasielastic $^3\overrightarrow{\mathrm{He}}(\overrightarrow{\mathrm{e}},\mathrm{e}')$ reaction. Phys. Rev. Lett. **74**, 654 (1994).

[1.11] M. Meyerhoff, D. Eyl, A. Frey, H.G. Andresen, J.R.M. Annand, K. Aulenbacher, J. Becker, J. Blume-Werry, Th. Dombo, P. Drescher, J.E. Ducret, H. Fischer, P. Grabmayr, S. Hall, P. Hartmann, T. Hehl, W. Heil, J. Hoffmann, J.D. Kellie, F. Klein, M. Leduc, H. Möller, Ch. Nachtigall, M. Ostrick, E.W. Otten, R.O. Owens, S. Plützer, E. Reichert, D. Rohe, M. Schäfer, L.D. Schearer, H. Schmieden, K.-H. Steffens, R. Surkau, and Th. Walcher. First measurement of the electric form factor of the neutron in the exclusive quasielastic scattering of polarized electrons from polarized ^{3}He. Phys. Lett. B **327**, 201 (1994).

[1.12] R. Madey *et al.* . The electric form factor of the neutron from the $\mathrm{d}(\overrightarrow{\mathrm{e}},\mathrm{e}'\overrightarrow{\mathrm{n}})\mathrm{p}$ reaction: feasibility test of the $\mathrm{d}(\overrightarrow{\mathrm{e}},\mathrm{e}'\overrightarrow{\mathrm{n}})\mathrm{p}$ reaction to measure G_E^n. Bates Annual Report, 51 (1990); CEBAF experiment 93-038, CEBAF homepage (1995).

[1.13] Bates Large Acceptance Spectrometer Toroid (BLAST) proposal (1992).

[1.14] Precision Measurement of the neutron spin structure function using a polarized ^{3}He target, E154 Collaboration.

[1.15] CEBAF experiment 94-010, CEBAF homepage (1995)— `http://www.cebaf.gov/general/visit/experiments/experiments.html`

[1.16] J. Friar. What is the S' state in ^{3}He and why is it important? BLAST proceedings, 210 (1992).

[1.17] J.L. Friar, B.F. Gibson, G.L. Payne, A.M. Bernstein, and T.E. Chupp. Phys. Rev. **C 42**, 2310 (1990).

[1.18] Michael A. Miller, Ph D. Thesis, University of Wisconsin—Madison (1995). item[1.19] Adam Smith, Ph D. Thesis, Indiana University (1995).

[1.20] K. Lee, M.A. Miller, A. Smith, J.-O. Hansen, C. Bloch, J.F.J. van den Brand, H.J. Bulten, R. Ent, C.D. Goodman, W.W. Jacobs, C.E. Jones, W. Korsch, M. Leuschner, W. Lorenzon, D. Marchlenski, H.O. Meyer, R.G. Milner, J.S. Neal, P.V. Pancella, S.F. Pate, W.K. Pitts, B. von Przewoski, T. Rinckel, J.

Sowinski, F. Sperisen, E. Sugarbaker, C. Tschalär, O. Unal, and Z-L. Zhou. Measurement of spin observables using a storage ring with polarized beam and polarized internal gas target. Phys. Rev. Lett. **70**, 738 (1993).

[2.21] M.A. Miller, K. Lee, A. Smith, J.-O. Hansen, C. Bloch, J.F.J. van den Brand, H.J. Bulten, D. DeSchepper, R. Ent, C.D. Goodman, W.W. Jacobs, C.E. Jones, W. Korsch, L.H. Kramer, M. Leuschner, W. Lorenzon, N.C.R. Makins, D. Marchlenski, H.O. Meyer, R.G. Milner, J.S. Neal, P.V. Pancella, S.F. Pate, W.K. Pitts, B. von Przewoski, T. Rinckel, G. Savopulos, J. Sowinski, F. Sperisen, E.R. Sugarbaker, C. Tschalär, O. Unal, and Z.-L. Zhou. Measurement of quasielastic ^{3}He(p,pN) scattering from polarized ^{3}He and the three body ground state spin structure. Phys. Rev. Lett. **74**, 502 (1995).

[1.22] Douglas Howard Beck, Ph.D. Thesis, MIT (1986).

[1.23] Karen Ann Dow, Ph.D. Thesis, MIT (1987).

[1.24] E. Jan, M. Bernheim, M.K. Brussel, G.P. Capitani, E. de Sanctis, S. Frullani, F. Garibaldi, J. Morgenstern, J. Mougey, I. Sick, and S. Turck-Chieze. The quasi-free ^{3}He(e,e′ p) reaction. Phys. Rev. Lett. **49**, 974 (1982).

[1.27] B. Blankleider and R.M. Woloshyn. Quasi-elastic scattering of polarized electrons on polarized ^{3}He. Phys. Rev. **C 29**, 538 (1984).

[1.28] R.W. Schulze and P.U. Sauer, Inelastic electron scattering from the three-nucleon bound states with polarization. Phys. Rev. C **48**, 38 (1993).

[1.31] E.J. Brash, O. Häusser, B. Larson, A. Rahav, P.W. Green, P.P.J. Delheij, R.S. Henderson, U. Oelfke, M.C. Vetterli, D.M. Whittal, R.M. Woloshyn. Proton-induced nucleon knockout from polarized ^{3}He at 220 MeV. Phys. Rev. **C 47**, 2064 (1993).

[1.29] A. Rahav, O. Häusser, C.A. Miller, P.P.J. Delheij, W.P. Alford, T.E. Chupp, K. Ferguson, R. Henderson, C.D.P. Levy, K.P. Jackson, J. Mildenberger, B. Morrissette, M.C. Vetterli, and R.M. Woloshyn. Proton-induced nucleon knockout from polarized ^{3}He at 290 MeV. Phys. Lett. **B 275**, 259 (1992).

[1.30] A. Rahav, O. Häusser, R.M. Woloshyn, T.E. Chupp, P.P.J. Delheij, K. Ferguson, R. Henderson, K.P. Jackson, C.D.P. Levy, J. Mildenberger, C.A. Miller, B. Morrissette, and M.C. Vetterli. Nucleon knocknout from polarized ^{3}He by polarized protons at 290 MeV. Phys. Rev. **C 46**, 1167 (1992).

[2.1] Jo van den Brand, Ph.D. Thesis, NIKHEF (1988).

[2.2] J. Golak, H. Witala, H. Kamada, D. Hüber, S. Ishikawa, and W. Glöckle. Inclusive electron scattering on ^{3}H and ^{3}He with full inclusion of final state interaction. Phys. Rev. **C 52**, 1216 (1995).

[2.3] P. Kitching, W.J. McDonald, Th.A.J. Maris, and C.A.Z. Vasconcellos; Recent developments in quasi-free nucleon-nucleon scattering in: Advances in nuclear physics, eds. J.W. Negele and E.W. Vogt, Vol 15 (Plenum, New York, 1985) p.43.

[2.5] S. Frullani and J. Mougey; in: Advances in nuclear physics, eds. J.W. Negele and E.W. Vogt, Vol 14 (Plenum, New York, 1984) p.1.

[2.6] M.B. Epstein, D.A. Krause, D.J. Margaziotis, A. Bracco, H.P. Gubler, D.K. Hasell, W.P. Lee, W.T.H. van Oers, R. Abegg, C.A. Miller, and A.W. Stetz. ^{3}He(p,2p)d and ^{3}He(p,pd)p reactions at large recoil momenta. Phys. Rev. **C 32**, 967 (1985).

[2.7] J. Bystricky, F. Lehar, and P. Winternitz. Formalism of nucleon-nucleon elastic scattering experiments. J. Phys. (Paris) **39**, 1 (1978).

[2.8] C. Lechanoine-LeLuc and F. Lehar. Nucleon-nucleon elastic scattering and total cross sections. Rev. Mod. Phys. **65**, 47 (1993).

[2.9] R.A. Arndt, L.D. Roper, R.A. Bryan, R.B. Clark, B.J. VerWest, and P. Signell. Nucleon-nucleon partial-wave analysis to 1 GeV. Phys. Rev. **D 28**, 97 (1983). R.A. Arndt, J.S. Hyslop III, and L.D. Roper. Nucleon-nucleon partial wave analysis to 1100 MeV. Phys. Rev. **D 35**, 128 (1987).

[2.10] R.A. Arndt *et al.* , Scattering analysis dial-in program (SAID), unpublished.

[2.11] M. Miller, private communication.

[3.1] R.G. Milner, R.D. McKeown, and C.E. Woodward. A polarized ^{3}He target for nuclear physics. Nucl. Instr. and Meth. **A257**, 286 (1987).

[3.2] G.K. Walters, F.D. Colegrove, and L.D. Schearer. Nuclear polarization of ^{3}He gas by metastability exchange with optically pumped metastable ^{3}He atoms. Phys. Rev. Lett. **8**, 439 (1962).

[3.3] F.D. Colegrove, L.D. Schearer, and G.K. Walters. Polarization of ^{3}He gas by optical pumping. Phys. Rev. **132**, 2561 (1963).

[3.4] G.C. Phillips, R.R. Perry, P.M. Windham, G.K. Walters, L.D. Schearer, and F.D. Colegrove. Demonstration of a polarized ^{3}He target for nuclear reactions. Phys. Rev. Lett. **9**, 502 (1962).

[3.5] L.D. Schearer and M. Leduc. IEEE J. Quant. Elect. **22**, 756 (1986); Technology news, Laser Focus, p. 34, Sept 1983.

[3.6] M. Leduc *et al.* , Nucl. Sci. Appl. **1** 1 (1983).

[3.7] Padetha Tin and L.D. Schearer. A high power, tunable, arc-lamp pumped Nd-doped lanthanum-hexaluminate laser. J. Appl. Phys. **68**, 950 (1990).

[3.8] T.R. Gentile and R.D. McKeown. Spin polarizing ^{3}He nuclei with an arc lamp-

pumped Nd:LMA laser. Phys. Rev. **A**, 456 (1993).

[3.9] K. Lee, J.-O Hansen, J.F.J. van den Brand and R.G. Milner. A laser optically pumped polarized ^{3}He target for storage rings. Nucl. Instr. and Meth. **A333**, 194 (1993).

[3.10] C. Bloch, J. Doskow, C.D. Goodman, W.W. Jacobs, M. Leuschner, H.O. Meyer, B. von Przewoski, T. Rinckel, G. Savopulos, A. Smith, J. Sowinski, F. Sperisen, W.K. Pitts, D. DeSchepper, R. Ent, J-O. Hansen, J. Kelsey, W. Korsch, L.H. Kramer, K. Lee, N.C.R. Makins, R.G. Milner, S.F. Pate, C. Tschalär, T.P. Welch, D. Marchlenski, E. Sugarbaker, W. Lorenzon, P.V. Pancella, J.F.J. van den Brand, J.J. Bulten, C.E. Jones, M.A. Miller, J. Neal, O. Unal, Z.-L. Zhou. Spin-dependent scattering of polarized protons from a polarized ^{3}He internal gas target. Nucl. Instr. and Meth. **A354**, 437 (1995).

[3.11] A. Kponou, V.W. Hughes, C.E. Johnson, S.A. Lewis, and F.M.J. Pichanick. Experiments on the 2^3P state of helium. III. Measurement of the 2^3P_0-2^3P_1 fine-structure interval. Phys. Rev. **A 24**, 264 (1981).

[3.12] M.A. Bouchiat, T.R. Carver, and C.M. Varnum. Nuclear polarization in ^{3}He gas induced by optical pumping and dipolar exchange. Phys. Rev. Lett. **5**, 373 (1960).

[3.13] P.J. Nacher and M. Leduc. Optical pumping in ^{3}He with a laser. **12** 2057 (1985).

[3.14] J. Dupont-Roc, M. Leduc, and F. Laloë. New value for the metastability exchange cross section in helium. Phys. Rev. Lett. **27**, 467 (1971).

[3.15] G. Eckert, W. Heil, M. Meyerhoff, E.W. Otten, R. Surkau, M. Werner, M. Leduc, P.J. Nacher, and L.D. Schearer. A dense polarized ^{3}He target based on compression of optically pumped gas. Nucl. Instr. and Meth. **A320**, 54 (1992).

[3.16] M. Pavlovic et Franck Lalöe, J. Phys. (Paris) **31**, 173 (1970)

[3.17] Selected Tables of Atomic Spectra, Charlotte E. Moore, NRDS-NBS3 (1965). National Bureau of Standards.

[3.18] W. Lorenzon, T.R. Gentile, H. Gao, and R.D. McKeown. NMR calibration of optical measurement of nuclear polarization in ^{3}He. Phys. Rev. **A 47**, 468 (1993).

[3.19] M. Pinard and J. Van Der Linde. Disorientation of ^{3}He ^1D states in ^{3}He-^{3}He collisions. Can. J. Phys. **52**, 1615 (1974).

item[3.29] Varian Associates, Vacuum Products Division, Lexington, MA.

[3.20] A. Roth, *Vacuum Technology*, North-Holland, Amsterdam, 1982, p.109.

[3.21] Finkenbeiner G. Inc., Scientific Glass Blower, 33 Rumford Avenue, Waltham, MA 02154.

[3.22] Meyer Tool & Mfg., Inc., 9211 South Kilpatrick, Oak Lawn, Illnois 60453.

[3.23] ULVAC North America corporation, P.O. Box 799, Kennebunk, Maine 04043.

[3.24] Wilmad Glass Company, Inc., Route 40 & Oak Road, Buena, NJ 08310.

[3.25] KONTES Chemistry and Life Sciences Products, 1022 Spruce Street, Vineland, NJ 08360-2841.

[3.26] Helicoflex, Components Division, P.O. Box 9889, Columbia, So. Carolina 29290.

[3.27] The color filter, manufactured by Schott Company, was cut and gold vapor coated by Finkenbeiner G. Inc., Scientific Glass Blower.

[3.31] Suncoast Technologies, Inc., 1625 Timocuan Way, Bldg. 113, Longwood, FL 32750.

[3.32] Union Carbide - Crystal Products, 750 S. 32nd Street, Washougal, WA 98671.

[3.33] T.R. Gentile, private communication.

[3.34] C.G. Aminoff, C. Larat, M. Leduc, B. Viana, and D. Vivien. Characterization and laser properties of lanthanum magnesium hexa-aluminate activated by neodymium and chromium. J. Lum. **50**, 21 (1991).

[3.35] INRAD Inc., 181 Legrand Avenue, Northvale, NJ 07647.

[3.36] ORIEL Corp., 250 Long Beach Blvd., P.O. Box 872, Stratford, CT 06497.

[3.37] Polaroid Corp., 100 Upland Road, Norwood, MA 02062.

[3.38] C VI Laser Corp., 200 Dorado Place, SE/P.O. Box 11308, Albuquerque, NM 87192.

[3.39] Fastpulse Technology, Inc., 200 Midland Avenue, Saddle Brook, NJ 07683.

[3.40] Catherine S. Trotter, Senior Thesis, MIT (1989).

[3.41] L.D. Schearer and G.K. Walters. Nuclear spin-lattice relaxation in the presence of magnetic field gradients. Phys. Rev. **A5**, A1398 (1965).

[3.42] R.S. Timsit, J.M. Daniels, and A.D. May. Nuclear relaxation of ^{3}He gas on various solid surfaces. Can. J. Phys. **49**, 560 (1971).

[3.43] L.H. Kramer, J.F. Kelsey, R.G. Milner, P. Winn, J. McGuire. A cryogenic storage cell for polarized internal gas targets. Nucl. Instr. and Meth. **A 565**, 49 (1995).

[3.44] TRIUMF Kinematics Handbook, Section VII, Interaction of Particles with Matter.

[3.45] R.G. Milner, R.D. McKeown, and C.E. Woodward. Study of spin relaxation by a charged particle beam in a polarized ^{3}He gas target. Nucl. Instr. and

Meth. **A257**, 286 (1987).

[4.1] R.E. Pollock. The IUCF Cooler after three years. Proceedings of the 19th Symposium on Cooler Rings and their Applications, eds. T. Katayama and A. Noda, (World Scientific Publishing Co., Singapore), 1991, p. 4.

[4.2] M. Alan Ross, Ph.D. Thesis, Indiana University (1991).

[4.3] K. Unser. A Toroidal DC beam current transformer with high resolutin. IEEE Trans. Nucl. Sci **28**, 2344 (1981).

[4.4] W. Haberli. Sources of polarized ions. Ann. Rev. Nucl. Sci. **17**, 373 (1967).

[4.5] The Bicron Corp., 12345 Kinsman Road, Newbury, OH 44065.

[4.6] S.E. Vigdor, W.W. Jacobs, L.D. Knutson, J. Sowinski, C. Bloch, P.L. Jolivette, S.W. Wissink, R.C. Byrd, and C. Whiddon. Charge symmetry breaking in $\overrightarrow{n}$-$\overrightarrow{p}$ scattering at 183 MeV. Phys. Rev. **C 46**, 410 (1992).

[4.7] Type "I", Micron Semiconductor, Ltd., Lancing, Sussex BN15 8UN, England.

[5.1] TRIUMF Kinematics Handbook, section VII, Interaction of particles with matter.

[5.2] E. Barouch. Approximations to the range-energy relationship. Nucl. Instr. and Meth. **61**, 113 (1968).

[5.3] A. Smith, private communication.

[6.1] B.T. Murdoch, D.K. Hasell, A.M. Sourkes, W.T.H. van Oers, P.J.T. Verheijen, and R.E. Brown. ^{3}He(p,p)^{3}He scattering in the energy range 19 to 48 MeV. Phys. Rev. **C 29**, 2001 (1984).

[6.2] J. Birchall, W.T.H. van Oers, J.W. Watson, H.E. Conzett, R.M. Larimer, B. Leemann, E.J. Stephenson, P. von Rossen, R.E. Brown. Analyzing power measurements for ^{3}He($\overrightarrow{p}$,p)^{3}He elastic scattering between 20 and 50 MeV. Phys. Rev. **C 29**, 2009 (1984).

[6.3] R.H. McCamis, P.J.T. Verheijen, W.T.H. van Oers, P. Drakopoulos, C. Lapointe, G.R. Maughan, N.T. Okumusoglu, and R.E. Brown. $^3\overrightarrow{He}$(p,p)^{3}He analyzing powers between 25 and 35 MeV. Phys. Rev. **C 31**, 1651 (1985).

[6.4] O. Häusser, B. Larson, W.P. Alford, C. Chan, P.P.J. Delheij, R.S. Henderson, K.P. Jackson, R.H. Landau, T. Mefford, C.A. Miller, A. Rahav, L. Ray, A. Trudel, and M.C. Vetterli. Elastic scattering of polarized protons from polarized ^{3}He. Phys. Lett. **B 343**, 36 (1995).

[6.5] J.M. Laget. On the measurement of the neutron electric form factor. Phys. Lett. **B 273**, 367 (1991).

[6.6] T.W. Donnelly, private communication.

Appendix A

The 197 MeV Quasielastic Data

p_m (MeV/c)	$\mathcal{A}_{000n}$	$\mathcal{A}_{00n0}$	$\mathcal{A}_{00nn}$
25	-0.1835 ± 0.0165	-0.0963 ± 0.0105	0.5832 ± 0.0227
75	-0.1597 ± 0.0099	-0.1217 ± 0.0063	0.5639 ± 0.0136
125	-0.2128 ± 0.0127	-0.1557 ± 0.0080	0.4812 ± 0.0175
175	-0.2177 ± 0.0203	-0.1809 ± 0.0128	0.3319 ± 0.0283
225	-0.1786 ± 0.0284	-0.2109 ± 0.0178	0.3553 ± 0.0390
275	-0.1806 ± 0.0386	-0.1494 ± 0.0244	0.2437 ± 0.0536
325	-0.0205 ± 0.0486	-0.0926 ± 0.0306	0.1722 ± 0.0682
375	-0.2064 ± 0.0718	-0.1820 ± 0.0456	0.1955 ± 0.1013

Table A.1. $\mathcal{A}_{000n}$, $\mathcal{A}_{00n0}$, and $\mathcal{A}_{00nn}$ for the left-proton-right-neutron $^3\overrightarrow{He}(\overrightarrow{p},pn)$ reaction. The uncertainties are only statistical.

p_m (MeV/c)	$\mathcal{A}_{000n}$	$\mathcal{A}_{00n0}$	$\mathcal{A}_{00nn}$
25	0.1108 ± 0.0162	0.2351 ± 0.0101	0.5163 ± 0.0223
75	0.0247 ± 0.0102	0.1951 ± 0.0064	0.4877 ± 0.0141
125	-0.0986 ± 0.0128	0.1198 ± 0.0082	0.2755 ± 0.0179
175	-0.1886 ± 0.0186	0.0127 ± 0.0121	0.1646 ± 0.0263
225	-0.1252 ± 0.0262	0.0053 ± 0.0169	0.1432 ± 0.0370
275	-0.1785 ± 0.0372	-0.0039 ± 0.0241	0.1118 ± 0.0525
325	0.0016 ± 0.0564	-0.0784 ± 0.0364	0.1735 ± 0.0796
375	-0.1110 ± 0.1188	-0.0412 ± 0.0752	0.1408 ± 0.1637

Table A.2. $\mathcal{A}_{000n}$, $\mathcal{A}_{00n0}$, and $\mathcal{A}_{00nn}$ for the left-neutron-right-proton $^3\overrightarrow{He}(\overrightarrow{p},pn)$ reaction. The uncertainties are only statistical.

q (MeV/c)	$\mathcal{A}_{000n}$	$\mathcal{A}_{00n0}$	$\mathcal{A}_{00nn}$
220	0.0351 ± 0.0631	0.2434 ± 0.0405	0.6694 ± 0.0895
260	0.2378 ± 0.0286	0.3755 ± 0.0175	0.6131 ± 0.0393
300	0.1666 ± 0.0232	0.4215 ± 0.0140	0.5548 ± 0.0316
340	0.1213 ± 0.0224	0.2963 ± 0.0140	0.5241 ± 0.0308
380	-0.0754 ± 0.0224	0.1547 ± 0.0144	0.4940 ± 0.0310
420	-0.0827 ± 0.0241	0.0346 ± 0.0156	0.4374 ± 0.0334
460	-0.1903 ± 0.0301	-0.0471 ± 0.0197	0.4977 ± 0.0421

Table A.3. $\mathcal{A}_{000n}$, $\mathcal{A}_{00n0}$, and $\mathcal{A}_{00nn}$ for the left-neutron-right-proton $^3\vec{\mathrm{He}}(\vec{\mathrm{p}},\mathrm{pn})$ reaction with a cut $\mathbf{p_m}$ <100 MeV/c. The uncertainties are only statistical.

q (MeV/c)	$\mathcal{A}_{000n}$	$\mathcal{A}_{00n0}$	$\mathcal{A}_{00nn}$
370	-0.0416 ± 0.0788	0.2848 ± 0.0512	0.5098 ± 0.1111
410	-0.0900 ± 0.0325	-0.0138 ± 0.0209	0.6335 ± 0.0445
450	-0.1569 ± 0.0225	-0.0700 ± 0.0144	0.5525 ± 0.0308
490	-0.1563 ± 0.0187	-0.1332 ± 0.0119	0.5471 ± 0.0257
530	-0.1811 ± 0.0188	-0.1776 ± 0.0119	0.6377 ± 0.0257
570	-0.1703 ± 0.0266	-0.1749 ± 0.0169	0.5682 ± 0.0365
610	-0.2664 ± 0.0762	-0.2290 ± 0.0487	0.8428 ± 0.1036

Table A.4. $\mathcal{A}_{000n}$, $\mathcal{A}_{00n0}$, and $\mathcal{A}_{00nn}$ for the left-proton-right-neutron $^3\vec{\mathrm{He}}(\vec{\mathrm{p}},\mathrm{pn})$ reaction with a cut $\mathrm{p_m}$ <100 MeV/c. The uncertainties are only statistical.

p_m (MeV/c)	$\mathcal{A}_{000n}$	$\mathcal{A}_{00n0}$	$\mathcal{A}_{00nn}$
25	-0.2073 ± 0.0224	-0.1400 ± 0.0142	0.5926 ± 0.0308
75	-0.1787 ± 0.0138	-0.1864 ± 0.0087	0.5712 ± 0.0190
125	-0.2292 ± 0.0177	-0.2257 ± 0.0111	0.4654 ± 0.0245
175	-0.2613 ± 0.0269	-0.2516 ± 0.0167	0.3671 ± 0.0374
225	-0.1971 ± 0.0369	-0.2588 ± 0.0229	0.3916 ± 0.0510
275	-0.2232 ± 0.0483	-0.2326 ± 0.0301	0.2640 ± 0.0672
325	-0.0092 ± 0.0558	-0.1155 ± 0.0346	0.2177 ± 0.0781
375	-0.2370 ± 0.0744	-0.1842 ± 0.0473	0.1687 ± 0.1051

Table A.5. $\mathcal{A}_{000n}$, $\mathcal{A}_{00n0}$, and $\mathcal{A}_{00nn}$ for the left-proton-right-neutron $^3\overrightarrow{He}(\overrightarrow{p},pn)$ reaction with a cut q>500 MeV/c. The uncertainties are only statistical.

p_m (MeV/c)	$\mathcal{A}_{000n}$	$\mathcal{A}_{00n0}$	$\mathcal{A}_{00nn}$
25	0.0102 ± 0.0033	-0.0857 ± 0.0021	-0.1405 ± 0.0046
75	0.0077 ± 0.0024	-0.0792 ± 0.0015	-0.1093 ± 0.0033
125	-0.0164 ± 0.0036	-0.0745 ± 0.0023	-0.0519 ± 0.0051
175	-0.0180 ± 0.0065	-0.0795 ± 0.0042	0.0249 ± 0.0091
225	-0.0738 ± 0.0106	-0.1458 ± 0.0067	0.0545 ± 0.0148
275	-0.2101 ± 0.0167	-0.2639 ± 0.0104	0.0822 ± 0.0233
325	-0.2806 ± 0.0276	-0.2995 ± 0.0169	0.1130 ± 0.0385
375	-0.2565 ± 0.0576	-0.2998 ± 0.0351	0.0941 ± 0.0801

Table A.6. $\mathcal{A}_{000n}$, $\mathcal{A}_{00n0}$, and $\mathcal{A}_{00nn}$ for the $^3\overrightarrow{He}(\overrightarrow{p},2p)$ reaction. The uncertainties are only statistical.

q (MeV/c)	$\mathcal{A}_{000n}$	$\mathcal{A}_{00n0}$	$\mathcal{A}_{00nn}$
370	-0.0235 ± 0.0170	0.0222 ± 0.0110	-0.0513 ± 0.0239
410	0.0023 ± 0.0068	-0.0058 ± 0.0044	-0.1025 ± 0.0095
450	0.0172 ± 0.0047	-0.0358 ± 0.0031	-0.0964 ± 0.0066
490	0.0090 ± 0.0042	-0.0836 ± 0.0027	-0.1228 ± 0.0058
530	0.0127 ± 0.0045	-0.1344 ± 0.0029	-0.1308 ± 0.0062
570	0.0156 ± 0.0064	-0.1803 ± 0.0041	-0.1309 ± 0.0090
610	0.0457 ± 0.0185	-0.2430 ± 0.0117	-0.1502 ± 0.0257

Table A.7. $\mathcal{A}_{000n}$, $\mathcal{A}_{00n0}$, and $\mathcal{A}_{00nn}$ for the $^3\overrightarrow{He}(\overrightarrow{p},2p)$ reaction with a cut p_m <100 MeV/c. The uncertainties are only statistical.

Appendix.B

Polarized Nucleon-Nucleon Elastic Scattering

Nucleons have spin and isospin values of $\frac{1}{2}$. Here in appendix B, a general polarized elastic scattering cross section expression is derived starting from the nucleon-nucleon scattering matrix element. A general form of the elastic scattering cross section for the nucleons can be written as

$$\begin{aligned} d\sigma^{NN} = & \frac{1}{\text{flux}^{NN}} \frac{1}{2E_0 2E_N} (2\pi)^4 \, \delta^{(4)}(p_1 + p_2 - p_0 - p_N) \\ & \times \Gamma(s_0, s_N)^{NN} \frac{d^3\mathbf{p}_1}{(2\pi)^3 2E_1} \frac{d^3\mathbf{p}_2}{(2\pi)^3 2E_2} , \end{aligned} \tag{B.1}$$

where

$$\begin{aligned} \Gamma(s_0, s_N)^{NN} &= \sum_{s_1, s_2} \left| \langle \mathbf{p}_1 s_1 t_1, \ \mathbf{p}_2 s_2 t_2, \ | \ M^{NN} \ | \mathbf{p}_0 s_0 t_0, \ \mathbf{p}_N s_N t_N \rangle \right|^2 \\ &= \langle s_0 s_N | \ M^{NN\dagger} M \ | s_N s_0 \rangle , \end{aligned} \tag{B.2}$$

is the "spin-specified" probability, and it has been summed over the final spin states of particles 1 and 2 since their spin states are not detected in the measurement. In the last step, the momentum and isospin states are dropped off for simplicity.

In order to facilitate the discussion of spin-dependence nucleon scattering, the observables are expressed in one specific set of unit vectors. The aim in the followings is then to formulate the interaction probability using the set of unit vectors below:

$$\hat{\mathbf{n}} = \frac{\mathbf{p}_0 \times \mathbf{p}_1}{|\mathbf{p}_0 \times \mathbf{p}_1|} , \quad \hat{\mathbf{k}} = \frac{\mathbf{p}_0}{|\mathbf{p}_0|} , \quad \hat{\mathbf{s}} = \hat{\mathbf{n}} \times \hat{\mathbf{k}} . \tag{B.3}$$

Let the quantum axis be along the unit vector $\hat{\mathbf{n}}$, and it follows that the operators $(\sigma_0 \cdot \hat{\imath})$ and $(\sigma_N \cdot \hat{\jmath})$ can be written explicitly as

$$\begin{aligned} (\sigma_i \cdot \hat{n}) &= \begin{pmatrix} 1 & 0 \\ 0 & -1 \end{pmatrix} \\ (\sigma_i \cdot \hat{k}) &= \begin{pmatrix} 0 & 1 \\ 1 & 0 \end{pmatrix} \\ (\sigma_i \cdot \hat{s}) &= \begin{pmatrix} 0 & -i \\ i & 0 \end{pmatrix} . \end{aligned} \tag{B.4}$$

In an experiment when both the beam and target particles are polarized, all four possible beam and target spin states in equations (B.2) could be measured.

"Spin-combined" probabilities which are related to the scattering asymmetries are then formed by combining the above spin-specified probabilities in the following ways:

$$\begin{aligned}
\Gamma^{NN}_{0000} &= \Gamma(\mathbf{s}_{0+},\mathbf{s}_{N+})^{NN} + \Gamma(\mathbf{s}_{0+},\mathbf{s}_{N-})^{NN} + \Gamma(\mathbf{s}_{0-},\mathbf{s}_{N+})^{NN} + \Gamma(\mathbf{s}_{0-},\mathbf{s}_{N-})^{NN} \\
\Gamma^{NN}_{00\mathbf{s}_0 0} &= \Gamma(\mathbf{s}_{0+},\mathbf{s}_{N+})^{NN} + \Gamma(\mathbf{s}_{0+},\mathbf{s}_{N-})^{NN} - \Gamma(\mathbf{s}_{0-},\mathbf{s}_{N+})^{NN} - \Gamma(\mathbf{s}_{0-},\mathbf{s}_{N-})^{NN} \\
\Gamma^{NN}_{000\mathbf{s}_N} &= \Gamma(\mathbf{s}_{0+},\mathbf{s}_{N+})^{NN} - \Gamma(\mathbf{s}_{0+},\mathbf{s}_{N-})^{NN} + \Gamma(\mathbf{s}_{0-},\mathbf{s}_{N+})^{NN} - \Gamma(\mathbf{s}_{0-},\mathbf{s}_{N-})^{NN} \\
\Gamma^{NN}_{00\mathbf{s}_0\mathbf{s}_N} &= \Gamma(\mathbf{s}_{0+},\mathbf{s}_{N+})^{NN} - \Gamma(\mathbf{s}_{0+},\mathbf{s}_{N-})^{NN} - \Gamma(\mathbf{s}_{0-},\mathbf{s}_{N+})^{NN} + \Gamma(\mathbf{s}_{0-},\mathbf{s}_{N-})^{NN} .
\end{aligned} \tag{B.5}$$

The combinations can be re-expressed as the trace operations of the nucleon-nucleon interaction operators and the Pauli spin operators dotted with the spin unit vectors $\mathbf{s}_0$ and $\mathbf{s}_N$ defined along the directions of the beam particle spin and the target particle spin. Expressing as the trace operations allows one to write out the spin-combined probabilities without any dependence of a particular basis of spin states. It also allows one to focus only on the spin operators dotted with the spin unit vectors. When the spin unit vectors are expanded in a particular basis of unit vectors, one obtains immediately the spin-combined probabilities defined in that basis of unit vectors,

$$\Gamma^{NN}_{0000} = \mathrm{Tr}_{\{\mathbf{s}_0\mathbf{s}_N\}}\, \mathrm{M}^{NN\dagger}\mathrm{M} , \tag{B.6a}$$

$$\begin{aligned}
\Gamma^{NN}_{00\mathbf{s}_0 0} &= \mathrm{Tr}_{\{\mathbf{s}_0\mathbf{s}_N\}}\, (\sigma_0\cdot\hat{\mathbf{s}_0})\, \mathrm{M}^{NN\dagger}\mathrm{M}^{NN} \\
&= \mathrm{Tr}_{\{\mathbf{s}_0\mathbf{s}_N\}} \left\{ \left[\hat{\mathbf{n}}\cdot\hat{\mathbf{s}}_0(\sigma_0\cdot\hat{\mathrm{n}}) + \hat{\mathbf{k}}\cdot\hat{\mathbf{s}}_0(\sigma_0\cdot\hat{\mathrm{k}}) + \hat{\mathbf{s}}\cdot\hat{\mathbf{s}}_0(\sigma_0\cdot\hat{\mathrm{s}}) \right] \mathrm{M}^{NN\dagger}\mathrm{M}^{NN} \right\} \\
&= \hat{\mathbf{n}}\cdot\hat{\mathbf{s}}_0\Gamma^{NN}_{000\mathrm{n}} + \hat{\mathbf{k}}\cdot\hat{\mathbf{s}}_0\Gamma^{NN}_{000\mathrm{k}} + \hat{\mathbf{s}}\cdot\hat{\mathbf{s}}_0\Gamma^{NN}_{000\mathrm{s}} ,
\end{aligned} \tag{B.6b}$$

$$\begin{aligned}
\Gamma^{NN}_{000\mathbf{s}_N} &= \mathrm{Tr}_{\{\mathbf{s}_0\mathbf{s}_N\}}\, (\sigma_N\cdot\hat{\mathbf{s}_N})\, \mathrm{M}^{NN\dagger}\mathrm{M}^{NN} \\
&= \mathrm{Tr}_{\{\mathbf{s}_0\mathbf{s}_N\}} \left\{ \left[\hat{\mathbf{n}}\cdot\hat{\mathbf{s}}_N(\sigma_N\cdot\hat{\mathrm{n}}) + \hat{\mathbf{k}}\cdot\hat{\mathbf{s}}_N(\sigma_N\cdot\hat{\mathrm{k}}) + \hat{\mathbf{s}}\cdot\hat{\mathbf{s}}_N(\sigma_N\cdot\hat{\mathrm{s}}) \right] \mathrm{M}^{NN\dagger}\mathrm{M}^{NN} \right\} \\
&= \hat{\mathbf{n}}\cdot\hat{\mathbf{s}}_N\Gamma^{NN}_{00\mathrm{n}0} + \hat{\mathbf{k}}\cdot\hat{\mathbf{s}}_N\Gamma^{NN}_{00\mathrm{k}0} + \hat{\mathbf{s}}\cdot\hat{\mathbf{s}}_N\Gamma^{NN}_{00\mathrm{s}0} ,
\end{aligned} \tag{B.6c}$$

and

$$\begin{aligned}
\Gamma^{NN}_{00\mathbf{s}_0\mathbf{s}_N} &= \mathrm{Tr}_{\{\mathbf{s}_0\mathbf{s}_N\}}\, (\sigma_0\cdot\hat{\mathbf{s}_0})(\sigma_N\cdot\hat{\mathbf{s}_N})\, \mathrm{M}^{NN\dagger}\mathrm{M}^{NN} \\
&= \mathrm{Tr}_{\{\mathbf{s}_0\mathbf{s}_N\}} \left\{ \left[\hat{\mathbf{n}}\cdot\hat{\mathbf{s}}_0\hat{\mathbf{n}}\cdot\hat{\mathbf{s}}_N(\sigma_0\cdot\hat{\mathrm{n}})(\sigma_N\cdot\hat{\mathrm{n}}) + \hat{\mathbf{n}}\cdot\hat{\mathbf{s}}_0\hat{\mathbf{k}}\cdot\hat{\mathbf{s}}_N(\sigma_0\cdot\hat{\mathrm{n}})(\sigma_N\cdot\hat{\mathrm{k}}) \right.\right.
\end{aligned}$$

$$
\begin{aligned}
&\qquad\qquad + \hat{\mathbf{n}}\cdot\hat{\mathbf{s}}_0\hat{\mathbf{s}}\cdot\hat{\mathbf{s}}_N(\sigma_0\cdot\hat{\mathrm{n}})(\sigma_N\cdot\hat{\mathrm{s}}) \\
&\hat{\mathbf{k}}\cdot\hat{\mathbf{s}}_0\hat{\mathbf{n}}\cdot\hat{\mathbf{s}}_N(\sigma_0\cdot\hat{\mathrm{k}})(\sigma_N\cdot\hat{\mathrm{n}}) + \hat{\mathbf{k}}\cdot\hat{\mathbf{s}}_0\hat{\mathbf{k}}\cdot\hat{\mathbf{s}}_N(\sigma_0\cdot\hat{\mathrm{k}})(\sigma_N\cdot\hat{\mathrm{k}}) \\
&\qquad\qquad + \hat{\mathbf{k}}\cdot\hat{\mathbf{s}}_0\hat{\mathbf{s}}\cdot\hat{\mathbf{s}}_N(\sigma_0\cdot\hat{\mathrm{k}})(\sigma_N\cdot\hat{\mathrm{s}}) \\
&\hat{\mathbf{s}}\cdot\hat{\mathbf{s}}_0\hat{\mathbf{n}}\cdot\hat{\mathbf{s}}_N(\sigma_0\cdot\hat{\mathrm{s}})(\sigma_N\cdot\hat{\mathrm{n}}) + \hat{\mathbf{s}}\cdot\hat{\mathbf{s}}_0\hat{\mathbf{k}}\cdot\hat{\mathbf{s}}_N(\sigma_0\cdot\hat{\mathrm{s}})(\sigma_N\cdot\hat{\mathrm{k}}) \\
&\qquad\qquad + \hat{\mathbf{s}}\cdot\hat{\mathbf{s}}_0\hat{\mathbf{s}}\cdot\hat{\mathbf{s}}_N(\sigma_0\cdot\hat{\mathrm{s}})(\sigma_N\cdot\hat{\mathrm{s}})\Big]\mathrm{M}^{\mathrm{NN}\dagger}\mathrm{M}^{\mathrm{NN}}\Big\} \\
= \;& \hat{\mathbf{n}}\cdot\hat{\mathbf{s}}_0\hat{\mathbf{n}}\cdot\hat{\mathbf{s}}_N\Gamma^{\mathrm{NN}}_{\mathrm{00nn}} + \hat{\mathbf{n}}\cdot\hat{\mathbf{s}}_0\hat{\mathbf{k}}\cdot\hat{\mathbf{s}}_N\Gamma^{\mathrm{NN}}_{\mathrm{00nk}} + \hat{\mathbf{n}}\cdot\hat{\mathbf{s}}_0\hat{\mathbf{s}}\cdot\hat{\mathbf{s}}_N\Gamma^{\mathrm{NN}}_{\mathrm{00ns}} \\
& \hat{\mathbf{k}}\cdot\hat{\mathbf{s}}_0\hat{\mathbf{n}}\cdot\hat{\mathbf{s}}_N\Gamma^{\mathrm{NN}}_{\mathrm{00kn}} + \hat{\mathbf{k}}\cdot\hat{\mathbf{s}}_0\hat{\mathbf{k}}\cdot\hat{\mathbf{s}}_N\Gamma^{\mathrm{NN}}_{\mathrm{00kk}} + \hat{\mathbf{k}}\cdot\hat{\mathbf{s}}_0\hat{\mathbf{s}}\cdot\hat{\mathbf{s}}_N\Gamma^{\mathrm{NN}}_{\mathrm{00ks}} \\
& \hat{\mathbf{s}}\cdot\hat{\mathbf{s}}_0\hat{\mathbf{n}}\cdot\hat{\mathbf{s}}_N\Gamma^{\mathrm{NN}}_{\mathrm{00sn}} + \hat{\mathbf{s}}\cdot\hat{\mathbf{s}}_0\hat{\mathbf{k}}\cdot\hat{\mathbf{s}}_N\Gamma^{\mathrm{NN}}_{\mathrm{00sk}} + \hat{\mathbf{s}}\cdot\hat{\mathbf{s}}_0\hat{\mathbf{s}}\cdot\hat{\mathbf{s}}_N\Gamma^{\mathrm{NN}}_{\mathrm{00ss}}\,.
\end{aligned}
\tag{B.6d}
$$

A summary of the spin-combined probabilities are given below in Table B.1.

	$(\sigma_0\cdot\hat{\imath})$	$(\sigma_N\cdot\hat{\jmath})$	Beam + Target Pol Directions	Spin-Combinations
$\Gamma^{\mathrm{NN}}_{\mathrm{0000}}$	1	1	unpol, unpol	$\frac{1}{4}(\Gamma_{11}+\Gamma_{22}+\Gamma_{33}+\Gamma_{44})$
$\Gamma^{\mathrm{NN}}_{\mathrm{00n0}}$	$(\sigma_0\cdot\hat{\mathrm{n}})$	1	normal, unpol	$1\frac{1}{4}(\Gamma_{11}+\Gamma_{22}-\Gamma_{33}-\Gamma_{44})$
$\Gamma^{\mathrm{NN}}_{\mathrm{00k0}}$	$(\sigma_0\cdot\hat{\mathrm{k}})$	1	longi, unpol	$\frac{1}{4}(\Gamma_{31}+\Gamma_{42}+\Gamma_{13}+\Gamma_{24})$
$\Gamma^{\mathrm{NN}}_{\mathrm{00s0}}$	$(\sigma_0\cdot\hat{\mathrm{s}})$	1	side, unpol	$\frac{i}{4}(-\Gamma_{31}-\Gamma_{42}+\Gamma_{13}-\Gamma_{24})$
$\Gamma^{\mathrm{NN}}_{\mathrm{000n}}$	1	$(\sigma_N\cdot\hat{\mathrm{n}})$	unpol, normal	$\frac{1}{4}(\Gamma_{11}-\Gamma_{22}+\Gamma_{33}-\Gamma_{44})$
$\Gamma^{\mathrm{NN}}_{\mathrm{000k}}$	1	$(\sigma_N\cdot\hat{\mathrm{k}})$	unpol, longi	$\frac{1}{4}(\Gamma_{21}+\Gamma_{12}+\Gamma_{43}+\Gamma_{34})$
$\Gamma^{\mathrm{NN}}_{\mathrm{000s}}$	1	$(\sigma_N\cdot\hat{\mathrm{s}})$	unpol, side	$\frac{i}{4}(-\Gamma_{21}+\Gamma_{12}-\Gamma_{43}+\Gamma_{34})$
$\Gamma^{\mathrm{NN}}_{\mathrm{00nn}}$	$(\sigma_0\cdot\hat{\mathrm{n}})$	$(\sigma_N\cdot\hat{\mathrm{n}})$	normal, normal	$\frac{1}{4}(\Gamma_{11}-\Gamma_{22}-\Gamma_{33}+\Gamma_{44})$
$\Gamma^{\mathrm{NN}}_{\mathrm{00nk}}$	$(\sigma_0\cdot\hat{\mathrm{n}})$	$(\sigma_N\cdot\hat{\mathrm{k}})$	normal, longi	$\frac{1}{4}(\Gamma_{21}+\Gamma_{12}-\Gamma_{43}-\Gamma_{34})$
$\Gamma^{\mathrm{NN}}_{\mathrm{00ns}}$	$(\sigma_0\cdot\hat{\mathrm{n}})$	$(\sigma_N\cdot\hat{\mathrm{s}})$	normal, side	$\frac{i}{4}(-\Gamma_{21}+\Gamma_{12}+\Gamma_{43}-\Gamma_{34})$
$\Gamma^{\mathrm{NN}}_{\mathrm{00kn}}$	$(\sigma_0\cdot\hat{\mathrm{k}})$	$(\sigma_N\cdot\hat{\mathrm{n}})$	longi, normal	$\frac{1}{4}(\Gamma_{31}-\Gamma_{42}+\Gamma_{13}-\Gamma_{24})$
$\Gamma^{\mathrm{NN}}_{\mathrm{00kk}}$	$(\sigma_0\cdot\hat{\mathrm{k}})$	$(\sigma_N\cdot\hat{\mathrm{k}})$	longi, longi	$\frac{1}{4}(\Gamma_{41}+\Gamma_{32}+\Gamma_{23}+\Gamma_{14})$
$\Gamma^{\mathrm{NN}}_{\mathrm{00ks}}$	$(\sigma_0\cdot\hat{\mathrm{k}})$	$(\sigma_N\cdot\hat{\mathrm{s}})$	longi, side	$\frac{i}{4}(-\Gamma_{41}+\Gamma_{32}-\Gamma_{23}+\Gamma_{14})$
$\Gamma^{\mathrm{NN}}_{\mathrm{00sn}}$	$(\sigma_0\cdot\hat{\mathrm{s}})$	$(\sigma_N\cdot\hat{\mathrm{n}})$	side, normal	$\frac{i}{4}(-\Gamma_{31}+\Gamma_{42}+\Gamma_{13}-\Gamma_{24}$
$\Gamma^{\mathrm{NN}}_{\mathrm{00sk}}$	$(\sigma_0\cdot\hat{\mathrm{s}})$	$(\sigma_N\cdot\hat{\mathrm{k}})$	side, longi	$\frac{i}{4}(-\Gamma_{41}-\Gamma_{32}+\Gamma_{23}+\Gamma_{14})$
$\Gamma^{\mathrm{NN}}_{\mathrm{00ss}}$	$(\sigma_0\cdot\hat{\mathrm{s}})$	$(\sigma_N\cdot\hat{\mathrm{s}})$	side, side	$\frac{1}{4}(-\Gamma_{41}+\Gamma_{32}+\Gamma_{23}-\Gamma_{14})$

Table B.1. The Pauli matrices dotted to particular directions, *i.e.* $\hat{\mathbf{n}}$, $\hat{\mathbf{k}}$, or $\hat{\mathbf{s}}$, extracts in the trace operations the interaction probabilities for combinations of the specified spin directions. The indices 00ij in $\Gamma^{\mathrm{NN}}_{\mathrm{00ij}}$ follow the convention of nucleon-nucleon scattering asymmetries given in the paper by Bystricky [2.7].

The $\Gamma_{\lambda\lambda'}$'s in the last column of table B.1 are scattering probabilities computed

using spin states in the direction $\hat{\mathbf{n}}$,

$$\Gamma_{\lambda\lambda'} = \langle\lambda|\, M^{NN\dagger} N^{NN}\, |\lambda'\rangle$$

where

$$|\lambda\rangle: \quad |1\rangle = |t_{0+} t_{N+}\rangle, \quad |2\rangle = |t_{0+} t_{N-}\rangle, \quad |3\rangle = |t_{0-} t_{N+}\rangle, \quad \text{and} \quad |4\rangle = |t_{0-} t_{N-}\rangle\ . \tag{B.7}$$

Furthermore, there are a total of sixteen spin-combined probabilities, and eight of them are zero due to parity conservation: Γ^{NN}_{00k0}, Γ^{NN}_{00s0}, Γ^{NN}_{000k}, Γ^{NN}_{000s}, Γ^{NN}_{00nk}, Γ^{NN}_{00kn}, Γ^{NN}_{00ns}, Γ^{NN}_{00sn}.

Using the spin-combined probabilities Γ^{NN}_{00ij} and the cross section expression in equation (B.1), one obtains the unpolarized cross section and asymmetries below

$$\frac{d\sigma_o}{d\Omega_1 d\Omega_2} = \frac{1}{\text{flux}^{NN}} \frac{1}{2E_0 2E_N} (2\pi)^4 \times \left[\int \frac{|\mathbf{p}_1|^2 d|\mathbf{p}_1|}{(2\pi)^3 2E_1} \frac{|\mathbf{p}_2|^2 d|\mathbf{p}_2|}{(2\pi)^3 2E_2} (2\pi)^3 \delta(\mathbf{p}_0 - \mathbf{p}_1 - \mathbf{p}_2 - \mathbf{p}_{N-1})\right] \Gamma^{NN}_{0000}\ ,$$

and

$$\frac{d\sigma_o}{d\Omega_1 d\Omega_2} A_{00ij} = \frac{1}{\text{flux}^{NN}} \frac{1}{2E_0 2E_N} (2\pi)^4 \times \left[\int \frac{|\mathbf{p}_1|^2 d|\mathbf{p}_1|}{(2\pi)^3 2E_1} \frac{|\mathbf{p}_2|^2 d|\mathbf{p}_2|}{(2\pi)^3 2E_2} (2\pi)^3 \delta(\mathbf{p}_0 - \mathbf{p}_1 - \mathbf{p}_2 - \mathbf{p}_{N-1})\right] \Gamma^{NN}_{00ij}\ . \tag{B.8}$$

In the following steps, the spin-combined probabilities Γ_{00ij}NN are rewritten to obtain cross section expressions given in terms of the beam and target polarizations. For a given polarization, there is some probability for the particle spin to be in the "up" or "(+)" state and some in the "down" or "(−)" state. Then, the beam and target polarizations can be then defined as

$$\mathbf{P}_b = P_{0+} - P_{0-}\ , \quad \mathbf{P}_t = P_{N+} - P_{N-}\ , \tag{B.9}$$

where

$$P_{0+} + P_{0-} = 1\ , \quad P_{N+} + P_{N-} = 1\ .$$

Let the normalized polarization states of the spin $\frac{1}{2}$ particles be defined as

$$|n_0\rangle = \langle s_{0+}|n_0\rangle\, |s_{0+}\rangle + \langle s_{0-}|n_0\rangle\, |s_{0-}\rangle$$
$$\text{and} \tag{B.10}$$
$$|n_N\rangle = \langle s_{N+}|n_N\rangle\, |s_{N+}\rangle + \langle s_{N-}|n_N\rangle\, |s_{N-}\rangle$$

where the (+) and (−) states are the two available states along the direction of polarizations for both the beam and the target particles, and the squares of the probability amplitudes are the probabilities P_{0+}, P_{0-}, P_{N+}, and P_{N-}.

Let the interaction probability for a given beam and target polarization be defined as, *i.e.* "polarization-specified",

$$\Gamma = \sum_{s_0, s_N} |\langle s_0|n_0\rangle|^2 \; |\langle s_N|n_N\rangle|^2 \; \Gamma(s_0, s_N) \tag{B.11}$$

which can be rewritten as the dot product of the row and the column matries as

$$\Gamma = \begin{pmatrix} P_{0+}P_{N+} & P_{0+}P_{N-} & P_{0-}P_{N+} & P_{0-}P_{N-} \end{pmatrix} \begin{pmatrix} \Gamma(s_{0+}, s_{N+})^{NN} \\ \Gamma(s_{0+}, s_{N-})^{NN} \\ \Gamma(s_{0-}, s_{N+})^{NN} \\ \Gamma(s_{0-}, s_{N-})^{NN} \end{pmatrix} . \tag{B.12}$$

The column vector of the spin-specified probabilities can be given in terms of spin-combined probabilities by writing equation (B.5) as a 4×4 matrix equation

$$\begin{pmatrix} \Gamma^{NN}_{0000} \\ \Gamma^{NN}_{00s_00} \\ \Gamma^{NN}_{000s_0} \\ \Gamma^{NN}_{00s_0s_N} \end{pmatrix} = \frac{1}{4} \begin{pmatrix} 1 & 1 & 1 & 1 \\ 1 & 1 & -1 & -1 \\ 1 & -1 & 1 & -1 \\ 1 & -1 & -1 & 1 \end{pmatrix} \begin{pmatrix} \Gamma(s_{0+}, s_{N+})^{NN} \\ \Gamma(s_{0+}, s_{N-})^{NN} \\ \Gamma(s_{0-}, s_{N+})^{NN} \\ \Gamma(s_{0-}, s_{N-})^{NN} \end{pmatrix} , \tag{B.13}$$

which can be inverted to give the spin-specified probabilities in terms of the spin-combined probabilities as

$$\begin{pmatrix} \Gamma(s_{0+}, s_{N+})^{NN} \\ \Gamma(s_{0+}, s_{N-})^{NN} \\ \Gamma(s_{0-}, s_{N+})^{NN} \\ \Gamma(s_{0-}, s_{N-})^{NN} \end{pmatrix} = \begin{pmatrix} 1 & 1 & 1 & 1 \\ 1 & 1 & -1 & -1 \\ 1 & -1 & 1 & -1 \\ 1 & -1 & -1 & 1 \end{pmatrix} \begin{pmatrix} \Gamma^{NN}_{0000} \\ \Gamma^{NN}_{00s_00} \\ \Gamma^{NN}_{000s_0} \\ \Gamma^{NN}_{00s_0s_N} \end{pmatrix} . \tag{B.14}$$

Inserting the results into equation (B.13) gives in terms of the beam and the target polarizations and the spin-combined probabilities

$$\Gamma = \left\{ \Gamma^{NN}_{0000} + P_b\Gamma^{NN}_{00s_00} + P_t\Gamma^{NN}_{000s_0} + P_bP_t\Gamma^{NN}_{00s_0s_A} \right\} . \tag{B.15}$$

Therefore, now an interaction probability is written in terms of the beam and the target polarizations and the spin-combined probabilities. Next, the spin-combined probabilities are expressed in terms of the spin-combined probabilities in Table C.1as

$$\Gamma = \Big\{ \Gamma^{NN}_{0000} + (\mathbf{P}_b \cdot \hat{\mathbf{n}})\Gamma^{NN}_{00n0} + (\mathbf{P}_t \cdot \hat{\mathbf{n}})\Gamma^{NN}_{000n} + (\mathbf{P}_b \cdot \hat{\mathbf{n}})(\mathbf{P}_t \cdot \hat{\mathbf{n}})\Gamma^{NN}_{00nn} + (\mathbf{P}_b \cdot \hat{\mathbf{k}})(\mathbf{P}_t \cdot \hat{\mathbf{l}})\Gamma^{NN}_{00kk} + (\mathbf{P}_b \cdot \hat{\mathbf{s}})(\mathbf{P}_t \cdot \hat{\mathbf{s}})\Gamma^{NN}_{00ss} + (\mathbf{P}_b \cdot \hat{\mathbf{k}})(\mathbf{P}_t \cdot \hat{\mathbf{s}})\Gamma^{NN}_{00ks} + (\mathbf{P}_b \cdot \hat{\mathbf{s}})(\mathbf{P}_t \cdot \hat{\mathbf{l}})\Gamma^{NN}_{00sk} \Big\}$$

where

$$\mathbf{P}_b = P_b \hat{\mathbf{s}}_0 \quad \text{and} \quad \mathbf{P}_t = P_t \hat{\mathbf{s}}_N \, . \tag{B.15}$$

Some of the spin-combined quantities given in equations Table B.1 are not included since as discussed earlier these quantities are zero due to parity conservation.

The polarization-specified interaction probability can now be substituted in the elastic cross section equation (B.1) in place of the spin-specified interaction probability to obtain

$$\frac{d\sigma}{d\Omega_1 d\Omega_2} = \frac{1}{\text{flux}^{NN}} \frac{1}{2E_0 2E_N} \left[\int \frac{|\mathbf{p}_1|^2 d|\mathbf{p}_1|}{(2\pi)^3 2E_1} \frac{|\mathbf{p}_2|^2 d|\mathbf{p}_2|}{(2\pi)^3 2E_2} (2\pi)^3 \delta(\mathbf{p}_0 - \mathbf{p}_1 - \mathbf{p}_2) \right]$$
$$\times \int dE \, (2\pi) \, \delta(E_0 + M_N - E_1 - E_2)$$
$$\Big\{ \Gamma^{NN}_{0000} + (\mathbf{P}_b \cdot \hat{\mathbf{n}})\Gamma^{NN}_{00n0} + (\mathbf{P}_t \cdot \hat{\mathbf{n}})\Gamma^{NN}_{000n} + (\mathbf{P}_b \cdot \hat{\mathbf{n}})(\mathbf{P}_t \cdot \hat{\mathbf{n}})\Gamma^{NN}_{00nn} + (\mathbf{P}_b \cdot \hat{\mathbf{l}})(\mathbf{P}_t \cdot \hat{\mathbf{l}})\Gamma^{NN}_{00ll} + (\mathbf{P}_b \cdot \hat{\mathbf{s}})(\mathbf{P}_t \cdot \hat{\mathbf{s}})\Gamma^{NN}_{00ss} + (\mathbf{P}_b \cdot \hat{\mathbf{l}})(\mathbf{P}_t \cdot \hat{\mathbf{s}})\Gamma^{NN}_{00ls} + (\mathbf{P}_b \cdot \hat{\mathbf{s}})(\mathbf{P}_t \cdot \hat{\mathbf{l}})\Gamma^{NN}_{00sl} \Big\} \, . \tag{B.16}$$

The cross section equation can finally be rewritten as

$$\frac{d\sigma}{d\Omega_1 d\Omega_2} = \frac{d\sigma_\circ}{d\Omega_1 d\Omega_2}$$
$$\times \Big\{ 1 + (\mathbf{P}_b \cdot \hat{\mathbf{n}})A_{00n0} + (\mathbf{P}_t \cdot \hat{\mathbf{n}})A_{000n} + (\mathbf{P}_b \cdot \hat{\mathbf{n}})(\mathbf{P}_t \cdot \hat{\mathbf{n}})A_{00nn} + (\mathbf{P}_b \cdot \hat{\mathbf{s}})(\mathbf{P}_t \cdot \hat{\mathbf{s}})A_{00ss} + (\mathbf{P}_b \cdot \hat{\mathbf{l}})(\mathbf{P}_t \cdot \hat{\mathbf{l}})A_{00kk} + (\mathbf{P}_b \cdot \hat{\mathbf{s}})(\mathbf{P}_t \cdot \hat{\mathbf{l}})A_{00sk} + (\mathbf{P}_b \cdot \hat{\mathbf{l}})(\mathbf{P}_t \cdot \hat{\mathbf{s}})A_{00ks} \Big\} \tag{B.17}$$

where

$$\frac{d\sigma_o}{d\Omega_1 d\Omega_2} = \frac{1}{flux^{NN}} \frac{1}{2E_0 2E_N} \left[\int \frac{|\mathbf{p}_1|^2 d|\mathbf{p}_1|}{(2\pi)^3 2E_1} \frac{|\mathbf{p}_2|^2 d|\mathbf{p}_2|}{(2\pi)^3 2E_2} (2\pi)^3 \delta(\mathbf{p}_0 - \mathbf{p}_1 - \mathbf{p}_2) \right]$$
$$\times \int dE\ (2\pi)\ \delta(E_0 + M_N - E_1 - E_2) \Gamma^{NN}_{0000}\ , \tag{B.18}$$

and

$$\frac{d\sigma_o}{d\Omega_1 d\Omega_2} A_{00ij} = \frac{1}{flux^{NN}} \frac{1}{2E_0 2E_N} \left[\int \frac{|\mathbf{p}_1|^2 d|\mathbf{p}_1|}{(2\pi)^3 2E_1} \frac{|\mathbf{p}_2|^2 d|\mathbf{p}_2|}{(2\pi)^3 2E_2} (2\pi)^3 \delta(\mathbf{p}_0 - \mathbf{p}_1 - \mathbf{p}_2) \right]$$
$$\times \int dE\ (2\pi)\ \delta(E_0 + M_N - E_1 - E_2) \Gamma^{NN}_{00ij}\ . \tag{B.19}$$

Appendix.C

Proton Spin-Dependent Quasielastic Scattering off ^{3}He

The general spin-dependent quasielastic scattering cross section for the ^{3}He(p,pN) can be written as

$$\frac{d\sigma(\mathbf{s}_0,\mathbf{s}_A)}{d\Omega_1 d\Omega_2 d|\mathbf{p}_{A-1}|} = \frac{1}{\text{flux}}\,\frac{1}{2E_0 2E_A} \times\left[\int \frac{|\mathbf{p}_1|^2 d|\mathbf{p}_1|}{(2\pi)^3 2E_1}\,\frac{|\mathbf{p}_2|^2 d|\mathbf{p}_2|}{(2\pi)^3 2E_2}\,\frac{|\mathbf{p}_{A-1}|^2 d\Omega_{A-1}}{(2\pi)^3}(2\pi)^3\delta(\mathbf{p}_0-\mathbf{p}_1-\mathbf{p}_2-\mathbf{p}_{A-1})\right] \times\int dE\,(2\pi)\,\delta\big(E_0+M_A-E_1-E_2-E_{A-1}(E)\big)\,\Gamma(\mathbf{s}_0,\mathbf{s}_A)\,, \tag{2.28}$$

where $\Gamma(\mathbf{s}_0,\mathbf{s}_A)$ is the "spin-specified" probability and can be written as the sum over spin states of the product of the nucleon-nucleon scattering amplitude and the spectral function,

$$\Gamma(\mathbf{s}_0,\mathbf{s}_A) = \sum_{\substack{\mathbf{s}_1,\mathbf{s}_2\\ \mathbf{s}'_N,\mathbf{s}_N}} \langle \mathbf{s}_0\mathbf{s}'_N|\, M^{NN\dagger}\,|\mathbf{s}_1\mathbf{s}_2\rangle\,\langle \mathbf{s}_1\mathbf{s}_2|\, M^{NN}\,|\mathbf{s}_0\mathbf{s}_N\rangle \times \langle \mathbf{s}_A\mathbf{s}_N|\,\widehat{S}(|\mathbf{p}_N|,E,t_N)\,|\mathbf{s}'_N\mathbf{s}_A\rangle\,. \tag{C.1}$$

The final spin states of particle 1 and 2 and the final states of the recoiling A−1 system have been summed over in the probability expression. The label A refers to the atomic number of the ^{3}He system. The derivation steps to formulate the final form of the quasielastic cross section expression in equation (2.28) below make use of the probabilty expressions for convenience.

The probability expression is simplified below showing only the spin variables that are going to be used in the derivations,

$$\Gamma(\mathbf{s}_0,\mathbf{s}_A) = \sum_{\mathbf{s}'_N,\mathbf{s}_N} \langle \mathbf{s}_0\mathbf{s}'_N|\, M^{NN\dagger}M^{NN}\,|\mathbf{s}_N\mathbf{s}_0\rangle\,\langle \mathbf{s}_A\mathbf{s}_N|\,\widehat{S}\,|\mathbf{s}'_N\mathbf{s}_A\rangle\,. \tag{C.2}$$

The spectral function has been parameterized by three scalar functions f_0, f_1, and f_2 in Schulze and Sauer [1.28] as

$$\widehat{S} = \frac{1}{2}\Big\{ f_0(|\mathbf{p}_N|,E,t_N) + \big[\, f_1(|\mathbf{p}_N|,E,t_N) - \frac{1}{3}f_2(|\mathbf{p}_N|,E,t_N)\,\big]\sigma_N\cdot\sigma_A + f_2(|\mathbf{p}_N|,E,t_N)\,\sigma_N\cdot\hat{\mathbf{p}}_N\sigma_A\cdot\hat{\mathbf{p}}_N\Big\}\,. \tag{1.9}$$

The three scalar functions are functions of the magnitude of the nucleon momentum, the removal energy, and the nucleon isospin. Below, matrix elements of the spectral function from equation (2.27) are introduced,

$$\begin{aligned} &S_{11} = \langle 1|\,\widehat{S}\,|1\rangle, \quad S_{12} = \langle 1|\,\widehat{S}\,|2\rangle, \quad S_{21} = \langle 2|\,\widehat{S}\,|1\rangle, \quad S_{22} = \langle 2|\,\widehat{S}\,|2\rangle, \\ &S_{33} = \langle 3|\,\widehat{S}\,|3\rangle, \quad S_{34} = \langle 3|\,\widehat{S}\,|4\rangle, \quad S_{43} = \langle 4|\,\widehat{S}\,|3\rangle, \text{ and } \quad S_{44} = \langle 4|\,\widehat{S}\,|4\rangle, \end{aligned} \tag{C.3}$$

where

$$|1\rangle = |s_{N+}s_{A+}\rangle,\ |2\rangle = |s_{N-}s_{A+}\rangle,\ |3\rangle = |s_{N+}s_{A-}\rangle, \text{ and } |4\rangle = |s_{N-}s_{A-}\rangle.$$

Note that the matrix elements are symmetric (or anti-symmetric) with the exchange of spin directions:

$$S_{11} = S_{44}, \quad S_{12} = -S_{43}, \quad S_{21} = -S_{34}, \text{ and } \quad S_{22} = S_{33}. \tag{C.4}$$

The sum of two diagonal elements that has either the nucleon or the nuclear spin direction flipped gives the spin-independent spectral function S,

$$\begin{aligned} S = \ S_{11} + S_{33} \ &= \ S_{22} + S_{44} \ = \ S_{11} + S_{22} \ = \ S_{33} + S_{44} \\ &= f_0\ . \end{aligned} \tag{C.5a}$$

And the difference of these diagonal matrix elements is proportional to the nucleon polarization r^N,

$$\begin{aligned} r^N = \frac{[S_{11} - S_{33}]}{S} &= \frac{-[S_{22} - S_{44}]}{S} = \frac{[S_{11} - S_{22}]}{S} = \frac{-[S_{33} - S_{44}]}{S} \\ &= \frac{1}{S}[f_1 - \frac{1}{3}f_2 + f_2(\hat{\mathbf{p}}_N \cdot \hat{\mathbf{s}}_0)^2]\ , \end{aligned} \tag{C.5b}$$

Let u_1^N be proportional to the sum of the off diagonal elements,

$$\begin{aligned} u_1^N = \frac{[S_{12} + S_{21}]}{S} &= \frac{-[(S_{34} + S_{43})]}{S} \\ &= \frac{1}{S}[(\hat{\mathbf{p}}_N \cdot \hat{\mathbf{s}}_A)(\hat{\mathbf{p}}_N \cdot \hat{\mathbf{s}}_A^{\perp 1})f_2]\ , \end{aligned} \tag{C.5c}$$

and let u_2^N be proportional to the difference of the off diagonal elements,

$$\begin{aligned} u_2^N = \frac{i[S_{12} - S_{21}]}{S} &= \frac{-i[S_{34} - S_{43}]}{S} \\ &= \frac{1}{S}[(\hat{\mathbf{p}}_N \cdot \hat{\mathbf{s}}_A)(\hat{\mathbf{p}}_N \cdot \hat{\mathbf{s}}_A^{\perp 2})f_2]\ . \end{aligned} \tag{C.5d}$$

The unit vectors $\hat{\mathbf{s}}_A$, $\hat{\mathbf{s}}_A^{\perp 1}$, and $\hat{\mathbf{s}}_A^{\perp 2}$ are orthogonal to each other and are defined such that

$$(\sigma_N \cdot \hat{\mathbf{s}}_A)|s_{N\pm}\rangle = \pm|s_{N\pm}\rangle,\ (\sigma_N \cdot \hat{\mathbf{s}}_A^{\perp 1})|s_{N\pm}\rangle = |s_{N\mp}\rangle,\ \text{and}\ (\sigma_N \cdot \hat{\mathbf{s}}_A^{\perp 2})|s_{N\pm}\rangle = \pm i|s_{N\pm}\rangle. \tag{C.6}$$

Below, these units vectors will be rewritten in terms of the basis of unit vectors for scattering, namely $\hat{\mathbf{n}}$, $\hat{\mathbf{k}}$, and $\hat{\mathbf{s}}$.

In a beam and target polarized experiment, the spin directions of the particles are flipped to measure all four possible beam and target spin states of the cross section expression in equation (2.28) or equivalently the interaction probability in equation (C.1). The four spin-specified probabilities are added below with different permutation of signs to form "spin-combined" probabilities which are related to the scattering asymmetries,

$$\begin{aligned}
\Gamma_{0000} &= \Gamma(s_{0+}, s_{A+}) + \Gamma(s_{0+}, s_{A-}) + \Gamma(s_{0-}, s_{A+}) + \Gamma(s_{0-}, s_{A-}) \\
\Gamma_{00\hat{s}_0 0} &= \Gamma(s_{0+}, s_{A+}) + \Gamma(s_{0+}, s_{A-}) - \Gamma(s_{0-}, s_{A+}) - \Gamma(s_{0-}, s_{A-}) \\
\Gamma_{000\hat{s}_A} &= \Gamma(s_{0+}, s_{A+}) - \Gamma(s_{0+}, s_{A-}) + \Gamma(s_{0-}, s_{A+}) - \Gamma(s_{0-}, s_{A-}) \\
\Gamma_{00\hat{s}_0\hat{s}_A} &= \Gamma(s_{0+}, s_{A+}) - \Gamma(s_{0+}, s_{A-}) - \Gamma(s_{0-}, s_{A+}) + \Gamma(s_{0-}, s_{A-}) .
\end{aligned} \tag{C.7}$$

These probability expressions can be rewritten as products of the nucleon-nucleon spin-combined probabilities with the nuclear structure functions. The spin-combined probabilities in equation (C.7) are then rewritten as

$$\begin{aligned}
\Gamma_{0000} &= \sum_{s_0, s_N, s'_N} \langle s_0 s_N|\, M^{NN\dagger} M^{NN}\, |s'_N s_0\rangle \sum_{s_A} \langle s_A s'_N|\, \widehat{S}\, |s_N s_A\rangle \\
&= \mathrm{Tr}_{\{s_0 s_N\}}\, M^{NN\dagger} M^{NN}\, \{\mathrm{Tr}_{\{s_A\}}\, \widehat{S}\,\} \\
&= \mathrm{Tr}_{\{s_0 s_N\}}\, M^{NN\dagger} M^{NN}\, S \\
&= \Gamma^{NN}_{0000} S\,,
\end{aligned} \tag{C.8a}$$

$$\begin{aligned}
\Gamma_{00\hat{s}_0 0} &= \sum_{s_0, s_N, s'_N} \langle s_0 s_N|\, (\sigma_0 \cdot \hat{s}_0) M^{NN\dagger} M^{NN}\, |s'_N s_0\rangle \sum_{s_A} \langle s_A s'_N|\, \widehat{S}\, |s_N s_A\rangle \\
&= \mathrm{Tr}_{\{s_0 s_N\}}\, (\sigma_0 \cdot \hat{s}_0) M^{NN\dagger} M^{NN}\, \{\mathrm{Tr}_{\{s_A\}}\, \widehat{S}\,\} \\
&= \mathrm{Tr}_{\{s_0 s_N\}}\, (\sigma_0 \cdot \hat{s}_0) M^{NN\dagger} M^{NN}\, S \\
&= \Gamma^{NN}_{00\hat{s}_0 0} S\,,
\end{aligned} \tag{C.8b}$$

$$\Gamma_{000\hat{\mathbf{s}}_A} = \sum_{\mathbf{s}_0,\mathbf{s}_N,\mathbf{s}'_N} \langle \mathbf{s}_0\mathbf{s}_N|\ \mathrm{M}^{NN\dagger}\mathrm{M}^{NN}\ |\mathbf{s}'_N\mathbf{s}_0\rangle \sum_{\mathbf{s}_A} \langle \mathbf{s}_A\mathbf{s}'_N|\ (\sigma_A\cdot\hat{\mathbf{s}}_A)\widehat{\mathrm{S}}\ |\mathbf{s}_N\mathbf{s}_A\rangle$$

$$= \mathrm{Tr}_{\{\mathbf{s}_0\mathbf{s}_N\}}\ \mathrm{M}^{NN\dagger}\mathrm{M}^{NN}\ \{\mathrm{Tr}_{\{\mathbf{s}_A\}}\ (\sigma_A\cdot\hat{\mathbf{s}}_A)\widehat{\mathrm{S}}\ \}$$

$$= \mathrm{Tr}_{\{\mathbf{s}_0\mathbf{s}_N\}}\ \mathrm{M}^{NN\dagger}\mathrm{M}^{NN}$$

$$\{\ [\mathrm{r}^N - \frac{\mathrm{f}_2}{\mathrm{S}}(\hat{\mathbf{p}}_N\cdot\hat{\mathbf{s}}_A)^2]\ \mathrm{S}\ (\sigma_N\cdot\hat{\mathbf{s}}_A)\ +\ \mathrm{f}_2\hat{\mathbf{p}}_N\cdot\hat{\mathbf{s}}_A(\sigma_N\cdot\hat{\mathbf{p}}_N)\ \}$$

$$= \Gamma^{NN}_{000\hat{\mathbf{s}}_A}[\mathrm{r}^N - \frac{\mathrm{f}_2}{\mathrm{S}}(\hat{\mathbf{p}}_N\cdot\hat{\mathbf{s}}_A)^2]\ \mathrm{S}\ +\ \Gamma^{NN}_{000\hat{\mathbf{p}}_N}\mathrm{f}_2\hat{\mathbf{p}}_N\cdot\hat{\mathbf{s}}_A$$

$$\approx \Gamma^{NN}_{000\hat{\mathbf{s}}_A}[\mathrm{r}^N - \frac{\mathrm{f}_2}{\mathrm{S}}(\hat{\mathbf{p}}_N\cdot\hat{\mathbf{s}}_A)^2]\ \mathrm{S}\ , \qquad \text{(C.8c)}$$

and

$$\Gamma_{00\hat{\mathbf{s}}_0\hat{\mathbf{s}}_A} = \sum_{\mathbf{s}_0,\mathbf{s}_N,\mathbf{s}'_N} \langle \mathbf{s}_0\mathbf{s}_N|\ (\sigma_0\cdot\hat{\mathbf{s}}_0)\mathrm{M}^{NN\dagger}\mathrm{M}^{NN}\ |\mathbf{s}'_N\mathbf{s}_0\rangle \sum_{\mathbf{s}_A} \langle \mathbf{s}_A\mathbf{s}'_N|\ (\sigma_A\cdot\hat{\mathbf{s}}_A)\widehat{\mathrm{S}}\ |\mathbf{s}_N\mathbf{s}_A\rangle$$

$$= \mathrm{Tr}_{\{\mathbf{s}_0\mathbf{s}_N\}}\ (\sigma_0\cdot\hat{\mathbf{s}}_0)\mathrm{M}^{NN\dagger}\mathrm{M}^{NN}\ \{\mathrm{Tr}_{\{\mathbf{s}_A\}}\ (\sigma_A\cdot\hat{\mathbf{s}}_A)\widehat{\mathrm{S}}\ \}$$

$$= \mathrm{Tr}_{\{\mathbf{s}_0\mathbf{s}_N\}}\ (\sigma_0\cdot\hat{\mathbf{s}}_0)\mathrm{M}^{NN\dagger}\mathrm{M}^{NN}$$

$$\{\ [\mathrm{r}^N - \frac{\mathrm{f}_2}{\mathrm{S}}(\hat{\mathbf{p}}_N\cdot\hat{\mathbf{s}}_A)^2]\ \mathrm{S}(\sigma_N\cdot\hat{\mathbf{s}}_A)\ +\ \mathrm{f}_2\hat{\mathbf{p}}_N\cdot\hat{\mathbf{s}}_A(\sigma_N\cdot\hat{\mathbf{p}}_N)\ \}$$

$$= \Gamma^{NN}_{00\hat{\mathbf{s}}_0\hat{\mathbf{s}}_A}[\mathrm{r}^N - \frac{\mathrm{f}_2}{\mathrm{S}}(\hat{\mathbf{p}}_N\cdot\hat{\mathbf{s}}_A)^2]\ \mathrm{S}\ +\ \Gamma^{NN}_{00\hat{\mathbf{s}}_0\hat{\mathbf{p}}_N}\mathrm{f}_2\hat{\mathbf{p}}_N\cdot\hat{\mathbf{s}}_A$$

$$\approx \Gamma^{NN}_{00\hat{\mathbf{s}}_0\hat{\mathbf{s}}_A}[\mathrm{r}^N - \frac{\mathrm{f}_2}{\mathrm{S}}(\hat{\mathbf{p}}_N\cdot\hat{\mathbf{s}}_A)^2]\ \mathrm{S}\ , \qquad \text{(C.8d)}$$

where r^N and S are the nuclear structure functions that have been defined in equations (C.5), and Γ^{NN}_{00ij}'s are the nucleon-nucleon spin-combined probabilities defined in the basis of unit vector directions $\hat{\mathbf{s}}_0$, $\hat{\mathbf{s}}_A$, and $\hat{\mathbf{p}}_N$.

The quantities $\Gamma_{000\hat{\mathbf{p}}_N}$ and $\Gamma_{00\hat{\mathbf{s}}_0\hat{\mathbf{p}}_N}$ can be reformulated in the basis of unit vectors $\hat{\mathbf{s}}_A$, $\hat{\mathbf{s}}_A^{\perp 1}$, and $\hat{\mathbf{s}}_A^{\perp 2}$, that are defined in equation (C.6),

$$\Gamma^{NN}_{000\hat{\mathbf{p}}_N} = \mathrm{Tr}_{\{\mathbf{s}_0\mathbf{s}_N\}}\ (\sigma_0\cdot\hat{\mathbf{p}}_N)\mathrm{M}^{NN\dagger}\mathrm{M}^{NN}$$

$$= \mathrm{Tr}_{\{\mathbf{s}_0\mathbf{s}_N\}}\ \Big[\hat{\mathbf{s}}_A\cdot\hat{\mathbf{p}}_N(\sigma_N\cdot\hat{\mathbf{s}}_A)\ +\ \hat{\mathbf{s}}_A^{\perp 1}\cdot\hat{\mathbf{p}}_N(\sigma_N\cdot\hat{\mathbf{s}}_A^{\perp 1})$$

$$+\ \hat{\mathbf{s}}_A^{\perp 2}\cdot\hat{\mathbf{p}}_N(\sigma_N\cdot\hat{\mathbf{s}}_A^{\perp 2})\Big]\ \mathrm{M}^{NN\dagger}\mathrm{M}^{NN}$$

$$= \hat{\mathbf{s}}_A\cdot\hat{\mathbf{p}}_N\Gamma^{NN}_{000\hat{\mathbf{s}}_A}\ +\ \hat{\mathbf{s}}_A^{\perp 1}\cdot\hat{\mathbf{p}}_N\Gamma^{NN}_{000\hat{\mathbf{s}}_A^{\perp 1}}\ +\ \hat{\mathbf{s}}_A^{\perp 2}\cdot\hat{\mathbf{p}}_N\Gamma^{NN}_{000\hat{\mathbf{s}}_A^{\perp 2}}\ , \qquad \text{(C.9a)}$$

and

$$\Gamma^{NN}_{00\hat{\mathbf{s}}_0\hat{\mathbf{p}}_N} = \mathrm{Tr}_{\{\mathbf{s}_0\mathbf{s}_N\}}\ (\sigma_0\cdot\hat{\mathbf{s}}_0)(\sigma_N\cdot\hat{\mathbf{p}}_N)\mathrm{M}^{NN\dagger}\mathrm{M}^{NN}$$

$$= \mathrm{Tr}_{\{\mathbf{s}_0\mathbf{s}_N\}} \Big[\hat{\mathbf{s}}_A \cdot \hat{\mathbf{p}}_N(\sigma_0 \cdot \hat{\mathbf{s}}_0)(\sigma_N \cdot \hat{\mathbf{s}}_A) + \hat{\mathbf{s}}_A^{\perp 1} \cdot \hat{\mathbf{p}}_N(\sigma_0 \cdot \hat{\mathbf{s}}_0)(\sigma_N \cdot \hat{\mathbf{s}}_A^{\perp 1}) + \hat{\mathbf{s}}_A^{\perp 2} \cdot \hat{\mathbf{p}}_N(\sigma_0 \cdot \hat{\mathbf{s}}_0)(\sigma_N \cdot \hat{\mathbf{s}}_A^{\perp 2}) \Big] M^{NN\dagger} M^{NN}$$

$$= \hat{\mathbf{s}}_A \cdot \hat{\mathbf{p}}_N \Gamma^{NN}_{00\hat{\mathbf{s}}_0\hat{\mathbf{s}}_A} + \hat{\mathbf{s}}_A^{\perp 1} \cdot \hat{\mathbf{p}}_N \Gamma^{NN}_{00\hat{\mathbf{s}}_0\hat{\mathbf{s}}_A^{\perp 1}} + \hat{\mathbf{s}}_A^{\perp 2} \cdot \hat{\mathbf{p}}_N \Gamma^{NN}_{00\hat{\mathbf{s}}_0\hat{\mathbf{s}}_A^{\perp 2}} , \qquad \text{(C.9b)}$$

where the epansion of the unit vector $\hat{\mathbf{p}}_N$

$$\hat{\mathbf{p}}_N = (\hat{\mathbf{s}}_A \cdot \hat{\mathbf{p}}_N)\hat{\mathbf{s}}_A + (\hat{\mathbf{s}}_A^{\perp 1} \cdot \hat{\mathbf{p}}_N)\hat{\mathbf{s}}_A^{\perp 1} + (\hat{\mathbf{s}}_A^{\perp 2} \cdot \hat{\mathbf{p}}_N)\hat{\mathbf{s}}_A^{\perp 2} \qquad \text{(C.10)}$$

has been used.

Therefore, the expressions in equations (C.8c,d) can be rewritten in terms of the nucleon-nucleon spin-combined probabilities defined in the basis of unit vectors, $\hat{\mathbf{n}}$, $\hat{\mathbf{k}}$, and $\hat{\mathbf{s}}$,

$$\Gamma_{000\hat{\mathbf{s}}_A} = \left\{ \Gamma^{NN}_{000\hat{\mathbf{s}}_A} r^N + \Gamma^{NN}_{000\hat{\mathbf{s}}_A^{\perp 1}} u_1^N + \Gamma^{NN}_{000\hat{\mathbf{s}}_A^{\perp 2}} u_2^N \right\} S$$

and

$$\Gamma_{00\hat{\mathbf{s}}_0\hat{\mathbf{s}}_A} = \left\{ \Gamma^{NN}_{00\hat{\mathbf{s}}_0\hat{\mathbf{s}}_A} r^N + \Gamma^{NN}_{00\hat{\mathbf{s}}_0\hat{\mathbf{s}}_A^{\perp 1}} u_1^N + \Gamma^{NN}_{00\hat{\mathbf{s}}_0\hat{\mathbf{s}}_A^{\perp 2}} u_2^N \right\} S . \qquad \text{(C.11)}$$

In any given experiment, the spin value of a large number of particles is parameterized by the polarization. Therefore, in the following a "polarization-specified" scattering probability is formulated with dependence on the beam and target polarizations instead of the spins. Since the steps are similar to that in equations (B.9-B.14), only the resulting polarization-specified probability is given below,

$$\Gamma = \left\{ \Gamma_{0000} + P_b \Gamma_{00\hat{\mathbf{s}}_0 0} + P_t \Gamma_{000\hat{\mathbf{s}}_0} + P_b P_t \Gamma_{00\hat{\mathbf{s}}_0\hat{\mathbf{s}}_A} \right\} , \qquad \text{(C.12)}$$

where P_b and P_t are the beam and the target polarizations respectively. Combining the equations (C.8), (C.11), and (C.12), the polarization-specified probability becomes

$$\Gamma = \Big\{ \Gamma^{NN}_{0000} + P_b \Gamma^{NN}_{00\hat{\mathbf{s}}_0 0} \Big[P_t \Gamma^{NN}_{000\hat{\mathbf{s}}_A} + P_b P_t \Gamma^{NN}_{00\hat{\mathbf{s}}_0\hat{\mathbf{s}}_A} \Big] r^N + \Big[P_t \Gamma^{NN}_{000\hat{\mathbf{s}}_A^{\perp 1}} + P_b P_t \Gamma^{NN}_{00\hat{\mathbf{s}}_0\hat{\mathbf{s}}_A^{\perp 1}} \Big] u_1^N + \Big[P_t \Gamma^{NN}_{000\hat{\mathbf{s}}_A^{\perp 2}} + P_b P_t \Gamma^{NN}_{00\hat{\mathbf{s}}_0\hat{\mathbf{s}}_A^{\perp 2}} \Big] u_2^N \Big\} S . \qquad \text{(C.13)}$$

In order to relate to nucleon-nucleon scattering data, the Γ^{NN}_{00ij}'s are redefined in the basis of unit vectors $\hat{\mathbf{n}}$, $\hat{\mathbf{k}}$, and $\hat{\mathbf{s}}$, [1]

$$\Gamma^{NN}_{0000} = \mathrm{Tr}_{\{\mathbf{s}_0\mathbf{s}_N\}}\, \mathrm{M}^{NN\dagger}\mathrm{M}^{NN} , \tag{C.14a}$$

$$\Gamma^{NN}_{00\hat{\mathbf{s}}_0 0} = \hat{\mathbf{n}}\cdot\hat{\mathbf{s}}_0\Gamma^{NN}_{000n} , \tag{C.14b}$$

$$\Gamma^{NN}_{000\hat{\mathbf{s}}_A} = \hat{\mathbf{n}}\cdot\hat{\mathbf{s}}_A\Gamma^{NN}_{00n0} , \tag{C.14c}$$

and

$$\begin{aligned}\Gamma^{NN}_{00\hat{\mathbf{s}}_0\hat{\mathbf{s}}_A} = {} & (\hat{\mathbf{n}}\cdot\hat{\mathbf{s}}_0)(\hat{\mathbf{n}}\cdot\hat{\mathbf{s}}_A)\Gamma^{NN}_{00nn} + (\hat{\mathbf{k}}\cdot\hat{\mathbf{s}}_0)(\hat{\mathbf{k}}\cdot\hat{\mathbf{s}}_A)\Gamma^{NN}_{00kk} + (\hat{\mathbf{s}}\cdot\hat{\mathbf{s}}_0)(\hat{\mathbf{s}}\cdot\hat{\mathbf{s}}_A)\Gamma^{NN}_{00ss} \\ & + (\hat{\mathbf{k}}\cdot\hat{\mathbf{s}}_0)(\hat{\mathbf{s}}\cdot\hat{\mathbf{s}}_A)\Gamma^{NN}_{00ks} + (\hat{\mathbf{s}}\cdot\hat{\mathbf{s}}_0)(\hat{\mathbf{k}}\cdot\hat{\mathbf{s}}_A)\Gamma^{NN}_{00sk} ,\end{aligned} \tag{C.14d}$$

$$\Gamma^{NN}_{000\hat{\mathbf{s}}^{\perp 1}_A} = (\hat{\mathbf{n}}\cdot\hat{\mathbf{s}}^{\perp 1}_A)\Gamma^{NN}_{00n0} , \tag{C.14e}$$

$$\begin{aligned}\Gamma^{NN}_{00\hat{\mathbf{s}}_0\hat{\mathbf{s}}^{\perp 1}_A} = {} & (\hat{\mathbf{n}}\cdot\hat{\mathbf{s}}_0)(\hat{\mathbf{n}}\cdot\hat{\mathbf{s}}^{\perp 1}_A)\Gamma^{NN}_{00nn} + (\hat{\mathbf{k}}\cdot\hat{\mathbf{s}}_0)(\hat{\mathbf{k}}\cdot\hat{\mathbf{s}}^{\perp 1}_A)\Gamma^{NN}_{00kk} + (\hat{\mathbf{s}}\cdot\hat{\mathbf{s}}_0)(\hat{\mathbf{s}}\cdot\hat{\mathbf{s}}^{\perp 1}_A)\Gamma^{NN}_{00ss} \\ & + (\hat{\mathbf{k}}\cdot\hat{\mathbf{s}}_0)(\hat{\mathbf{s}}\cdot\hat{\mathbf{s}}^{\perp 1}_A)\Gamma^{NN}_{00ks} + (\hat{\mathbf{s}}\cdot\hat{\mathbf{s}}_0)(\hat{\mathbf{k}}\cdot\hat{\mathbf{s}}^{\perp 1}_A)\Gamma^{NN}_{00sk} ,\end{aligned} \tag{C.14f}$$

$$\Gamma^{NN}_{000\hat{\mathbf{s}}^{\perp 2}_A} = (\hat{\mathbf{n}}\cdot\hat{\mathbf{s}}^{\perp 2}_A)\Gamma^{NN}_{00n0} , \tag{C.14g}$$

$$\begin{aligned}\Gamma^{NN}_{00\hat{\mathbf{s}}_0\hat{\mathbf{s}}^{\perp 2}_A} = {} & (\hat{\mathbf{n}}\cdot\hat{\mathbf{s}}_0)(\hat{\mathbf{n}}\cdot\hat{\mathbf{s}}^{\perp 2}_A)\Gamma^{NN}_{00nn} + (\hat{\mathbf{k}}\cdot\hat{\mathbf{s}}_0)(\hat{\mathbf{k}}\cdot\hat{\mathbf{s}}^{\perp 2}_A)\Gamma^{NN}_{00kk} + (\hat{\mathbf{s}}\cdot\hat{\mathbf{s}}_0)(\hat{\mathbf{s}}\cdot\hat{\mathbf{s}}^{\perp 2}_A)\Gamma^{NN}_{00ss} \\ & + (\hat{\mathbf{k}}\cdot\hat{\mathbf{s}}_0)(\hat{\mathbf{s}}\cdot\hat{\mathbf{s}}^{\perp 2}_A)\Gamma^{NN}_{00ks} + (\hat{\mathbf{s}}\cdot\hat{\mathbf{s}}_0)(\hat{\mathbf{k}}\cdot\hat{\mathbf{s}}^{\perp 2}_A)\Gamma^{NN}_{00sk} .\end{aligned} \tag{C.14h}$$

These expressions of the nucleon-nucleon spin-combined probabilities can be substituted into the expression of the polarization-specified probability in equation (C.13) to obtain

$$\begin{aligned}\Gamma = {} & \Big\{ \Gamma^{NN}_{0000} + (\hat{\mathbf{n}}\cdot\mathbf{P}_b)\Gamma^{NN}_{00n0} \\ & + \Big[(\hat{\mathbf{n}}\cdot\mathbf{P}_t)\Gamma^{NN}_{000n} + (\hat{\mathbf{n}}\cdot\mathbf{P}_b)(\hat{\mathbf{n}}\cdot\mathbf{P}_t)\Gamma^{NN}_{00nn} \\ & + (\hat{\mathbf{k}}\cdot\mathbf{P}_b)(\hat{\mathbf{k}}\cdot\mathbf{P}_t)\Gamma^{NN}_{00kk} + (\hat{\mathbf{s}}\cdot\mathbf{P}_b)(\hat{\mathbf{s}}\cdot\mathbf{P}_t)\Gamma^{NN}_{00ss} \\ & + (\hat{\mathbf{k}}\cdot\mathbf{P}_b)(\hat{\mathbf{s}}\cdot\mathbf{P}_t)\Gamma^{NN}_{00ks} + (\hat{\mathbf{s}}\cdot\mathbf{P}_b)(\hat{\mathbf{k}}\cdot\mathbf{P}_t)\Gamma^{NN}_{00sk} \Big]\, \mathrm{r}^N \\ & + \mathrm{P}_t\,(\hat{\mathbf{n}}\cdot\mathbf{u}^N)\Gamma^{NN}_{000n} + (\hat{\mathbf{n}}\cdot\mathbf{P}_b)\,\mathrm{P}_t\,(\hat{\mathbf{n}}\cdot\mathbf{u}^N)\Gamma^{NN}_{00nn}\end{aligned}$$

[1] The results in equations (C.14a – d) are similar to that in Appendix B.

$$+ (\hat{\mathbf{k}}\cdot\mathbf{P}_b)\,P_t\,(\hat{\mathbf{k}}\cdot\mathbf{u}^N)\Gamma^{NN}_{00kk} + (\hat{\mathbf{s}}\cdot\mathbf{P}_b)\,P_t\,(\hat{\mathbf{s}}\cdot\mathbf{u}^N)\Gamma^{NN}_{00ss}$$
$$+ (\hat{\mathbf{k}}\cdot\mathbf{P}_b)\,P_t\,(\hat{\mathbf{s}}\cdot\mathbf{u}^N)\Gamma^{NN}_{00ks} + (\hat{\mathbf{s}}\cdot\mathbf{P}_b)\,P_t\,(\hat{\mathbf{k}}\cdot\mathbf{u}^N)\Gamma^{NN}_{00sk}\Big\}\,S\,, \tag{C.15}$$

where

$$\mathbf{u}^N = \hat{\mathbf{s}}^{\perp 1}_A u^N_1 + \hat{\mathbf{s}}^{\perp 2}_A u^N_2\,.$$

Finally, the above polarization-specified probability is substituted in the cross section expression in equation (2.28) to give

$$\frac{d\sigma}{d\Omega_1 d\Omega_2 d|\mathbf{p}_{A-1}|} = \frac{1}{\text{flux}}\,\frac{1}{2E_0 2E_A}$$

$$\times\left[\int \frac{|\mathbf{p}_1|^2 d|\mathbf{p}_1|}{(2\pi)^3 2E_1}\,\frac{|\mathbf{p}_2|^2 d|\mathbf{p}_2|}{(2\pi)^3 2E_2}\,\frac{|\mathbf{p}_{A-1}|^2 d\Omega_{A-1}}{(2\pi)^3}(2\pi)^3\delta(\mathbf{p}_0-\mathbf{p}_1-\mathbf{p}_2-\mathbf{p}_{A-1})\right]$$

$$\times\int dE\,(2\pi)\,\delta\big(E_0+M_A-E_1-E_2-E_{A-1}(E)\big)$$

$$\Big\{\Gamma_{0000} + (\hat{\mathbf{n}}\cdot\mathbf{P}_b)\Gamma_{00n0} + \Big[(\hat{\mathbf{n}}\cdot\mathbf{P}_t)\Gamma^{NN}_{000n} + (\hat{\mathbf{n}}\cdot\mathbf{P}_b)(\hat{\mathbf{n}}\cdot\mathbf{P}_t)\Gamma^{NN}_{00nn}$$
$$+ (\hat{\mathbf{k}}\cdot\mathbf{P}_b)(\hat{\mathbf{k}}\cdot\mathbf{P}_t)\Gamma^{NN}_{00kk} + (\hat{\mathbf{s}}\cdot\mathbf{P}_b)(\hat{\mathbf{s}}\cdot\mathbf{P}_t)\Gamma^{NN}_{00ss}$$
$$+ (\hat{\mathbf{k}}\cdot\mathbf{P}_b)(\hat{\mathbf{s}}\cdot\mathbf{P}_t)\Gamma^{NN}_{00ks} + (\hat{\mathbf{s}}\cdot\mathbf{P}_b)(\hat{\mathbf{k}}\cdot\mathbf{P}_t)\Gamma^{NN}_{00sk}\Big]\,r^N$$
$$+ P_t\,(\hat{\mathbf{n}}\cdot\mathbf{u}^N)\Gamma^{NN}_{000n} + (\hat{\mathbf{n}}\cdot\mathbf{P}_b)\,P_t\,(\hat{\mathbf{n}}\cdot\mathbf{u}^N)\Gamma^{NN}_{00nn}$$
$$+ (\hat{\mathbf{k}}\cdot\mathbf{P}_b)\,P_t\,(\hat{\mathbf{k}}\cdot\mathbf{u}^N)\Gamma^{NN}_{00kk} + (\hat{\mathbf{s}}\cdot\mathbf{P}_b)\,P_t\,(\hat{\mathbf{s}}\cdot\mathbf{u}^N)\Gamma^{NN}_{00ss}$$
$$+ (\hat{\mathbf{k}}\cdot\mathbf{P}_b)\,P_t\,(\hat{\mathbf{s}}\cdot\mathbf{u}^N)\Gamma^{NN}_{00ks} + (\hat{\mathbf{s}}\cdot\mathbf{P}_b)\,P_t\,(\hat{\mathbf{k}}\cdot\mathbf{u}^N)\Gamma^{NN}_{00sk}\Big\}\,S\,. \tag{C.16}$$

The cross section equation can finally be rewritten as in equations (2.29, 2.30),

$$\frac{d\sigma}{d\Omega_1 d\Omega_2 d|\mathbf{p}_{A-1}|} = \frac{d\sigma_\circ}{d\Omega_1 d\Omega_2 d|\mathbf{p}_{A-1}|}\Big\{1 + (\hat{\mathbf{n}}\cdot\mathbf{P}_b)A_{00n0}$$
$$+ \Big[(\hat{\mathbf{n}}\cdot\mathbf{P}_t)A_{000n} + (\hat{\mathbf{n}}\cdot\mathbf{P}_b)(\hat{\mathbf{n}}\cdot\mathbf{P}_t)A_{00nn}$$
$$+ (\hat{\mathbf{k}}\cdot\mathbf{P}_b)(\hat{\mathbf{k}}\cdot\mathbf{P}_t)A_{00kk} + (\hat{\mathbf{s}}\cdot\mathbf{P}_b)(\hat{\mathbf{s}}\cdot\mathbf{P}_t)A_{00ss}$$
$$+ (\hat{\mathbf{k}}\cdot\mathbf{P}_b)(\hat{\mathbf{s}}\cdot\mathbf{P}_t)A_{00ks} + (\hat{\mathbf{s}}\cdot\mathbf{P}_b)(\hat{\mathbf{k}}\cdot\mathbf{P}_t)A_{00sk}\Big]$$
$$+ P_t\,A'_{000n} + (\hat{\mathbf{n}}\cdot\mathbf{P}_b)\,P_t\,A'_{00nn}$$

$$+ (\hat{\mathbf{k}} \cdot \mathbf{P}_b)\, P_t\, A'_{00kk} + (\hat{\mathbf{s}} \cdot \mathbf{P}_b)\, P_t\, A'_{00ss}$$
$$+ (\hat{\mathbf{k}} \cdot \mathbf{P}_b)\, P_t\, A'_{00ks} + (\hat{\mathbf{s}} \cdot \mathbf{P}_b)\, P_t\, A'_{00sk} \Big\}\, S\,, \tag{C.17a}$$

where

$$\frac{d\sigma_\circ}{d\Omega_1 d\Omega_2 d|\mathbf{p}_{A-1}|} = \int dE |\mathbf{p}_{A-1}|^2 d\Omega_{A-1}\, \frac{flux^{NN}}{flux}\, \frac{d\sigma_\circ^{NN}}{d\Omega_1 d\Omega_2}\, S(|\mathbf{p}_N|, E, t_N)\,, \tag{C.17b}$$

$$A_{00n0} \frac{d\sigma_\circ}{d\Omega_1 d\Omega_2 d|\mathbf{p}_{A-1}|} = \int dE |\mathbf{p}_{A-1}|^2 d\Omega_{A-1}\, A_{00n0}^{NN}\, \frac{d\sigma_\circ^{NN}}{d\Omega_1 d\Omega_2}\, S(|\mathbf{p}_N|, E, t_N)\,, \tag{C.17c}$$

$$A_{00ij} \frac{d\sigma_\circ}{d\Omega_1 d\Omega_2 d|\mathbf{p}_{A-1}|} = \int dE |\mathbf{p}_{A-1}|^2 d\Omega_{A-1}\, \frac{flux^{NN}}{flux}\, A_{00ij}^{NN}\, \frac{d\sigma_\circ^{NN}}{d\Omega_1 d\Omega_2}$$
$$r^N(|\mathbf{p}_N|, E, t_N)\, S(|\mathbf{p}_N|, E, t_N)\,, \tag{C.17d}$$

and

$$A'_{00ij} \frac{d\sigma_\circ}{d\Omega_1 d\Omega_2 d|\mathbf{p}_{A-1}|} = \int dE |\mathbf{p}_{A-1}|^2 d\Omega_{A-1}\, \frac{flux^{NN}}{flux}\, A_{00ij}^{NN}\, \frac{d\sigma_\circ^{NN}}{d\Omega_1 d\Omega_2}$$
$$(\hat{\imath} \cdot \mathbf{u}^N)(\hat{\jmath} \cdot \mathbf{u}^N)\, S(|\mathbf{p}_N|, E, t_N)\,, \tag{C.17e}$$

and where the index {ij} is either for the target asymmetry or a spin-correlation parameter, and

$$\frac{1}{flux} = \frac{E_0}{\sqrt{E_0^2 - m_0^2}}$$

and

$$\frac{1}{flux^{NN}} = \frac{E_0 E_N - \mathbf{p}_0 \cdot \mathbf{p}_N}{\sqrt{(E_0 E_N - \mathbf{p}_0 \cdot \mathbf{p}_N)^2 - (m_0 m_N)^2}}\,.$$

In PWIA, the missing momentum $\mathbf{p}_m$ and the missing energy E_m are identified with the nucleon momentum $\mathbf{p}_{A-1}$ and the separation energy E. Moreover, implicit in the spectral function $S(|\mathbf{p}_N|, E, t_N)$ is the equality in the lab frame of the nucleon momentum $|\mathbf{p}_N|$ and the recoiling system momentum $|\mathbf{p}_{A-1}|$. Therefore, the expression for the polarized quasielastic scattering in equation (C.17a-e) can be rewritten in terms of the missing momentum p_m. Finally, since the neutron polarization r^n is one at low p_m values and the beam related neutron-proton scattering asymmetry is identical to the target related neutron-proton asymmetry, the target related asymmetry A_{000n}^n becomes identical to the beam related asymmetry A_{00n0}^n in the PWIA model at low p_m values.

Appendix D

Detector Electronics and Scalers

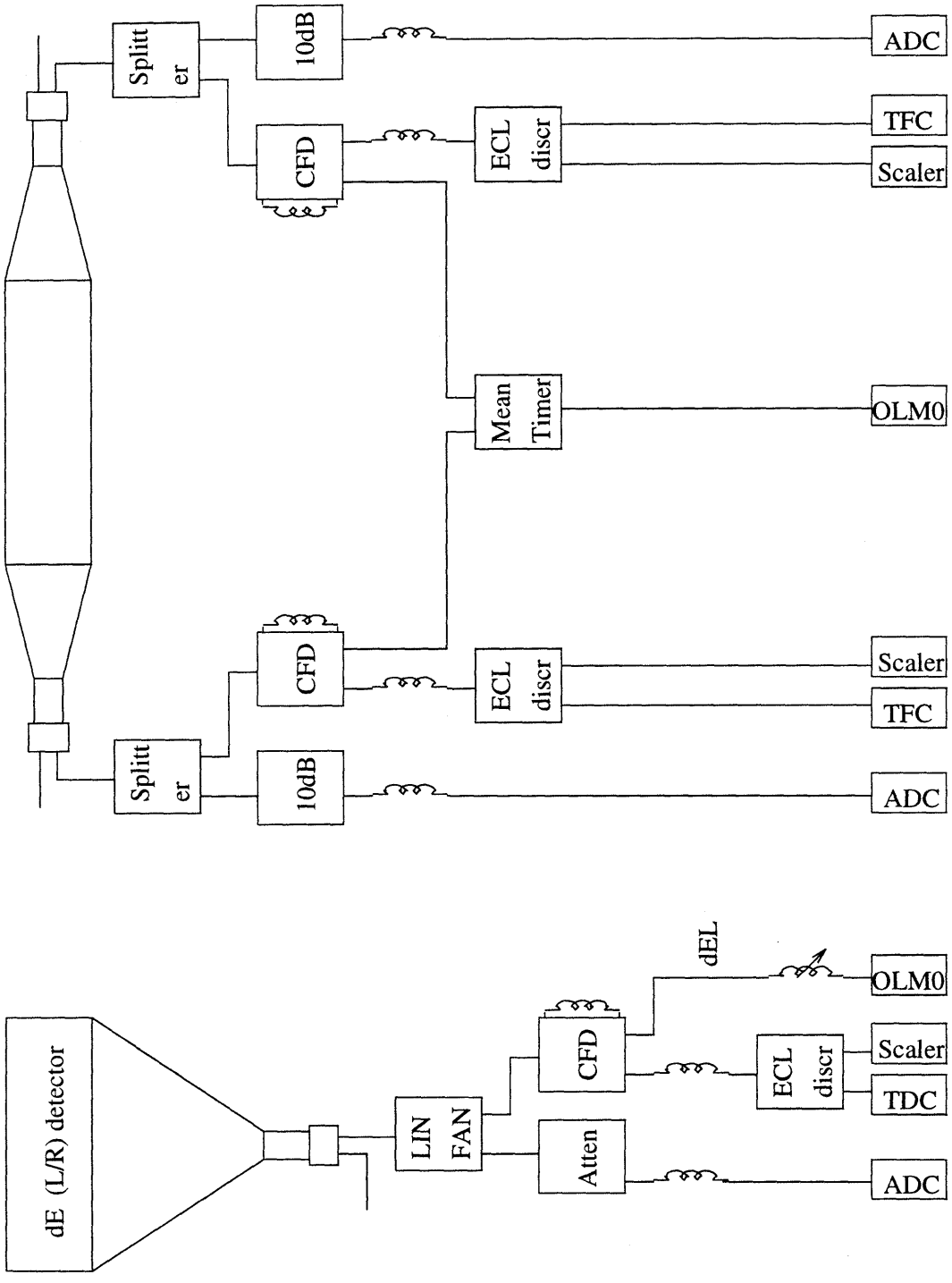

Figure D.1. A schematic diagram of the dE and the E detector electronics.

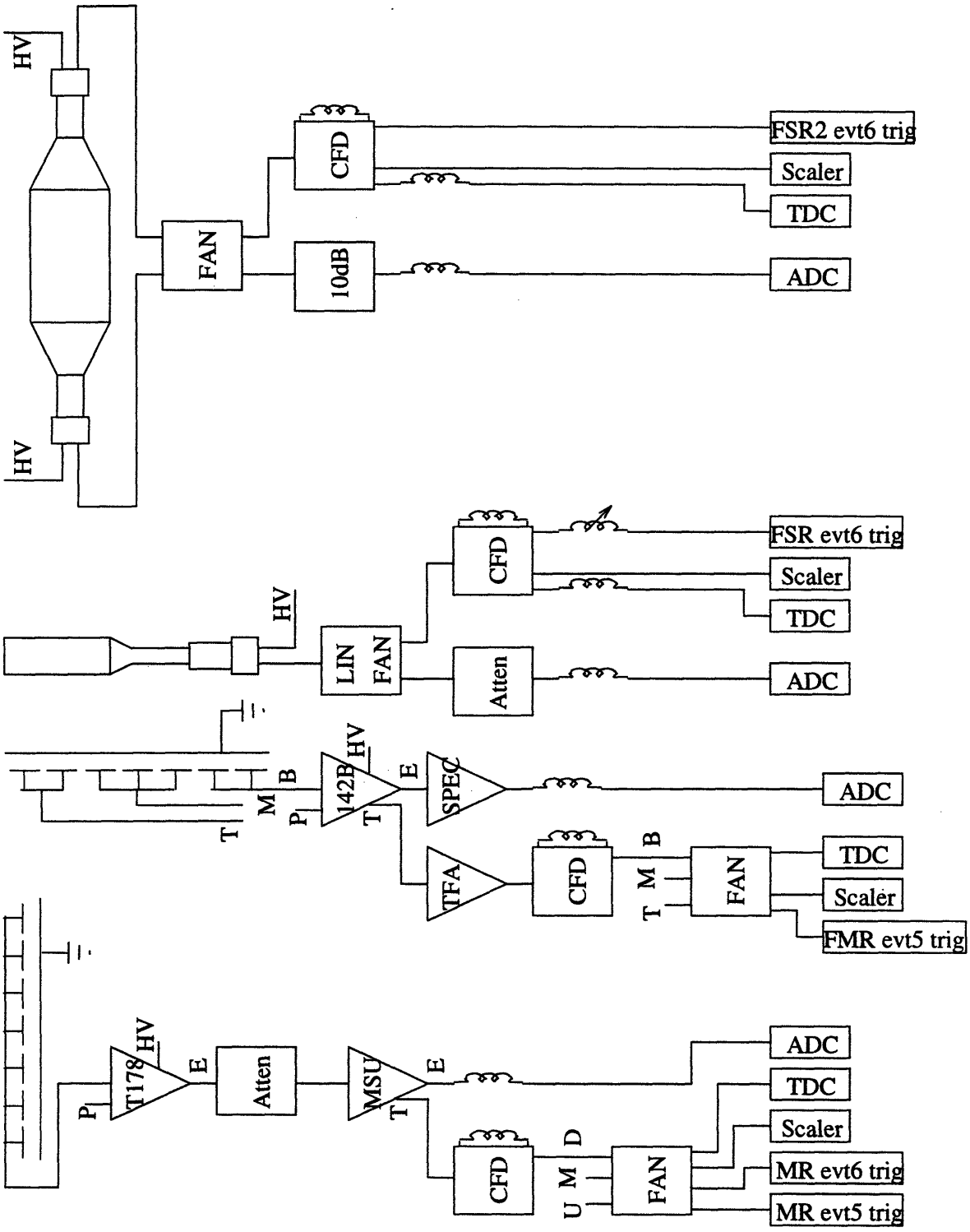

Figure D.2. A schematic diagram of the side microstrip detectors, the forward microstrip detectors, the forward scintillator, and the outside forward scintillator2 electronics.

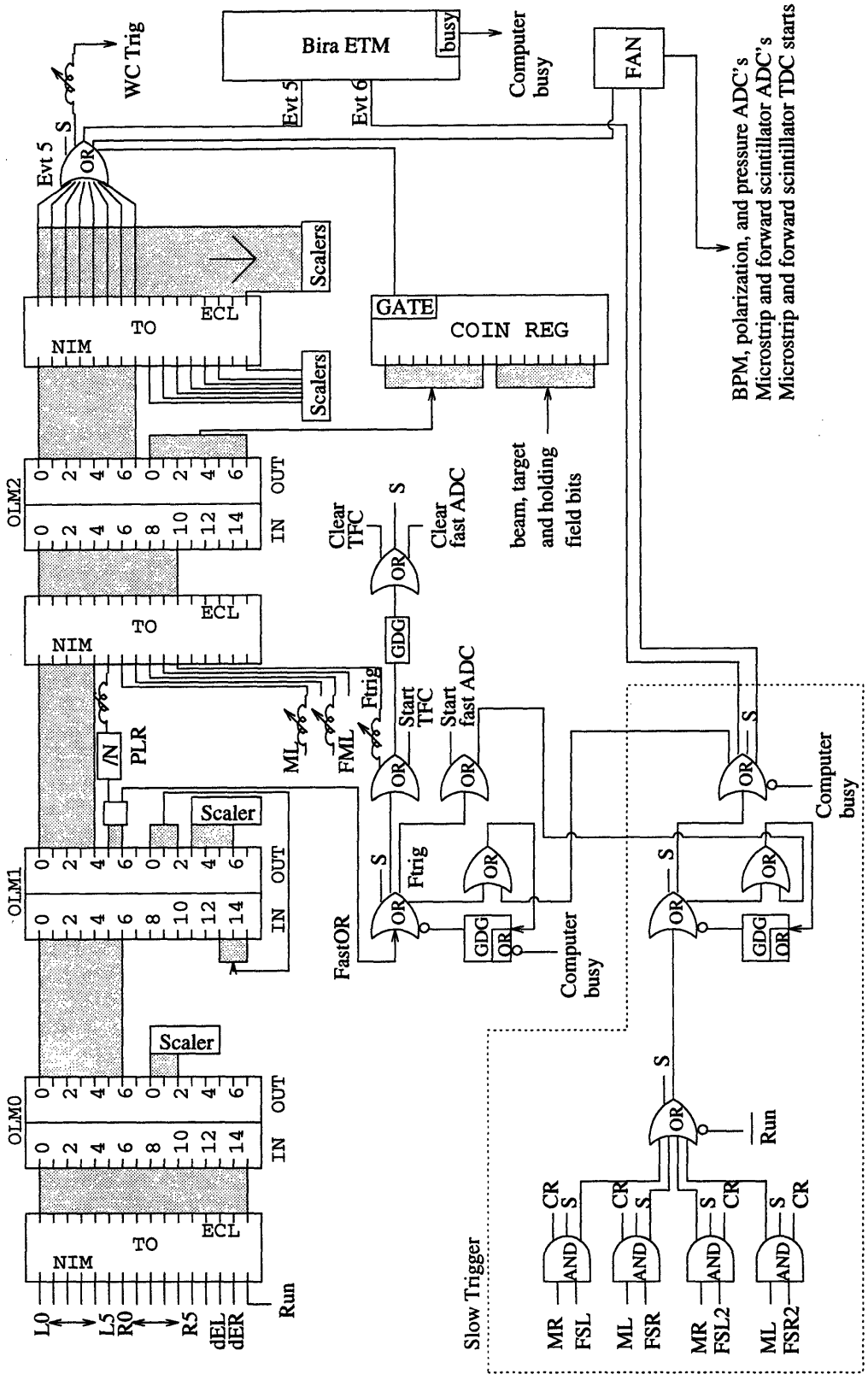

Figure D.3. A schematic diagram of the "fast" and the "slow" trigger system.

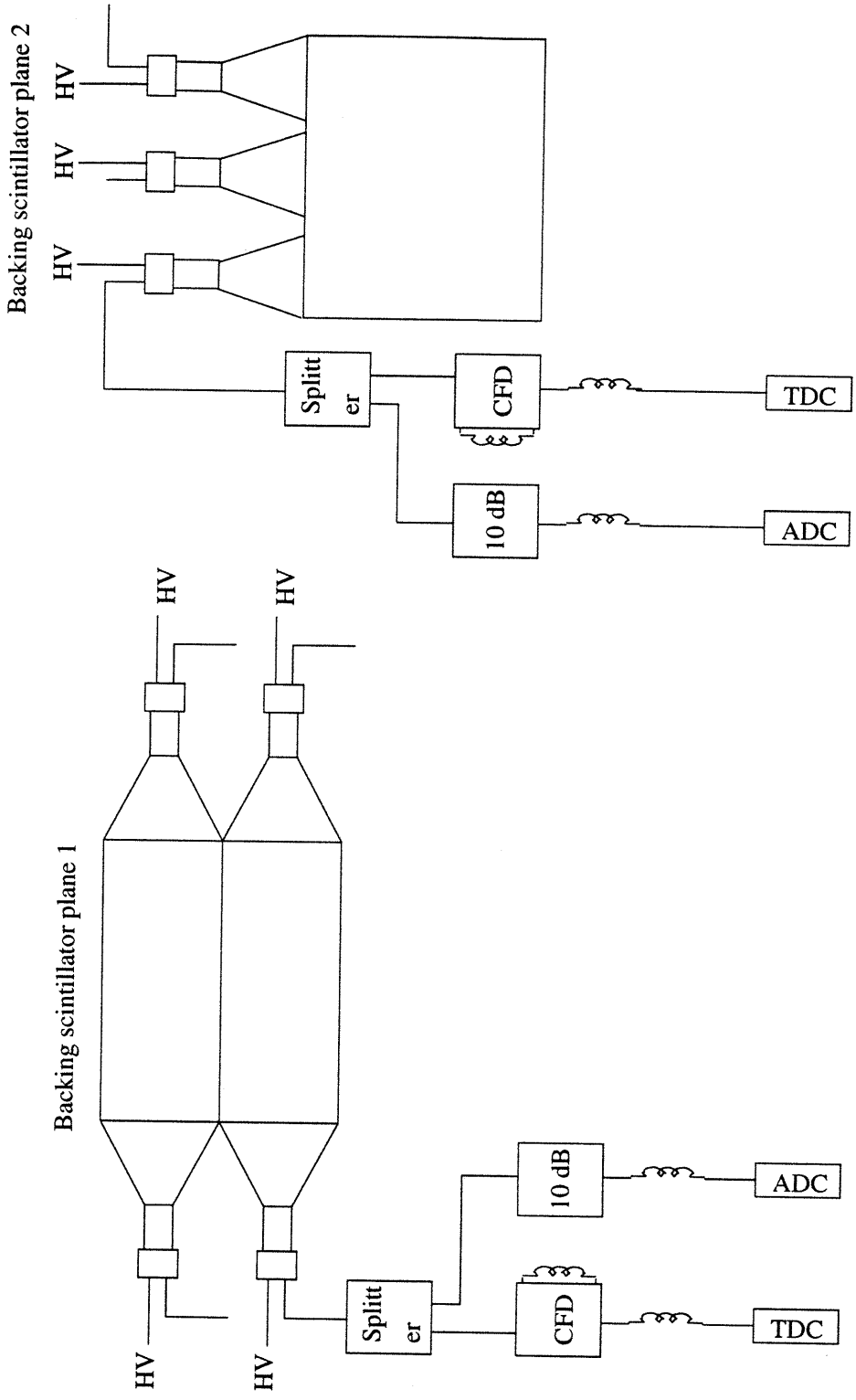

Figure D.4. A schematic diagram of the backing scintillators and the multiwire proportional chamber electronics.

	scalers		scalers		scalers
1	mLU	37	L2+	73	ftrig
2	mLM	38	R0−	74	fast clear
3	mLD	39	L3+	75	pLR / n
4	mRU	40	R5−	76	dt clock ungtd
5	mRM	41	L4+	77	dt clock gated
6	mRD	42	R4−	78	pLnR accidental
7	mL or	43	L5+	79	pRnL accidental
8	mR or	44	R3−	80	sclr_80
9	fsL = Mon1 L	45	R0+	81	EL
10	fsR = Mon1 R	46	L2−	82	ER
11	fsL2 = Mon2 L	47	R1+	83	pLR
12	fsR2 = Mon2 R	48	L1−	84	Fast OR
13	fmL	49	R2+	85	cosmic L
14	fmR	50	L0−	86	cosmic R
15	PCT: do not use	51	R3+	87	sclr_87
16	BIM	52	L5−	88	sclr_88
17	cosmic evt 5	53	R4+	89	sclr_89
18	pLnR	54	L4−	90	sclr_90
19	pRnL	55	R5+	91	sclr_91
20	p-sing / n	56	L3−	92	sclr_92
21	pLmR evt5	57	dEL	93	sclr_93
22	pRmL evt5	58	BPR1	94	sclr_94
23	pLfmR evt5	59	deR	95	sclr_95
24	pRfmL evt5	60	BPL1	96	sclr_96
25	evt5 OR	61	BPR2	97	mRfsL evt 6
26	p2p	62	BPL2	98	mLfsR evt 6
27	ppn	63	sclr_63	99	slow OR
28	sclr_28	64	sclr_64	100	STRIG ungated
29	sclr_29	65	wc R x1	101	STRIG gated
30	cycles	66	wc R y1	102	evt 5 OR evt 6
31	sclr_31	67	wc R x2	103	mRfsL2 evt 6
32	10Hz clock	68	wc R y2	104	mLfsR2 evt 6
33	L0+	69	wc L x1	105	sclr_105
34	R2−	70	wc L y1	106	beam spin 1
35	L1+	71	wc L x2	107	beam spin 2
36	R1−	72	wc L y2	108	sclr_108

Table D.1. The CE-25 scalers.

Appendix E

Time of Flight Calibration

A different time of flight (tof) calibration is presented below. Towards the end of the analysis of the 197 MeV data, it was noticed in a hydrogen target run that the distribution of speed β in the right detector arm for the 'neutron' was slightly higher than that for the proton while the two were in agreement in the left detector arm. The unexpected finding prompted a study of the tof calibration, particularly the particle trajectory of the LpRn reaction.

The intersection position on the E detector scintillator bars obtained using the timing between tfc signal of the two end PMT's were compared with that obtained from the wire chamber trajectories in figures E.1 and E.2. One finds in figure E.2 that the tfc-intersection positions were different from the wire-chamber-intersection positions , 3-7 cm, for each detector bar in the right side detector arm. The differences were found only after the data analysis. Since the offset in each bar were not uniform for the whole stack, the E detector as a stack could not simply be rotated in angle to adjust for the position offsets although offsets could be added for individual bars. After much trial and error, it was pointed out that due to poor momentum resolution these offsets were not significant at all to cause any diference in the asymmetry results. Three different ^{3}He runs were analyzed with new positon offsets, and the results were found to be identical to that analyzed using old tfc-intersection offsets. If the discrepancies were corrected for, the missing momentum resolution could be improved slightly. The almost null effect on the final asymmetries, however, was not sufficient to not carry out a new tof calibration as the unexpected discrepancy needed to be understood.

The discrepancy was not resolved by a simple procedure of the adjustment of the intersection position offsets of individual scintillator bar and the angle of the whole stack in the right detector arm. The adjustment did not center simultaneously around zero for the LpRn reaction the missing momentum components p_{mx} and p_{mz}—the component p_{my} was almost always centered. Moreover, the adjustment changed the missing momentum distributions for the p-p reaction. It was decided that a new tof calibration for the LpRn reaction was needed to center simultaneously all three missing momentum components. Furthermore, in the first calibration analysis, the missing momentum resolution for the LpRn and LnRp reactions was not calculated. In order to determine the resolutions, calibration was needed of the mechanism that measured the 'neutron' tof using the hydrogen target data. A new

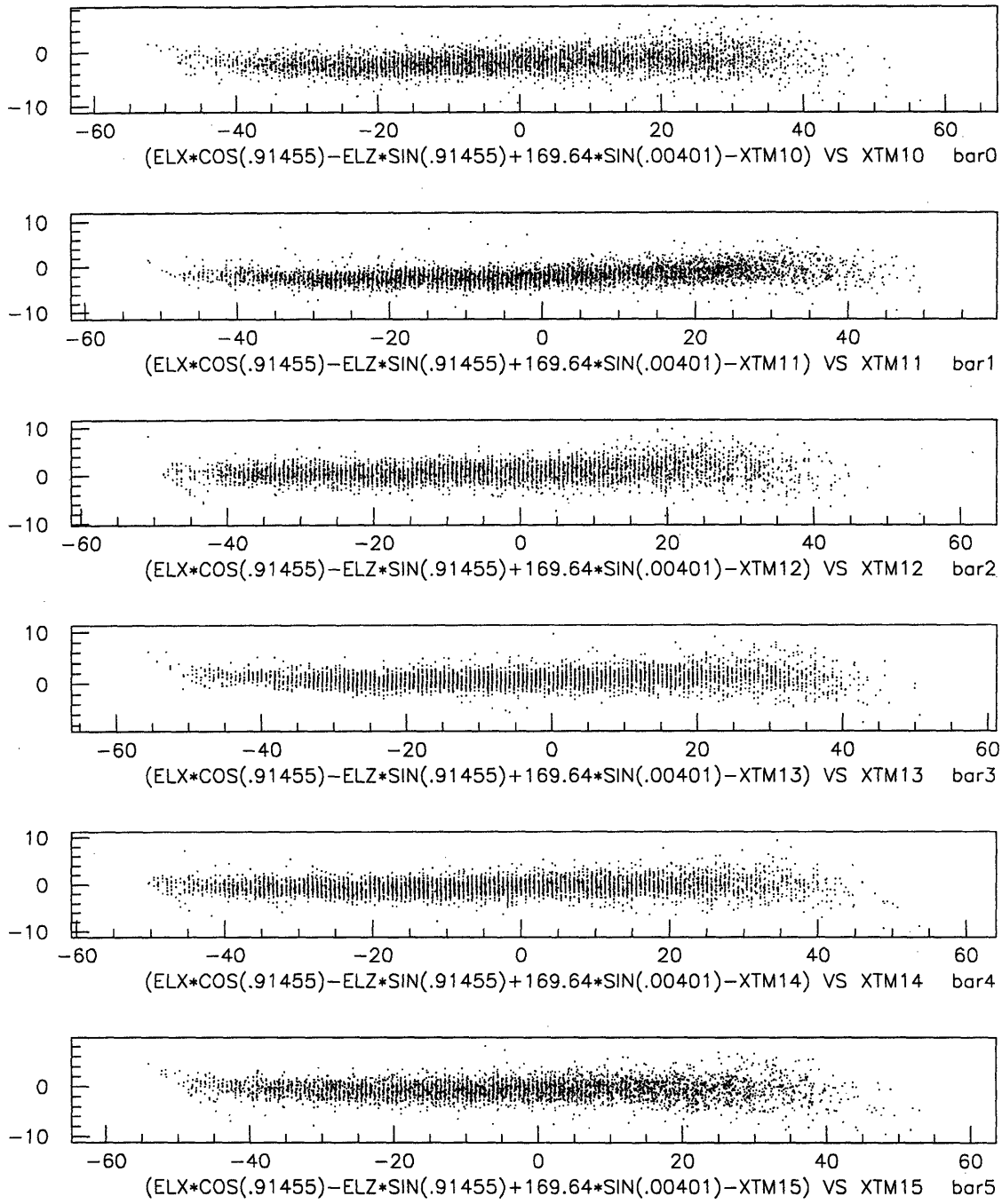

Figure E.1. The difference of intersection position between that calculated using the detector bar end PMTs' timing informations and that using the wire chamber informations is plotted against the hit position from timing informations for the left side detector bars 0, 1, 2, 3, 4, and 5.

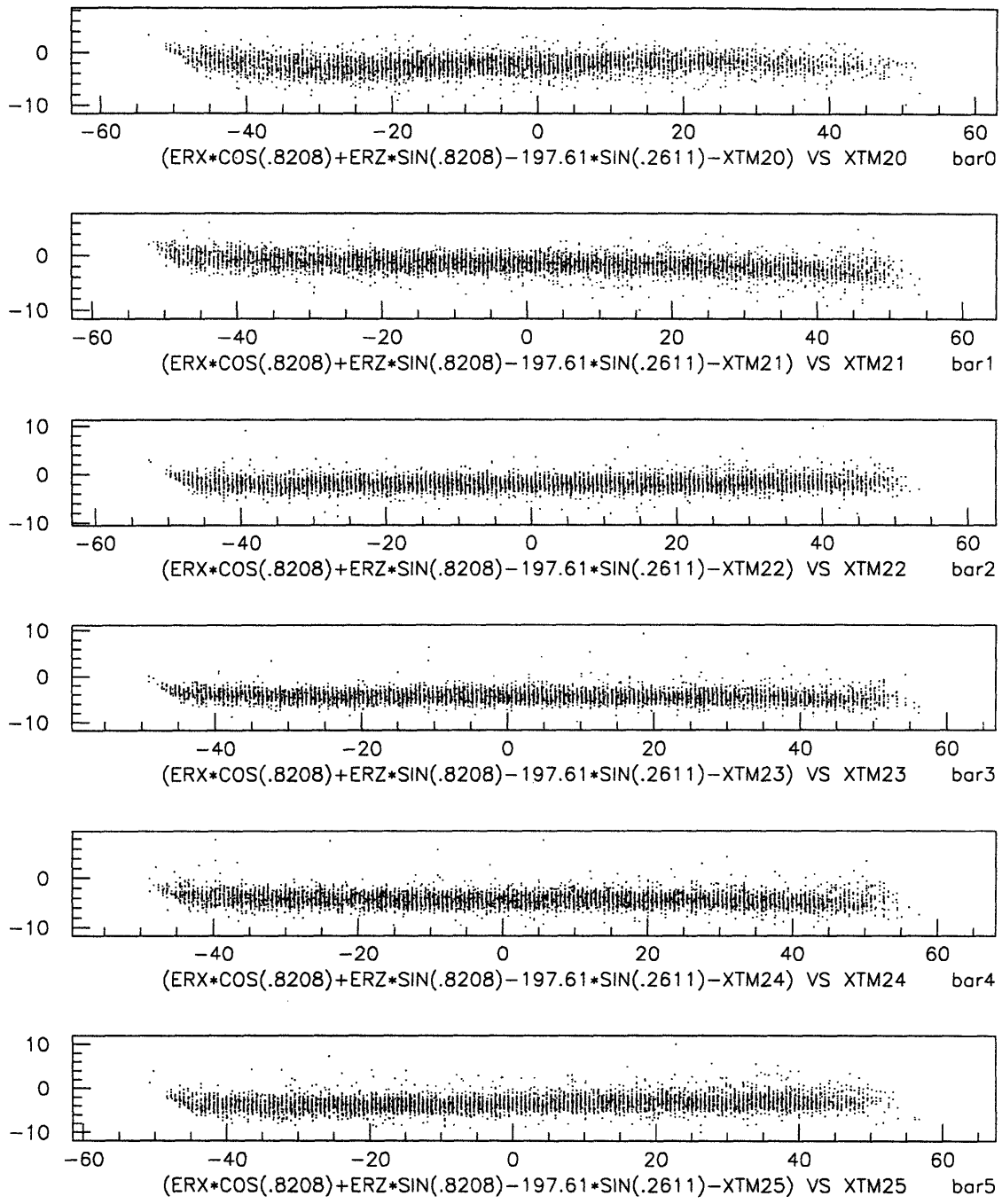

Figure E.2. The difference of intersection position between that calculated using the detector bar end PMTs' timing informations and that using the wire chamber informations is plotted against the hit position from timing informations for the right side detector bars 0, 1, 2, 3, 4, and 5.

tof calibration was undertaken to resolve the above questions.

In section 5.3.3, it was mentioned that the 'neutron' tof offsets were obtained by comparing the missing momentum p_m distribution of the ^{3}He neutron and the ^{3}He proton. The individual missing momentum components, particularly p_{m_x} and p_{m_z} were not centered around zero nor was it clear then that it should be centered without any knowledge of the experimetal acceptance for the missing momentum components.

As discussed in section 5.2, the 'neutron' tof was obtained from the E detector tfc and the time at the vertex projected backward from proton dE tdc in the detector arm on opposite side of the beam. In the time projection, the proton energy loss at the passage through the dE start scintillator, the thin aluminum target chamber window, and the silicon microstrip detector were corrected. Similar energy loss correction was made for the outgoing 'neutron' on the other side of the beam. For each scintillator bar, the measured momentum was then fitted to a calculation to determine the time offsets discussed in section 5.2. The fit program was a combined product of the relevant parts from the analyzer and the PCT fitting codes. The fit analysis was carried out in detail only for one hydrogen run, and the results are presented below.

Since, small changes in the position offsets provided by the cosmic ray analysis of the Ohio State University, as mentioned above, had no effects on the asymmetries, the position offsets were left unchanged from the original values. The correction of ionization loss of the proton energy in each medium was determined by path integration of the Bethe-Bloch equation, The kinetic energy before passage through a medium can be projected by an iterative procedure from either the final kinetic energy after energy loss or the averaged kinetic energy determined from the tof measurement. This allowed determination of the particle kinematics at the vertex. The time offsets obtained for the tof were dependent on the procedure of energy loss correction. If the Bethe-Bloch equation were slightly modified, the data could still be fitted to the calculation reasonably well giving new tof offsets. Also, changing slightly the detector location or angular position changed slightly the tof offsets. Therefore the tof offsets obtained could only be used with corresponding energy correction procedure and detector configuration. Below are plots of the momentum distributions for the proton and the 'neutron' in the left detector arm.

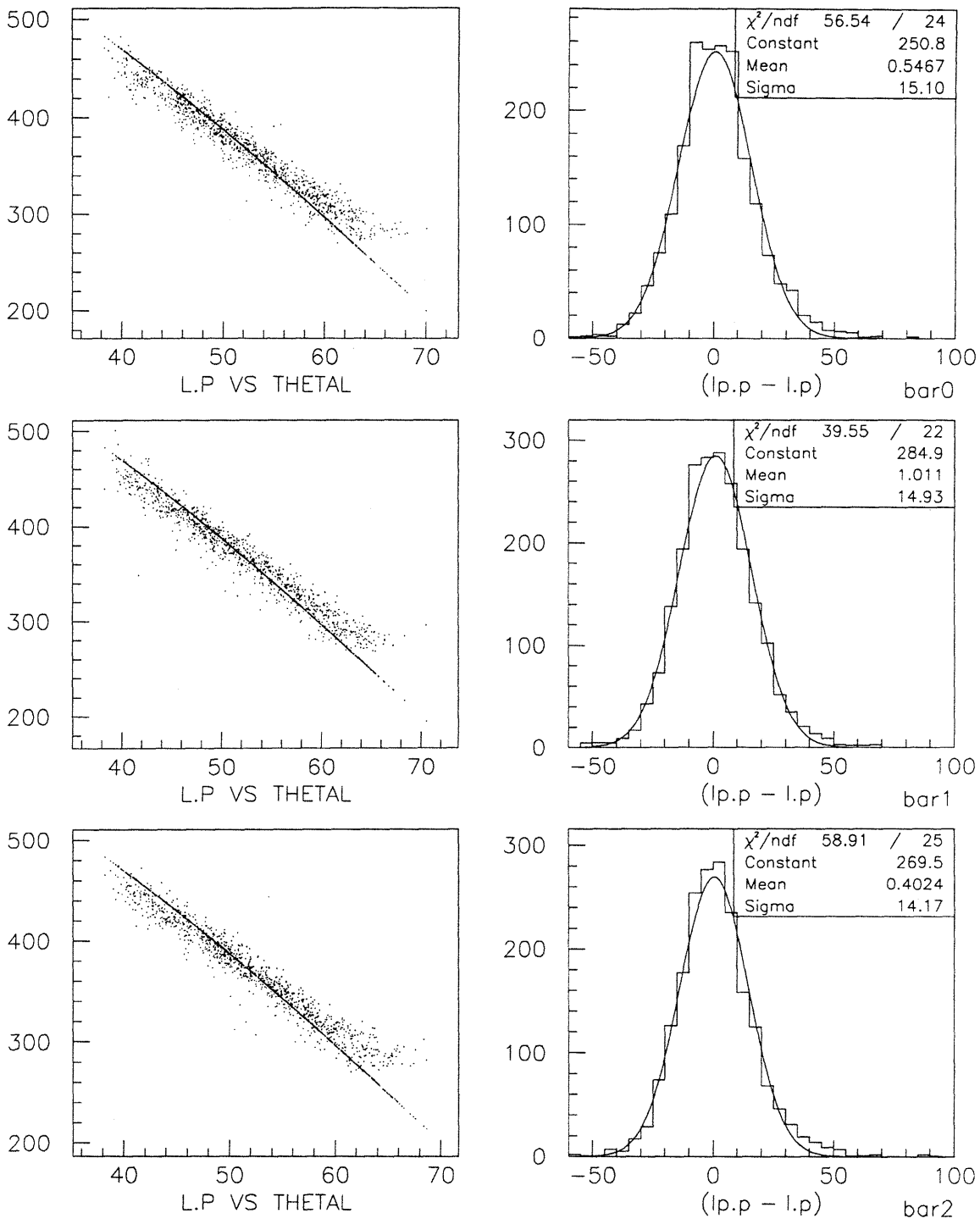

Figure E.3. Momentum fit of the 197 MeV hydrogen data for the proton tof mechanism in the left detector for bars 0, 1, and 2.

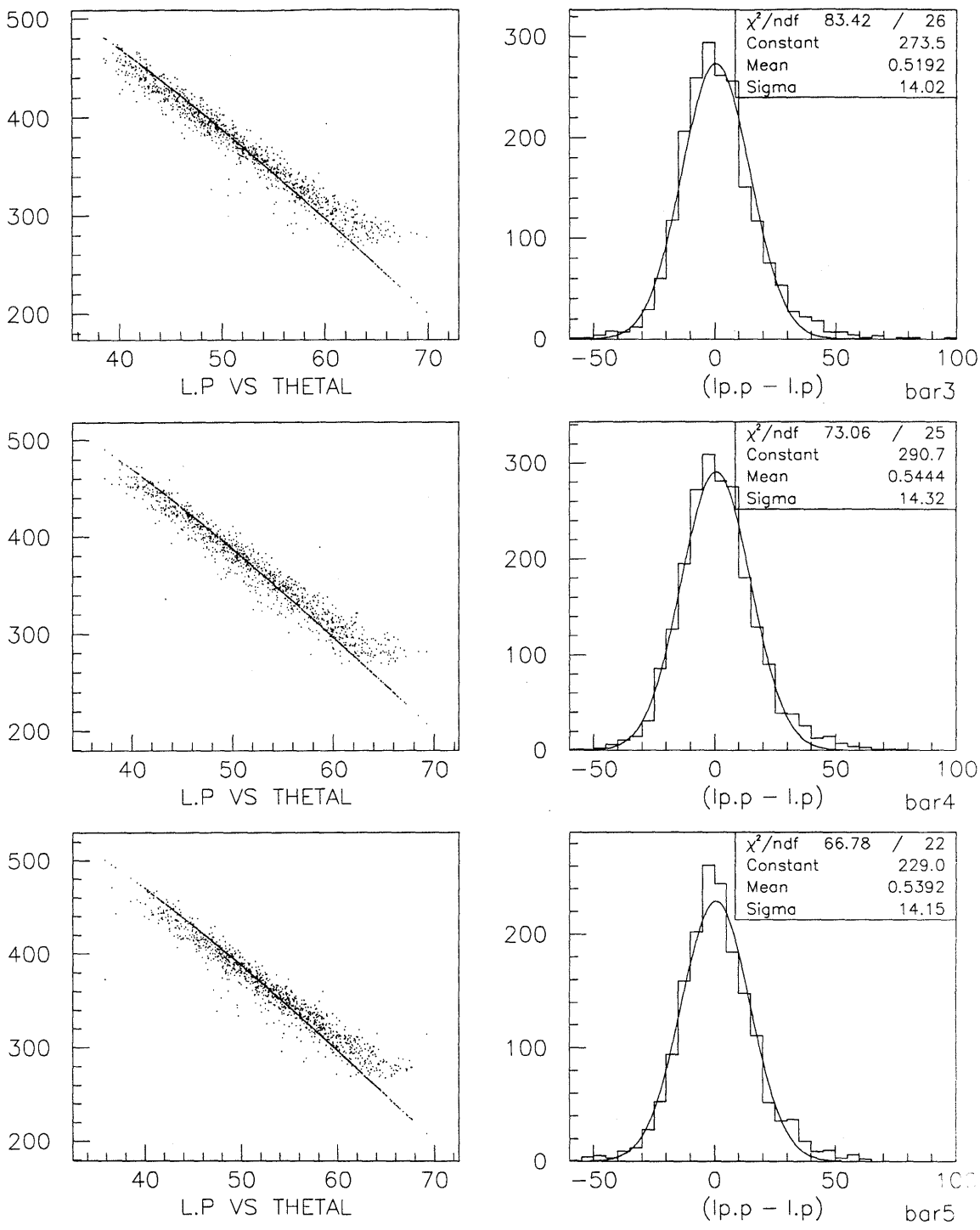

Figure E.4. Momentum fit of the 197 MeV hydrogen data for the proton tof mechanism in the left detector for bars 3, 4, and 5.

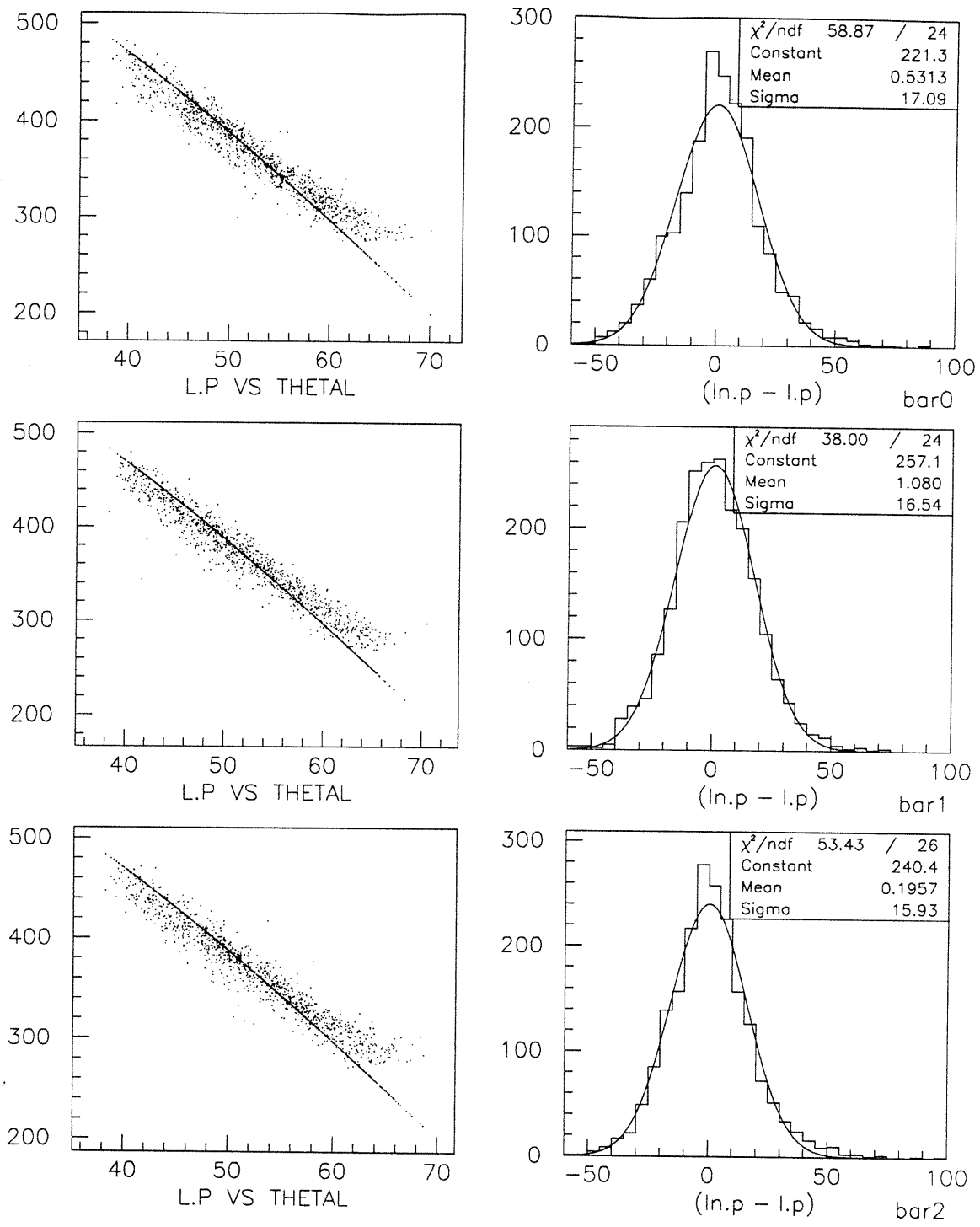

Figure E.5. Momentum fit of the 197 MeV hydrogen data for the neutron tof mechanism in the left detector for bars 0, 1, and 2.

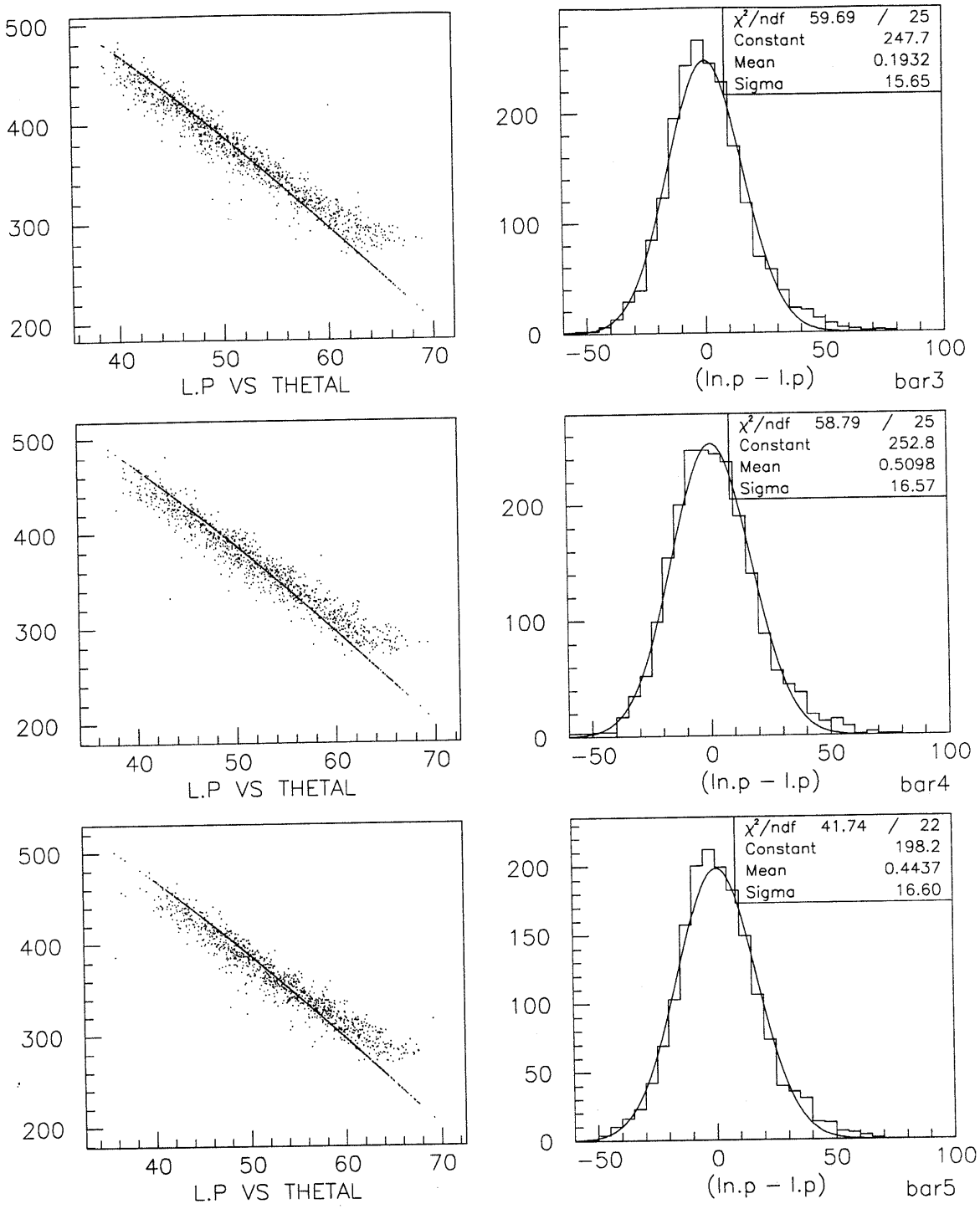

Figure E.6. Momentum fit of the 197 MeV hydrogen data for the neutron tof mechanism in the left detector for bars 3, 4, and 5.

When the missing momentum distributions for the p-p reaction were generated, it was noticed that the distributions for p_{m_x} and p_{m_z} were not centered exactly at zero. It was later found that the angle of the wire chamber planes in the right side detector arm could be closed in, to center the peaks at zero. The right side wire chamber planes angle was closed in by 0.8°, an equal amount as the offset seen in the opening angle of the recoiling p-p's when compared to the calculation in figure E.7. The results of the fit to the momentum for each scintillator bar in figures E.3-E.6 were with the wire chamber angle in the right detector arm adjusted by 0.8°. The position of the peak was very sensitive to the error in the angular postion of the detector arms. A difference of of 0.8° in each detector arm could cause a shift of the peak by 5-7 MeV in the missing momentum in the y or the z direction. The missing momentum and energy resolutions for the reactions pp, LnRp, and LpRn are given in table E.1.

Reaction	Pm (MeV/c)	Em (MeV)
pp	25	7.8
LnRp	27	7.8
LpRn	24	7.9

Table E.1. Missing momentum and energy resolutions for the reactions pp, LnRp, and LpRn, obtained from the results of the tof fitting above.

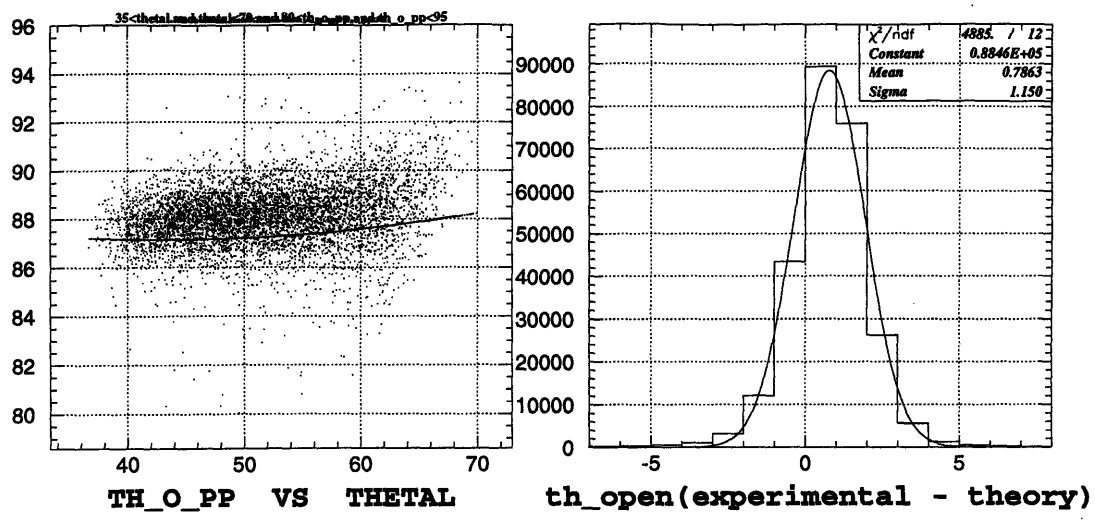

Figure E.7. θ_{open} is plotted as a function of θ_{L}; the calculated θ_{open} as a function of θ_{L} is the heavy line. The difference between the two shown in the histogram on the right is only $0.8 \pm 1.2°$. The results shown are before the wire chamber angle in the right detector arm was closed by 0.8°.

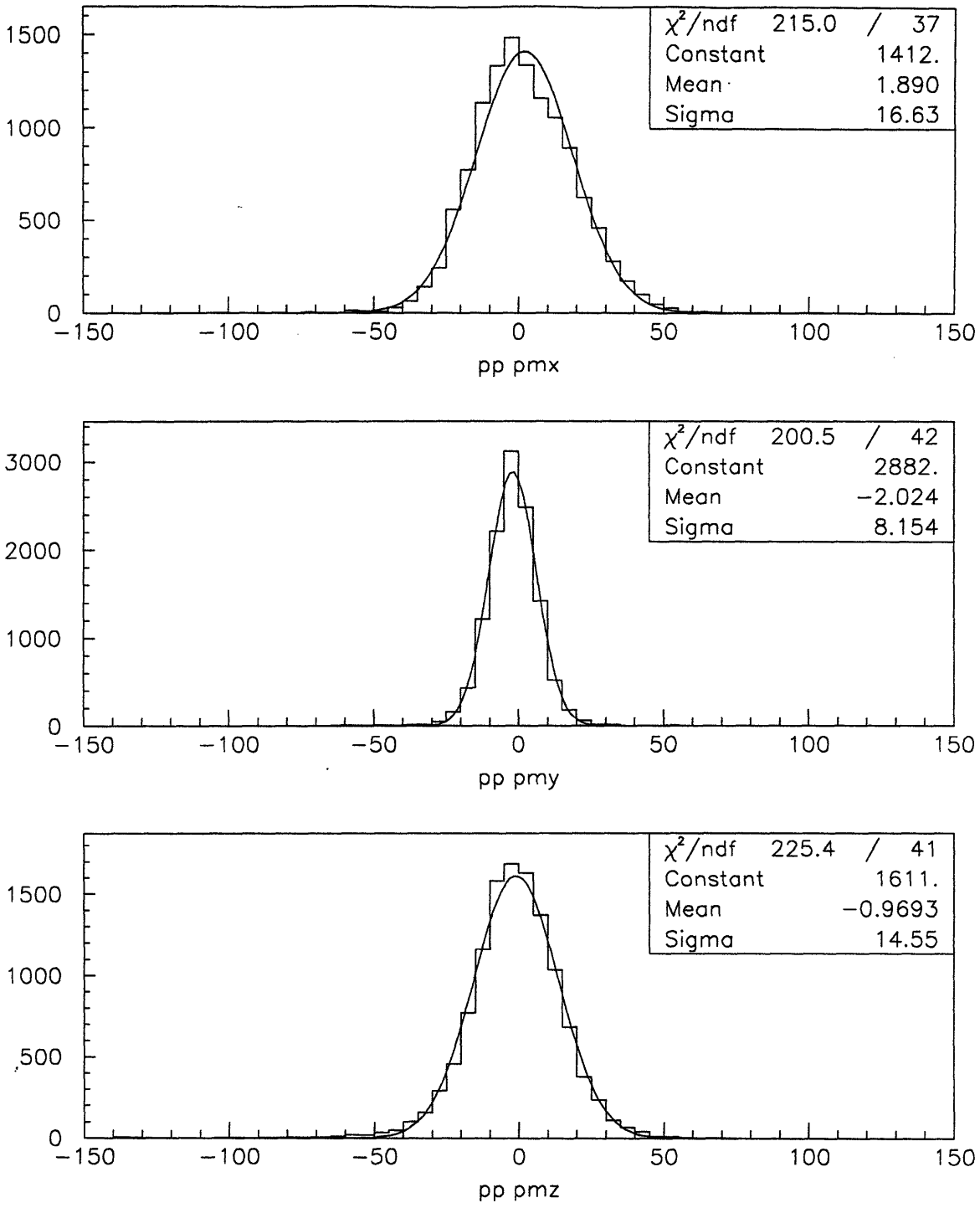

Figure E.8. Missing momentum distributions of the 197 MeV hydrogen data for the pp reaction.

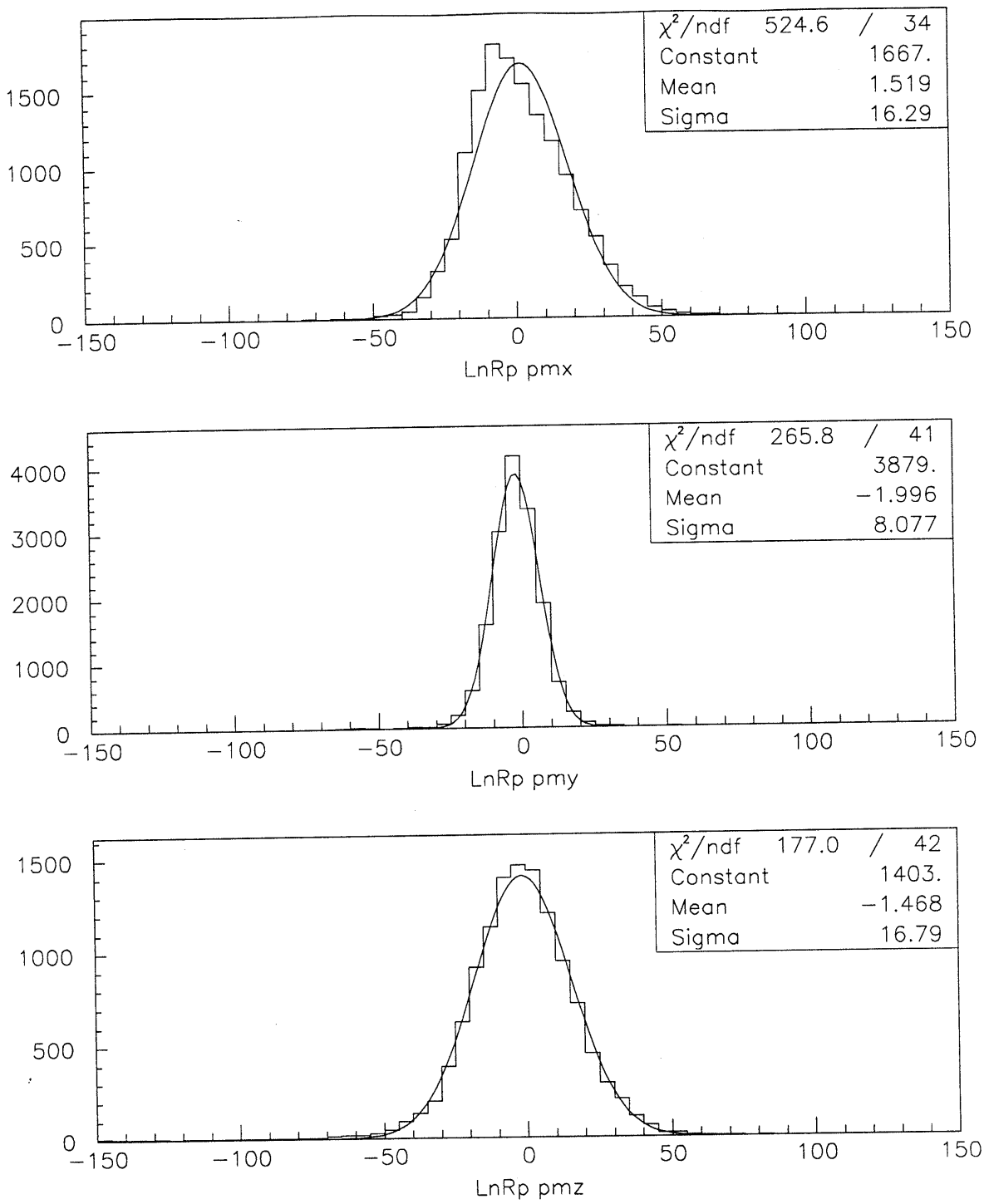

Figure E.9. Missing momentum distributions of the 197 MeV hydrogen data for the LnRp reaction.

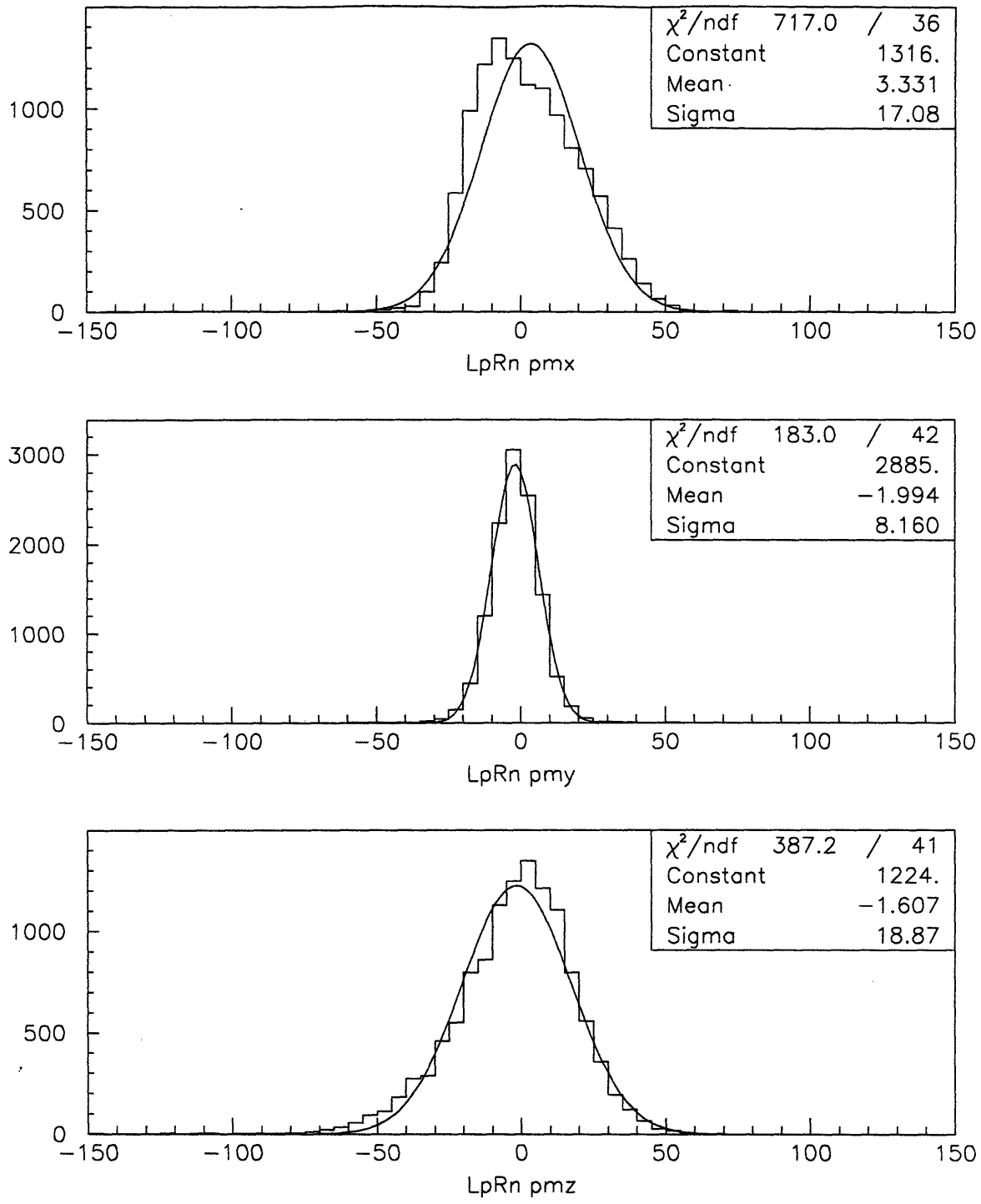

Figure E.10. Missing momentum distributions of the 197 MeV hydrogen data for the LpRn reaction.

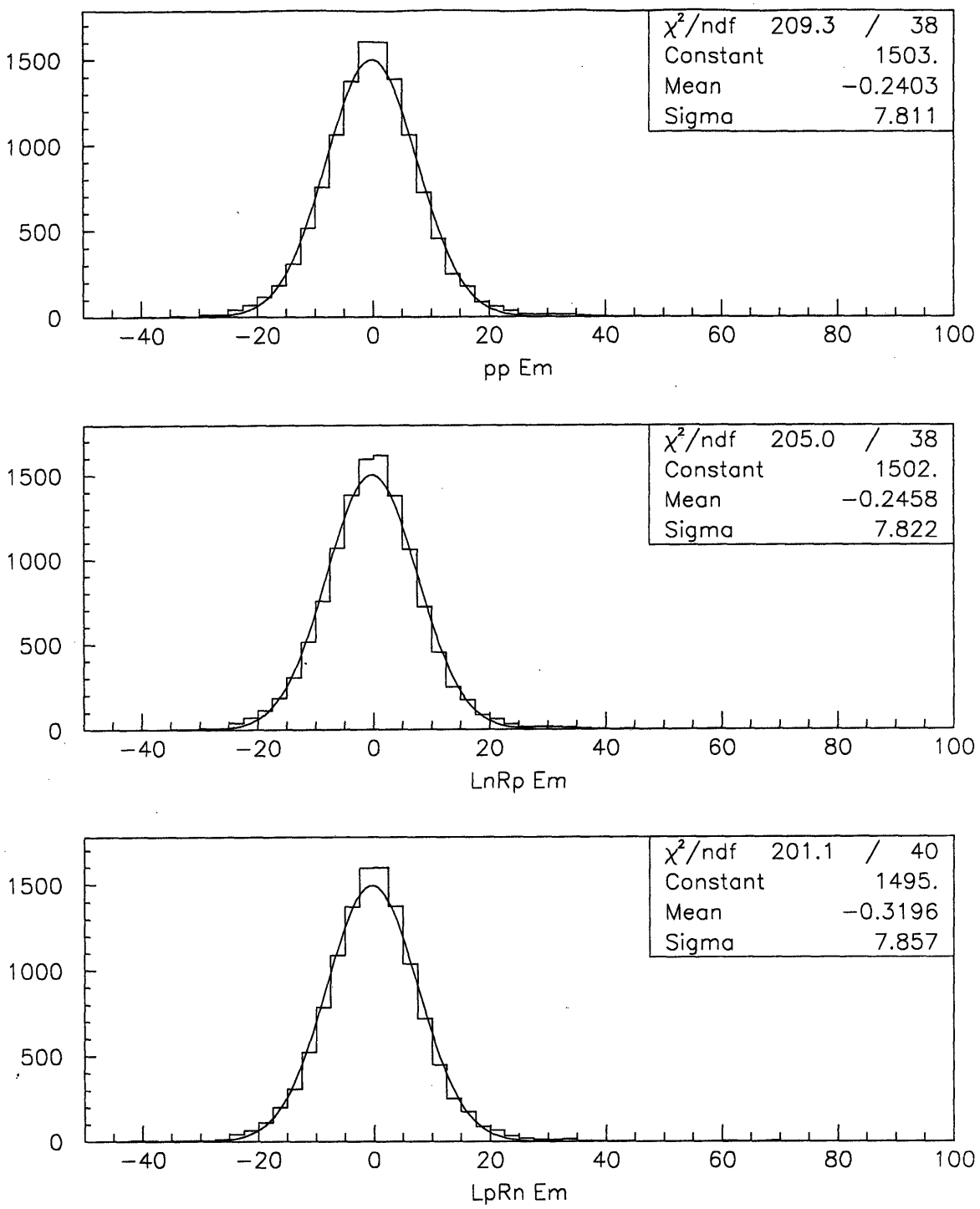

Figure E.11. Missing energy distributions of the 197 MeV hydrogen data.

4271-23